Title

Interface Energy and Particle Size Effects on Effective Properties and Damage Energy Dissipation in Nanocomposites

Permalink

https://escholarship.org/uc/item/9r1264vf

Author

Chuang, Chung-Wen

Publication Date

2014

Peer reviewed|Thesis/dissertation

UNIVERSITY OF CALIFORNIA

Los Angeles

Interface Energy and Particle Size Effects on Effective Properties

and Damage Energy Dissipation in Nanocomposites

A dissertation submitted in partial satisfaction of the

requirements for the degree Doctor of Philosophy

in Civil Engineering

by

Chung-Wen Chuang

2014

ABSTRACT OF THE DISSERTATION

Interface Energy and Particle Size Effects on Effective Properties and Damage Energy Dissipation in Nanocomposites

by

Chung-Wen Chuang

Doctor of Philosophy in Civil Engineering

University of California, Los Angeles, 2014

Professor Jiann-Wen Ju, Chair

Nowadays, since the materials science and technique have been further advanced to the characteristic size of solids in nano-size structures and nanocomposites, the interface/surface energy effect on mechanical and physical properties and damage energy dissipation of a nano-scale material or composite becomes significant and cannot be ignored. Therefore, the interface/surface energy and particle size effects on the effective properties and the damage dissipation in nanocomposites are investigated. In this research, two viewpoints of observing the

interface/surface energy effect are provided in Chapters 3-5 and Chapter 6. The first is to study

the interface/surface energy effect on the effective properties of the composite material upon the

mechanism of micromechanics, while the second is to investigate the interface/surface energy

effect on the energy dissipation due to the interfacial debonding between the particles and the

matrix in the framework of the probability, such as the logarithmic normal distribution and

Weibull's distribution function. In addition, another method, called Rigid-Body-Spring Model

(RBSM) method, is introduced in Chapter 7. In reality, the practical construction materials

usually contain multi-phases, like concrete, wood, brick, masonry, etc. Accordingly, finding an

easy and convenient method to estimate the interface/surface energy effect on those materials

with multiple phases, so as to replace time-consuming and complicated micromechanical

operations for the multiple-phase composites, is worth investigating and developing. 3D RBSM

method is easy to incorporate with our present model by adding the illustrative results based on

the interface/surface energy effect into RBSM's constitutive model. In conclusion, the objective

of this research is to develop the characteristic analytical expressions of the effective properties

and the damage energy dissipation of the composite, especially the nanocomposite, with the

interface/surface energy and particle size effects. Furthermore, since parts of the special

cases/illustrations and/or formulations in the research is simplified with some assumptions, such

as the axisymmetric stresses or loads, symmetric geometry of structures, fewer phases of

composites, small deformations, linear elastic moduli of materials, linearized parameters, etc., more complicated conditions and/or multi-physical parameters can be modified and induced in the present analytical models in the future.

The dissertation of Chung-Wen Chuang is approved.

Ertugrul Taciroglu

Jian Zhang

Jenn-Ming Yang

Jiann-Wen Ju, Committee Chair

University of California, Los Angeles

2014

To my beloved wife

Chien-Yun Ku

&

To my parents

TABLE OF CONTENTS

3. INTERFACE ENERGY EFFECT ON SIZE-DEPENDENT EFFECTIVE PROPERTIES OF A HETEROGENEOUS MATERIAL **30**

4. INTERFACE ENERGY EFFECT ON SIZE-DEPENDENT EFFECTIVE ELASTIC MODULI OF THREE-PHASE COMPOSITES WITH RANDOMLY LOCATED AND INTERACTING SPHERICAL PARTICLES OF DISTINCT PROPERTIES **84**

5.   INTERFACE ENERGY EFFECT ON SIZE-DEPENDENT EFFECTIVE TRANSVERSE ELASTIC MODULI OF THREE-PHASE HYBRID FIBER-REINFORCED COMPOSITES WITH RANDOMLY LOCATED AND INTERACTING ALIGNED CIRCULAR FIBERS OF DISTINCT ELASTIC PROPERTIES AND SIZES 144

7. INTRODUCTION TO RIGID-BODY-SPRING MODEL (RBSM) METHOD AND PAVE THE WAY FOR FUTURE INVESTIGATIONS IN INTERFACE ENERGY EFFECT ... 249

LIST OF FIGURES

LIST OF TABLES

ACKNOWLEDGMENTS

student researcher at Nagoya University during the summer time in 2013.

Last but not least, I would like to express my deepest gratitude and appreciation to my lovely wife, Chien-Yun Ku, my parents and all other family members for their generous support and devotion. Without their endless love, encouragement and dedication, my doctoral study at UCLA would not have ever come true.

VITA

1996-2000   B.S., Civil Engineering Department

                    National Taiwan University (NTU), Taipei, Taiwan

2002-2003   Teaching Assistant/Lecturer

                    Tien-Yi Civil Engineering and Architecture Academy, Taichung, Taiwan

2003-2004   Associate Technical Specialist

                    Department of Public Works at Taipei County Government, Taipei, Taiwan

2004   Licensed Professional Engineer in Civil Engineer, Taiwan

2004-2005   Licensed Civil Engineer/Project Manager

                    Kuan-Pon Engineering Consultants, Inc., Taichung, Taiwan

2005-2007   M.S., Department of Civil and Environmental Engineering

                    University of California, Davis (UCD), Davis, CA

2007-2008   M.S., Department of Civil and Environmental Engineering

                    University of Southern California (USC), Los Angeles, CA

2009-2014   Graduate Student Researcher

                    Teaching Assistant/Teaching Associate/Teaching Fellow

Department of Civil and Environmental Engineering

University of California, Los Angeles (UCLA), Los Angeles, CA

2013   Visiting Graduate Student Researcher

Department of Civil Engineering

Nagoya University, Nagoya, Japan

2014   Licensed Professional Engineer in Civil Engineer, CA

PUBLICATIONS AND PRESENTATIONS

Chuang, C.W. (2013). "Simulation of RC structures under cyclic loading." *JUACEP Summer Program 2013 at Nagoya University*, 95-104.

Ju, J.W., Wu, Y., and **Chuang, C.W.** (2010). "Project Summary Report for Army SBIR Phase-II Project." PredictionProbe, Inc., Newport Beach, CA.

Ju, J.W., Yanase, K., Wu, Y., and **Chuang, C.W.** (2009). "Project Progress Reports for Army SBIR Phase-II Project." PredictionProbe, Inc., Newport Beach, CA.

Chapter 1

INTRODUCTION

1.1 Introduction to Composite Materials

The word "composite" means, "consisting of two or more distinct parts". That is to say, a material consisting of two or more distinct constituent materials or phases can be considered as a composite material (Agarwal et al., 2006). In composite materials, one of the phases, called the "inclusion" or "reinforcement", is usually stiffer and stronger than the continuous phase, whereas the less stiff and weaker continuous phase is called the "matrix". The inclusions/reinforcements in composites can be of various forms, such as fibers, whiskers, and particulates, which can be made of alumina, silicon carbide, silicon nitride, boron, and graphite, etc. Otherwise, the matrix material in composites serves as the binder material, which is made of polymers, metals, ceramics, or carbons, etc. In essence, the matrix is used not only to support and protect the inclusions/reinforcements but also to transfer local stresses between perfectly bonded and partially debonded/broken from one inclusion/reinforcement to another under three-dimensional complex loadings. The properties of composites are strongly influenced by the properties of the constituent materials, their distributions, and the interactions between heterogeneous constituent materials. Furthermore, the properties of composite materials may be predicted by the volume-fraction sum of the properties of the constituents, or the constituents may interact with each other in a synergic manner to provide the properties of the composites, which may not be

accounted for by a simple volume-fraction sum of the constituent properties. Moreover, the geometry of inclusion/reinforcement, such as shape and size, usually dominates the properties of composites. In reality, however, it is challenging to take all of them into account in the development of theoretical descriptions of composites.

Composite materials, consisting of two or more materials or phases, are admitted and employed extensively to form specific new materials with certain desirable material properties and advanced performance capabilities. Due to the outstanding features of low density/weight, high strength, high stiffness, high toughness, high corrosion resistance, high temperature resistance, better wear resistance, and better wear environmental durability, composite materials have been widely applied the aircraft, automobile, sporting goods, and biomedical industries in the late 1970s (cf. **Figure 1.1**). However, the origin of the composite material can be traced back earlier to straw-reinforced bricks in ancient Egypt. In the nineteenth century, the masonry reinforced by iron rods becomes the predecessor of the present reinforced concrete. In 1942, the first boat reinforced by the glass fibers was made, and extensive applications of reinforced plastics to aircraft and electrical components were introduced. In the 1960s, boron and high strength carbon fibers were developed with the application of advanced composites to aircraft components. Metal matrix composites (MMCs), such as boron/aluminum, were introduced in the late 1970s. In 1973, DuPont developed Kevlar fibers (Daniel and Ishai, 1994).

(a) A carbon-fiber composite fuselage section (Boeing)
http://boeingblogs.com/randy/archives/photos/composite_barrel.html

(b) A carbon-fiber composite frame and wheels (Lamborghini)
http://www.autoblog.com/photos/lamborghini-aventador/

(c) A carbon fiber composite bike (Giant)
http://sanfrancisco.olx.com/pictures/giant-tcr-0-carbon-fiber-composite-bike-iid-222119644

Figure 1.1 Application of composite materials

In addition to the applications of composites in practice, the study of composite is a subject with a long history, and many theories and concepts of composites were developed by some of the greatest scientists. For example, Poisson (1826) established a theory of induced magnetism in the body, which was assumed to be composed of conducting spheres embedded in a nonconducting material. Faraday (1839) proposed a model for dielectric materials that composed of metallic globules separated by insulating material. Maxwell (1873) solved for the conductivity of a diluted suspension of conducting spheres in a conducting matrix. Rayleigh (1892) found a system of linear equation, which could five the effective conductivity of nondilute square arrays of cylinders or cubic lattices of spheres. Einstein (1905) calculated the effective shear viscosity of a suspension of a rigid sphere in a fluid.

1.2 Classification of Composite Materials

A brief classification of composite materials is shown in **Figure 1.2**. Ther are four commonly acknowledged types of composite materials, including

(1) Fibrous composite materials that consist of fibers in a matrix.

(2) Laminated composite materials that consist of layers of various materials.

(3) Particulate composite materials that are composed of particles in a matrix.

(4) Combinations of some or all of the first three types.
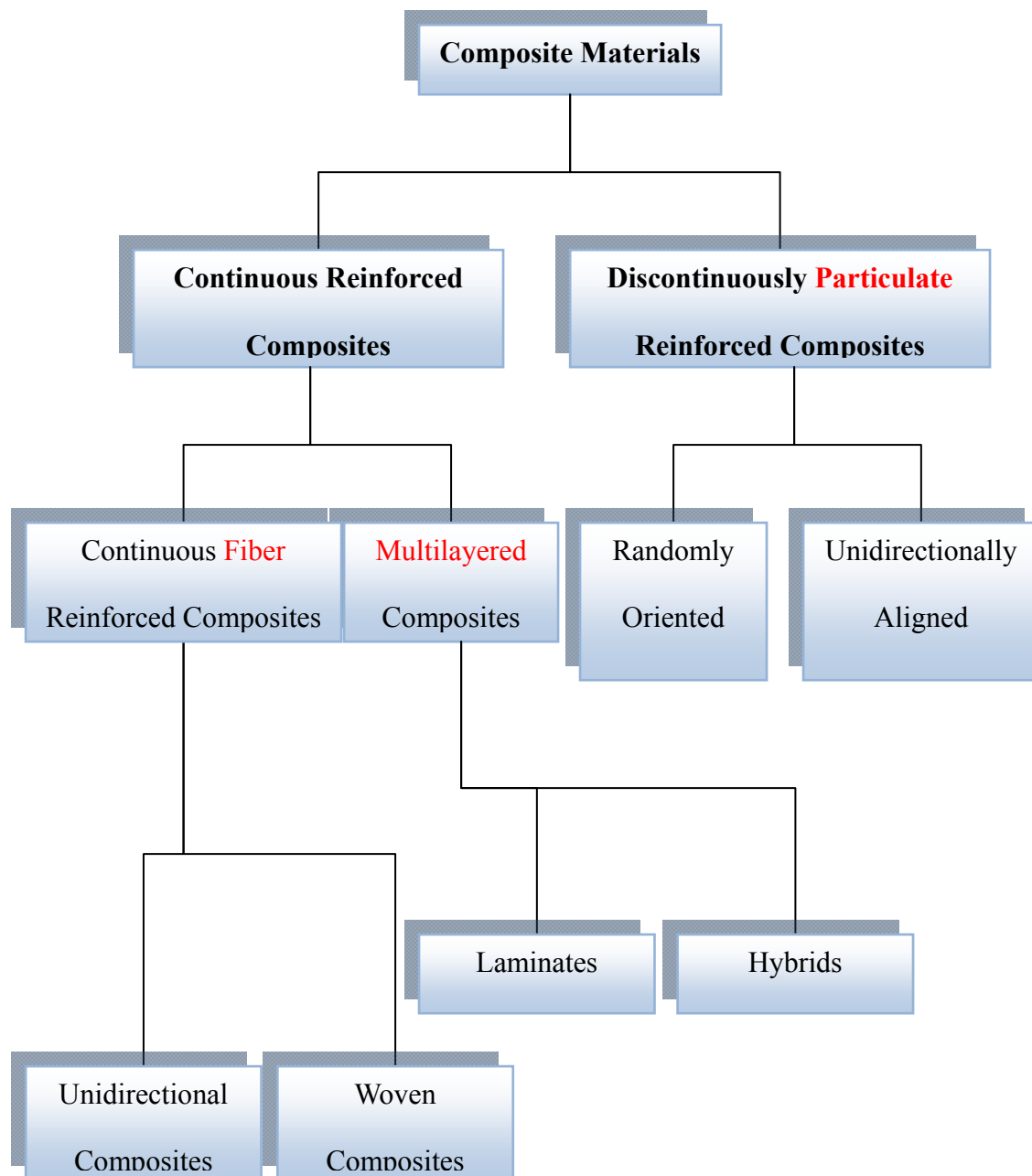
Figure 1.2 Classification of composite materials (Sun, 1998)

Composite materials can also be classified according to their matrix phase. For example, polymer matrix composites (PMCs), ceramic matrix composites (CMCs), and metal matrix composites (MMCs) are the most popular matrix materials in composites. Materials within these categories are often called the advanced composite materials. Advanced materials combine the properties of high strength, high stiffness, low weight, corrosion resistance, high temperature resistance, and in some cases special electrical properties. This combination of properties makes advanced composite materials very attractive in the applications of next generation aircraft and aerospace structural parts. Advanced composite materials are originally developed primarily for the applications of aerospace and defense industries. To date, the advanced composite materials are also widely adopted in civil engineering applications. For instance, carbon-fiber and glass-fiber have been used as prestressing materials, particularly for areas in which the corrosion and stress embrittlement of conventional prestressed steel easily take place. Moreover, a corresponding research has been conducted to enhance the efficiency and convenience of column retrofit by bonding jackets composed of composite materials, like glass-fiber and carbon-fiber, to the column with epoxy (Priestley et al., 1995).

1.3 Micromechanics and Representative Volume Element (RVE)

Traditional continuum mechanics deals with idealized materials under the assumptions of

(1) The elastic properties of a solid at a given point are the same in every direction (isotropy).

(2) The material property is the same at all points within the solid (homogeneity).

These two assumptions render a uniform stress/strain distribution within an infinitesimal material

element. Through the optical morphology, however, it is found that the microscopic structure of a solid is complex, consisting of grain boundaries, inclusions, cracks and other defects (Nemat-Nasser and Hori, 1993). Obviously, the stress/strain fields within such an infinitesimal material element and its neighborhood are not uniform at the microscopic level. Furthermore, it is impractical, even impossible, to account for each of them in engineering design and analysis. Hence, it is adequate to characterize the overall or effective properties of those heterogeneous/anisotropic materials by taking advantage of a rigorous theoretical framework (Qu and Cherkaoui, 2006), and this is the major objective of micromechanics in practice.

In micromechanics, an important concept used to characterize the effect of inhomogeneities is the RVE (Representative Volume Element) (cf. Nemat-Nasser and Hori, 1993). An RVE for a material point of a continuum mass defines a material volume that statistically represents the infinitesimal material neighborhood of that material point. In other words, an RVE features the "mesoscopic" length scale that is much larger than the characteristic length scale of inhomogeneity/inclusion but is much smaller than the characteristic length scale of the "macroscopic" specimen. On the foundation of the concept of the RVE, micromechanics can describe the continuum constitutive relations in terms of the properties and structure of the micro-constituents within the RVE. Mathematically, this type of procedure is related to the ensemble-average (homogenization) method and leads to an overall micromechanical governing field equation.

1.4 Nanocomposite and Interface/Surface Energy

If a composite material contains nano-scale inclusions/reinforcements, this composite is called a nanocomposite. Moreover, in this research, the mechanism of nanocomposites is mainly derived based on the micromechanics of solids. The only difference is that the effect of the interface/surface energy between the particles and the matrix is considered in the derivations. Therefore, the interface/surface tension (and interface/surface energy) is introduced first here. Interface/surface tension is a contractive tendency of the surface of a liquid that allows the surface of the liquid to resist an external force. It is revealed, for example, in the floating of some objects on the surface of water, even though they are denser than water, and in the ability of some insects (e.g. water striders, as shown in **Figure 1.3**) to run on the water surface. This property is caused by cohesion of similar molecules, and is responsible for many of the behaviors of liquids. Furthermore, in composites, many researchers have been provided that the interface/surface tension also exists between inclusions and the matrix. Specifically, as the characteristic size of inclusions is smaller, the effect of the interface/surface tension becomes larger, especially in nano-scale composites. Therefore, since the nanocomposites is considered in this research, the effect of the interface/surface tension should be taken into account on the mechanical and physical properties of composites, for instance, such as the influence on the effective moduli in Chapter 3 and on the damage energy dissipation in Chapter 4.

Interface/surface tension has the dimension of force per unit length, or of energy per unit area. These two are equivalent. But when the dimension of energy per unit of area is regarded, the term of "interface/surface energy", which is a more general term in the sense that it applies to not only liquids but also solids, is commonly used. Moreover, in materials science,

interface/surface tension is used for either surface stress or surface free energy.

The values at the specific temperature of the interface/surface energy, in the units of energy per unit area or force per unit length, for some kinds of common liquids are tabulated, as shown in **Table 1.1**. It is found that the typical values of the interface/surface energy are within the range between 10 and 90 mJ/m^2, or 0.010 and 0.090 J/m^2, except for the extreme value of Mercury.

Figure 1.3 Water Strider (Charles Lewallen)

Liquid	Temperature (°C)	Interface energy (mJ/m² or mN/m)
Acetic acid	20	27.6
Acetic acid (40.1%) + Water	30	40.68
Acetic acid (10.0%) + Water	30	54.56
Acetone	20	23.7
Diethyl ether	20	17.0
Ethanol	20	22.27
Ethanol (40%) + Water	25	29.63
Ethanol (11.1%) + Water	25	46.03
Glycerol	20	63
n-Hexane	20	18.4
Hydrochloric acid 17.7M aqueous solution	20	65.95
Isopropanol	20	21.7
Mercury	15	487
Methanol	20	22.6
n-Octane	20	21.8
Sodium chloride 6.0M aqueous solution	20	82.55
Sucrose (55%) + water	20	76.45
Water	0	75.64
Water	25	71.97
Water	50	67.91
Water	100	58.85

Table 1.1 Values of the interface/surface energy for some kinds of common liquids (Dean, 1985)

1.5 Objectives

In this research, two viewpoints of observing the interface/surface energy effect are provided. First, in Chapters 3, 4, and 5, the interface/surface energy effect on the effective properties of the composite material upon the mechanism of micromechanics is studied. In Chapter 6, the interface/surface energy effect on the energy dissipation due to the interfacial debonding between the particles and the matrix in the framework of the probability, such as the logarithmic normal distribution and Weibull's distribution function is investigated. In addition, another method, called Rigid-Body-Spring Method (RBSM), is introduced in Chapter 7, to provide an idea for future investigations in the interface/surface energy effect on the effective properties of the multi-phase composites.

1.6 References

[1] Agarwal, B. D., Broutman, L. J., and Chandrashekhara, K. C. (2006). "Analysis and performance of fiber reinforced composites." (3rd edition), John Wiley and Sons, Inc.

[2] Daniel, I. M., and Ishai, O. (1994). "Engineering Mechanics of Composite Material." Oxford University Press.

[3] Dean, J. A. (1985). "Lange's Handbook of Chemistry" (13th edition), McGraw-Hill, 1661−1665.

[4] Einstein, A. (1906). "Eine neue Bestimmung der Molekul-Dimension." *Annalen der Physik* 19, 289-306; and (errata) 34, 591-692 (1911). English translation in: Investigation on the

theory of Brownian motion, 36-62, Dover, 1956.

[5] Faraday, M. (1839). "Experimental researches in electricity." Richeard and John Edward Taylor. Pars. 1669, 1670.

[6] Ko, Y. F. (2005). "Effective elastoplastic-damage model for fiber-reinforced metal matrix composites with evolutionary fibers debonding." Ph.D. Dissertation at University of California, Los Angeles, CA.

[7] Maxwell, J. C. (1873). "A treatise on electricity and magnetism." Clarendon Press, Oxford, United Kingdom.

[8] Nemat-Nasser, S., and Hori, M. (1993). "Micromechanics: overall properties heterogeneous materials." Elsevier Science Publisher B.V, Netherland.

[9] Nimmer, R. P., Bankert, R. J., Russell, E. S., Smith, G. A., and Wright, P. K. (1991). "Micromechanical modeling of fiber matrix interface effects in transversely loaded SiC Ti-6-4 metal matrix composites." *Journal of Composites Technology & Research*, 13(1), 3-13.

[10] Priestley, M. J. N., and Seible, F. (1995). "Design of seismic retrofit measures for concrete and masonry structures." *Construction and Building Materials*, 9(6), 365-377.

[11] Qu, J., and Cherkaoui, M. (2006). "Fundamentals of micromechanics of solids." John Wiley & Sons, Inc.

[12] Sun, L. Z. (1998). "Micromechanics and overall elastoplasticity of discontinuously reinforced metal matrix composites." Ph.D. Dissertation at University of California, Los Angeles, CA.

[13] Yanase, K. (2009). "Micromechanics and effective thermo-mechanical damage and deformation responses of composite materials." Ph.D. Dissertation at University of

California, Los Angeles, CA

Chapter 2

LITERATURE REVIEW

Based on the theory of micromechanics, when a material contains inhomogeneities of different material properties, such as voids, cracks, grains, inclusions and other defects, there exists an internal stress (eigenstress) field in that material, even if under no external load. Such an internal stress field may be caused by the eigenstrain inside the inhomogeneities due to the misfit and phase transformation. Eshelby (1957) first introduced that under an applied stress, and the stress perturbation due to the presence of an inhomogeneity can be simulated by an eigenstress due to an inclusion when an eigenstrain is chosen properly.

2.1 Eshelby's Micromechanical Theory

Consider an infinitely extended material domain D of the elastic modulus $\mathbf{L}^{(0)}$ containing an inclusion (inhomogeneity) domain Ω of the elastic modulus $\mathbf{L}^{(1)}$. Suppose that the applied stress at infinity is $\boldsymbol{\sigma}^0(\mathbf{x})$ and the corresponding stain is $\boldsymbol{\varepsilon}^0(\mathbf{x})$. Moreover, the perturbed stress field and perturbed strain field are denoted by $\boldsymbol{\sigma}^{'}(\mathbf{x})$ and $\boldsymbol{\varepsilon}^{'}(\mathbf{x})$, respectively. In this regard, the Hooke's law leads to the form

$$\sigma_{ij}^0(\mathbf{x}) + \sigma_{ij}^{'}(\mathbf{x}) = L_{ijkl}^{(1)}\left[\varepsilon_{kl}^0(\mathbf{x}) + \varepsilon_{kl}^{'}(\mathbf{x})\right] \qquad \text{in } \Omega \qquad (2.1)$$

14

$$\sigma_{ij}^{0}\left(\mathbf{x}\right)+\sigma_{ij}^{'}\left(\mathbf{x}\right)=L_{ijkl}^{(0)}\left[\varepsilon_{kl}^{0}\left(\mathbf{x}\right)+\varepsilon_{kl}^{'}\left(\mathbf{x}\right)\right] \qquad \text{in } D-\Omega \qquad (2.2)$$

To deal with heterogeneous solids, it is convenient and effective to consider the equivalent homogeneous solids (Eshelby, 1957). First, an eigenstrain (eigenstress) field is developed to be equivalent to an inhomogeneity distribution. That is, such the distribution of inhomogeneities may be replaced by an eigenstrain field upon the equivalent mechanical effect. This equivalency mapping process is called the Eshelby's equivalent eigenstrain (eigenstress) principle (or named Eshelby's equivalence principle), which is a homogenization method. Specifically, Eshelby's equivalent eigenstrain (eigenstress) principle is used to establish a homogenized field by replacing the inhomogeneity with a homogenized inclusion through a prescribed eigenstrain field, and this homogenized field can then be mechanically equivalent to the original inhomogeneous field, as shown in **Figure 2.1**.
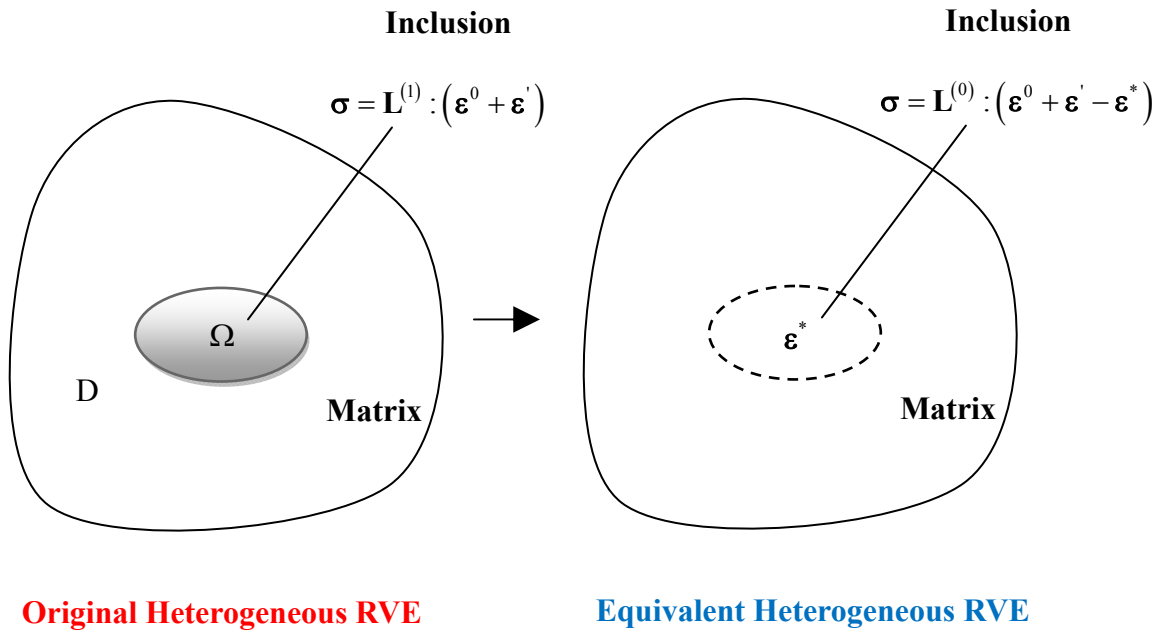
Figure 2.1 The equivalent RVE and eigenstrain

A stress-free strain $\boldsymbol{\varepsilon}^*(\mathbf{x})$ is introduced in the inclusion domain Ω to account for the mismatch of the material properties between the matrix and inclusion. Through the Eshelby's equivalence principle (see an illustrative scheme in **Figure 2.2**), the application of Hooke's law in Ω and $D-\Omega$ yields

$$\sigma_{ij}^0(\mathbf{x}) + \sigma_{ij}^{'}(\mathbf{x}) = L_{ijkl}^{(0)}\left[\varepsilon_{kl}^0(\mathbf{x}) + \varepsilon_{kl}^{'}(\mathbf{x}) - \varepsilon_{kl}^*(\mathbf{x})\right] \qquad \text{in } \Omega \qquad (2.3)$$

$$\sigma_{ij}^0(\mathbf{x}) + \sigma_{ij}^{'}(\mathbf{x}) = L_{ijkl}^{(0)}\left[\varepsilon_{kl}^0(\mathbf{x}) + \varepsilon_{kl}^{'}(\mathbf{x})\right] \qquad \text{in } D-\Omega \qquad (2.4)$$

It is found apparently that the necessary and sufficient condition for the equivalency of Eqs. (2.1) and (2.3) is

$$L_{ijkl}^{(1)}\left[\varepsilon_{kl}^0(\mathbf{x}) + \varepsilon_{kl}^{'}(\mathbf{x})\right] = L_{ijkl}^{(0)}\left[\varepsilon_{kl}^0(\mathbf{x}) + \varepsilon_{kl}^{'}(\mathbf{x}) - \varepsilon_{kl}^*(\mathbf{x})\right] \qquad (2.5)$$

In the case of an uniform stress $\boldsymbol{\sigma}^0(\mathbf{x})$ at the far field, this stress-free $\boldsymbol{\varepsilon}^*(\mathbf{x})$ is supposed to be uniform in inclusion domain Ω. Alternatively, Eq. (2.5) can also be written in form of matrix notations as following,

$$\mathbf{L}^{(1)} : \left(\boldsymbol{\varepsilon}^0 + \boldsymbol{\varepsilon}^{'}\right) = \mathbf{L}^{(0)} : \left(\boldsymbol{\varepsilon}^0 + \boldsymbol{\varepsilon}^{'} - \boldsymbol{\varepsilon}^*\right) \qquad (2.6)$$

where $\mathbf{L}^{(0)}$ and $\mathbf{L}^{(1)}$ represent the elastic stiffness of the matrix and inclusion, respectively; $\boldsymbol{\varepsilon}^0$ and $\boldsymbol{\varepsilon}^{'}$ signify the far-field strain and perturbed strain, respectively.

In addition, based on the local stress and strain field, the ensemble-averaging process (homogenization) can be performed within the representative volume element (RVE) to obtain overall effective constitutive equations and properties of the homogenized heterogeneous materials. For instance, the ensemble-averaged stress and strain are expressed by the following equations,

$$\bar{\boldsymbol{\sigma}} \equiv \frac{1}{V}\int_V \boldsymbol{\sigma}(\mathbf{x})\, d\mathbf{x} = \frac{1}{V}\left[\int_{V_0} \boldsymbol{\sigma}(\mathbf{x})\, d\mathbf{x} + \sum_{r=1}^{n}\int_{V_r} \boldsymbol{\sigma}(\mathbf{x})\, d\mathbf{x}\right] \qquad (2.7)$$

$$\overline{\boldsymbol{\varepsilon}} \equiv \frac{1}{V}\int_{V} \boldsymbol{\varepsilon}(\mathbf{x})\, d\mathbf{x} = \frac{1}{V}\left[\int_{V_0} \boldsymbol{\varepsilon}(\mathbf{x})\, d\mathbf{x} + \sum_{r=1}^{n}\int_{V_r} \boldsymbol{\varepsilon}(\mathbf{x})\, d\mathbf{x}\right] \tag{2.8}$$

where V is the volume of an RVE. Further, V_0 and V_r represent the volume of the matrix and the r th-phase inhomogemeity, respectively; n denotes the number of phases of different material properties with an exception of the matrix material. By combining the Eshelby's equivalence principle with the ensemble-averaging method, the overall constitutive relations and elastic and elastoplastic behaviors of the heterogeneous materials can then be described.

A composite RVE embedded in an infinite matrix

RVE

inhomogeneities

Eshelby's equivalence principle

$\varepsilon^{*}(\mathbf{x}) \neq 0$

+

homogeneous strain field $\varepsilon^{0}(\mathbf{x})$

perturbed strain field $\varepsilon^{'}(\mathbf{x})$

Homogeneous medium (matrix)
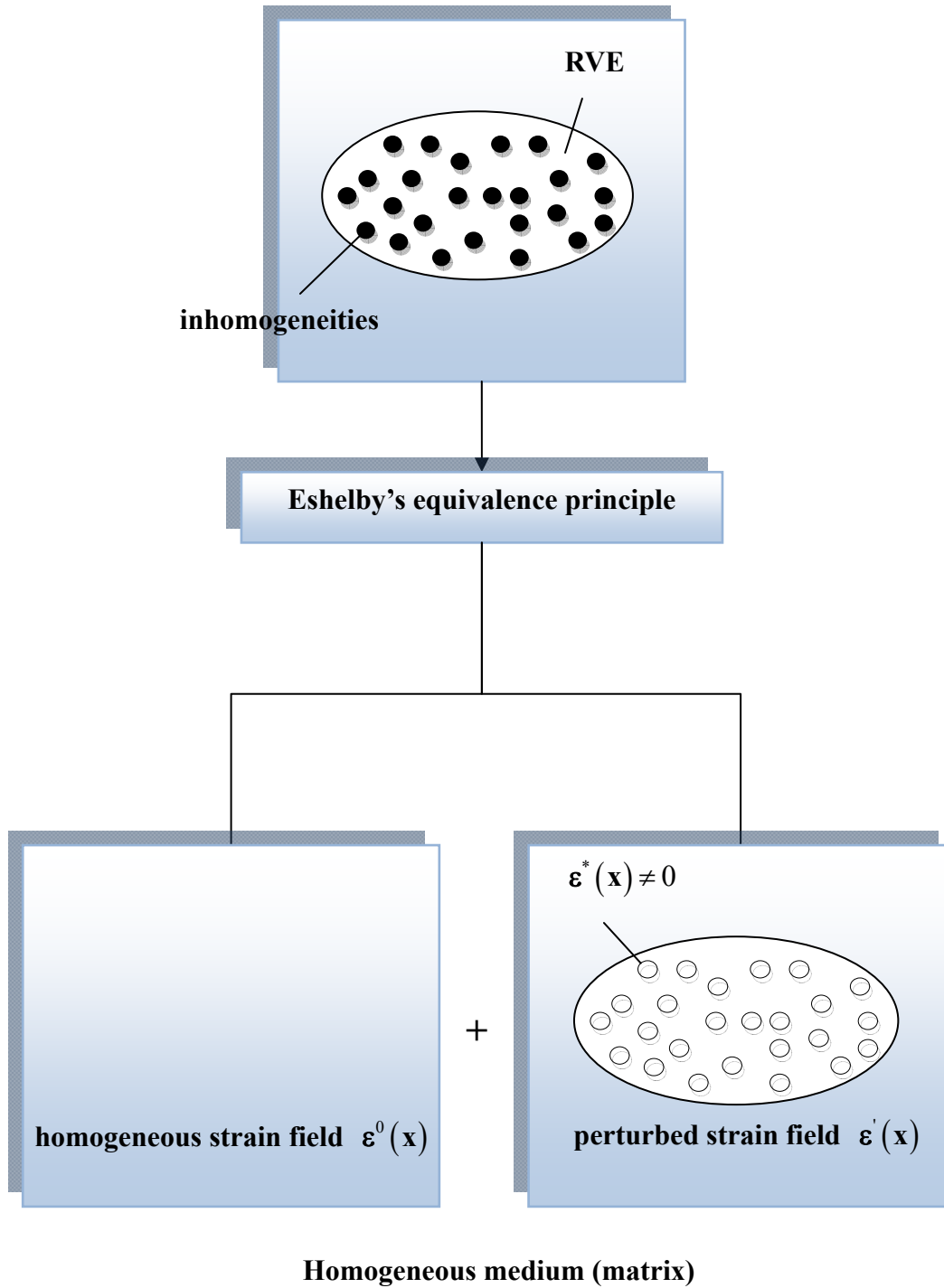
Figure 2.2 Schematic presentation of Eshelby's equivalence principle and eigenstrain concept

2.2 Interior-Point Eshelby Tensor

The stress-free $\boldsymbol{\varepsilon}^{*}(\mathbf{x})$ is referred to as the transformation strain by Eshelby (1957) or the eigenstrain by Mura (1987). Thermal expansion, phase transformation, initial strains, plastic strains and misfit strains can all be categorized as a form of eigenstrain. On the other hand, the eigenstress is a generic name for the self-equilibrated internal stresses caused by one or several of these eigenstrains in bodies, which are free from any other external force and surface constraint. The eigenstress is created by the incompatibility of the eigenstrain. For micromechanical modeling of elastic heterogeneous solids, Eshelby pointed out following significant results:

If

(1) The matrix is homogeneous, linearly elastic and extended infinitely.

(2) The inclusion domain is ellipsoidal.

Then

(1) The eigenstrain is uniformly distributed within the inclusion domain.

(2) Perturbed strain $\boldsymbol{\varepsilon}'$ and the perturbed stress $\boldsymbol{\sigma}'$ caused by the presence of the inclusions are also uniform within the inclusion domain.

(3) Specifically, the perturbed strain in the inclusion domain is demonstrated by

$$\boldsymbol{\varepsilon}' = \mathbf{S} : \boldsymbol{\varepsilon}^{*}$$

(2.9)

$$\mathbf{S} \equiv \int_{\Omega_i} \mathbf{G}(\mathbf{x} - \mathbf{x}') d\mathbf{x}' \quad ; \quad \mathbf{x}, \ \mathbf{x}' \in \Omega_i$$

Since the perturbed strain is evaluated in the inclusion in Eq. (2.9), the tensor of $\mathbf{S}$ is called the interior-point Eshelby's tensor. Furthermore, $\mathbf{S}$ is dependent on not only the material properties

of the inclusion, but also the shape of the ellipsoidal inclusion in domain Ω_i and Poisson's ratio of the isotropic matrix material (ν_0).

2.3 Determination of Effective Moduli

In this research, several methods to evaluate approximately the effective properties of heterogeneous materials are developed. All the approaches presented are based on the Eshelby inclusion solution. The basic idea of micromechanics is to derive solutions of either the global or local strain concentration tensors. Once such strain concentration tensors are known, the effective properties can be easily obtained. One common approach of developing the strain concentration tensors is to use Eshelby solution in conjunction with the equivalent inclusion method. For example, consider the r th ellipsoidal inhomogeneity Ω_r with stiffness tensor $\mathbf{L}_r$ is placed within a uniform matrix Ω_0 of stiffness tensor $\hat{\mathbf{L}}_0$, which is subjected to the uniform strain $\hat{\varepsilon}^0$ before the inhomogeneity is embedded, as shown in **Figure 2.3**.

(a)   (b)
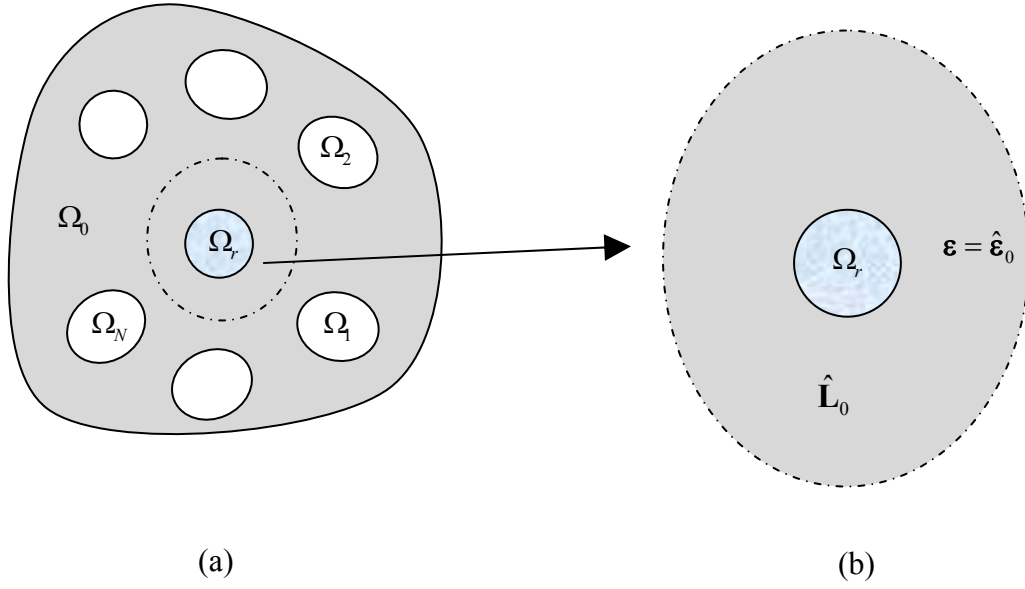
Figure 2.3 (a) The r th inhomogeneity in the composite; (b) The r th inhomogeneity in a uniform matrix of stiffness $\hat{\mathbf{L}}_0$, which is subjected to the uniform strain $\hat{\boldsymbol{\varepsilon}}^0$ before the inhomogeneity is embedded

In this case, the equivalent inclusion equation is

$$\mathbf{L}_r : \left(\hat{\boldsymbol{\varepsilon}}^0 + \boldsymbol{\varepsilon}_r^{'} \right) = \hat{\mathbf{L}}_0 : \left(\hat{\boldsymbol{\varepsilon}}^0 + \boldsymbol{\varepsilon}_r^{'} - \boldsymbol{\varepsilon}_r^{*} \right) \tag{2.10}$$

and according to the Eshelby solution,

$$\boldsymbol{\varepsilon}_r^{'} = \hat{\mathbf{S}}_r \boldsymbol{\varepsilon}_r^{*} \tag{2.11}$$

where $\hat{\mathbf{S}}_r$ is the Eshelby tensor computed using the elastic constants of $\hat{\mathbf{L}}_0$ and the geometry of the r th inhomogeneity Ω_r. Substitution of the Eshelby solution into the equivalent inclusion equation yields the eigenstrain

$$\varepsilon_r^* = \left[\left(\mathbf{L}_r - \hat{\mathbf{L}}_0 \right) \hat{\mathbf{S}}_r + \hat{\mathbf{L}}_0 \right]^{-1} \left(\mathbf{L}_r - \hat{\mathbf{L}}_0 \right) \hat{\boldsymbol{\varepsilon}}^0 \tag{2.12}$$

The total strain in the r th inhomogeneity can then be written as

$$\boldsymbol{\varepsilon}_r = \hat{\boldsymbol{\varepsilon}}^0 + \boldsymbol{\varepsilon}_r' = \hat{\boldsymbol{\varepsilon}}^0 + \hat{\mathbf{S}}_r \boldsymbol{\varepsilon}_r^* = \hat{\mathbf{A}}^0 \hat{\boldsymbol{\varepsilon}}^0 \tag{2.13}$$

and

$$\hat{\mathbf{A}}^0 = \left[\mathbf{I} + \hat{\mathbf{S}}_r \hat{\mathbf{L}}_0^{-1} \left(\mathbf{L}_r - \hat{\mathbf{L}}_0 \right) \right]^{-1} \tag{2.14}$$

where $\hat{\mathbf{A}}^0$ is the local strain concentration tensor for the r th inhomogeneity. The corresponding stress on the r th inhomogeneity is

$$\boldsymbol{\sigma}_r = \mathbf{L}_r \boldsymbol{\varepsilon}_r = \mathbf{L}_r \hat{\mathbf{A}}^0 \hat{\boldsymbol{\varepsilon}}^0 \tag{2.15}$$

The strain and stress fields in the r th inhomogeneity are now related to an unknown strain field $\hat{\boldsymbol{\varepsilon}}^0$ and a fictitious matrix material with $\hat{\mathbf{L}}_0$. Once $\hat{\boldsymbol{\varepsilon}}^0$ and $\hat{\mathbf{L}}_0$ are known from the micromechanics schemes discussed in the following sections, the strain concentration tensors, as well as the effective properties of the composite, can be obtained.

2.3.1 Eshelby Method

If the inhomogeneities in the composite are far apart from each other, their interactions may be neglected. In other words, each inhomogeneity can be regarded as if it exists in a homogeneous matrix without the interference by other inhomogeneities. Therefore, a typical inhomogeneity, for example, the r th inhomogeneity, can be treated as an ellipsoidal inhomogeneity in an otherwise uniform matrix of $\mathbf{L}_0$, which is subjected to a uniform strain $\boldsymbol{\varepsilon}^0$ before the inhomogeneity is imbedded. Hence, based on the scheme of the Eshelby method,

$$\hat{\mathbf{L}}_0 = \mathbf{L}_0$$

$$\hat{\boldsymbol{\varepsilon}}^0 = \boldsymbol{\varepsilon}^0$$

(2.16)

and consequently,

$$\hat{\mathbf{S}}_r = \mathbf{S}_r$$
(2.17)

Moreover, the average strain tensor of the composite can be easily seen to equal to $\boldsymbol{\varepsilon}^0$, namely,

$$\overline{\boldsymbol{\varepsilon}} = \frac{1}{V}\int_V \boldsymbol{\varepsilon}\, dV = \boldsymbol{\varepsilon}^0$$
(2.18)

Therefore, the strain in the r th inhomogeneity is expressed as

$$\boldsymbol{\varepsilon}_r = \mathbf{A}^0 \overline{\boldsymbol{\varepsilon}}$$
(2.19)

Accordingly, the global strain concentration tensor for the r th inhomogeneity can be found as

$$\mathbf{A}_r = \mathbf{A}^0$$
(2.20)

Thus, the effective stiffness tensor of the composite is written by

$$\overline{\mathbf{L}} = \mathbf{L}_0 + f\left(\mathbf{L}_r - \mathbf{L}_0\right)\mathbf{A}^0$$
(2.21)

where f is the volume-fraction sum of all inhomogeneities in the composite. Since the derivations given by Eshelby method assumes that the inhomogeneities in the composite are so far apart that they do not interfere with each other. Hence, the Eshelby estimate is valid only for very low volume fraction of inhomogeneities, or the dilute case.

2.3.2 Ju and Chen's Scheme and Mori-Tanaka Method

For a typical inhomogeneity of the stiffness $\mathbf{L}_r$ ($r > 0$) in the composite, the effects (or the existence) of other inhomogeneities are communicated to it through the strain and stress fields in its surrounding matrix material. Although the strain and stress fields are different from one

23

location to another in the matrix, the averages ($\overline{\varepsilon}_0$ and $\overline{\sigma}_0$) represent good approximations of the actual fields in the matrix surrounding each inhomogeneity, when a large number of inhomogeneities exist and are randomly distributed in the matrix (which is the case for most engineering composites). Moreover, it would be reasonable to assume that the overall elastic behavior of the composite cannot be affected if only one inhomogeneity is taken out. In other words, when the r th inhomogeneity is removed and replaced by the matrix material (or equivalently, let $\mathbf{L}_r = \mathbf{L}_0$), the averages ($\overline{\varepsilon}_0$ and $\overline{\sigma}_0$) would remain the same. Therefore, as far as the r th inhomogeneity is concerned, it can be viewed as an ellipsoidal inhomogeneity with the stiffness tensor $\mathbf{L}_r$ place within a uniform matrix of stiffness tensor $\mathbf{L}_0$, which is subjected to the uniform strain $\overline{\varepsilon}_0$ before the inhomogeneity is embedded. Hence, in the case of the Ju and Chen's scheme (or equivalently, Mori-Tanaka method in this case),

$$\hat{\mathbf{L}}_0 = \mathbf{L}_0$$

$$\hat{\boldsymbol{\varepsilon}}^0 = \overline{\boldsymbol{\varepsilon}}_0$$

(2.22)

and consequently,

$$\hat{\mathbf{S}}_r = \mathbf{S}_r$$

(2.23)

Therefore, the strain in the r th inhomogeneity is described as

$$\boldsymbol{\varepsilon}_r = \mathbf{A}^0 \overline{\boldsymbol{\varepsilon}}_0$$

(2.24)

Accordingly, the global strain concentration tensor for the r th inhomogeneity can be expressed as

$$\mathbf{A}_r = \mathbf{A}^0 \left[(1-f)\mathbf{I} + f\mathbf{A}^0 \right]^{-1}$$

(2.25)

Thus, the effective stiffness tensor of the composite is written by

$$\overline{\mathbf{L}} = \mathbf{L}_0 + f\left(\mathbf{L}_r - \mathbf{L}_0\right)\mathbf{A}_r \tag{2.26}$$

It is noted that in order to accelerate the understanding and formulating of the interface/surface energy effect on the composite, in this research, the derivations developed by Ju and Chen method are somewhat simplified and hence most of them coincide with the corresponding results given by Mori-Tanaka method.

2.4 Various Stresses in Continuum Mechanics

In continuum mechanics, stress is a measure of the internal forces acting within a deformable body. Quantitatively, it is a measure of the average force per unit area of a surface within the body on which internal forces act. These internal forces arise as a reaction to external forces applied to the body. Because the loaded deformable body is assumed to behave as a continuum, these internal forces are distributed continuously within the volume of the material body, and result in the deformation of the body's shape. Beyond certain limits of the material strength, this can lead to a permanent shape change or structural failure.

The most commonly used measure of stress is the Cauchy stress. However, several other measures of stress can be defined. Some such stress measures that are widely used in continuum mechanics, particularly in the computational context, are the Cauchy stress (or true stress), the Kirchhoff stress, the nominal stress, the first Piola-Kirchhoff stress, the second Piola-Kirchhoff stress and the Biot stress. Among them, the Cauchy stress (or true stress), the first Piola-Kirchhoff stress and the second Piola-Kirchhoff stress are emphasized here since these three stresses are further used in Chapter 3.

Consider the situation shown in **Figure 2.4**. In the reference (or original) configuration Ω_0, the outward normal unit vector of a surface element $d\Gamma_0$ is $\mathbf{n}_0$ and the traction acting on that surface is $\mathbf{t}_0$ leading to a force vector $d\mathbf{f}_0$. In the current (or deformed) configuration Ω, the surface element changes to $d\Gamma$ with outward normal unit vector $\mathbf{n}$ and the traction vector $\mathbf{t}$ leading to a force $d\mathbf{f}$. It is noted that this surface can either be a hypothetical cut inside the body or an actual surface.
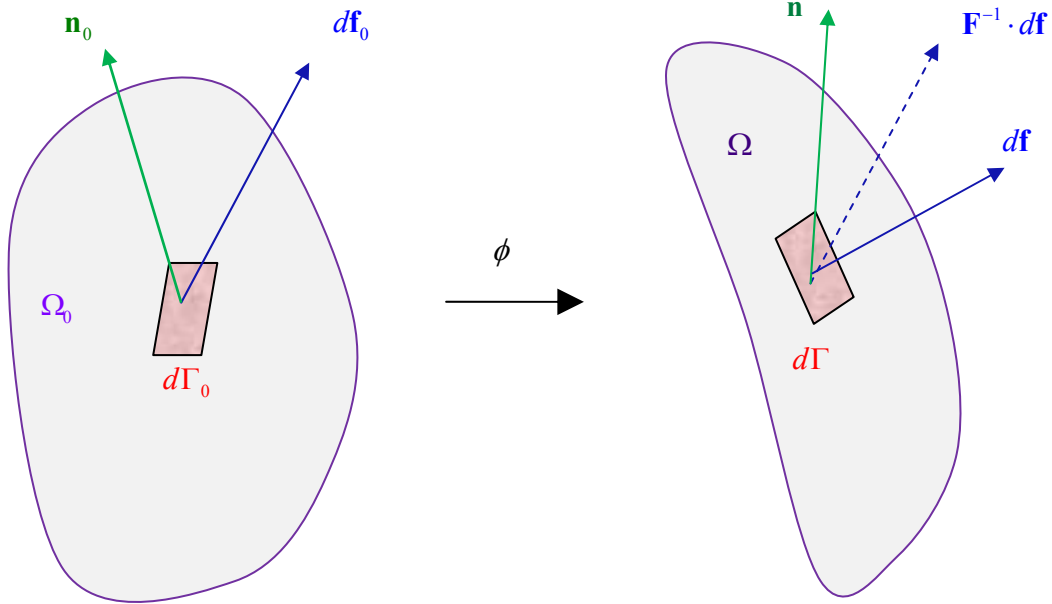
Figure 2.4 Quantities used in the definition of stress measures

2.4.1 Cauchy Stress

The Cauchy stress (or true stress), σ, is a measure of the force acting on an element of area

in the current configuration. The tensor is symmetric and is defined via

$$d\mathbf{f} = \mathbf{t}\,d\Gamma = \boldsymbol{\sigma}\cdot\mathbf{n}\,d\Gamma \qquad (2.27)$$

or

$$\mathbf{t} = \boldsymbol{\sigma}^T\cdot\mathbf{n}$$

$$(2.28)$$

$$t_i = \sigma_{ji}n_j \quad or \quad t_j = \sigma_{ij}n_i$$

where $\mathbf{t}$ is the traction and $\mathbf{n}$ is the normal unit vector of the surface on which the traction acts. The Cauchy stress tensor is used for stress analysis of material bodies experiencing small deformation where the differences in stress distribution in most cases can be neglected. For large deformations, also called finite deformations, other measures of stress, such as the first and second Piola-Kirchhoff stress tensors, the Biot stress tensor and the Kirchhoff stress tensor, are required.

2.4.2   First Piola-Kirchhoff Stress

In the case of finite deformations, the Piola-Kirchhoff stress tensors express the stress relative to the reference configuration. This is in contrast to the Cauchy stress tensor which expresses the stress relative to the current configuration. For infinitesimal deformations or rotations, the Cauchy and Piola-Kirchhoff tensors are identical.

The nominal stress $\mathbf{N} = \mathbf{P}^T$ is the transpose of the first Piola-Kirchhoff stress (PK1 stress) $\mathbf{P}$ and is defined via

$$d\mathbf{f} = \mathbf{t}_0\,d\Gamma_0 = \mathbf{N}^T\cdot\mathbf{n}_0\,d\Gamma_0 = \mathbf{P}\cdot\mathbf{n}_0\,d\Gamma_0 \qquad (2.29)$$

or

$$\mathbf{t}_0 = \mathbf{N}^T\cdot\mathbf{n}_0 = \mathbf{P}\cdot\mathbf{n}_0 \qquad (2.30)$$

This stress is not symmetric and is a two point tensor like the deformation gradient. This is because it relates the force in the current configuration to an oriented area vector in the reference configuration.

2.4.3 Second Piola-Kirchhoff Stress

If $d\mathbf{f}$ is pulled back to the reference configuration, then,

$$d\mathbf{f}_0 = \mathbf{F}^{-1} \cdot d\mathbf{f} \tag{2.31}$$

or

$$d\mathbf{f}_0 = \mathbf{F}^{-1} \cdot \mathbf{N}^T \cdot \mathbf{n}_0 \, d\Gamma_0 = \mathbf{F}^{-1} \cdot \mathbf{t}_0 \, d\Gamma_0 \tag{2.32}$$

The second Piola-Kirchhoff stress (PK2 stress) $\mathbf{S}$ is symmetric and is defined via

$$d\mathbf{f}_0 = \mathbf{S}^T \cdot \mathbf{n}_0 \, d\Gamma_0 = \mathbf{F}^{-1} \cdot \mathbf{t}_0 \, d\Gamma_0 \tag{2.33}$$

Therefore,

$$\mathbf{S}^T \cdot \mathbf{n}_0 = \mathbf{F}^{-1} \cdot \mathbf{t}_0 \tag{2.34}$$

Whereas the first Piola-Kirchhoff stress relates forces in the current configuration to areas in the reference configuration, the second Piola-Kirchhoff stress relates forces in the reference configuration to areas in the reference configuration.

2.5 References

[1] Bonet, J., and Wood, R. W. (1997). "Nonlinear continuum mechanics for finite element

analysis." (1st Edition), Cambridge University Press.

[2]   Eshelby, J. D. (1957). "The Determination of the elastic field of an ellipsoidal inclusion, and related problems." *Proceedings of the Royal Society of London Series a-Mathematical and Physical Sciences*, 241(1226), 376-396.

[3]   Ko, Y. F. (2005). "Effective elastoplastic-damage model for fiber-reinforced metal matrix composites with evolutionary fibers debonding." Ph.D. Dissertation at University of California, Los Angeles, CA.

[4]   Ju, J. W., and Chen, T. M. (1994a). "Micromechanics and effective moduli of elastic composites containing randomly dispersed ellipsoidal inhomogeneities." *Acta Mechanica*, 103(1-4), 103-121.

[5]   Ju, J. W., and Chen, T. M. (1994b). "Effective elastic-moduli of 2-phase composites containing randomly dispersed spherical inhomogeneities." *Acta Mechanica*, 103(1-4), 123-144.

[6]   Ju, J. W., and Chen, T. M. (1994c). "Micromechanics and effective elastoplastic behavior of 2-phase metal-matrix composites." *Journal of Engineering Materials and Technology-Transactions of the Asme*, 116(3), 310-318.

[7]   Mura, T. (1987). "Micromechanics of defects in solids." (2nd Edition), Martinus Nijhoff Publishers, Dordrecht.

[8]   Qu, J., and Cherkaoui, M. (2006). "Fundamentals of micromechanics of solids." John Wiley & Sons, Inc.

[9]   Yanase, K. (2009). "Micromechanics and effective thermo-mechanical damage and deformation responses of composite materials." Ph.D. Dissertation at University of California, Los Angeles, CA.

Chapter 3

INTERFACE ENERGY EFFECT ON SIZE-DEPENDENT EFFECTIVE PROPERTIES OF A HETEROGENEOUS MATERIAL

ABSTRACT

In this chapter, the interface/surface energy effect is regarded as the change of the residual elastic field induced by the interface stress from the reference configuration to the current configuration. At the beginning, with consideration to the framework of finite deformation theory, the interface/surface energy effect is accounted into the governing equations. Then, upon the infinitesimal strain analysis, the approximate formulation of a finitely deformed multi-phase elastic medium is derived. Accordingly, after two kinds of fundamental equations, the interface/surface constitutive relations and the Young-Laplace equations, are executed, the analytical equations of the size-dependent effective moduli of a composite material containing heterogeneous particles with the interface/surface energy effect are developed. Lastly, the analytical equations together with the corresponding illustrative results in the cases of the influence of the liquid-like interface/surface energy, as a type of residual stress terms, on the effective properties of a heterogeneous material are discussed. By comparing the present model with other models established based on the Eshelby and Mori-Tanaka methods, it is

demonstrated that the present model is more applicable to characterize real composite materials. Further, it is found that the results with the interface/surface energy effect in our model, different from the results given by preceding researchers, can be applied to the nanocomposites.

Key Words: Interface/surface energy effect; Two-phase composite; Finite deformation theory; Infinitesimal strain analysis; Nanocomposite

3.1 Introduction

Nowadays, since the materials science and technique have been advanced to the characteristic size of a nano-scale solid in structures and composites, the interface/surface energy effect on mechanical and physical properties of nanocomposites and nano-size structures becomes significant and cannot be ignored. Therefore, the interface/surface energy effect should be accounted into the deformation analysis of solids.

Many studies have been published in the literature to present the concept of interface/surface energy in solids. Among them, Gibbs (1906) was the first researcher who introduced the concept of the interface/surface free energy in solids. Since then, this concept has been investigated by many researchers. For example, Shuttleworth (1950) and Herring (1953) worked on the interface/surface energy problems in solids; Orowan (1970) expanded the interface/surface energy problems to both solid and liquid materials; Gurtin and Murdoch (1975) established a continuum theory of elastic material surfaces. Moreover, the mechanism of the interface/surface energy was gradually developed by Cahn (1978), Cammarata (1994), Ibach

31

(1997), Haiss (2001), Muller and Saul (2004), Fried and Gurtin (2004), and Murdoch (2005).

In Huang and Sun (2007), the change of the elastic fields induced by the interface energies and the interface stresses from the reference configuration to the current configuration was considered. It was emphasized that there are two kinds of fundamental equations required to be introduced in the solution of boundary-value problems for stress fields with the interface/surface energy effect. The first is the interface/surface constitutive relations, whereas the second is the discontinuity conditions of the stress across the interface, namely, the Young-Laplace equations. These two fundamental equations are used to predict the effective moduli of a composite material with the interface/surface energy effect. Although an infinitesimal strain analysis is employed to establish the governing equations induced by the interface/surface energy, the finite deformation analysis (also known as the large deformation analysis) of a multi-phase hyperelastic medium should be concerned at the beginning, according to reasons as follows:

(1) The mechanical response from the reference configuration to the current configuration should be considered in the study of the mechanical behavior of a composite material or a structure. In this regard, the change of the size and the shape of the interface in the process of the deformation reflect the change of the curvature tensor in the governing equations. In other words, the change of the deformation and the configuration leads to the change of the residual elastic field induced by the interface energy. In essence, hence, this is a finite deformation problem. Furthermore, the interface/surface energy effect is explicitly verified by the change of the residual elastic field due to the change of the configuration.

(2) To develop the governing equations with the interface/surface energy effect, a residual elastic field induced by the interface energy and the interface stress in the material should be introduced, even though there is no external loading. That is to say, through accounting for

the change of the residual elastic field upon the change of the configuration, the effect of the liquid-like interface/surface energy on the effective properties of a composite material can then be included. In this chapter, this type of the interface energy model is emphasized and discussed.

(3) The constitutive relations for the hyperelastic solids with the interface/surface energy effect at the finite deformation have been formulated by Huang and Wang (2006) and Huang and Sun (2007), as introduced in Section 3.5 Appendix A. Moreover, the approximation expressions of the changes of the interface stress and the Young-Laplace equations due to the change of the configuration through the infinitesimal deformation analysis can be found in Section 3.6 Appendix B. These constitutive relations are expressed in terms of the free energy of the interface per unit area at the current configuration, denoted by γ (see Section 3.6 Appendix B for more details).

In addition, composite materials have developed rapidly over the last several decades. They are usually designed to meet the diverse needs for enhancing material performance with advanced thermo-mechanical properties, reduced unit weights, versatile directionality, optimal anisotropy, etc., and for improving material mechanical strengths, elastic moduli, delamination resistance, fracture toughness and fatigue resistance. Reinforcements could be continuous in the form of fibers, or discontinuous in the form of particles or whiskers. Especially, for engineers and scientists, to predict and estimate overall mechanical properties and behaviors of random heterogeneous multi-phase composites are of quite interest in many science, technology, engineering and mathematical disciplines. In general, mechanical properties and behaviors of composites are dependent on properties of constituent phases and microstructures of inhomogeneities, such as shapes, orientations, aspect ratios, volume fractions, random locations,

etc.

3.2 Effective Moduli of a Particle-Filled Composite

Based on the theoretical framework formulated in Section 3.5 Appendix A and Section 3.6 Appendix B, analytical equations used to predict the effective properties of a composite reinforced by spherical particles are developed in this section. Many models in traditional micromechanics have been used to predict effective moduli of composites, such as the models developed by Mura (1987), Nemat-Nasser and Hori (1999), Milton (2002), and Torquato (2002). Moreover, many investigations on the inhomogeneities with the imperfect interfacial bonding conditions or the interface effects have been provided by the works of Benveniste(1985), Benveniste and Miloh (2001), Hashin (1991; 2002), and Duan et al. (2005). In the past, Sharma and Ganti (2004) have formulated the effective bulk moduli of spherical particle-filled composites with the interface effect using the composite spheres assemblage (CSA) model (Hashin, 1962). Duan et al. (2005) derived the effective bulk and shear moduli of such composites using the composite spheres assemblage model, the Mori-Tanaka method (MTM) (Mori and Tanaka, 1973) and the generalized self-consistent method (GSCM) (Christensen and Lo, 1979). The difference between the present work in this chapter and those of Sharma and Ganti (2004) and Duan et al. (2005) is that: at the outset with the finite deformation theory proposed by Huang and Wang (2006), the infinitesimal deformation approximations of the interface/surface constitutive relation and the Young-Laplace equation based on the Lagrangian description in consideration to the change of configuration are derived. Therefore, the

34

requirement for using the asymmetric interface stress in the Young-Laplace equation is clearly verified and the effect of the residual interface/surface energy γ_0^* on the effective elastic moduli is shown. Assuming that the inhomogeneity incorporated with the interface is regarded as an "equivalent inhomogeneity", for a problem on the inhomogeneity with the interface/surface energy effect, the micromechanical scheme upon the present work for a two-phase composite is applicable immediately. In this case, the volume averages of the stress and strain for the "equivalent inhomogeneity" have to be calculated on the matrix side due to the discontinuity of the stress across the interface. Consequently, the explicit derivation of the stress discontinuity conditions across the interface is significant. The work in this chapter gives an understanding of the interface/surface energy effect by accounting for the change of the interface stress in Eq. (3.43) and Eq. (3.50) due to the change of configuration, and the interface moduli are directly related to the parameters of the interface energy. Moreover, in order for the comparison of the differences, as well as the finding of the advantages, between the present work and the models based on the Mori-Tanaka approximation method (Mori and Tanaka, 1973) and the Eshelby method (Eshelby, 1957), the corresponding expressions established by these two methods are also displayed in the following sections if they differ from those obtained by the present model.

Consider a two-phase composite composed of the matrix and randomly distributed spherical inhomogeneities, in which the radius of the inhomogeneity is assumed to be a. The effective stiffness tensor of the composite, $\overline{\mathbf{L}}$, can be described as

$$\overline{\mathbf{L}} = \mathbf{L}_0 + \phi\left(\mathbf{L}_* - \mathbf{L}_0\right) : \mathbf{A}_r \qquad (3.1)$$

where $\mathbf{L}_0$ and $\mathbf{L}_*$ are the stiffness tensors of the matrix and the "equivalent inhomogeneity" (namely, an inhomogeneity incorporated with the interface), respectively; ϕ is the volume

fraction of the sum of all inhomogeneities; $\mathbf{A}_r$ denotes the fourth-order global strain concentration tensor for the rth equivalent inhomogeneity. If the Ju and Chen's scheme (1994a; 1994b; 1994c) is applied, $\mathbf{A}_r$ is given by

$$\mathbf{A}_r \equiv \left(\mathbf{L}_* - \mathbf{L}_0\right)^{-1} \cdot \mathbf{L}_0 \tag{3.2}$$

Assuming all particles are spherical and both matrix and particles are isotropic elastic, $\mathbf{A}_r$ in Eq. (3.2) can be advanced to express as

$$\mathbf{A}_r = \mathbf{A}^0 : \left[\left(1 - \phi\right)\mathbf{I}^{(1)} + \phi\mathbf{A}^0\right]^{-1} \tag{3.3}$$

where $\mathbf{I}^{(1)}$ is the fourth-order unit tensor; $\mathbf{A}^0$ is the strain concentration tensor of the equivalent inhomogeneity in an infinite matrix corresponding to dilute distribution of inhomogeneities, or simply named the local strain concentration tensor if $\mathbf{A}_r$ is relatively considered as a global strain concentration tensor. It can be found that Eq. (3.3) coincides with the corresponding results obtained by using the Mori-Tanaka method (Benveniste, 1987; Weng, 1990) in the case of this section. Whereas, the corresponding expression of $\mathbf{A}_r$ given by the Eshelby method is written as

$$\mathbf{A}_r = \mathbf{A}^0 \tag{3.4}$$

Eq. (3.4) implies that the interactions among equivalent inhomogeneities may be neglected. In other words, each equivalent inhomogeneity can be treated as if it exists in a homogeneous matrix without the interference by other inhomogeneities.

In addition, if the inhomogeneities are randomly distributed, the composite material is statistically isotropic and the elastic moduli in Eq. (3.1) can be expressed as

$$\overline{\mathbf{L}} = 3\overline{K}\mathbf{I}_m + 2\overline{\mu}\mathbf{I}_s$$

$$\mathbf{L}_0 = 3K_0\mathbf{I}_m + 2\mu_0\mathbf{I}_s \tag{3.5}$$

$$\mathbf{L}_* = 3K_*\mathbf{I}_m + 2\mu_*\mathbf{I}_s$$

where K_0, K_* and $\overline{K}$ are the bulk moduli of the matrix, the equivalent inhomogeneity and the composite, respectively; μ_0, μ_* and $\overline{\mu}$ are the shear moduli of the matrix, the equivalent inhomogeneity and the composite, respectively. It is also known that

$$\mathbf{I}_m = \frac{1}{3}\mathbf{I}\otimes\mathbf{I}, \quad \mathbf{I}_s = \mathbf{I}^{(1)} - \mathbf{I}_m \tag{3.6}$$

Substituting Eq. (3.6) into Eq. (3.5), Eq. (3.1) is further decoupled into

$$\overline{K} = K_0 + \phi\left(K_* - K_0\right)A_m$$

$$\overline{\mu} = \mu_0 + \phi\left(\mu_* - \mu_0\right)A_s \tag{3.7}$$

where A_m and A_s are the constants in the strain concentration tensors corresponding to the bulk and shear moduli, respectively, as follows,

$$A_m = \frac{K_0}{K_0 + \left(1-\phi\right)\left(K_* - K_0\right)\omega_m}$$

$$A_s = \frac{\mu_0}{\mu_0 + \left(1-\phi\right)\left(\mu_* - \mu_0\right)\omega_s} \tag{3.8}$$

Here,

$$\omega_m = \frac{3K_0}{3K_0 + 4\mu_0}$$

$$\omega_s = \frac{6\left(K_0 + 2\mu_0\right)}{5\left(3K_0 + 4\mu_0\right)} \tag{3.9}$$

ω_m and ω_n are components of the fourth-order Eshelby inclusion tensor. It is noted that the

elastic moduli K_* and μ_* of the equivalent inhomogeneity can be obtained by using Eqs. (3.43) and (3.50) for this purpose. In the case of the spherical inhomogeneity of radius a, $\nabla_{0s}\mathbf{u}$ can be described in terms of the physical components $(u_r, u_\theta, u_\varphi)$ in a spherical polar coordinate system as the following equation,

$$\nabla_{0s}\mathbf{u} = \left(\frac{\partial u_\theta}{r\partial\theta} + \frac{u_r}{r}\right)\mathbf{e}_\theta \otimes \mathbf{e}_\theta + \left(\frac{\partial u_\varphi}{r\partial\theta} + \frac{u_r}{r}\right)\mathbf{e}_\theta \otimes \mathbf{e}_\varphi + \left(\frac{1}{r\sin\theta}\frac{\partial u_\theta}{\partial\varphi} - \cot\theta\frac{u_\varphi}{r}\right)\mathbf{e}_\varphi \otimes \mathbf{e}_\theta$$

$$+ \left(\frac{1}{r\sin\theta}\frac{\partial u_\varphi}{\partial\varphi} + \cot\theta\frac{u_\theta}{r} + \frac{u_r}{r}\right)\mathbf{e}_\varphi \otimes \mathbf{e}_\varphi$$

(3.10)

For the axisymmetric loading, $u_\varphi = 0$. Since u_r and u_θ are not dependent on φ, $\nabla_{0s}\mathbf{u}$ is a symmetric tensor, as shown below,

$$\nabla_{0s}\mathbf{u} = \left(\frac{\partial u_\theta}{r\partial\theta} + \frac{u_r}{r}\right)\mathbf{e}_\theta \otimes \mathbf{e}_\theta + \left(\cot\theta\frac{u_\theta}{r} + \frac{u_r}{r}\right)\mathbf{e}_\varphi \otimes \mathbf{e}_\varphi$$

(3.11)

In the above case, Eq. (3.50) may be replaced by Eq. (3.51). It is noticed that, in the reference configuration, the curvature tensor on the surface of the sphere with radius a is

$$\mathbf{b}_0 = -\frac{1}{a}\mathbf{i}_0$$

(3.12)

Eq. (3.43) can be expressed as

$$[\![\sigma_{rr}]\!]|_{r=a} = \frac{1}{a^2}\left(\gamma_0^* + 2\gamma_1^* + \gamma_1\right)\left(2u_r + u_\theta\cot\theta + \frac{\partial u_\theta}{\partial\theta}\right)\Big|_{r=a}$$

$$-\frac{1}{a^2}\gamma_0^*\left(\frac{\partial^2 u_r}{\partial\theta^2} - \frac{\partial u_\theta}{\partial\theta} + \frac{\partial u_r}{\partial\theta}\cot\theta - u_\theta\cot\theta\right)\Big|_{r=a}$$

(3.13)

$$[\![\sigma_{r\theta}]\!]|_{r=a} = \frac{1}{a^2}\left[\left(2\gamma_0^* + \gamma_1^*\right)u_\theta + \left(\gamma_1^* + \gamma_1\right)\left(u_\theta\cot^2\theta - \frac{\partial u_\theta}{\partial\theta}\cot\theta - \frac{\partial^2 u_\theta}{\partial\theta^2}\right)\right]\Big|_{r=a}$$

$$-\frac{1}{a^2}\left[\left(2\gamma_0^* + 2\gamma_1^* + \gamma_1\right)\frac{\partial u_r}{\partial\theta}\right]\Big|_{r=a}$$

In order to compute the bulk modulus K_* of the equivalent inhomogeneity, suppose that a spherical inhomogeneity is embedded in an infinite medium under the hydrostatic loading with the remote strain as

$$\mathbf{E}^\infty = \frac{1}{3} E_m \mathbf{I} \tag{3.14}$$

In this case, the displacement and stress fields in the inhomogeneity and matrix are given by

$$u_r^i = F_i r + \frac{G_i}{r^2}$$

$$\sigma_{rr}^i = 3 K_i F_i - 4 \mu_i \frac{G_i}{r^3} \tag{3.15}$$

The superscript $i = 1, 0$ denotes the quantities of the inhomogeneity and matrix, respectively. F_1, F_0, G_1 and G_0 are constants to be determined. In addition to the displacement continuity condition at the interface $r = a$, the elastic solution needs to satisfy the stress discontinuity condition in Eq. (3.13), namely,

$$\left(\sigma_{rr}^0 - \sigma_{rr}^1 \right)\big|_{r=a} = \frac{2}{a^2} \left(\gamma_0^* + 2\gamma_1^* + \gamma_1 \right) \left(u_r\big|_{r=a} \right) \tag{3.16}$$

According to the above conditions, the non-singular condition at the origin and the condition at infinity, the constants in Eq. (3.15) can be determined. Therefore, the (secant) bulk modulus K_* of the equivalent inhomogeneity can be obtained by

$$K_* = \frac{tr \langle \boldsymbol{\sigma}_* \rangle}{3 tr \langle \boldsymbol{\varepsilon}_* \rangle} \bigg|_{r=a} = K_1 + \frac{2 \left(\gamma_0^* + 2\gamma_1^* + \gamma_1 \right)}{3a} \tag{3.17}$$

where $\langle \boldsymbol{\sigma}_* \rangle$ and $\langle \boldsymbol{\varepsilon}_* \rangle$ represent the volume averages of the stress and strain of the equivalent inhomogeneity that includes the inhomogeneity and the interface, respectively. $\gamma_0^* = \gamma_0 + \gamma_1 + \gamma_2$,

$\gamma_1^* = \gamma_1 + 2\gamma_2 + \gamma_{11} + 2\gamma_{12} + \gamma_{22}$, and γ_0^* and γ_1^* form the residual interface/surface energy. Further, it is found that there are at least three independent material parameters γ_0^*, γ_1^* and γ_1 required in the above equation. About the detailed description of the interface/surface free energy γ, it can refer to Section 3.6 Appendix B.

Moreover, the shear modulus μ_* of the equivalent inhomogeneity can be found by imposing a pure deviatoric remote strain at infinity as,

$$\mathbf{E}^\infty = E_e \left[\mathbf{e}_3 \otimes \mathbf{e}_3 - \frac{1}{2}\left(\mathbf{e}_1 \otimes \mathbf{e}_1 + \mathbf{e}_2 \otimes \mathbf{e}_2 \right) \right] \tag{3.18}$$

where $\mathbf{e}_1$, $\mathbf{e}_2$ and $\mathbf{e}_3$ are the base vectors in a rectangular Cartesian coordinate system. From the solution of Lur'e (1964), the displacement and stress fields in the inhomogeneity and matrix can be written by

$$u_r^1 = \left(12v_1 A r^3 + 2Br\right) P_2\left(\cos\theta\right)$$

$$u_r^0 = \left(E_e r + \frac{2\left(5 - 4v_0\right)}{r^2} C - \frac{3}{r^4} D\right) P_2\left(\cos\theta\right)$$

$$u_\theta^1 = \left[\left(7 - 4v_1\right) A r^3 + Br\right] \frac{dP_2\left(\cos\theta\right)}{d\theta}$$

$$u_\theta^0 = \left[\frac{1}{2} E_e r + \frac{\left(2 - 4v_0\right)}{r^2} C - \frac{1}{r^4} D\right] \frac{dP_2\left(\cos\theta\right)}{d\theta}$$

$$\sigma_{rr}^1 = 2\mu_1 \left(-6v_1 A r^2 + 2B\right) P_2\left(\cos\theta\right)$$

$$\sigma_{rr}^0 = 2\mu_0 \left[E_e - \frac{4\left(5 - v_0\right)}{r^3} C + \frac{12}{r^5} D\right] P_2\left(\cos\theta\right)$$

$$\sigma_{r\theta}^1 = 2\mu_1 \left[\left(7 + 2v_1\right) A r^2 + B\right] \frac{dP_2\left(\cos\theta\right)}{d\theta} \tag{3.19}$$

$$\sigma_{r\theta}^0 = 2\mu_0 \left[\frac{1}{2} E_e + \frac{2\left(1 + v_0\right)}{r^3} C - \frac{4}{r^5} D\right] \frac{dP_2\left(\cos\theta\right)}{d\theta}$$

The superscripts 1 and 0 denote the quantities of the inhomogeneity and matrix, respectively. v_1 and v_0 are Poisson's ratios of the inhomogeneity and matrix, respectively. $P_2\left(\cos\theta\right)$ is the second-order Legendre polynomial. A, B, C and D are constants to be determined. Similarly, in addition to the displacement continuity condition at the interface $r = a$, the elastic solution needs to satisfy the stress discontinuity condition in Eq. (3.13). Then, the unknown constants can be determined in a way similar to that for the bulk modulus. The shear modulus μ_* of the equivalent inhomogeneity can be calculated by

$$\mu_* = \frac{\langle \sigma_* \rangle_e}{3\langle \varepsilon_* \rangle_e}\bigg|_{r=a} = \mu_1 + \frac{L_1 + L_2}{L_3 + L_4}$$

$$L_0 = 2\gamma_0^{*2} - \gamma_1\left(\gamma_1 + 2\gamma_1^*\right) - \gamma_0^*\left(5\gamma_1 + 2\gamma_1^*\right)$$

$$L_1 = 10\left(7 - 10\nu_1\right)L_0$$

(3.20)

$$L_2 = -\frac{1}{10a}\left(2\gamma_0^* - 7\gamma_1 - 2\gamma_1^*\right)L_4$$

$$L_3 = 4\left(-7 + 10\nu_1\right)a\left(13\gamma_0^* + 7\gamma_1 + 12\gamma_1^*\right)$$

$$L_4 = 10a^2\left[4\left(-7 + 10\nu_1\right)\mu_0 - \left(7 + 5\nu_1\right)\mu_1\right]$$

where $\langle \sigma_* \rangle_e$ and $\langle \varepsilon_* \rangle_e$ are the effective average stress and the effective average strain of the equivalent inhomogeneity, respectively. It can be easily found that K_* and μ_* are not only functions of the elastic moduli of the inhomogeneity, such as K_1 and μ_1, but also the functions of the size of particles, a. Substituting the obtained K_* in Eq. (3.17) and μ_* in Eq. (3.20) into Eq. (3.7), the analytical expressions of the effective moduli $\bar{K}$ and $\bar{\mu}$ of the composite can be expressed by

$$\bar{K} = \frac{1}{3}\left[\frac{12K_0\mu_0\left(1 - \phi\right) + 3K_1\left(3K_0 + 4\mu_0\phi\right) + 2\left(3K_0 + 4\mu_0\phi\right)\left(\gamma_0^* + 2\gamma_1^* + \gamma_1\right)/a}{3K_0\phi + 4\mu_0 + 3K_1\left(1 - \phi\right) + 2\left(1 - \phi\right)\left(\gamma_0^* + 2\gamma_1^* + \gamma_1\right)/a}\right]$$

(3.21)

$$\bar{\mu} = \mu_0 + \frac{15\mu_0\phi(1-v_0)\left[-L_1 - L_2 + (L_3 + L_4)(\mu_0 - \mu_1)\right]}{L_5 + L_6}$$

$$L_5 = 2(1-\phi)(-4+5v_0)(L_1 + L_2)$$

(3.22)

$$L_6 = (L_3 + L_4)\left[(-7+5v_0)\mu_0 + 2(-4+5v_0)(\phi\mu_0 + \mu_1 - \phi\mu_1)\right]$$

$$v_0 = \frac{3K_0 - 2}{6K_0 + 2} \quad \text{or} \quad K_0 = \frac{2(1+v_0)}{3(1-2v_0)}$$

Furthermore, it is found that the above effective bulk modulus can also be given by using the composite sphere assemblage (CSA) model, as referred to Sun et al. (2004).

In addition, the corresponding expressions of $\bar{K}$ and $\bar{\mu}$ established upon the Eshelby method, by following the same procedure mentioned above, can be written as

$$\bar{K} = K_0 + \frac{\phi(K_* - K_0)(3K_0 + 4\mu_0)}{3K_* + 4\mu_0}$$

(3.23)

$$K_* = K_1 + \frac{2(\gamma_0^* + 2\gamma_1^* + \gamma_1)}{3a}$$

$$\bar{\mu} = \mu_0 + \frac{5\mu_0\phi(\mu_* - \mu_0)(3K_0 + 4\mu_0)}{3K_0(3\mu_0 + 2\mu_*) + 4\mu_0(2\mu_0 + 3\mu_*)}$$

$$\mu_* = \mu_1 + \frac{L_1 + L_2}{L_3 + L_4}$$

$$L_0 = 2\gamma_0^{*2} - \gamma_1(\gamma_1 + 2\gamma_1^*) - \gamma_0^*(5\gamma_1 + 2\gamma_1^*)$$

$$L_1 = 10(7 - 10\nu_1)L_0$$

$$L_2 = -\frac{1}{10a}(2\gamma_0^* - 7\gamma_1 - 2\gamma_1^*)L_4$$

$$L_3 = 4(-7 + 10\nu_1)a(13\gamma_0^* + 7\gamma_1 + 12\gamma_1^*)$$

$$L_4 = 10a^2\left[4(-7 + 10\nu_1)\mu_0 - (7 + 5\nu_1)\mu_1\right] \tag{3.24}$$

3.3 Illustrative Results and Discussion

Two special cases of the two-phase composite materials are discussed in this section. The first special case is a porous material containing spherical nano-voids, and the corresponding effective bulk and shear moduli of the composite with the interface/surface energy effect can be obtained by substituting $K_1 = 0$ and $\mu_1 = 0$ into Eqs. (3.21) and (3.22), as follows,

$$\bar{K}_{void} = \frac{1}{3}\left[\frac{12K_0\mu_0(1 - \phi) + 2(3K_0 + 4\mu_0\phi)n_3}{3K_0\phi + 4\mu_0 + 2(1 - \phi)n_3}\right] \tag{3.25a}$$

$$n_3 = \frac{(\gamma_0^* + 2\gamma_1^* + \gamma_1)}{a}$$

$$\bar{\mu}_{void} = \mu_0 + 15\mu_0\phi(1-v_0)\frac{L_0+M_1+M_2}{N_0+N_1+N_2}$$

$$M_1 = 2\left(3\gamma_0^* + 2\gamma_1^*\right)\mu_0 a$$

$$M_2 = 4\mu_0^2 a^2$$

$$L_0 = 2\gamma_0^{*2} - \gamma_1\left(\gamma_1 + 2\gamma_1^*\right) - \gamma_0^*\left(5\gamma_1 + 2\gamma_1^*\right)$$

$$N = -5 + 3v_0 + 2\phi\left(-4+5v_0\right)$$

$$N_0 = 2(1-\phi)(4-5v_0)L_0$$

$$N_1 = 2\left[3N\gamma_0^* + 21(-1+v_0)\gamma_1 + 2(N-5+5v_0)\gamma_1^*\right]\mu_0 a$$

$$N_2 = 4a^2\left(N-2+2v_0\right)\mu_0^2 \qquad\qquad (3.26a)$$

As this special case is assumed to be a composite containing the liquid-like spherical inhomogeneities, namely, $\gamma_0^* = \gamma_0$, $\gamma_1^* = \gamma_1 = 0$. Furthermore, assuming the matrix material becomes incompressible, i.e., $v_0 = 0$, Eqs. (3.25a) and (3.26a) become,

$$\bar{K}_{void} = \frac{1}{3}\left[\frac{12K_0\mu_0(1-\phi)+2(3K_0+4\mu_0\phi)n_3}{3K_0\phi+4\mu_0+2(1-\phi)n_3}\right]$$

$$(3.25b)$$

$$n_3 = \frac{\gamma_0}{a}$$

$$\bar{\mu}_{void} = \mu_0 + 15\mu_0\phi \frac{L_0 + M_1 + M_2}{N_0 + N_1 + N_2}$$

$$M_1 = 6\gamma_0\mu_0 a$$

$$M_2 = 4\mu_0^2 a^2$$

$$L_0 = 2\gamma_0^2$$

$$N = -5 - 8\phi$$

$$N_0 = 8(1-\phi)L_0$$

$$N_1 = 6N\gamma_0\mu_0 a$$

$$N_2 = 4a^2(N-2)\mu_0^2 \tag{3.26b}$$

It is noted that the same expressions of the effective bulk and shear moduli of a porous material containing nano-voids with the interface/surface energy effect can be found upon the Mori-Tanaka approximation method. In addition, if the Eshelby method is executed, the corresponding effective bulk modulus of a porous material containing spherical nano-voids with the interface/surface energy effect is given by

$$\bar{K}_{void} = \frac{1}{3}\left[\frac{6K_0 n_3(1+\phi) + 12K_0\mu_0(1-\phi) + 8\mu_0\phi n_3 - 9K_0^2\phi}{2n_3 + 4\mu_0} \right] \tag{3.27}$$

$$n_3 = \frac{\left(\gamma_0^* + 2\gamma_1^* + \gamma_1\right)}{a}$$

The second special case is a two-phase composite containing the liquid-like spherical inhomogeneities, namely, $\gamma_0^* = \gamma_0$, $\gamma_1^* = \gamma_1 = 0$, then the effective bulk and shear moduli of the composite with the interface/surface energy effect are

$$\bar{K}_{(\gamma_0)} = K_0 \left\{ 1 + \frac{\phi \left[(K_1 + \frac{2\gamma_0}{3a}) - K_0 \right] (3K_0 + 4\mu_0\phi)}{3K_0 \left[(1-\phi) \left(K_1 + \frac{2\gamma_0}{3a} \right) + \phi K_0 \right] + 4K_0\mu_0} \right\} \tag{3.28}$$

$$\bar{\mu}_{(\gamma_0)} = \mu_0 + \frac{15\mu_0\phi(1-\nu_0)\left[-L_1 - L_2 + (L_3 + L_4)(\mu_0 - \mu_1) \right]}{L_5 + L_6}$$

$$L_0 = 2\gamma_0^2$$

$$L_1 = 10(7 - 10\nu_1)L_0$$

$$L_2 = -\frac{\gamma_0}{5a}L_4$$

$$L_3 = 52(-7 + 10\nu_1)a\gamma_0$$

$$L_4 = 10a^2 \left[4(-7 + 10\nu_1)\mu_0 - (7 + 5\nu_1)\mu_1 \right]$$

$$L_5 = 2(1-\phi)(-4 + 5\nu_0)(L_1 + L_2)$$

$$L_6 = (L_3 + L_4)\left[(-7 + 5\nu_0)\mu_0 + 2(-4 + 5\nu_0)(\phi\mu_0 + \mu_1 - \phi\mu_1) \right] \tag{3.29}$$

From Eqs. (3.28) and (3.29), it is obviously seen that the interface/surface energy γ_0 affects the effective moduli of the composite. Furthermore, if the Mori-Tanaka approximation method is considered, the corresponding effective bulk modulus of a two-phase composite containing the liquid-like spherical inhomogeneities with the interface/surface energy effect is evaluated as

$$\bar{K}_{(\gamma_0)} = \frac{1}{3} \left[\frac{12K_0\mu_0(1-\phi) + 3K_1(3K_0 + 4\mu_0\phi) + 2(3K_0 + 4\mu_0\phi)\gamma_0/a}{3K_0\phi + 4\mu_0 + 3K_1(1-\phi) + 2(1-\phi)\gamma_0/a} \right] \tag{3.30}$$

It can be found that the above expression of the effective bulk modulus of the composite is

slightly different from the one obtained by the Ju and Chen's scheme. Moreover, if the Eshelby method is performed, the corresponding effective bulk modulus of a two-phase composite containing the liquid-like spherical inhomogeneities with the interface/surface energy effect is written by

$$\bar{K}_{(\gamma_0)} = K_0 + \frac{\phi\left[\left(K_1 + \frac{2}{3}n_3\right) - K_0\right](3K_0 + 4\mu_0)}{3\left(K_1 + \frac{2}{3}n_3\right) + 4\mu_0} \tag{3.31}$$

In addition, in order to compare the above results with those obtained by other interface models, an interface with the following properties is considered: the displacement across the interface is continuous, but the traction is allowed to be a discontinuity across the interface; furthermore, assume that there is no residual elastic field induced by the interface/surface energy when the material is not under any external loading. This kind of interface can also be considered as an equivalency of a thin and stiff interphase, as referred to the works by Benveniste and Miloh (2001) and Wang et al. (2005). In the case of the infinitesimal deformation, the constitutive relation of the above interface can be expressed by

$$\boldsymbol{\sigma}_s = \lambda_s' \left(tr\, \mathbf{E}_s\right) \mathbf{i}_0 + 2\mu_s' \mathbf{E}_s \tag{3.32}$$

Eq. (3.32) can be given directly by setting $\gamma_0^* = 0$ in Eqs. (3.47), (3.48) and (3.52), where

$$\lambda_s' = \gamma_1^*$$

$$\mu_s' = \frac{1}{2}\gamma_1 \tag{3.33}$$

In this case, there is no need to distinguish between the interface Piola-Kirchhoff stress of the first kind $\mathbf{S}_s$ and the Cauchy stress of the interface $\boldsymbol{\sigma}_s$. Therefore, we can apply the infinitesimal deformation formulation from the beginning. Further, based on Eq. (3.32), the

effective bulk and shear moduli of the composite filled with spherical particles can be calculated by simply substituting $\gamma_0^* = 0$ into Eqs. (3.21) and (3.22), as shown in the following equations,

$$\bar{K} = \bar{K}_0 = \frac{1}{3}\left[\frac{12 K_0 \mu_0 (1-\phi) + 3 K_1 (3 K_0 + 4 \mu_0 \phi)}{3 K_0 \phi + 4 \mu_0 + 3 K_1 (1-\phi)}\right] \tag{3.34}$$

$$\bar{\mu} = \bar{\mu}_0 = \mu_0 + \frac{15 \mu_0 \phi (1-\nu_0)\left[L_4 (\mu_1 - \mu_0)\right]}{L_6}$$

$$L_4 = 10 a^2 \left[4(-7 + 10\nu_1)\mu_0 - (7 + 5\nu_1)\mu_1\right] \tag{3.35}$$

$$L_6 = (L_3 + L_4)\left[(-7 + 5\nu_0)\mu_0 + 2(-4 + 5\nu_0)(\phi \mu_0 + \mu_1 - \phi \mu_1)\right]$$

It is obvious that the effective moduli obtained by this way are not influenced by the residual interface energy, γ_0^*. Meanwhile, Eqs. (3.34) and (3.35) become the same as the expressions based on the traditional micromechanics given by the previous researcher (e.g., Qu and Cherkaoui, 2006). In particular, from Eqs. (3.28) and (3.29), the effective moduli of the composite material with a liquid-like interface would be the same as those of a perfectly-bonded composite material, if Eq. (3.32) is employed.

After the above formulations of the effective moduli of the composite with the interface/surface energy effect are derived, the corresponding illustrative results, for an example, are displayed as follows. Suppose that the bulk modulus of the matrix material is $K_0 = 2.5\,\text{GPa}$, and the shear modulus is $\mu_0 = 0.5\,\text{GPa}$. The surface is assumed to be liquid-like with a interface/surface energy $\gamma_0 = 0.05\,\text{J/m}^2$. The volume fractions of the sum of all voids are assumed to be $\phi = 5\%$, $\phi = 10\%$, $\phi = 15\%$, $\phi = 20\%$ and $\phi = 25\%$, respectively. Accordingly, the variations of the normalized effective bulk and shear moduli proposed in Eqs. (3.25b) and (3.26b) for polypropylene containing spherical voids are illustrated in **Figure 3.1** and

Figure 3.2. In the figures, $\overline{K}_0$ and $\overline{\mu}_0$ are the effective bulk and shear moduli of the material without the interface/surface energy effect. From these two figures, it is found that the interface/surface effect decreases with the increase of the size of the voids and almost can be neglected when the radius of the void is larger than 10 nm. (The x-axis in **Figure 3.1** used maximum of 5 nm is for the purpose of compactness).

However, the experimental data for the nanocomposite particle sizes between 1 nm and 10 nm are currently not available due to the difficulties in performing experimental works for the nanocomposite materials with such small particles. To the best of our knowledge, although the science and technology of the smallest characteristic sizes of nanocomposite particles have potentially advanced to about 25 nm to 75 nm, the experimental data within this scope are still unavailable. In other words, there exists difficulty in performing nanocomposite experiments containing the particles of smaller than 25-75 nm to compare with our model.

Moreover, in order to fit the framework of the micromechanics, the theory of the continuum mechanics, and investigate the scope within the nano-scale level, we set the minimum size of nano-particles limited to 0.1 nm in our model.

In addition, by comparing **Figure 3.1** and **Figure 3.2**, it is interesting to note that the size of particles affected by the interface/surface energy in the effective bulk modulus is stronger than that in the effective shear modulus. For example, in **Figure 3.1**, the interface/surface energy effect is considered to influence the effective bulk modulus of the composite when the size of particles is smaller than 10 nm, whereas the interface/surface energy effect is considered to influence the effective shear modulus of the composite when the size of particles is smaller than around 0.18 nm, as shown in **Figure 3.2**. The reason is that a series expansion of the interface energy (Huang and Wang, 2006) is used in our model. As we know, in the sight of mathematics,

the effects/quantities of higher-order terms are getting smaller and smaller in the exact solution of a series expansion. Moreover, in the sight of micromechanics, the higher-order terms are composed of more deviatoric effect, whereas the volumetric effect greatly relies on the lower-order terms. Therefore, as a special case of the liquid-like interface materials, because the higher-order terms in the equation of the interface/surface energy are neglected, in contrast with the effective shear modulus, the effective bulk modulus is affected more by the volumetric effects of the interface/surface energy. In that event, as shown in **Figure 3.1** and **Figure 3.2**, , we can hence explore that the effective bulk modulus, dependent more on volumetric effects of the liquid-like interface/surface energy, has stronger effect on particle sizes than the effective shear modulus does. This outcome meets our expectations.

Figure 3.1 Normalized effective bulk modulus against the radius of voids in the range of nanometer size with five different volume fractions and $\gamma_0 = 0.05$ J/m^2

Figure 3.2 Normalized effective shear modulus against the radius of voids in the range of nanometer size with five different volume fractions and $\gamma_0 = 0.05$ J/m^2

In **Figure 3.3** and **Figure 3.4**, the variations of the normalized effective bulk and shear moduli against the radius of voids with various values of the interface/surface energy are plotted. It is found that the larger the interface/surface energy becomes, the more the effect of the interface/surface energy is on the effective moduli of the composite. Moreover, the effects of the different values of the interface/surface energy on the effective moduli of the composite may be convergent to coincide with the increase of the size of the voids.

In addition, suppose that the bulk moduli of the matrix material and particles are $K_0 = 2.5\,\text{GPa}$ and $K_1 = 2.5\,\text{GPa}$, respectively. The shear moduli of the matrix material and particles are $\mu_0 = 0.5\,\text{GPa}$ and $\mu_1 = 0.5\,\text{GPa}$, respectively. The surface is assumed to be liquid-like with the interface/surface energy $\gamma_0 = 0.05\,\text{J/m}^2$. The volume fractions of the sum of all voids or particles are assumed to be $\phi = 10\%$, $\phi = 20\%$ and $\phi = 25\%$, respectively. Accordingly, the variations of the normalized effective bulk and shear moduli proposed for polypropylene containing spherical particles are illustrated in **Figure 3.5** and **Figure 3.6**, respectively. In the figures, $\overline{K}_0$ and $\overline{\mu}_0$ are the effective bulk and shear moduli of the material without the interface/surface energy effect. Moreover, the variations of the normalized effective bulk modulus for polypropylene containing spherical voids are also illustrated simultaneously in **Figure 3.5** for the purpose of a comparison; so are the variations of the normalized effective shear modulus for polypropylene containing spherical voids in **Figure 3.6** for the purpose of a comparison.

In **Figure 3.5**, it is found that the stiffer the inclusion becomes, the less the effect of the interface/surface energy is on the effective bulk modulus of the composite if the same volume fraction is proposed. However, it is obviously seen that the higher the volume fraction become, the more the effect of the interface/surface energy is on the effective bulk modulus of the

composite.

By contrast, **Figure 3.6** shows the variations of the normalized effective shear modulus proposed for polypropylene containing spherical particles. It can be seen that the effect of the interface/surface energy is quite significant on the effective shear modulus of the composite no matter which stiffness or volume fraction of the inclusions is proposed. In addition, if the higher volume fraction (with the same strength) of the particles is executed, it is found that the interface/surface effect on the effective shear modulus of the composite increases. Further, at the same strength of particles, more volume fraction used results in larger size of the particles is affected by the interface/surface energy. This phenomenon coincides with the result from the effective bulk modulus of the composite containing spherical particles in **Figure 3.5**, but becomes more obvious on the interface/surface energy effect.
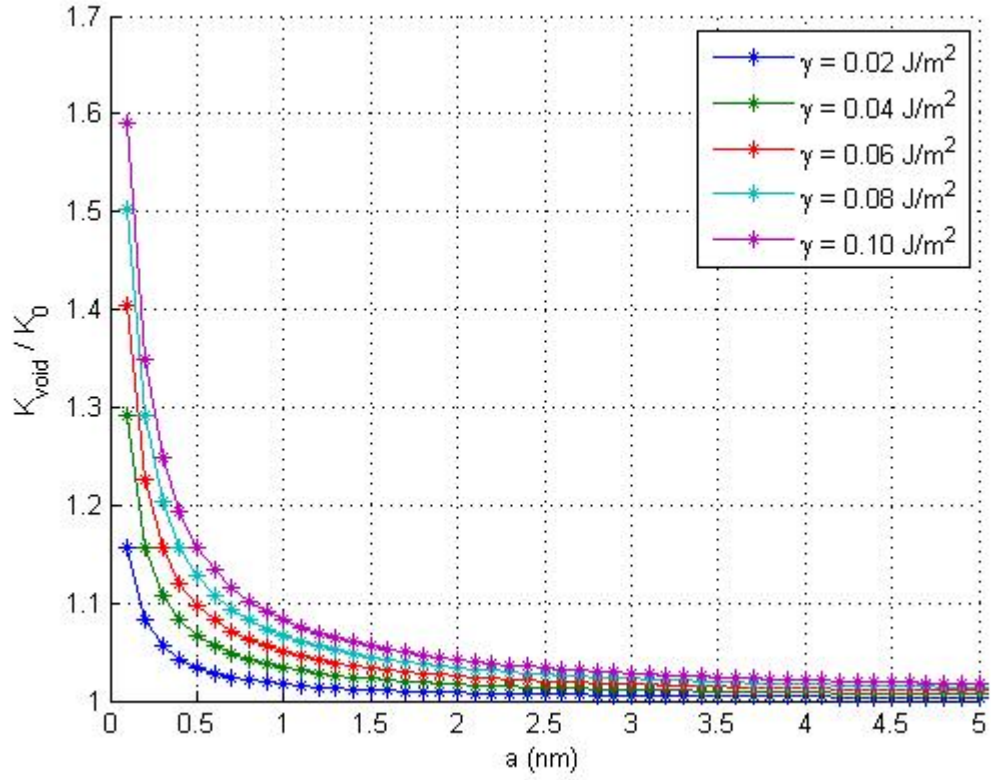
Figure 3.3 Normalized effective bulk modulus against the radius of voids in the range of nanometer size with five different interface/surface energies and 20% volume fraction ($\phi = 20\%$)
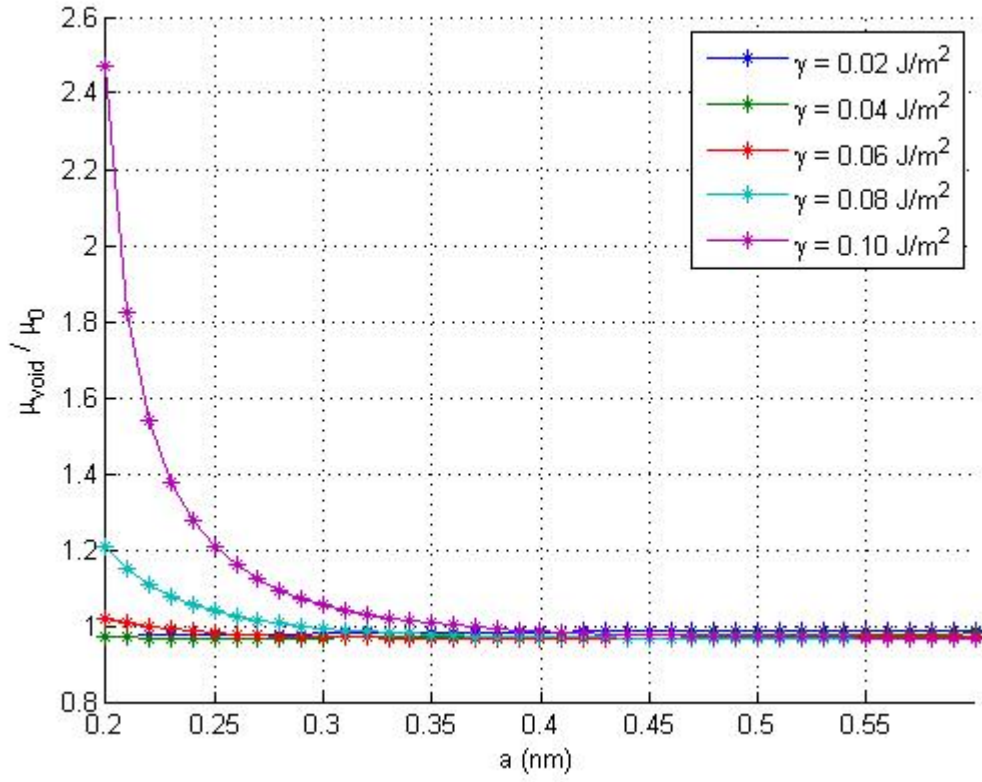
Figure 3.4 Normalized effective shear modulus against the radius of voids in the range of nanometer size with five different interface/surface energies and 20% volume fraction ($\phi = 20\%$)
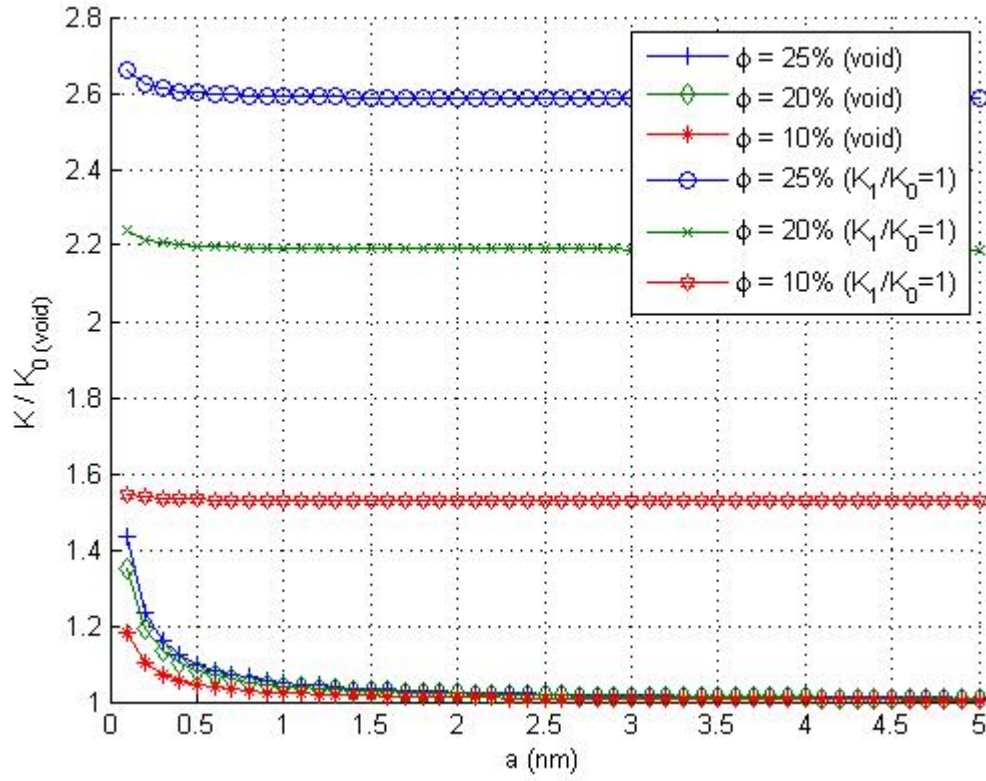
Figure 3.5 Normalized effective bulk modulus against the radius of voids and particles in the range of nanometer size with different volume fractions ($\phi = 10\%$, $\phi = 20\%$ and $\phi = 25\%$) and $\gamma_0 = 0.05 \text{ J/m}^2$ in two cases:

1) $K_0 = 2.5 \text{ GPa}$ & $K_1 = 0$ (void);

2) $K_0 = K_1 = 2.5 \text{ GPa}$.
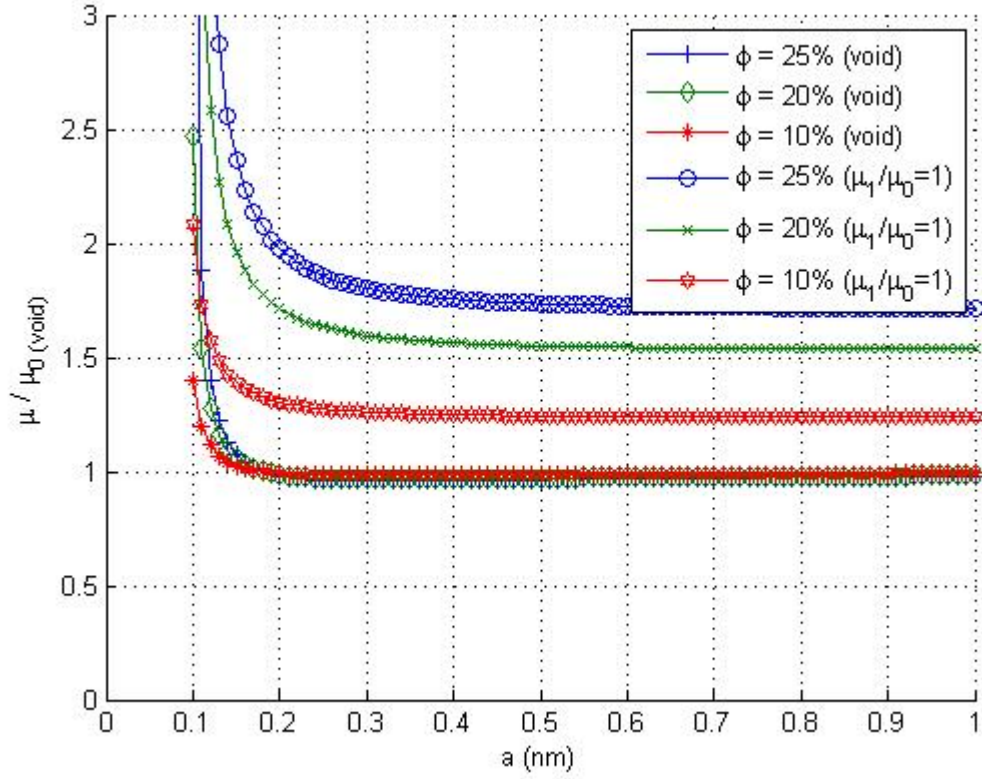
Figure 3.6 Normalized effective shear modulus against the radius of voids and particles in the range of nanometer size with different volume fractions ($\phi = 10\%$, $\phi = 20\%$ and $\phi = 25\%$) and $\gamma_0 = 0.05 \text{ J/m}^2$ in two cases:

1) $\mu_0 = 0.5 \text{ GPa}$ & $\mu_1 = 0$ (void);

2) $\mu_0 = \mu_1 = 0.5 \text{ GPa}$.

Figure 3.7 shows the comparison among three different schemes developed by Ju and Chen (1994), Mori and Tanaka (1973) and Eshelby (1957). It can be seen that, except the result produced by the Eshelby method, the results developed by Ju and Chen's model and Mori-Tanaka's model are extremely approaching. Furthermore, **Figure 3.8** illustrates the difference of the normalized effective bulk modulus against the radius of voids by using the Ju and Chen's scheme and Eshelby method with different volume fractions of the voids. It can be found that while the volume fractions of the sum of all voids become smaller, the results obtained by these two schemes are closer. This is because the scheme developed by the Eshelby method neglects the interaction among the equivalent inhomogeneities. That is, each equivalent inhomogeneity is regarded as if it exists in a homogeneous matrix without the interference by other equivalent inhomogeneities. As a result, when the volume fraction is smaller, the interaction among the equivalent inhomogeneities becomes less. In other words, even if the interaction is considered in the model established by the Ju and Chen's scheme, the smaller the volume fraction is, the less the interaction among the equivalent inhomogeneities becomes, leading to closer results from these two different schemes.
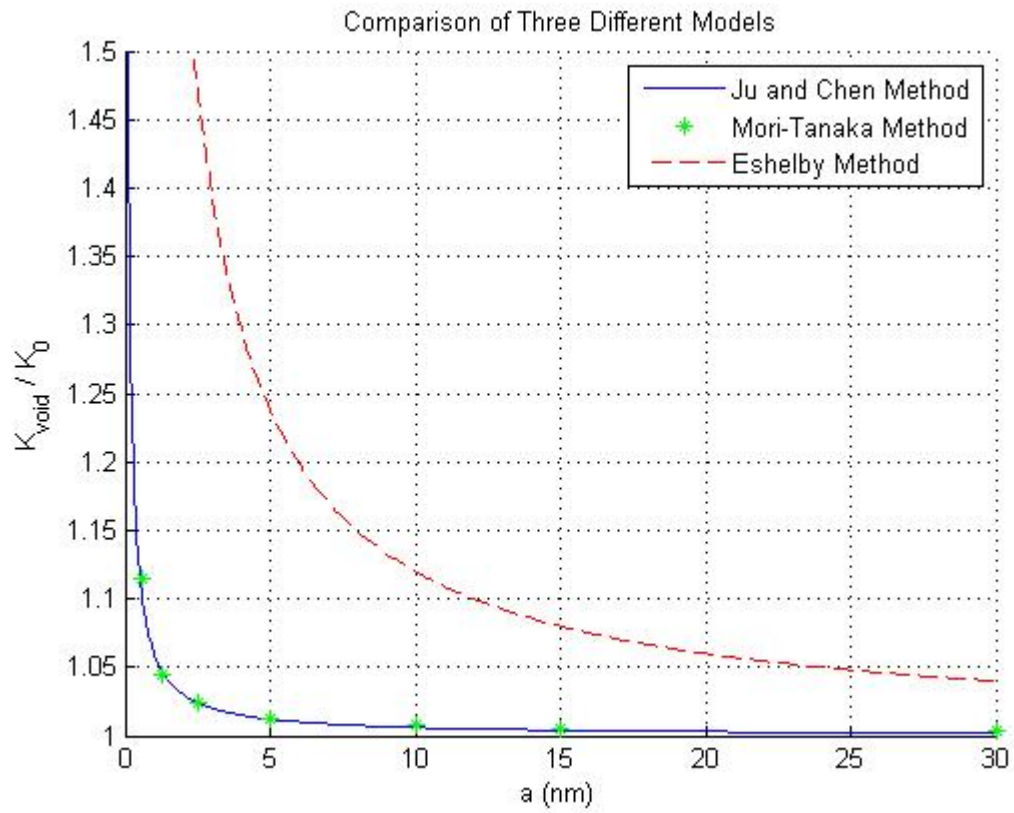
Figure 3.7 Comparison of the normalized effective bulk modulus against the radius of voids using three different models
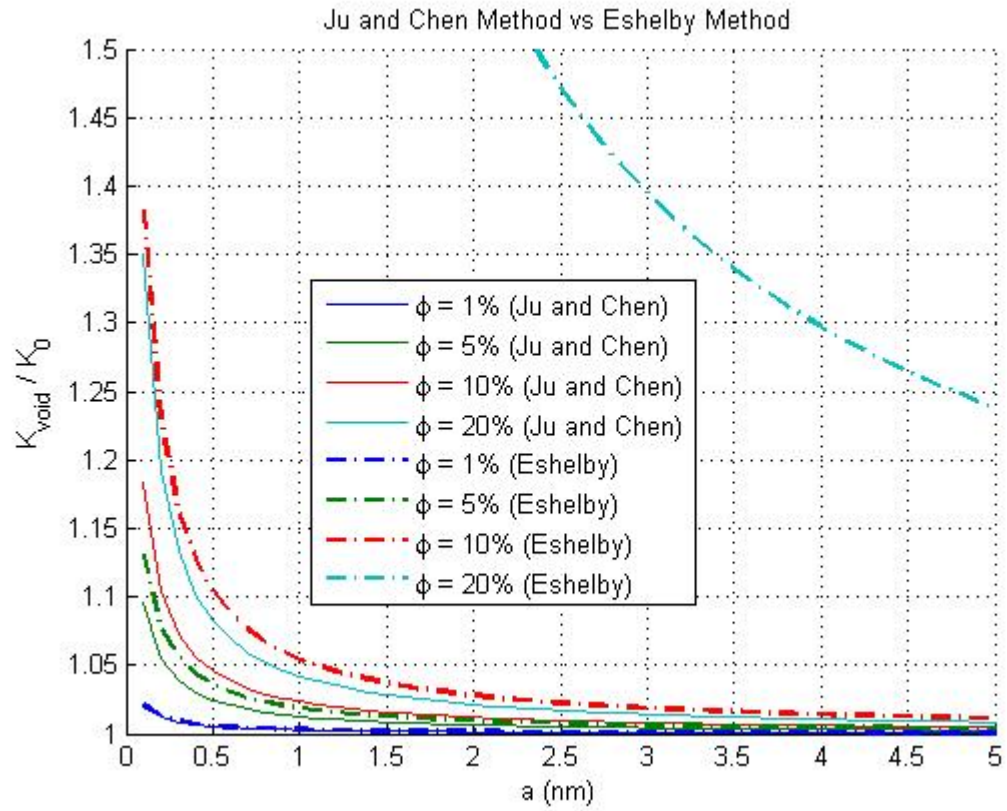
Figure 3.8 Comparison of the normalized effective bulk modulus against the radius of voids using the Ju and Chen's scheme and Eshelby method with different volume fractions of the voids

In order to investigate the parametric effects of the interface/surface energy, in **Figure 3.9**, we execute the primary term of the interface energy, γ_0, from 0.05 J/m^2, 0.10 J/m^2 (cf. interface energy of water is 0.059 J/m^2 (100℃) - 0.076 J/m^2 (0℃)), 0.25 J/m^2 and 0.50 J/m^2 (cf. interface energy of mercury is 0.059 J/m^2), respectively, to perform the interface/surface energy of liquid-like property. From **Figure 3.9**, it is seen that the interface energy will expand the effect to larger size of particles in a composite material when the primary term of the interface/surface energy, γ_0, is getting larger and larger. For example, when the values of γ_0 are 0.05 J/m^2, 0.10 J/m^2, 0.25 J/m^2 and 0.50 J/m^2, the interface/surface energy effect on the particle size of the composite are about 10, 20, 30, and 40 nm, respectively. In **Figure 3.10**, the normalized effective bulk modulus against the radius of voids with four different values of the liquid-like interface/surface energy is plotted together for the purpose of comparison. However, even though the interface/surface energy effect can reach to the scope of within 25 nm to 75 nm, as mentioned before, the experimental data with the characteristic size of nanocomposite particles within this scope are still unavailable. Therefore, further experimental validations and comparisons will be performed once the associated experimental data become available.
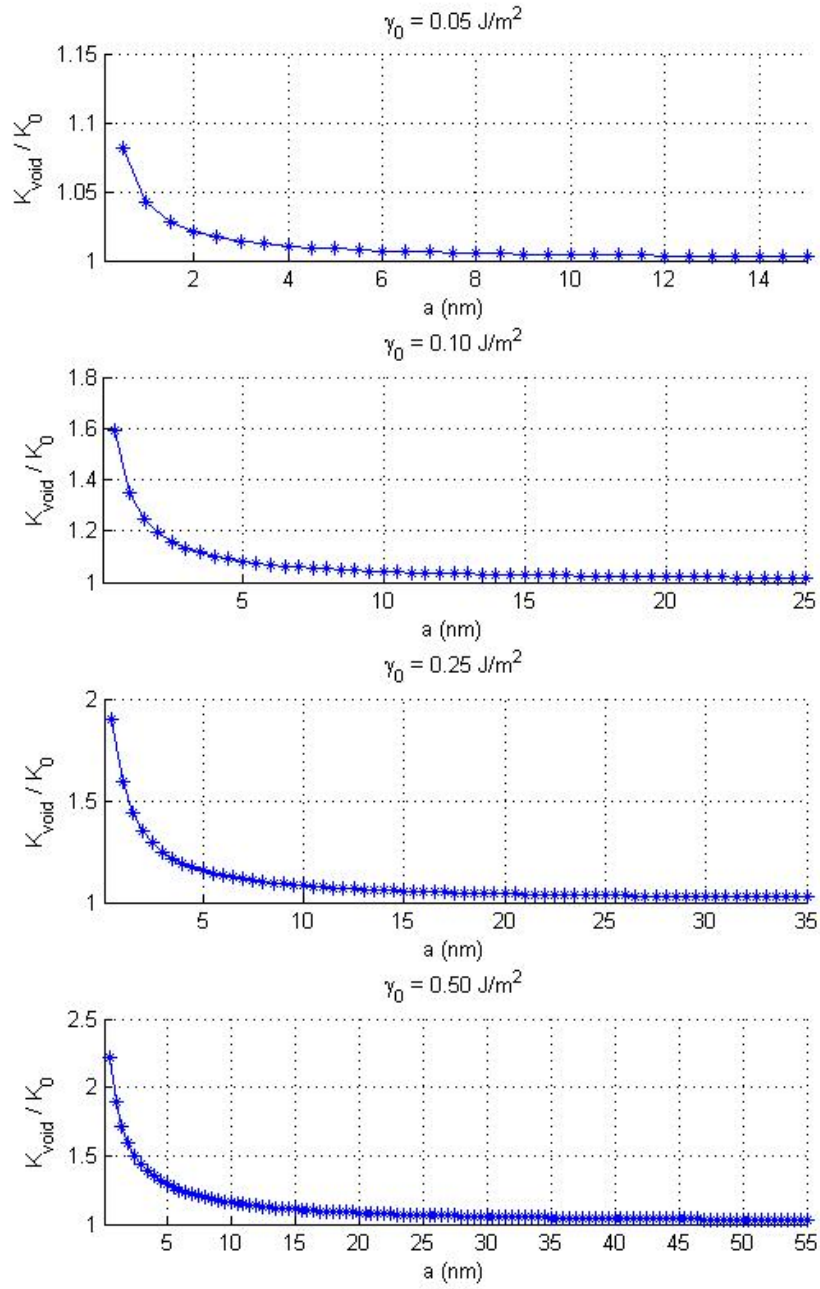
Figure 3.9 Individual plots for normalized effective bulk modulus against the radius of voids in the range of nanometer size with four different interface/surface energies and 20% volume fraction ($\phi = 20\%$)
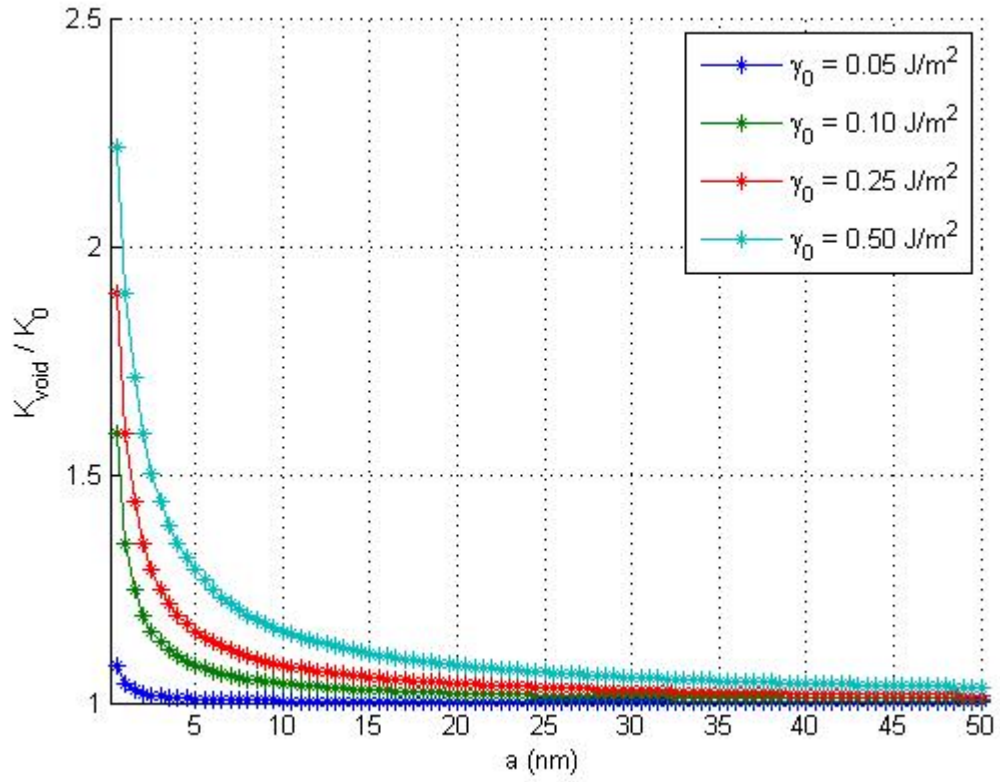
Figure 3.10 Normalized effective bulk modulus against the radius of voids in the range of nanometer size with four different interface/surface energies and 20% volume fraction ($\phi = 20\%$)

Lastly, a sequent discussion is followed by **Figure 3.11**, **Figure 3.12**, **Figure 3.13**, and **Figure 3.14**, we explore the effect of the secondary parametric term of the interface/surface energy, γ_1, on the particle size of the composite when the γ_0 is assumed to be consistent. For instance, **Figure 3.11** plots the variation of the effective bulk modulus for the five different γ_1 when the $\gamma_0 = 0.05$ J/m^2. In this case, in addition to the slightly variations of the effective bulk modulus of the composite within the range of 0.1 to 10nm, all of five sub-figures show that the interface/surface energy effect can be ignored when the particle size is greater than 10 nm. Therefore, we can conclude that the secondary term of the interface/surface energy influences much less than the primary term of the interface/surface energy. Moreover, the secondary term of the interface/surface energy performs barely on changing the interface/surface energy effect on the particle sizes of the composite. In other words, the interface/surface energy remains the effect on the particle size of smaller than 10 nm regardless of the change of the secondary term of the interface/surface energy. The similar results can be observed from **Figure 3.12**, **Figure 3.13**, and **Figure 3.14** for the different cases of $\gamma_0 = 0.10$ J/m^2, 0.25 J/m^2, and 0.50 J/m^2, respectively. Hence, we can bravely come to a conclusion that the other higher-order terms of the interface/surface energy would perform scarcely on the effect size change of the nanocomposite particles influenced by the interface/surface energy.
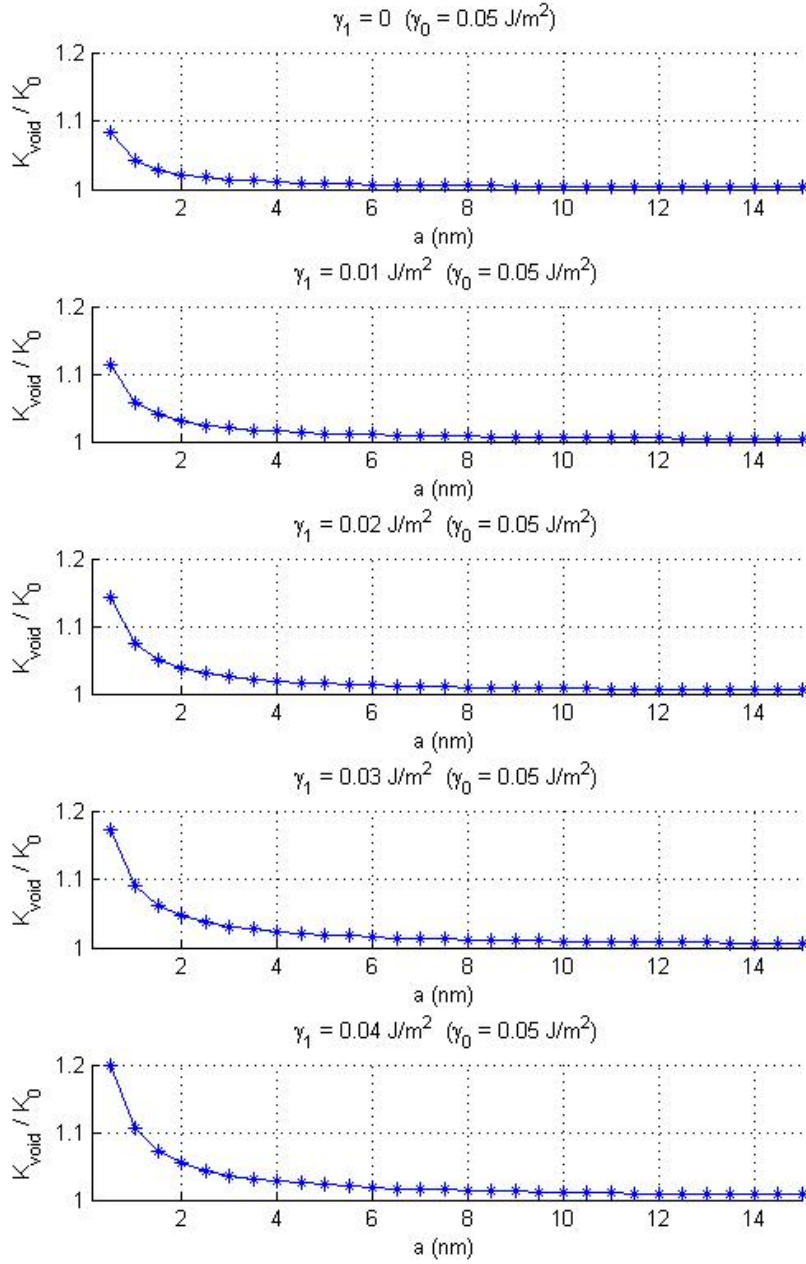
Figure 3.11 Individual plots for normalized effective bulk modulus against the radius of voids in the range of nanometer size with five different secondary terms, γ_1, of the interface/surface energy with $\gamma_0 = 0.05$ J/m^2
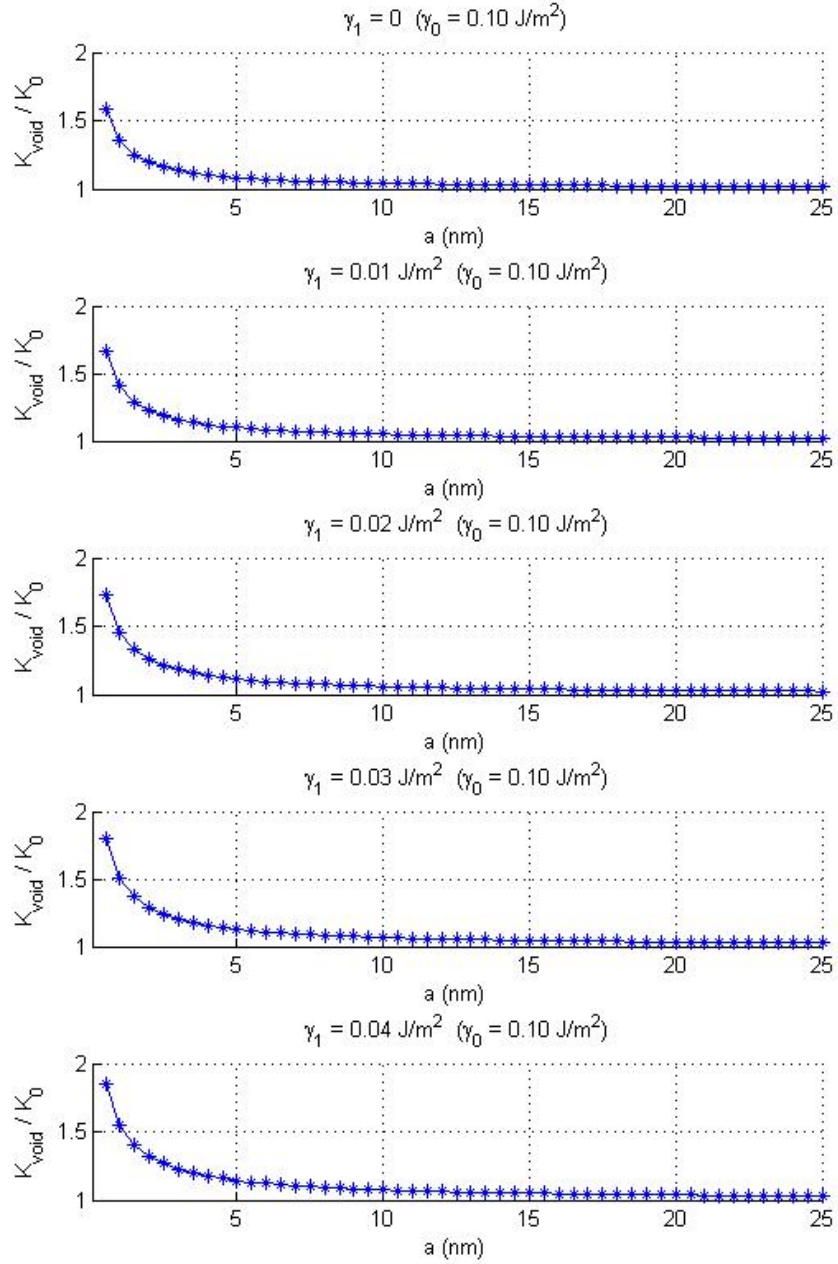
Figure 3.12 Individual plots for normalized effective bulk modulus against the radius of voids in the range of nanometer size with five different secondary terms, γ_1, of the interface/surface energy with $\gamma_0 = 0.10$ J/m^2
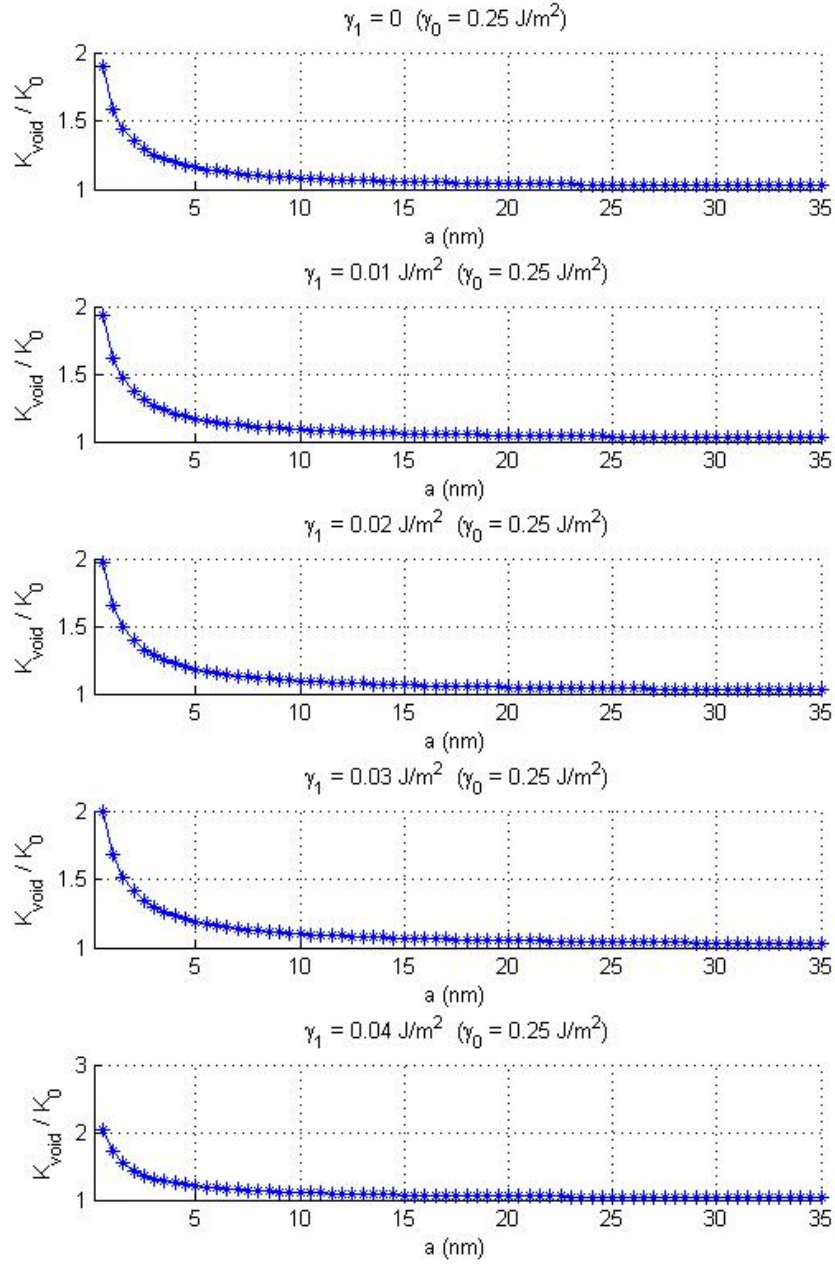
Figure 3.13 Individual plots for normalized effective bulk modulus against the radius of voids in the range of nanometer size with five different secondary terms, γ_1, of the interface/surface energy with $\gamma_0 = 0.25$ J/m^2
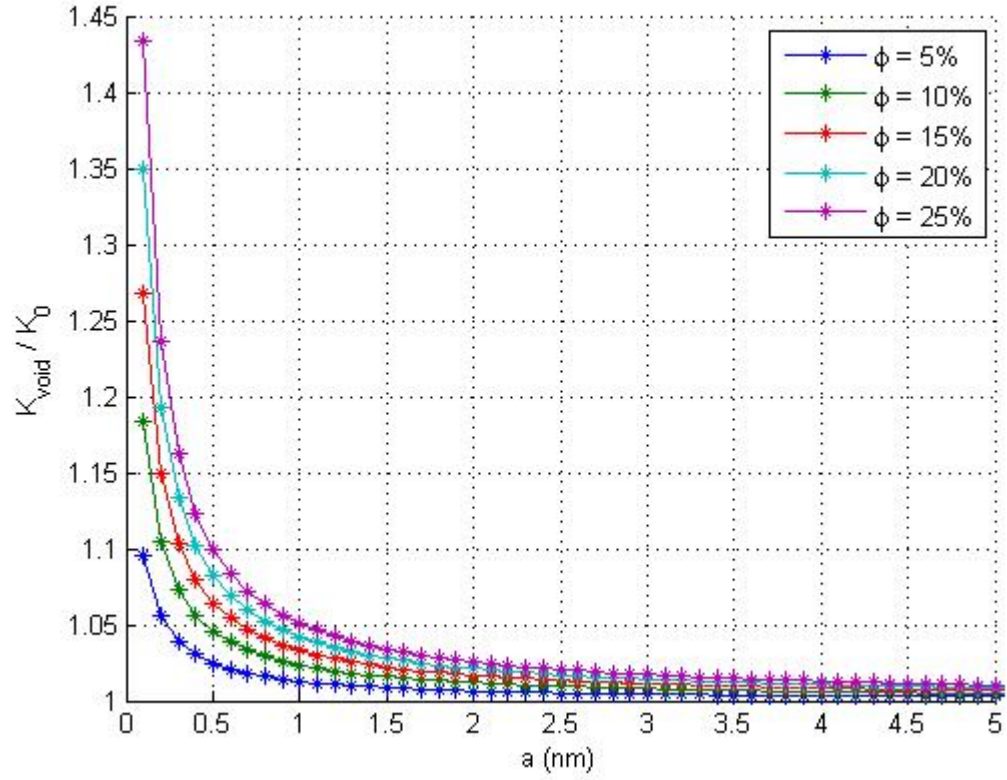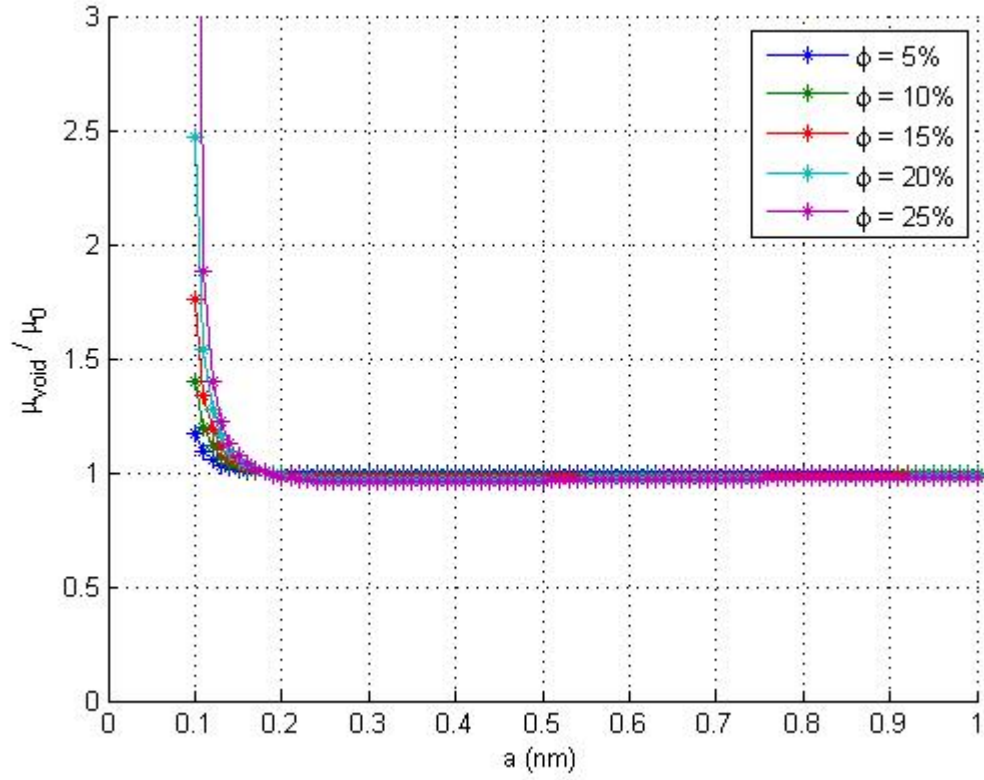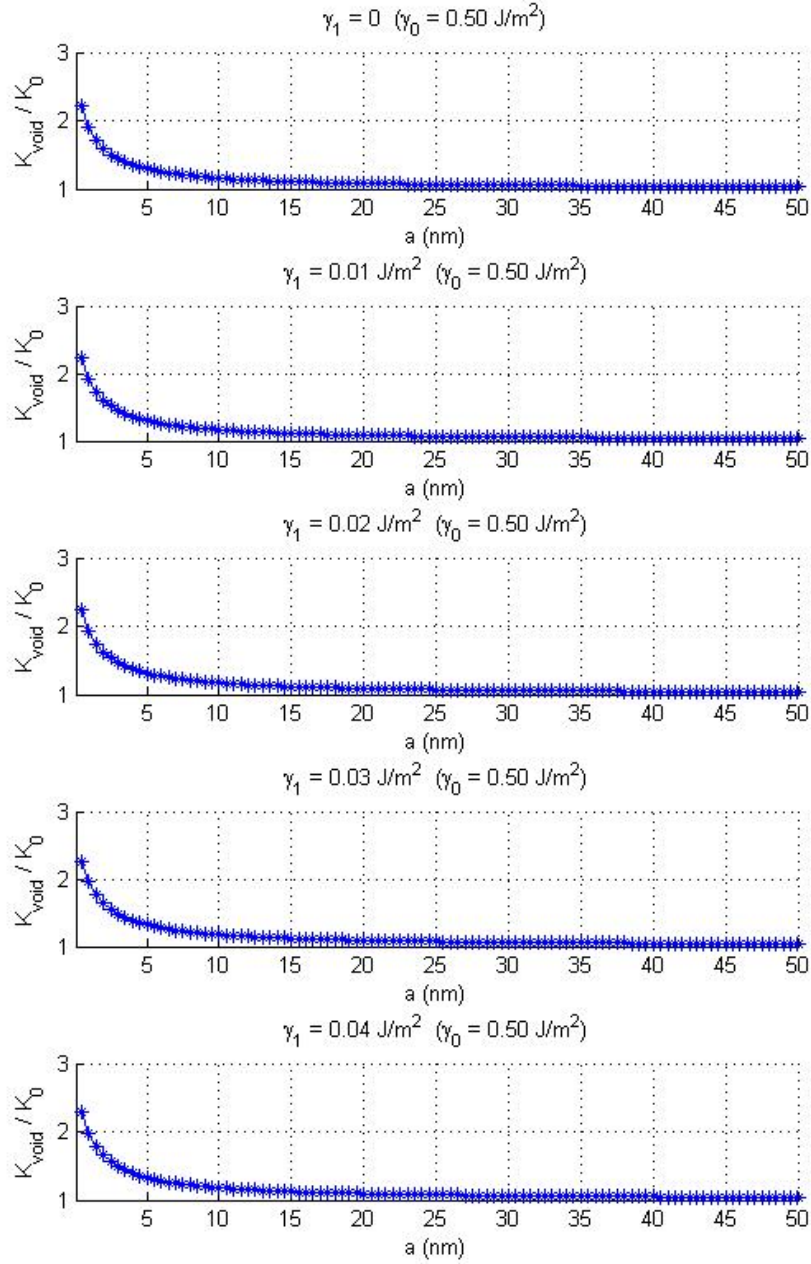
Figure 3.14 Individual plots for normalized effective bulk modulus against the radius of voids in the range of nanometer size with five different secondary terms, γ_1, of the interface/surface energy with $\gamma_0 = 0.50$ J/m^2

3.4 Conclusions

The interface/surface energy effect on the macroscopic mechanical behavior of a composite is investigated through starting with the finite deformation theory of a multi-phase hyperelastic medium. Then, the approximate formulation of a finitely deformed multiphase elastic medium by an infinitesimal deformation analysis is executed. According to the existence of the interface energy, even though under no external loading, there is still a "residual elastic field" induced by the interface stress. During the deformation process of a composite from the reference configuration to the current configuration, the changes of the size and shape of the interface leads to the change of this "residual elastic field". It is noticed that the governing equations describing the change of the "residual elastic field" due to the change of the configuration are formulated under the infinitesimal deformation approximation and hence lead to the use of the asymmetric interface stress in the prediction of the effective properties of heterogeneous materials with interface/surface energy effect. Therefore, the influence of the residual interface/surface energy can be taken into account. In particular, the theoretical framework is applied to obtain the analytical expressions of the effective bulk and shear moduli of a composite with spherical "equivalent inhomogeneities" (i.e. the inhomogeneities together with the interface/surface energy). Moreover, it can be seen that the mechanical behavior of the composite reveals the size-dependent effect when the interface energy effect is considered. Furthermore, it is found that the analytical results developed in this chapter are applicable in the study of nanocomposites, even if the formulations are mainly derived based on the mechanism of micromechanics.

In addition, through the illustrative figures developed based on the analytical expressions, it is found that the interface/surface effect decreases with the increase of the size of the voids and

almost can be neglected when the radius of the void is larger than 10 nm. Moreover, it can be seen that the larger the interface/surface energy becomes, the more the effect of the interface/surface energy is on the effective moduli of the composite. In addition, if the higher volume fraction of the particles (with the same strength/stiffness) is executed, it is found that the interface/surface effect on the effective bulk and shear moduli of the composite increases. Further, at the same strength of particles, more volume fraction used results in larger size of the particles is affected by the interface/surface energy. Lastly, except the result produced by the Eshelby method, the results developed by Ju and Chen's model and Mori-Tanaka's model are extremely approaching.

3.5 Appendix A: Formulations upon Finite Deformation Theory

The constitutive relations of the interface have been widely investigated by many researchers in the literature. But most of works on this subject are confined to the infinitesimal deformation approximations. Suppose that the interface/surface energy per unit area in the current configuration is denoted by γ. If the interface is assumed to be isotropic relative to the reference configuration κ_0, i.e. the underlying reference configuration is an undistorted state, then γ can be expressed as a function of the invariants of $\mathbf{U}_s$ and $\mathbf{V}_s$, or a function of J_1 and J_2, as follows,

$$J_1 = tr\,\mathbf{U}_s = tr\,\mathbf{V}_s$$

$$J_2 = \det\mathbf{U}_s = \det\mathbf{V}_s$$

(3.36)

where $\mathbf{U}_s$ and $\mathbf{V}_s$ are the right and left stretch tensors of the interface, respectively; J_1 and J_2 are the first and second invariants of $\mathbf{U}_s$ and $\mathbf{V}_s$. If the small deformation is concerned, the strain at the interface may be approximately expressed by

$$\mathbf{E}_s = \frac{1}{2}\left(\mathbf{u}\nabla_{0s} + \nabla_{0s}\mathbf{u}\right) = \mathbf{U}_s - \mathbf{i}_0 \tag{3.37}$$

where ∇_{0s} is the surface gradient operator on operator in the reference configuration κ_0; $\mathbf{u}\nabla_{0s}$ is the displacement gradient of the interface; $\mathbf{i}_0$ is the second-order identity tensor in the tangent plane of the interface in the reference configuration. Substituting Eq. (3.37) into Eq. (3.36), J_1 and J_2 can be re-written as

$$J_1 = 2 + tr\,\mathbf{E}_s$$
$$\tag{3.38}$$
$$J_2 = 1 + tr\,\mathbf{E}_s + \det\mathbf{E}_s$$

In the case of the isotropic interface and the small deformation, the interface Piola-Kirchhoff stresses of the first kind and second kind including "out-of-plane term" can be formulated as

$$\overset{(in)}{\mathbf{S}_s} = \overset{(in)}{\mathbf{F}_s} \cdot \overset{(1)}{\mathbf{T}_s}$$
$$= J_2\left(\frac{\partial\gamma}{\partial J_1} + J_2\frac{\partial\gamma}{\partial J_2} + \gamma\right)\mathbf{i}_0 + J_2\frac{\partial\gamma}{\partial J_1}\mathbf{E}_s - J_2\left(\frac{\partial\gamma}{\partial J_1} + J_2\frac{\partial\gamma}{\partial J_2} + \gamma\right)(\nabla_{0s}\mathbf{u})$$

$$\overset{(out)}{\mathbf{S}_s} = \overset{(out)}{\mathbf{F}_s} \cdot \overset{(1)}{\mathbf{T}_s} \tag{3.39}$$
$$= J_2\left(\frac{\partial\gamma}{\partial J_1} + J_2\frac{\partial\gamma}{\partial J_2} + \gamma\right)\overset{(out)}{\mathbf{F}_s}$$

$$\mathbf{S}_s = \overset{(in)}{\mathbf{S}_s} + \overset{(out)}{\mathbf{S}_s}$$

$$\mathbf{T}_s = J_2\left(\frac{\partial\gamma}{\partial J_1} + J_2\frac{\partial\gamma}{\partial J_2} + \gamma\right)\mathbf{i}_0 - J_2\left(\frac{\partial\gamma}{\partial J_1} + 2J_2\frac{\partial\gamma}{\partial J_2} + 2\gamma\right)\mathbf{E}_s \tag{3.40}$$

where $\mathbf{F}_s$ is the "out-of-plane term" of surface gradient. And the Cauchy stress of the interface can be described by

$$\boldsymbol{\sigma}_s = \left(\frac{\partial \gamma}{\partial J_1} + J_2 \frac{\partial \gamma}{\partial J_2} + \gamma \right) \mathbf{i}_0 + \frac{\partial \gamma}{\partial J_1} \mathbf{E}_s + \left(\frac{\partial \gamma}{\partial J_1} + J_2 \frac{\partial \gamma}{\partial J_2} + \gamma \right) \left(\overset{(out)}{\mathbf{F}_s} + \overset{(out)^T}{\mathbf{F}_s} \right) \tag{3.41}$$

Therefore, it is found that $\mathbf{S}_s$, $\mathbf{T}_s$ and the Cauchy stress of the interface $\boldsymbol{\sigma}_s$ are not the same, even if the infinitesimal deformation approximation is performed. The situation is totally different from that in the three dimensional analysis in the traditional elasticity, in which there is no residual stress in the reference configuration. In other words, only through the beginning with the finite deformation theory, an appropriate infinitesimal interface stress is then chosen in the governing equations if the interface/interface energy effect is taken into account on the mechanical properties of a heterogeneous material.

3.6 Appendix B: Approximations upon Infinitesimal Deformation Analysis

In this section, the approximate equations of the changes of the interface stress and the Young-Laplace equation due to the change of configuration under the infinitesimal deformation is introduced. Then, the analytical equations for the effective moduli of a particle-reinforced composite is given through the application of the theory by Huang and Sun (2007), which depicts the effect of the liquid-like interface/surface energy on the effective moduli.

The governing equations, such as the equilibrium equations, based on one configuration are well-known in the infinitesimal analysis in the traditional elasticity. In order to study the interface energy effect, however, the residual elastic field induced by the interface energy should

be taken into account. Although the interface induced the residual elastic field in the reference configuration or in the current configuration is not cared for, the change of the residual elastic field induced by the interface energy from the reference configuration to the current configuration is strongly concerned. Since after and before deformation, the Cauchy stresses (in the bulk material and at the interface) are not in the same configuration based on the Eulerian description, it is obvious that the difference of the Cauchy stresses cannot be used to represent this change. Therefore, the Lagrangian description is applicable, so that the generalized Young-Laplace equation based on the Lagrangian description given by Huang and Wang (2006) can then be expressed in terms of the interface Piola-Kirchhoff stress of the first kind in the following,

$$\mathbf{N} \cdot \left[\!\left[\mathbf{S}^0 \right]\!\right] \cdot \mathbf{N} = - \overset{(in)}{\mathbf{S}}_s : \mathbf{b}_0 - \left[\mathbf{N} \cdot \left(\overset{(out)}{\mathbf{S}}_s \right) \right] \cdot \nabla_{0s}$$

$$\mathbf{P}_0 \cdot \left[\!\left[\mathbf{S}^0 \right]\!\right] \cdot \mathbf{N} = - \overset{(in)}{\mathbf{S}}_s \cdot \nabla_{0s} + \left[\mathbf{N} \cdot \left(\overset{(out)}{\mathbf{S}}_s \right) \cdot \mathbf{b}_0 \right] \qquad (3.42)$$

$$\mathbf{P}_0 = \mathbf{I} - \mathbf{N} \otimes \mathbf{N}$$

where the symbol $\left[\!\left[\cdot \right]\!\right]$ denotes the discontinuity of a quantity across the interface; $\mathbf{S}^0$ is the first kind Piola-Kirchhoff stress in the bulk material; $\mathbf{I}$ is the unit tensor in three-dimensional space; $\mathbf{N}$ is the unit normal vector to the interface in the reference configuration κ_0; $\mathbf{b}_0$ is the curvature tensor of the interface in κ_0.

Obviously, the change of the residual elastic field induced by the interface energy can be re-written by adding the difference sign into the above equation, as follows,

$$N \cdot \left[\!\left[\Delta S^0\right]\!\right] \cdot N = -\Delta \overset{(in)}{S}_s : b_0 - \left[N \cdot \left(\Delta \overset{(out)}{S}_s\right)\right] \cdot \nabla_{0s}$$

$$P_0 \cdot \left[\!\left[\Delta S^0\right]\!\right] \cdot N = -\Delta \overset{(in)}{S}_s \cdot \nabla_{0s} + \left[N \cdot \left(\Delta \overset{(out)}{S}_s\right) \cdot b_0\right]$$

(3.43)

where Δ denotes the difference of the quantities between the current and reference configurations. In order to account for the interface energy effect, the interface Piola-Kirchhoff stress of the first kind S_s should be employed in the analysis, as shown in the equations above. This is the key point addressed by Huang and Wang (2006), but the previous researchers seemed to ignore that in the study of the effective properties of a heterogeneous material with interface energy effect. Next, an infinitesimal deformation approximation is executed. In the case of the infinitesimal deformation, ΔS^0 in Eq. (3.43) could be approximated by the difference of the bulk Cauchy stress between the current and reference configurations, while S_s in Eq. (3.39) is described in terms of the interface/surface free energy γ.

In addition, the equation of the interface/surface free energy is linearized in order to simplify the algebraic operations at the beginning of the research. Accordingly, γ can be written as

$$\gamma = \gamma_0 + \gamma_1 (J_1 - 2) + \gamma_2 (J_2 - 1) + \frac{1}{2}\gamma_{11}(J_1 - 2)^2 + \gamma_{12}(J_1 - 2)(J_2 - 1) + \frac{1}{2}\gamma_{22}(J_2 - 1)^2 + \cdots$$

(3.44)

$$\gamma_1 = \frac{\partial \gamma}{\partial J_1}\Big|_{J_1=2, J_2=1} \quad , \quad \gamma_2 = \frac{\partial \gamma}{\partial J_2}\Big|_{J_1=2, J_2=1}$$

Where γ_0, γ_1, γ_2 represent the intrinsic physical properties of the interface, and they are, and should be determined by the joining materials and the adhering condition. $\gamma_0 = \gamma(2,1)$ is

equivalent to the interface/surface energy of a liquid-like material and hence reflects the nature of liquids, whereas γ_1 and γ_2 reflect the nature of solids; $J_1 - 2$ and $J_2 - 1$ are first-order small quantities. Suppose that only the first-order small quantities are considered in Eq. (3.39) and higher-order small quantities are neglected, from

$$J_2\left(\frac{\partial\gamma}{\partial J_1} + J_2\frac{\partial\gamma}{\partial J_2} + \gamma\right) = \gamma_0^* + \left(\gamma_0^* + \gamma_1^*\right)tr\,\mathbf{E}_s \tag{3.45}$$

and

$$J_2\frac{\partial\gamma}{\partial J_1} = \gamma_1 + \left(\gamma_0 + \gamma_{11} + \gamma_{12}\right)tr\,\mathbf{E}_s \tag{3.46}$$

Then,

$$\mathbf{S}_s = \gamma_0^*\mathbf{i}_0 + \left(\gamma_0^* + \gamma_1^*\right)(tr\mathbf{E}_s)\mathbf{i}_0 - \gamma_0^*\nabla_{0s}\mathbf{u} + \gamma_1\mathbf{E}_s + \gamma_0^*\overset{(out)}{\mathbf{F}_s} \tag{3.47}$$

$$\boldsymbol{\sigma}_s = \gamma_0^*\mathbf{i}_0 + \gamma_1^*\left(tr\,\mathbf{E}_s\right)\mathbf{i}_0 + \gamma_1\mathbf{E}_s + \gamma_0^*\left(\overset{(out)}{\mathbf{F}_s} + \overset{(out)^T}{\mathbf{F}_s}\right) \tag{3.48}$$

where $\gamma_0^* = \gamma_0 + \gamma_1 + \gamma_2$, $\gamma_1^* = \gamma_1 + 2\gamma_2 + \gamma_{11} + 2\gamma_{12} + \gamma_{22}$, and γ_0^* and γ_1^* form the residual interface/surface energy. For small deformation, $\mathbf{i}_0 + \left(\overset{(out)}{\mathbf{F}_s} + \overset{(out)^T}{\mathbf{F}_s}\right) = \mathbf{i}$ in the tangent plane T_y.

The similar expression with an assumption of the interface stress is dependent on the isotropic linear function of the interface strain can be found by Gurtin and Murdoch (1975). Here, the present formulation shows the interface stress in terms of the interface/surface energy. Later, as the change of the interface stress due to the change of the configuration is discussed, this theoretical framework is applied to predict the effective moduli of heterogeneous media with the interface/surface energy effect. In the reference configuration κ_0, the "residual" interface Piola-Kirchhoff stress of the first kind is expressed by

77

$$\mathbf{S}_s\,|_0 = \gamma_0^* \mathbf{i}_0 \qquad\qquad\qquad (3.49)$$

Accordingly, in the case of the infinitesimal deformation, the difference of the interface Piola-Kirchhoff stress of the first kind between the current and reference configurations, $\Delta\mathbf{S}_s$, can be written as

$$\Delta\mathbf{S}_s = \left(\gamma_0^* + \gamma_1^*\right)\left(tr\mathbf{E}_s\right)\mathbf{i}_0 - \gamma_0^*\nabla_{0s}\mathbf{u} + \gamma_1\mathbf{E}_s + \gamma_0^*\overset{(out)}{\mathbf{F}_s} \qquad (3.50)$$

It is found that there are at least three independent material parameters γ_0^*, γ_1^* and γ_1 required in the above equation. For some special cases, such as a spherical inhomogeneity embedded in an infinite matrix material under the axisymmetric loading, $\nabla_{0s}\mathbf{u}$ may be regarded as a symmetric second-order tensor in two-dimensional space. Eq. (3.50) is then written as

$$\Delta\mathbf{S}_s = \left(\gamma_0^* + \gamma_1^*\right)\left(tr\,\mathbf{E}_s\right)\mathbf{i}_0 - \left(\gamma_0^* - \gamma_1\right)\mathbf{E}_s + \gamma_0^*\overset{(out)}{\mathbf{F}_s}$$

$$(3.51)$$

$$\text{Or,}\quad \Delta\mathbf{S}_s = \lambda_s\left(tr\,\mathbf{E}_s\right)\mathbf{i}_0 + 2\mu_s\mathbf{E}_s + \gamma_0^*\overset{(out)}{\mathbf{F}_s}$$

where λ_s and μ_s are called interface moduli, shown as follows,

$$\lambda_s = \gamma_0^* + \gamma_1^*$$

$$(3.52)$$

$$\mu_s = -\frac{1}{2}\left(\gamma_0^* - \gamma_1\right) = -\frac{1}{2}\left(\gamma_0 + \gamma_2\right)$$

It is noted that μ_s could be negative in some cases. In general, the interface/surface energy γ_0 at κ_0 is positive; otherwise a liquid or a solid would gain energy upon fragmentation, for example, as referred to the research by Haiss (2001). γ_2 is the change rate of the interface energy due to the change of the interface area, and the negative μ_s has been confirmed by Shenoy (2005) in his atomistic calculations. Substituting $\Delta\mathbf{S}_s$ in Eq. (3.50) or (3.51) into Eq.

(3.43), the discontinuity conditions of the traction across the interface in the reference configuration κ_0 is generated. These discontinuity conditions, associated with other governing equations, can be used to predict the macroscopic mechanical response of composites with the interface energy effect.

3.7 References

[1] Benveniste, Y. (1985). "The effective mechanical-behavior of composite-materials with imperfect contact between the constituents." *Mechanics of Materials*, 4(2), 197-208.

[2] Benveniste, Y. (1987). "A new approach to the application of Mori-Tanaka theory in composite-materials." *Mechanics of Materials*, 6(2), 147-157.

[3] Benveniste, Y., and Miloh, T. (2001). "Imperfect soft and stiff interfaces in two-dimensional elasticity." *Mechanics of Materials*, 33(6), 309-323.

[4] Cahn, J. W. (1978). "Thermodynamics of solid and fluid surface." *Interfacial segregation*, American Society for Metals, Metals Park, Ohio, 3-23.

[5] Cammarata, R. C. (1994). "Surface and interface stress effects in thin-films." *Progress in Surface Science*, 46(1), 1-38.

[6] Christensen, R. M., and Lo, K. H. (1979). "Solutions for effective shear properties in 3 phase sphere and cylinder models." *Journal of the Mechanics and Physics of Solids*, 27(4), 315-330.

[7] Duan, H. L., Wang, J., Huang, Z. P., and Karihaloo, B. L. (2005). "Size-dependent effective elastic constants of solids containing nano-inhomogeneities with interface stress." *Journal*

of the Mechanics and Physics of Solids, 53(7), 1574-1596.

[8] Duan, H. L., Wang, J., Huang, Z. P., and Luo, Z. Y. (2005). "Stress concentration tensors of inhomogeneities with interface effects." *Mechanics of Materials*, 37(7), 723-736.

[9] Eshelby, J. D. (1957). "The determination of the elastic field of an ellipsoidal inclusion, and related problems." *Proceedings of the Royal Society of London Series a-Mathematical and Physical Sciences*, 241(1226), 376-396.

[10] Fried, E., and Gurtin, M. E. (2004). "A unified treatment of evolving interfaces accounting for small deformations and atomic transport with emphasis on grain-boundaries and epitaxy." *Advances in Applied Mechanics, Vol 40*, 40, 1-177.

[11] Fried, E., and Gurtin, M. E. (2004). "A unified treatment of evolving interfaces accounting for small deformations and atomic transport with emphasis on grain-boundaries and epitaxy." *Advances in Applied Mechanics, Vol 40*, 40, 1-177.

[12] Gibbs, J. W. (1906). "The scientific papers of J. Willard Gibbs." Longmans-Green, London, Vol 1.

[13] Gurtin, M. E., and Murdoch, A. I. (1975). "Continuum theory of elastic-material surfaces." *Archive for Rational Mechanics and Analysis*, 57(4), 291-323.

[14] Haiss, W. (2001). "Surface stress of clean and adsorbate-covered solids." *Reports on Progress in Physics*, 64(5), 591-648.

[15] Hashin, Z., Shtrikman, S. A. (1963). "A variational approach to the theory of the elastic behavior of multiphase materials." *Journal of the Mech. Phys. Solids*, 11, 127-140.

[16] Hashin, Z. (1991). "Thermoelastic properties particulate composites with imperfect interface." *Journal of the Mechanics and Physics of Solids*, 39(6), 745-762.

[17] Hashin, Z. (1962). "The elastic moduli of heterogeneous materials." *Journal of the Applied*

Mechanics, 29, 143-150.

[18] Hashin, Z. (2002). "Thin interphase/imperfect interface in elasticity with application to coated fiber composites." *Journal of the Mechanics and Physics of Solids*, 50(12), 2509-2537.

[19] Herring, C. (1953). "The use of classical macroscopic concepts in surface energy problems." *Structure and properties of solid surfaces*, The University of Chicago, Chicago, pp.5-81.

[20] Huang, Z. P., and Sun, L. (2007). "Size-dependent effective properties of a heterogeneous material with interface energy effect: from finite deformation theory to infinitesimal strain analysis." *Acta Mechanica*, 190(1-4), 151-163.

[21] Huang, Z. P., and Wang, J. (2006). "A theory of hyperelasticity of multi-phase media with surface/interface energy effect." *Acta Mechanica*, 182(3-4), 195-210.

[22] Ibach, H. (1997). "The role of surface stress in reconstruction, epitaxial growth and stabilization of mesoscopic structures." *Surface Science Reports*, 29(5-6).

[23] Ju, J. W., and Chen, T. M. (1994a). "Micromechanics and effective moduli of elastic composites containing randomly dispersed ellipsoidal inhomogeneities." *Acta Mechanica*, 103(1-4), 103-121.

[24] Ju, J. W., and Chen, T. M. (1994b). "Effective elastic-moduli of 2-phase composites containing randomly dispersed spherical inhomogeneities." *Acta Mechanica*, 103(1-4), 123-144.

[25] Ju, J. W., and Chen, T. M. (1994c). "Micromechanics and effective elastoplastic behavior of 2-phase metal-matrix composites." *Journal of Engineering Materials and Technology-Transactions of the Asme*, 116(3), 310-318.

[26] Lur'e, A. I. (1964). "Three-dimensional problems of theory of elasticity." Interscience, New York.

[27] Milton, G. W. (2002). "The theory of composites." Cambridge University Press, Cambridge.

[28] Mori, T., and Tanaka, K. (1973). "Average stress in matrix and average elastic energy of materials with misfitting inclusions." *Acta Metallurgica*, 21(5), 571-574.

[29] Muller, P., and Saul, A. (2004). "Elastic effects on surface physics." *Surface Science Reports*, 54(5-8), 157-258.

[30] Mura, T. (1987). "Micromechanics of defects in solids." Martinus Nijhoff, Dordrecht.

[31] Murdoch, A. I. (2005). "Some fundamental aspects of surface modelling." *Journal of Elasticity*, 80(1-3), 33-52.

[32] Nemat-Nasser, S., Hori, M. (1999). "Micromechanics: overall properties of heterogeneous elastic solids." North-Holland, Amsterdam, 2nd edition.

[33] Orowan, E. (1970). "Surface energy and surface tension in solids and liquids." *Proceedings of the Royal Society of London Series a-Mathematical and Physical Sciences*, 316(1527), 473-491.

[34] Qu, J., and Cherkaoui, M. (2006). "Fundamentals of micromechanics of solids." John Wiley & Sons, Inc.

[35] Sharma, P., and Ganti, S. (2004). "Size-dependent Eshelby's tensor for embedded nano-inclusions incorporating surface/interface energies." *Journal of Applied Mechanics-Transactions of the Asme*, 71(5), 663-671.

[36] Shenoy, V. B. (2005). "Atomistic calculations of elastic properties of metallic fcc crystal surfaces." *Physical Review B*, 71(9).

[37] Shuttleworth, R. (1950). "The surface tension of solids." *Proceedings of the Physical Society of London Section A*, 63(365), 444-457.

[38] Sun, L., Wu, Y. M., Huang, Z. P., and Wang, J. X. (2004). "Interface effect on the effective bulk modulus of a particle-reinforced composite." *Acta Mechanica Sinica*, 20(6), 676-679.

[39] Torquato, S. (2002). "Random heterogeneous materials: microstructure and macroscopic properties." Springer, New York.

[40] Wang, J., Duan, H. L., Zhang, Z., and Huang, Z. P. (2005). "An anti-interpenetration model and connections between interphase and interface models in particle-reinforced composites." *International Journal of Mechanical Sciences*, 47(4-5), 701-718.

[41] Weng, G. J. (1990). "The theoretical connection between Mori-Tanaka theory and the Hashin-Shtrikman-Walpole bounds." *International Journal of Engineering Science*, 28(11), 1111-1120.

[42] Zheng, Q. S., and Du, D. X. (2001). "An explicit and universally applicable estimate for the effective properties of multiphase composites which accounts for inclusion distribution." *Journal of the Mechanics and Physics of Solids*, 49(11), 2765-2788.

Chapter 4

INTERFACE ENERGY EFFECT ON SIZE-DEPENDENT EFFECTIVE ELASTIC MODULI OF THREE-PHASE COMPOSITES WITH RANDOMLY LOCATED AND INTERACTING SPHERICAL PARTICLES OF DISTINCT PROPERTIES

ABSTRACT

In Chapter 3, the interface/surface energy effect, regarded as the change of the residual elastic field induced by the interface stress from the reference configuration to the current configuration, has been derived. Accordingly, the analytical equations of the size-dependent effective moduli of a composite material containing identical spherical particles of the same property and size (so-called "two-phase" composite) with the interface/surface energy effect are thus developed. In this chapter, a micromechanical analytical framework is separately rendered to predict effective elastic moduli of "three-phase" composites containing many randomly dispersed and pairwisely interacting spherical particles with no interface/surface energy effect. Specifically, the two inhomogeneity phases feature distinct elastic properties. A higher-order structure is proposed based on the probabilistic spatial distribution of spherical particles, the

pairwise particle interactions, and the ensemble-volume homogenization method. Subsequently, by integrating the above two mechanisms, two non-equivalent formulations are considered in detail to derive effective elastic moduli of a three-phase composite containing two distinct heterogeneous particles with the interface/surface energy effect. Lastly, the analytical equations in some special cases for the influence of the liquid-like interface/surface energy on the effective properties of three-phase composites containing two distinct particles are discussed. Following numerical examples are implemented to illustrate the potential of the present method. Further, it is demonstrated that the results with the interface/surface energy effect in our model, different from the results given by preceding researchers, would be more applicable to the nanocomposites.

Key Words: Interface/surface energy effect; Three-phase composite; Finite deformation theory; Infinitesimal strain analysis; Micromechanical analytical framework; Probabilistic spatial distribution; Pairwise particle interactions; Ensemble-volume homogenization; Nanocomposite

4.1 Introduction

There are many published literatures and studies on the subject of predicting the effective elastic moduli of random heterogeneous multi-phase particle/fiber-reinforced composites. Most researchers, however, mainly focus on conventional composites with a single type of fiber/particle embedded in the matrix without considering the effects of different fiber/particle properties. Among them, several categories are of considerable interest to investigate.

The first category employs variational principles or linear comparison composites to obtain mathematical lower and upper bounds for effective elastic moduli of composites. For example, Hashin and Shtrikman (1962a; 1962b; 1963) proposed the upper and lower bounds for effective elastic moduli of multiphase materials based on the variational principles within the linear elasticity theory and, in generally, it is better than the Voigt and Reuss bounds. Furthermore, Hill (1964a; 1964b), Hashin and Rosen (1964), Hashin (1965), Walpole (1966a; 1966b; 1969), and Hashin (1972) are also selected references for this category. Nevertheless, Silnutnzer (1972), Milton (1982), Milton and Phan-Thien (1982), and Torquato and Lado (1992) investigated the "improved" higher-order mathematical bounds, which depend on the statistical microstructural information of random heterogeneous composite. For instance, Silnutzer (1972) derived improved bounds, which are referred to as the third-order (three-point) bounds, on effective in-plane bulk and shear moduli. Moreover, it is noted that the third-order bounds are narrower than the two-point bounds of Hashin's type.

The second category is known as the "effective medium approach" used for micromechanical estimation about effective moduli of composites, including the self-consistent method, the differential scheme, the generalized self-consistent method, and the Mori-Tanaka method (Mori and Tanaka, 1973). In the meanwhile, Hill (1965a; 1965b), Christensen and Lo (1979), Mori and Tanaka (1973), Benveniste (1987), and Weng (1990) are the popular references for the effective medium method. However, the effective medium methods as a group depend only on geometries of particles (inclusions) and volume fractions; in other words, they do not consider the spatial locations and/or probabilistic distributions of particles (inclusions). As the effective medium methods are inherently independent of the spatial or statistical particles distribution, it is best appropriate for low particle concentrations or some limited special

configurations.

The third category, in contrast with the second category, directly determined the micromechanics of effective properties of composites with randomly located and interacting inclusions by employing some approximations with certain special geometric configurations of inclusions dispersing in matrix materials. For example, Eshelby (1957) proposed an ellipsoidal inclusion embedded in an infinite matrix and developed the famous "Eshelby's equivalence principle". Mura (1987) mainly considered rigorous "local" micromechanics. Honein (1991) pointed out a general framework to solve the problem of two-circular inclusions in plane elastostatics, subjected to arbitrary loading by utilizing Kolosov–Muskhelishvili complex potentials. Nemat-Nasser and Hori (1993) also made a great contribution to this approach. However, only "local" field solutions were obtained through this approach. For this reason, a micromechanical higher-order ensemble-volume average method was constrcted by Ju and Chen (1994a; 1994b), based upon the framework by Eshelby (1957), to obtain the elastic effective moduli of multi-phase composites containing randomly dispersed ellipsoidal and spherical inhomogeneities, respectively. Upon this method, which considered the pairwise inclusion interactions, both "local" and "overall" field solutions can be obtained, and accordingly, the ensemble-volume averaged micromechanical field equations were formulated by the homogenization process. Soon after, along the line of Ju and Chen (1994a; 1994b), Ju and Zhang (1998), Ju and Yanase (2010; 2011), and Lin and Ju (2009) established the effective elastic moduli of composites with randomly located aligned circular fibers or randomly dispersed spherical particles featuring same/distinct elastic properties and the same sizes. Subsequently, Ko and Ju (2012; 2013) rendered the effective transverse elastic moduli of a three-phase composites with randomly located aligned circular fibers of distinct elastic properties and sizes. In addition,

emanating from the general framework of Ju and Chen (1994a; 1994b), Ju and co-workers further explored the micromechanical effective elastoplastic behaviors of two-phase metal matrix composites (Ju and Chen, 1994c; Ju and Tseng, 1996; Ju and Tseng, 1997; Ju and Zhang, 2001; Ju and Sun, 2001; Sun and Ju, 2001), the exact formulation for the exterior-point Eshelby's tensor of an ellipsoidal inclusion (Ju and Sun, 1999) and micromechanical damage models for effective elastoplastic behaviors of ductile matrix composites accommodating evolutionary particle debonding/cracking and interfacial fiber debonding with/without thermal residual stresses effects (Ju and Lee, 2000; Ju and Lee, 2001; Sun et al., 2003a; Sun et al., 2003b; Liu et al., 2004a; Liu et al., 2004b; Ko, 2005; Ju et al., 2006; Liu et al., 2006; Ju et al., 2008; Ju and Ko, 2008; Ju and Yanase, 2008; Lee and Ju, 2008; Ju et al., 2009; Ju and Yanase, 2009; Ju and Yanase, 2011; Ko and Ju, 2012).

Lastly, other categories utilized numerical solutions to analyze the effective properties of multi-phase composites. For example, Adams and Crane (1984), Nimmer et al. (1991), and Doghri and Friebel (2005) were based on the "finite element methods" to provide the effective properties of a composite by the developed "unit cell model" and some assumed periodic arrays of fibers. On contrast, "Rigid-Body-Spring-Model (RBSM) method" is another numerical approach to construct the effective properties of multi-phase composites, which can refer to Kawai (1978), Bolander and Saito (1998), Gedil et al. (2011; 2012), and Yamamoto et al. (2013). The introduction to RBSM and its application for finding the effective properties of multi-phase composites are presented in Chapter 7 of my research as well.

Nowadays, since the materials science and technique have been advanced to the characteristic size of a nano-scale solid in structures and composites, the interface/surface energy effect on mechanical and physical properties of nanocomposites and nano-size structures

becomes significant and cannot be ignored. Therefore, the interface/surface energy effect should be accounted into the deformation analysis of solids.

In Huang and Sun (2007), the change of the elastic fields induced by the interface energies and the interface stresses from the reference configuration to the current configuration was considered. It was emphasized that there are two kinds of fundamental equations required to be introduced in the solution of boundary-value problems for stress fields with the interface/surface energy effect. The first is the interface/surface constitutive relations, whereas the second is the discontinuity conditions of the stress across the interface, namely, the Young-Laplace equations. These two fundamental equations are used to predict the effective moduli of a composite material with the interface/surface energy effect. Although an infinitesimal strain analysis is employed to establish the governing equations induced by the interface/surface energy, the finite deformation analysis (also known as the large deformation analysis) of a multi-phase hyperelastic medium should be concerned at the beginning, according to reasons as follows:

(1) The mechanical response from the reference configuration to the current configuration should be considered in the study of the mechanical behavior of a composite material or a structure. In this regard, the change of the size and the shape of the interface in the process of the deformation reflect the change of the curvature tensor in the governing equations. In other words, the change of the deformation and the configuration leads to the change of the residual elastic field induced by the interface energy. In essence, hence, this is a finite deformation problem. Furthermore, the interface/surface energy effect is explicitly verified by the change of the residual elastic field due to the change of the configuration.

(2) To develop the governing equations with the interface/surface energy effect, a residual elastic field induced by the interface energy and the interface stress in the material should be

introduced, even though there is no external loading. That is to say, through accounting for the change of the residual elastic field upon the change of the configuration, the effect of the liquid-like interface/surface energy on the effective properties of a composite material can then be included. In this chapter, this type of the interface energy model is emphasized and discussed.

(3) The constitutive relations for the hyperelastic solids with the interface/surface energy effect at the finite deformation have been formulated by Huang and Wang (2006) and Huang and Sun (2007), as introduced in Section 4.7 Appendix A. Moreover, the approximation expressions of the changes of the interface stress and the Young-Laplace equations due to the change of the configuration through the infinitesimal deformation analysis can be found in Section 4.8 Appendix B. These constitutive relations are expressed in terms of the free energy of the interface per unit area at the current configuration, denoted by γ (see Section 4.8 Appendix B for more details).

Furthermore, composite materials have developed rapidly over the last several decades. They are usually designed to meet the diverse needs for enhancing material performance with advanced thermo-mechanical properties, reduced unit weights, versatile directionality, optimal anisotropy, etc., and for improving material mechanical strengths, elastic moduli, delamination resistance, fracture toughness and fatigue resistance. Reinforcements could be continuous in the form of fibers, or discontinuous in the form of particles or whiskers. Especially, for engineers and scientists, to predict and estimate overall mechanical properties and behaviors of random heterogeneous multi-phase composites are of quite interest in many science, technology, engineering and mathematical disciplines. In general, mechanical properties and behaviors of composites are dependent on properties of constituent phases and microstructures of

inhomogeneities, such as shapes, orientations, aspect ratios, volume fractions, random locations, etc.

The primary objective of the present chapter is to extend the work regarding the interface/surface energy effect on size-dependent effective moduli of a "two-phase" composite containing identical particles of the same property and size, based on the framework of Lin and Ju (2009) and the methodology of Huang and Sun (2007), to the one regarding the interface/surface energy effect on size-dependent effective moduli of a "three-phase" composite containing two particles of the distinct properties with the same size. This model is achieved with consideration to mechanical properties of the constituent phases, volume fractions, spatial distributions of particles, and direct inter-particle interactions. Specifically, the two inhomogeneity inclusions/phases feature distinct elastic properties. All particles are considered non-intersecting, randomly dispersed, and embedded firmly in the matrix with perfect interfaces. Two non-equivalent formulations are considered in detail to derive effective elastic moduli of three-phase composites leading to new higher-order bounds. Hence, a higher-order micromechanical analytical framework is constructed based on the probabilistic spatial distribution of spherical particles, pairwise particle interactions, and the ensemble-volume averaging (homogenization) procedure for three-phase elastic composites.

In this chapter, before the analytical framework for the interface/surface energy effect on the size-dependent effective moduli of a three-phase composite with randomly located and interacting spherical particles of distinct properties is investigated, the interface/surface energy effect on the size-dependent effective moduli of a two-phase composite consisting of the matrix and randomly distributed spherical inhomogeneities is first considered in Section 4.2. Subsequently, in Section 4.3, the effective bulk and shear moduli of a three-phase composite

containing randomly dispersed spherical particles of distinct elastic properties are separately formulated based on another framework with consideration to the concepts of probabilistic spatial distribution of spherical particles, pairwise particle interactions, and the ensemble-volume averaging (homogenization) procedure for three-phase elastic composites. Those concepts can be found in Section 4.9 Appendix C and Section 4.10 Appendix D. Specifically, in Section 4.9 Appendix C, the approximate analytical solutions for the direct interactions between two different randomly located elastic spheres embedded in the matrix material are presented, followed by the ensemble-volume averaged eigenstrains through the probabilistic pairwise particle interaction mechanism developed in Section 4.10 Appendix D. Also in Section 4.3, two non-equivalent formulations are considered in detail to derive effective elastic moduli of three-phase composites with no the interface/surface energy effect. Later on, in combination with the results from Section 4.2 and Section 4.3, effective elastic moduli of three-phase composites containing randomly dispersed distinct spherical particles with the interface/surface energy effect are analytically derived in Section 4.4. Numerical results and the corresponding discussions are rendered in Section 4.5 to demonstrate the potential of this present model. Specifically, some special cases of the interface/surface energy effect on a three-phase composite containing randomly dispersed spheres of same/distinct properties embedded in an elastic matrix are executed in Section 4.5. Lastly, the conclusion is summarized in Section 4.6.

4.2 Effective Moduli of a Particle-Filled Composite

Based on the theoretical framework formulated in Section 4.7 Appendix A and Section 4.8

Appendix B, analytical equations used to predict the effective properties of a composite reinforced by spherical particles are developed in this section. In the past, Sharma and Ganti (2004) have formulated the effective bulk moduli of spherical particle-filled composites with the interface effect using the composite spheres assemblage (CSA) model (Hashin, 1962). Duan et al. (2005) derived the effective bulk and shear moduli of such composites using the composite spheres assemblage model, the Mori-Tanaka method (MTM) (Mori and Tanaka, 1973) and the generalized self-consistent method (GSCM) (Christensen and Lo, 1979). The difference between the present work in this chapter and those of Sharma and Ganti (2004) and Duan et al. (2005) is that: at the outset with the finite deformation theory proposed by Huang and Wang (2006), the infinitesimal deformation approximations of the interface/surface constitutive relation and the Young-Laplace equation based on the Lagrangian description in consideration to the change of configuration are derived. Therefore, the requirement for using the asymmetric interface stress in the Young-Laplace equation is clearly verified and the effect of the residual interface/surface energy γ_0^* on the effective elastic moduli is shown. Assuming that the inhomogeneity incorporated with the interface is regarded as an "equivalent inhomogeneity", for a problem on the inhomogeneity with the interface/surface energy effect, the micromechanical scheme upon the present work for a two-phase or three-phase composite is applicable immediately. In this case, the volume averages of the stress and strain for the "equivalent inhomogeneity" have to be calculated on the matrix side due to the discontinuity of the stress across the interface. Consequently, the explicit derivation of the stress discontinuity conditions across the interface is significant. The work in this chapter gives an understanding of the interface/surface energy effect by accounting for the change of the interface stress in Eq. (4.47) and Eq. (4.54) due to the change of configuration, and the interface moduli are directly related to the parameters of the interface

energy.

In this section, before the analytical framework for the interface/surface energy effect on the size-dependent effective moduli of a "three-phase" composite with randomly located and interacting spherical particles of distinct properties is formulated, the interface/surface energy effect on the size-dependent effective moduli of a "two-phase" composite consisting of the matrix and randomly distributed spherical inhomogeneities is first considered.

Consider a two-phase composite composed of the matrix and randomly distributed spherical inhomogeneities, in which the radius of the inhomogeneity is assumed to be a. The effective stiffness tensor of the composite, $\overline{\mathbf{L}}$, can be described as

$$\overline{\mathbf{L}} = \mathbf{L}_0 + \phi\left(\mathbf{L}_* - \mathbf{L}_0\right) : \mathbf{A}_r \tag{4.1}$$

where $\mathbf{L}_0$ and $\mathbf{L}_*$ are the stiffness tensors of the matrix and the "equivalent inhomogeneity" (namely, an inhomogeneity incorporated with the interface), respectively; ϕ is the volume fraction of the sum of all inhomogeneities; $\mathbf{A}_r$ denotes the fourth-order global strain concentration tensor for the rth equivalent inhomogeneity. If the Ju and Chen's scheme (1994a; 1994b; 1994c) is applied, $\mathbf{A}_r$ is given by

$$\mathbf{A}_r \equiv \left(\mathbf{L}_* - \mathbf{L}_0\right)^{-1} \cdot \mathbf{L}_0 \tag{4.2}$$

Assuming all particles are spherical and both matrix and particles are isotropic elastic, $\mathbf{A}_r$ in Eq. (4.2) can be advanced to express as

$$\mathbf{A}_r = \mathbf{A}^0 : \left[\left(1 - \phi\right)\mathbf{I}^{(1)} + \phi\mathbf{A}^0\right]^{-1} \tag{4.3}$$

where $\mathbf{I}^{(1)}$ is the fourth-order unit tensor; $\mathbf{A}^0$ is the strain concentration tensor of the equivalent inhomogeneity in an infinite matrix corresponding to dilute distribution of

inhomogeneities, or simply named the local strain concentration tensor if $\mathbf{A}_r$ is relatively

considered as a global strain concentration tensor. It can be found that Eq. (4.3) coincides with

the corresponding results obtained by using the Mori-Tanaka method (Benveniste, 1987; Weng,

1990) in the case of this section. Whereas, the corresponding expression of $\mathbf{A}_r$ given by the

Eshelby method is written as

$$\mathbf{A}_r = \mathbf{A}^0 \tag{4.4}$$

Eq. (4.4) implies that the interactions among equivalent inhomogeneities may be neglected. In

other words, each equivalent inhomogeneity can be treated as if it exists in a homogeneous

matrix without the interference by other inhomogeneities.

In addition, if the inhomogeneities are randomly distributed, the composite material is

statistically isotropic and the elastic moduli in Eq. (4.1) can be expressed as

$$\overline{\mathbf{L}} = 3\overline{K}\mathbf{I}_m + 2\overline{\mu}\mathbf{I}_s$$

$$\mathbf{L}_0 = 3K_0\mathbf{I}_m + 2\mu_0\mathbf{I}_s \tag{4.5}$$

$$\mathbf{L}_* = 3K_*\mathbf{I}_m + 2\mu_*\mathbf{I}_s$$

where K_0, K_* and $\overline{K}$ are the bulk moduli of the matrix, the equivalent inhomogeneity and

the composite, respectively; μ_0, μ_* and $\overline{\mu}$ are the shear moduli of the matrix, the equivalent

inhomogeneity and the composite, respectively. It is also known that

$$\mathbf{I}_m = \frac{1}{3}\mathbf{I} \otimes \mathbf{I}, \quad \mathbf{I}_s = \mathbf{I}^{(1)} - \mathbf{I}_m \tag{4.6}$$

Substituting Eq. (4.6) into Eq. (4.5), Eq. (4.1) is further decoupled into

$$\bar{K} = K_0 + \phi(K_* - K_0)A_m$$

$$\bar{\mu} = \mu_0 + \phi(\mu_* - \mu_0)A_s$$

(4.7)

where A_m and A_s are the constants in the strain concentration tensors corresponding to the bulk and shear moduli, respectively, as follows,

$$A_m = \frac{K_0}{K_0 + (1-\phi)(K_* - K_0)\omega_m}$$

$$A_s = \frac{\mu_0}{\mu_0 + (1-\phi)(\mu_* - \mu_0)\omega_s}$$

(4.8)

Here,

$$\omega_m = \frac{3K_0}{3K_0 + 4\mu_0}$$

$$\omega_s = \frac{6(K_0 + 2\mu_0)}{5(3K_0 + 4\mu_0)}$$

(4.9)

ω_m and ω_n are components of the fourth-order Eshelby inclusion tensor. It is noted that the elastic moduli K_* and μ_* of the equivalent inhomogeneity can be obtained by using Eqs. (4.47) and (4.54) for this purpose. In the case of the spherical inhomogeneity of radius a, $\nabla_{0s}\mathbf{u}$ can be described in terms of the physical components $(u_r, u_\theta, u_\varphi)$ in a spherical polar coordinate system as the following equation,

$$\nabla_{0s}\mathbf{u} = \left(\frac{\partial u_\theta}{r\partial\theta} + \frac{u_r}{r}\right)\mathbf{e}_\theta \otimes \mathbf{e}_\theta + \left(\frac{\partial u_\varphi}{r\partial\theta} + \frac{u_r}{r}\right)\mathbf{e}_\theta \otimes \mathbf{e}_\varphi + \left(\frac{1}{r\sin\theta}\frac{\partial u_\theta}{\partial\varphi} - \cot\theta\frac{u_\varphi}{r}\right)\mathbf{e}_\varphi \otimes \mathbf{e}_\theta$$

(4.10)

$$+ \left(\frac{1}{r\sin\theta}\frac{\partial u_\varphi}{\partial\varphi} + \cot\theta\frac{u_\theta}{r} + \frac{u_r}{r}\right)\mathbf{e}_\varphi \otimes \mathbf{e}_\varphi$$

For the axisymmetric loading, $u_\varphi = 0$. Since u_r and u_θ are not dependent on φ, $\nabla_{0s}\mathbf{u}$ is a

96

symmetric tensor, as shown below,

$$\nabla_{0s}\mathbf{u} = \left(\frac{\partial u_\theta}{r\partial\theta} + \frac{u_r}{r}\right)\mathbf{e}_\theta \otimes \mathbf{e}_\theta + \left(\cot\theta\frac{u_\theta}{r} + \frac{u_r}{r}\right)\mathbf{e}_\varphi \otimes \mathbf{e}_\varphi \qquad (4.11)$$

In the above case, Eq. (4.54) may be replaced by Eq. (4.55). It is noticed that, in the reference configuration, the curvature tensor on the surface of the sphere with radius a is

$$\mathbf{b}_0 = -\frac{1}{a}\mathbf{i}_0 \qquad (4.12)$$

Eq. (4.47) can be expressed as

$$\llbracket \sigma_{rr} \rrbracket |_{r=a} = \frac{1}{a^2}\left(\gamma_0^* + 2\gamma_1^* + \gamma_1\right)\left(2u_r + u_\theta\cot\theta + \frac{\partial u_\theta}{\partial\theta}\right)|_{r=a}$$

$$-\frac{1}{a^2}\gamma_0^*\left(\frac{\partial^2 u_r}{\partial\theta^2} - \frac{\partial u_\theta}{\partial\theta} + \frac{\partial u_r}{\partial\theta}\cot\theta - u_\theta\cot\theta\right)|_{r=a}$$

$$\qquad (4.13)$$

$$\llbracket \sigma_{r\theta} \rrbracket |_{r=a} = \frac{1}{a^2}\left[\left(2\gamma_0^* + \gamma_1^*\right)u_\theta + \left(\gamma_1^* + \gamma_1\right)\left(u_\theta\cot^2\theta - \frac{\partial u_\theta}{\partial\theta}\cot\theta - \frac{\partial^2 u_\theta}{\partial\theta^2}\right)\right]|_{r=a}$$

$$-\frac{1}{a^2}\left[\left(2\gamma_0^* + 2\gamma_1^* + \gamma_1\right)\frac{\partial u_r}{\partial\theta}\right]|_{r=a}$$

In order to compute the bulk modulus K_* of the equivalent inhomogeneity, suppose that a spherical inhomogeneity is embedded in an infinite medium under the hydrostatic loading with the remote strain as

$$\mathbf{E}^\infty = \frac{1}{3}E_m\mathbf{I} \qquad (4.14)$$

In this case, the displacement and stress fields in the inhomogeneity and matrix are given by

$$u_r^i = F_i r + \frac{G_i}{r^2}$$

$$\qquad (4.15)$$

$$\sigma_{rr}^i = 3K_i F_i - 4\mu_i\frac{G_i}{r^3}$$

The superscript $i = 1, 0$ denotes the quantities of the inhomogeneity and matrix, respectively. F_1, F_0, G_1 and G_0 are constants to be determined. In addition to the displacement continuity condition at the interface $r = a$, the elastic solution needs to satisfy the stress discontinuity condition in Eq. (4.13), namely,

$$\left(\sigma_{rr}^0 - \sigma_{rr}^1\right)\big|_{r=a} = \frac{2}{a^2}\left(\gamma_0^* + 2\gamma_1^* + \gamma_1\right)\left(u_r\big|_{r=a}\right) \tag{4.16}$$

According to the above conditions, the non-singular condition at the origin and the condition at infinity, the constants in Eq. (4.15) can be determined. Therefore, the (secant) bulk modulus K_* of the equivalent inhomogeneity can be obtained by

$$K_* = \frac{tr\langle\boldsymbol{\sigma}_*\rangle}{3tr\langle\boldsymbol{\varepsilon}_*\rangle}\big|_{r=a} = K_1 + \frac{2\left(\gamma_0^* + 2\gamma_1^* + \gamma_1\right)}{3a} \tag{4.17}$$

where $\langle\boldsymbol{\sigma}_*\rangle$ and $\langle\boldsymbol{\varepsilon}_*\rangle$ represent the volume averages of the stress and strain of the equivalent inhomogeneity that includes the inhomogeneity and the interface, respectively. $\gamma_0^* = \gamma_0 + \gamma_1 + \gamma_2$, $\gamma_1^* = \gamma_1 + 2\gamma_2 + \gamma_{11} + 2\gamma_{12} + \gamma_{22}$, and γ_0^* and γ_1^* form the residual interface/surface energy. Further, it is found that there are at least three independent material parameters γ_0^*, γ_1^* and γ_1 required in the above equation. About the detailed description of the interface/surface free energy γ, it can refer to Section 4.8 Appendix B.

Moreover, the shear modulus μ_* of the equivalent inhomogeneity can be found by imposing a pure deviatoric remote strain at infinity as,

$$\mathbf{E}^\infty = E_e\left[\mathbf{e}_3 \otimes \mathbf{e}_3 - \frac{1}{2}\left(\mathbf{e}_1 \otimes \mathbf{e}_1 + \mathbf{e}_2 \otimes \mathbf{e}_2\right)\right] \tag{4.18}$$

where $\mathbf{e}_1$, $\mathbf{e}_2$ and $\mathbf{e}_3$ are the base vectors in a rectangular Cartesian coordinate system. From

the solution of Lur'e (1964), the displacement and stress fields in the inhomogeneity and matrix can be written by

$$u_r^1 = \left(12\nu_1 A r^3 + 2Br\right) P_2\left(\cos\theta\right)$$

$$u_r^0 = \left(E_e r + \frac{2\left(5-4\nu_0\right)}{r^2}C - \frac{3}{r^4}D\right) P_2\left(\cos\theta\right)$$

$$u_\theta^1 = \left[\left(7-4\nu_1\right) A r^3 + Br\right]\frac{dP_2\left(\cos\theta\right)}{d\theta}$$

$$u_\theta^0 = \left[\frac{1}{2}E_e r + \frac{\left(2-4\nu_0\right)}{r^2}C - \frac{1}{r^4}D\right]\frac{dP_2\left(\cos\theta\right)}{d\theta}$$

$$\sigma_{rr}^1 = 2\mu_1\left(-6\nu_1 A r^2 + 2B\right) P_2\left(\cos\theta\right)$$

$$\sigma_{rr}^0 = 2\mu_0\left[E_e - \frac{4\left(5-\nu_0\right)}{r^3}C + \frac{12}{r^5}D\right] P_2\left(\cos\theta\right)$$

$$\sigma_{r\theta}^1 = 2\mu_1\left[\left(7+2\nu_1\right) A r^2 + B\right]\frac{dP_2\left(\cos\theta\right)}{d\theta} \tag{4.19}$$

$$\sigma_{r\theta}^0 = 2\mu_0\left[\frac{1}{2}E_e + \frac{2\left(1+\nu_0\right)}{r^3}C - \frac{4}{r^5}D\right]\frac{dP_2\left(\cos\theta\right)}{d\theta}$$

The superscripts 1 and 0 denote the quantities of the inhomogeneity and matrix, respectively. ν_1 and ν_0 are Poisson's ratios of the inhomogeneity and matrix, respectively. $P_2\left(\cos\theta\right)$ is the second-order Legendre polynomial. A, B, C and D are constants to be determined. Similarly, in addition to the displacement continuity condition at the interface $r = a$, the elastic solution needs to satisfy the stress discontinuity condition in Eq. (4.13). Then, the unknown constants can be determined in a way similar to that for the bulk modulus. The shear modulus

μ_* of the equivalent inhomogeneity can be calculated by

$$\mu_* = \frac{\langle \sigma_* \rangle_e}{3 \langle \varepsilon_* \rangle_e}\Big|_{r=a} = \mu_1 + \frac{L_1 + L_2}{L_3 + L_4}$$

$$L_0 = 2\gamma_0^{*2} - \gamma_1\left(\gamma_1 + 2\gamma_1^*\right) - \gamma_0^*\left(5\gamma_1 + 2\gamma_1^*\right)$$

$$L_1 = 10\left(7 - 10\nu_1\right)L_0$$

$$L_2 = -\frac{1}{10a}\left(2\gamma_0^* - 7\gamma_1 - 2\gamma_1^*\right)L_4$$

$$L_3 = 4\left(-7 + 10\nu_1\right)a\left(13\gamma_0^* + 7\gamma_1 + 12\gamma_1^*\right)$$

$$L_4 = 10a^2\left[4\left(-7 + 10\nu_1\right)\mu_0 - \left(7 + 5\nu_1\right)\mu_1\right]$$

(4.20)

where $\langle \sigma_* \rangle_e$ and $\langle \varepsilon_* \rangle_e$ are the effective average stress and the effective average strain of the equivalent inhomogeneity, respectively. It can be easily found that K_* and μ_* are not only functions of the elastic moduli of the inhomogeneity, such as K_1 and μ_1, but also the functions of the size of particles, a.

In order to simplify the discussion, the expression of the interface/surface free energy can be linearized. Therefore, γ can be expanded as:

$$\gamma = \gamma_0 + \gamma_1\left(J_1 - 2\right) + \gamma_2\left(J_2 - 1\right) + \frac{1}{2}\gamma_{11}\left(J_1 - 2\right)^2 + \gamma_{12}\left(J_1 - 2\right)\left(J_2 - 1\right) + \frac{1}{2}\gamma_{22}\left(J_2 - 1\right)^2 + \cdots$$

(4.21)

$$\gamma_1 = \frac{\partial \gamma}{\partial J_1}\Big|_{J_1=2, J_2=1} \quad , \quad \gamma_2 = \frac{\partial \gamma}{\partial J_2}\Big|_{J_1=2, J_2=1}$$

where γ_0, γ_1, γ_2 represent the intrinsic physical properties of the interface, and they are, and

should be determined by the joining materials and the adhering condition. $\gamma_0 = \gamma(2,1)$ is equivalent to the interface/surface energy of a liquid-like material and hence reflects the nature of liquids, whereas γ_1 and γ_2 reflect the nature of solids; $J_1 - 2$ and $J_2 - 1$ are first-order small quantities.

Moreover, the expression of the (secant) bulk modulus K_{*m} of the equivalent inhomogeneity in Eq. (4.17) is derived for identical particles of the same property. Therefore, it is rewritten in a general form for two different particles of distinct properties as follows,

$$K_{*m} = \frac{tr\langle\boldsymbol{\sigma}_*\rangle_m}{3tr\langle\boldsymbol{\varepsilon}_*\rangle_m}\Big|_{r=a} = K_m + \frac{2\left(\gamma_0^* + 2\gamma_1^* + \gamma_1\right)}{3a}; \quad m = 1,2 \tag{4.22}$$

where $\langle\boldsymbol{\sigma}_*\rangle_m$ and $\langle\boldsymbol{\varepsilon}_*\rangle_m$ represent the volume averages of the stress and strain for two distinct equivalent inhomogeneities, and each equivalent inhomogeneity includes the inhomogeneity and the interface, respectively. $\gamma_0^* = \gamma_0 + \gamma_1 + \gamma_2$, $\gamma_1^* = \gamma_1 + 2\gamma_2 + \gamma_{11} + 2\gamma_{12} + \gamma_{22}$, and γ_0^* and γ_1^* form the residual interface/surface energy. Further, it is found that there are at least three independent material parameters γ_0^*, γ_1^* and γ_1 required in the above equation. Here, the property of the interface/surface free energy γ is assumed to be the same and the interface/surface surrounds two distinct particles.

Similarly, the shear modulus μ_{*m} in Eq. (4.20) of the equivalent inhomogeneity for two distinct particles can be obtained as:

$$\mu_{*m} = \frac{\langle \sigma_* \rangle_{em}}{3 \langle \varepsilon_* \rangle_{em}} \bigg|_{r=a} = \mu_m + \frac{L_{1m} + L_{2m}}{L_{3m} + L_{4m}}; \quad m = 1,2$$

$$L_0 = 2\gamma_0^{*2} - \gamma_1(\gamma_1 + 2\gamma_1^*) - \gamma_0^*(5\gamma_1 + 2\gamma_1^*)$$

$$L_{1m} = 10(7 - 10\nu_m)L_0$$

(4.23)

$$L_{2m} = -\frac{1}{10a}(2\gamma_0^* - 7\gamma_1 - 2\gamma_1^*)L_{4m}$$

$$L_{3m} = 4(-7 + 10\nu_m)a(13\gamma_0^* + 7\gamma_1 + 12\gamma_1^*)$$

$$L_{4m} = 10a^2\left[4(-7 + 10\nu_m)\mu_0 - (7 + 5\nu_m)\mu_m\right]$$

where $\langle \sigma_* \rangle_{em}$ and $\langle \varepsilon_* \rangle_{em}$ are the effective average stress and the effective average strain of the equivalent inhomogeneity, respectively. For each equivalent inhomogeneity ($m = 1,2$), it can be easily found that K_{*m} and μ_{*m} are not only functions of the elastic moduli of the inhomogeneity, such as K_m and μ_m, but also the functions of the size of particles, a.

4.3 Effective Bulk and Shear Moduli of Three-Phase Composites Containing Randomly Dispersed Spherical Particles of Distinct Elastic Properties (with No Interface Energy Effect)

In this section, the effective elastic moduli of composites containing many randomly dispersed spherical particles of different elastic properties (with no interface/surface energy effect), based on the theoretical framework formulated in Section 4.9 Appendix C and Section

4.10 Appendix D, are derived. Specifically, the probabilistic ensemble-volume averaged pairwise local interaction solutions for $\left\langle \overline{\boldsymbol{\varepsilon}}_{(i)}^{*} \right\rangle$ and other ensemble-volume averaged field equations are utilized. In what follows, angle brackets for the ensemble-average operators will be dropped for the purpose of compactness.

According to Ju and Chen (1994a) and Zhao et al. (1989), the following relations governing the ensemble-volume averaged stress $\overline{\boldsymbol{\sigma}}$, the averaged strain $\overline{\boldsymbol{\varepsilon}}$, the uniform remote strain $\boldsymbol{\varepsilon}^0$ and the averaged eigenstrain $\overline{\boldsymbol{\varepsilon}}_{(i)}^{*}$ take the form

$$\overline{\boldsymbol{\sigma}} = \mathbf{C}_0 : \left(\overline{\boldsymbol{\varepsilon}} - \sum_{i=1}^{2} \phi_i \, \overline{\boldsymbol{\varepsilon}}_{(i)}^{*} \right) \tag{4.24}$$

$$\overline{\boldsymbol{\varepsilon}} = \boldsymbol{\varepsilon}^0 + \sum_{i=1}^{2} \phi_i \mathbf{S} : \overline{\boldsymbol{\varepsilon}}_{(i)}^{*} \tag{4.25}$$

Upon substitution of the solution of $\overline{\boldsymbol{\varepsilon}}_{(i)}^{*}$ in Eqs. (4.93) and (4.97) into Eq. (4.25), and invoking the relation between $\boldsymbol{\varepsilon}^0$ and $\boldsymbol{\varepsilon}_{(i)}^{*0}$ given by Eq. (4.65), the relations between the averaged eigenstrain $\overline{\boldsymbol{\varepsilon}}_{(i)}^{*}$ and the averaged strain $\overline{\boldsymbol{\varepsilon}}$ are rendered as

$$\overline{\boldsymbol{\varepsilon}}_{(1)}^{*} = \boldsymbol{\Gamma}^1 \cdot \left(\mathbf{T}^1 \right)^{-1} : \overline{\boldsymbol{\varepsilon}}$$
$$\overline{\boldsymbol{\varepsilon}}_{(2)}^{*} = \boldsymbol{\Gamma}^2 \cdot \left(\mathbf{T}^2 \right)^{-1} : \overline{\boldsymbol{\varepsilon}} \tag{4.26}$$

where

$$\mathbf{T}^1 = \left(-\mathbf{A}_1 - \mathbf{S} + \phi_1 \mathbf{S} \cdot \boldsymbol{\Gamma}^1 + \phi_2 \mathbf{S} \cdot \boldsymbol{\Gamma}^2 \cdot \left(\mathbf{A}_2 + \mathbf{S} \right)^{-1} \cdot \left(\mathbf{A}_1 + \mathbf{S} \right) \right) \tag{4.27}$$

$$\mathbf{T}^2 = \left(-\mathbf{A}_2 - \mathbf{S} + \phi_2 \mathbf{S} \cdot \boldsymbol{\Gamma}^2 + \phi_1 \mathbf{S} \cdot \boldsymbol{\Gamma}^1 \cdot \left(\mathbf{A}_1 + \mathbf{S} \right)^{-1} \cdot \left(\mathbf{A}_2 + \mathbf{S} \right) \right) \tag{4.28}$$

Substituting Eq. (4.26) into (4.24) leads to the effective stiffness $\overline{\mathbf{C}}$ relating $\overline{\boldsymbol{\sigma}}$ and $\overline{\boldsymbol{\varepsilon}}$:

$$\bar{\sigma} = \bar{C} : \bar{\varepsilon}$$

$$\bar{C} = C_0 \cdot \left\{ I - \phi_1 \Gamma^1 \cdot \left(T^1 \right)^{-1} - \phi_2 \Gamma^2 \cdot \left(T^2 \right)^{-1} \right\} \tag{4.29}$$

Since all fourth-rank tensors on the right-hand side of Eq. (4.29) are isotropic in three dimensions, the effective stiffness tensor $\bar{C}$ for a three-phase composite is isotropic as well.

In what follows, two non-equivalent formulations are considered in detail to derive effective elastic moduli of three-phase composites with no interface/surface energy effect, that is, "Formulation II" and "Formulation I". The following notations are adopted: the superscript "II" and "I" stand for Formulation II and Formulation I, respectively.

Formulation II: the effective bulk modulus $\bar{K}_T^{II}$ and shear modulus $\bar{\mu}_T^{II}$ of a three-phase composite with no interface/surface energy effect can be explicitly derived as

$$\bar{K}_T^{II} = K_0 \left(1 + \frac{30(1-v_0)\left[\omega_2 \phi_1 \left(3r_1 + 2r_2 \right) + \omega_1 \phi_2 \left(3r_3 + 2r_4 \right) \right]}{\omega_1 \omega_2 - 10(1+v_0)\left[\omega_2 \phi_1 \left(3r_1 + 2r_2 \right) + \omega_1 \phi_2 \left(3r_3 + 2r_4 \right) \right]} \right)$$

$$\omega_i = 3\alpha_i + 2\beta_i; \quad i = 1,2$$

$$\alpha_m = 2(5v_0 - 1) + 10(1 - v_0)\left(\frac{K_0}{K_m - K_0} - \frac{\mu_0}{\mu_m - \mu_0} \right), \quad m = 1,2 \tag{4.30}$$

$$\beta_m = 2(4 - 5v_0) + 15(1 - v_0)\left(\frac{\mu_0}{\mu_m - \mu_0} \right), \quad m = 1,2$$

$$K_0 = \frac{2(1 + v_0)}{3(1 - 2v_0)}$$

where K_0, K_m and μ_0, μ_m denote the bulk and shear moduli of the matrix and the m-phase particle, respectively; r_1, r_2, r_3 and r_4 have been defined in Section 4.10 Appendix D.

$$\bar{\mu}^{II} = \mu_0 \left(1 + \frac{30(1-\nu_0)(\beta_2\phi_1 r_2 + \beta_1\phi_2 r_4)}{\beta_1\beta_2 - 4(4-5\nu_0)(\beta_2\phi_1 r_2 + \beta_1\phi_2 r_4)} \right)$$

(4.31)

$$\beta_m = 2(4-5\nu_0) + 15(1-\nu_0)\left(\frac{\mu_0}{\mu_m - \mu_0} \right), \quad m = 1,2$$

where μ_0 and μ_m denote the shear moduli of the matrix and the m-phase particle, respectively; r_1, r_2, r_3 and r_4 have been defined in Section 4.10 Appendix D.

Formulation I: The effective bulk modulus $\bar{K}_T^I$ and shear modulus $\bar{\mu}_T^I$ of a three-phase composite with no interface/surface energy effect can be explicitly expressed as

$$\bar{K}_T^I = K_0 \left(1 + \frac{30(1-\nu_0)\left[\omega_2\phi_1(3r_1 + 2r_2) + \omega_1\phi_2(3r_3 + 2r_4) \right]}{\omega_1\omega_2 - 10(1+\nu_0)\left[\omega_2\phi_1(3r_1 + 2r_2) + \omega_1\phi_2(3r_3 + 2r_4) \right]} \right)$$

$$\omega_i = 3\alpha_i + 2\beta_i; \quad i = 1,2$$

$$\alpha_m = 2(5\nu_0 - 1) + 10(1-\nu_0)\left(\frac{K_0}{K_m - K_0} - \frac{\mu_0}{\mu_m - \mu_0} \right), \quad m = 1,2$$ (4.32)

$$\beta_m = 2(4-5\nu_0) + 15(1-\nu_0)\left(\frac{\mu_0}{\mu_m - \mu_0} \right), \quad m = 1,2$$

$$K_0 = \frac{2(1+\nu_0)}{3(1-2\nu_0)}$$

where K_0, K_m and μ_0, μ_m denote the bulk and shear moduli of the matrix and the m-phase particle, respectively; r_1, r_2, r_3 and r_4 have been defined in Section 4.10 Appendix D.

$$\bar{\mu}_T^I = \mu_0 \left(1 + \frac{30(1-\nu_0)(\beta_2\phi_1 r_2 + \beta_1\phi_2 r_4)}{\beta_1\beta_2 - 4(4-5\nu_0)(\beta_2\phi_1 r_2 + \beta_1\phi_2 r_4)} \right)$$

(4.33)

$$\beta_m = 2(4-5\nu_0) + 15(1-\nu_0)\left(\frac{\mu_0}{\mu_m - \mu_0} \right), \quad m = 1,2$$

where μ_0 and μ_m denote the shear moduli of the matrix and the *m*-phase particle, respectively; r_1, r_2, r_3 and r_4 have been defined in Section 4.10 Appendix D.

4.4 Effective Bulk and Shear Moduli of Three-Phase Composites Containing Randomly Dispersed Spherical Particles of Distinct Elastic Properties with Interface Energy Effect

In combination with the results from Section 4.2 and Section 4.3, the effective elastic moduli of three-phase composites containing randomly dispersed distinct spherical particles with the interface/surface energy effect are analytically derived in this section. In what follows, two non-equivalent formulations are considered in detail to derive effective elastic moduli of three-phase composites with the interface/surface energy effect, that is, "Formulation II" and "Formulation I." The following notations are adopted: the superscript "II" and "I" stand for Formulation II and Formulation I, respectively.

Formulation II: the effective bulk modulus $\bar{K}^{II}$ and shear modulus $\bar{\mu}^{II}$ of a three-phase composite with interface/surface energy effect can be explicitly derived as

$$\overline{K}^{II} = K_0 \left(1 + \frac{30(1-v_0)\left[\omega_2 \phi_1 \left(3r_1 + 2r_2 \right) + \omega_1 \phi_2 \left(3r_3 + 2r_4 \right) \right]}{\omega_1 \omega_2 - 10(1+v_0)\left[\omega_2 \phi_1 \left(3r_1 + 2r_2 \right) + \omega_1 \phi_2 \left(3r_3 + 2r_4 \right) \right]} \right)$$

$$\omega_m = 3\alpha_{*m} + 2\beta_{*m}, \quad m = 1,2$$

$$\alpha_{*m} = 2(5v_0 - 1) + 10(1-v_0)\left(\frac{K_0}{K_{*m} - K_0} - \frac{\mu_0}{\mu_{*m} - \mu_0} \right), \quad m = 1,2 \tag{4.34}$$

$$\beta_{*m} = 2(4 - 5v_0) + 15(1-v_0)\left(\frac{\mu_0}{\mu_{*m} - \mu_0} \right), \quad m = 1,2$$

$$K_0 = \frac{2(1+v_0)}{3(1-2v_0)}$$

where K_0, K_{*m} and μ_0, μ_{*m} denote the bulk and shear moduli of the matrix and the

m-phase equivalent inhomogeneity, respectively. K_{*m} and μ_{*m} are defined in Eq. (4.22) and

Eq. (4.23). r_1, r_2, r_3 and r_4 can be found in Section 4.10 Appendix D.

$$\overline{\mu}^{II} = \mu_0 \left(1 + \frac{30(1-v_0)\left(\beta_{*2} \phi_1 r_2 + \beta_{*1} \phi_2 r_4 \right)}{\beta_{*1} \beta_{*2} - 4(4 - 5v_0)\left(\beta_{*2} \phi_1 r_2 + \beta_{*1} \phi_2 r_4 \right)} \right)$$

$$\tag{4.35}$$

$$\beta_{*m} = 2(4 - 5v_0) + 15(1-v_0)\left(\frac{\mu_0}{\mu_{*m} - \mu_0} \right), \quad m = 1,2$$

where μ_0 and μ_{*m} denote the shear moduli of the matrix and the m-phase equivalent

inhomogeneity, respectively. μ_{*m} is defined in Eq. (4.22) and Eq. (4.23). r_1, r_2, r_3 and r_4 can be

found in Section 4.10 Appendix D.

Formulation I: The effective bulk modulus $\overline{K}^I$ and shear modulus $\overline{\mu}^I$ of a three-phase

composite with no interface/surface energy effect can be explicitly expressed as

$$\bar{K}^I = K_0 \left(1 + \frac{30(1-v_0)\left[\omega_2\phi_1(3r_1 + 2r_2) + \omega_1\phi_2(3r_3 + 2r_4)\right]}{\omega_1\omega_2 - 10(1+v_0)\left[\omega_2\phi_1(3r_1 + 2r_2) + \omega_1\phi_2(3r_3 + 2r_4)\right]} \right)$$

$$\omega_i = 3\alpha_i + 2\beta_i; \quad i = 1,2$$

$$\alpha_{*m} = 2(5v_0 - 1) + 10(1-v_0)\left(\frac{K_0}{K_{*m} - K_0} - \frac{\mu_0}{\mu_{*m} - \mu_0} \right), \quad m = 1,2 \qquad (4.36)$$

$$\beta_{*m} = 2(4 - 5v_0) + 15(1-v_0)\left(\frac{\mu_0}{\mu_{*m} - \mu_0} \right), \quad m = 1,2$$

$$K_0 = \frac{2(1+v_0)}{3(1-2v_0)}$$

where K_0, K_{*m} and μ_0, μ_{*m} denote the bulk and shear moduli of the matrix and the

m-phase equivalent inhomogeneity, respectively. K_{*m} and μ_{*m} are defined in Eq. (4.22) and

Eq. (4.23). r_1, r_2, r_3 and r_4 can be found in Section 4.10 Appendix D.

$$\bar{\mu}^I = \mu_0 \left(1 + \frac{30(1-v_0)(\beta_2\phi_1 r_2 + \beta_1\phi_2 r_4)}{\beta_1\beta_2 - 4(4 - 5v_0)(\beta_2\phi_1 r_2 + \beta_1\phi_2 r_4)} \right)$$

$$\qquad (4.37)$$

$$\beta_{*m} = 2(4 - 5v_0) + 15(1-v_0)\left(\frac{\mu_0}{\mu_{*m} - \mu_0} \right), \quad m = 1,2$$

where μ_0 and μ_{*m} denote the shear moduli of the matrix and the m-phase equivalent

inhomogeneity, respectively. μ_{*m} is defined in Eq. (4.22) and Eq. (4.23). r_1, r_2, r_3 and r_4 can be

found in Section 4.10 Appendix D.

4.5 Some numerical examples

In the special event that a matrix material contains identical spherical particles (i.e., $\mu_1 = \mu_2$, $K_1 = K_2$, $a_1 = a_2$), Eqs. (4.36) and (4.37) reduce to

$$\bar{K} = K_0 \left(1 + \frac{30(1-v_0)\phi(3r_1 + 2r_2)}{3\alpha_* + 2\beta_* - 10(1+v_0)\phi(3r_1 + 2r_2)} \right)$$

$$\alpha_* = 2(5v_0 - 1) + 10(1-v_0)\left(\frac{K_0}{K_* - K_0} - \frac{\mu_0}{\mu_* - \mu_0} \right) \tag{4.38}$$

$$\beta_* = 2(4 - 5v_0) + 15(1-v_0)\left(\frac{\mu_0}{\mu_* - \mu_0} \right)$$

$$K_0 = \frac{2(1+v_0)}{3(1-2v_0)}$$

$$\bar{\mu} = \mu_0 \left(1 + \frac{30(1-v_0)\phi r_2}{\beta_* - 4(4 - 5v_0)\phi r_2} \right)$$

$$\tag{4.39}$$

$$\beta_* = 2(4 - 5v_0) + 15(1-v_0)\left(\frac{\mu_0}{\mu_* - \mu_0} \right)$$

with $\alpha_* = \alpha_{*1} = \alpha_{*2}$, $\beta_* = \beta_{*1} = \beta_{*2}$, $r_1 = r_3$, $r_2 = r_4$ and $\phi = \phi_1 + \phi_2$. Here, ϕ denotes the total particle volume fraction. $K_* = K_{*1} = K_{*2}$ and $\mu_* = \mu_{*1} = \mu_{*2}$ can be evaluated by using Eq. (4.22) and Eq. (4.23). r_1, r_2, r_3 and r_4 can be found in Section 4.10 Appendix D.

Suppose that a porous material containing spherical nano-voids is analyzed, so that its corresponding effective bulk and shear moduli of the composite with the interface/surface energy effect can be obtained by substituting $K_1 = 0$ and $\mu_1 = 0$ into Eqs. (4.38) and (4.39). Assume that the bulk modulus of the matrix material is $K_0 = 2.5\,\text{GPa}$, and the shear modulus is $\mu_0 = 0.5\,\text{GPa}$. The surface is assumed to be liquid-like with a interface/surface energy $\gamma_0 = 0.05\,\text{J/m}^2$. The volume fractions sum of all voids are assumed to be $\phi = 20\%$ and

$\phi = 30\%$, respectively. Accordingly, the variations of the normalized effective bulk and shear moduli proposed in Eqs. (4.38) and (4.39) for polypropylene containing spherical voids are illustrated in **Figure 4.1** and **Figure 4.2**. In the figures, $\bar{K}_0$ and $\bar{\mu}_0$ are the effective bulk and shear moduli of the material without the interface/surface energy effect. From these two figures, it is found that the interface/surface effect decreases with the increase of the size of the voids and almost can be neglected when the radius of the void is larger than about 10 nm. Furthermore, these two results pretty coincide with the illustrations in **Figure 3.1** and **Figure 3.2**. It is further demonstrated that this developed analytical model for the interface/surface energy effect on effective moduli of three-phase composites containing randomly dispersed spherical particles of distinct elastic properties is applicable to reveal the influence of interface/surface energy in nano-scale composites.
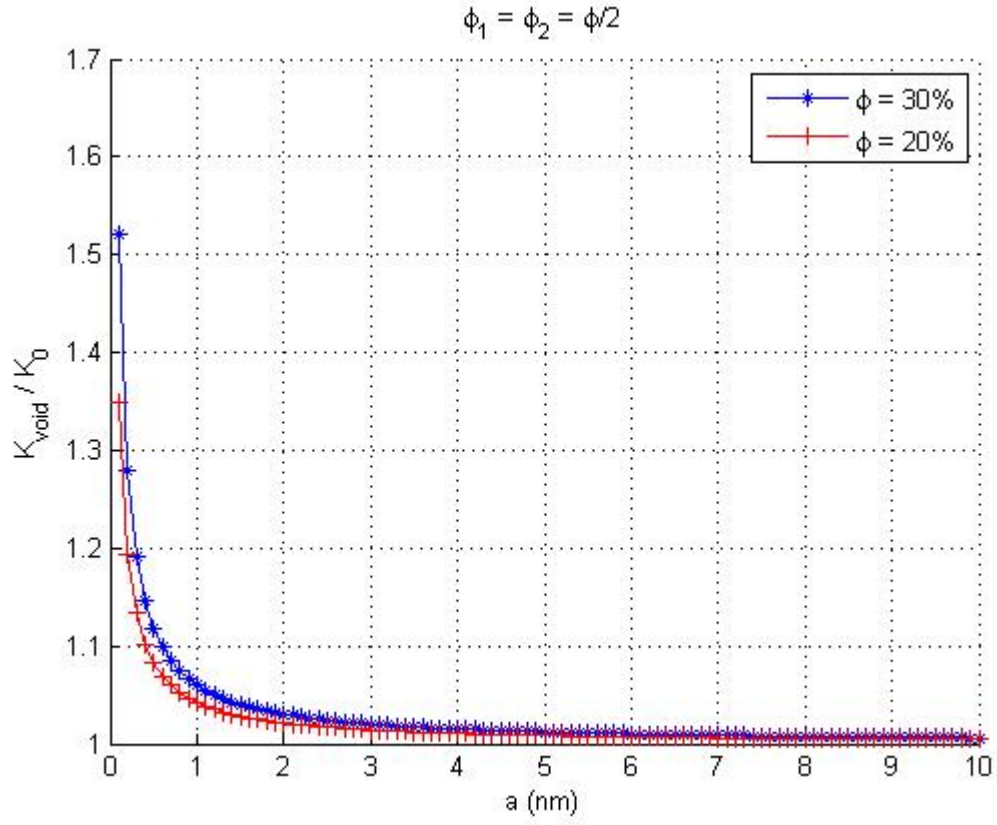
Figure 4.1 Normalized effective bulk modulus against the radius of voids in the range of nanometer size with two different volume fractions and $\gamma_0 = 0.05 \, J/m^2$
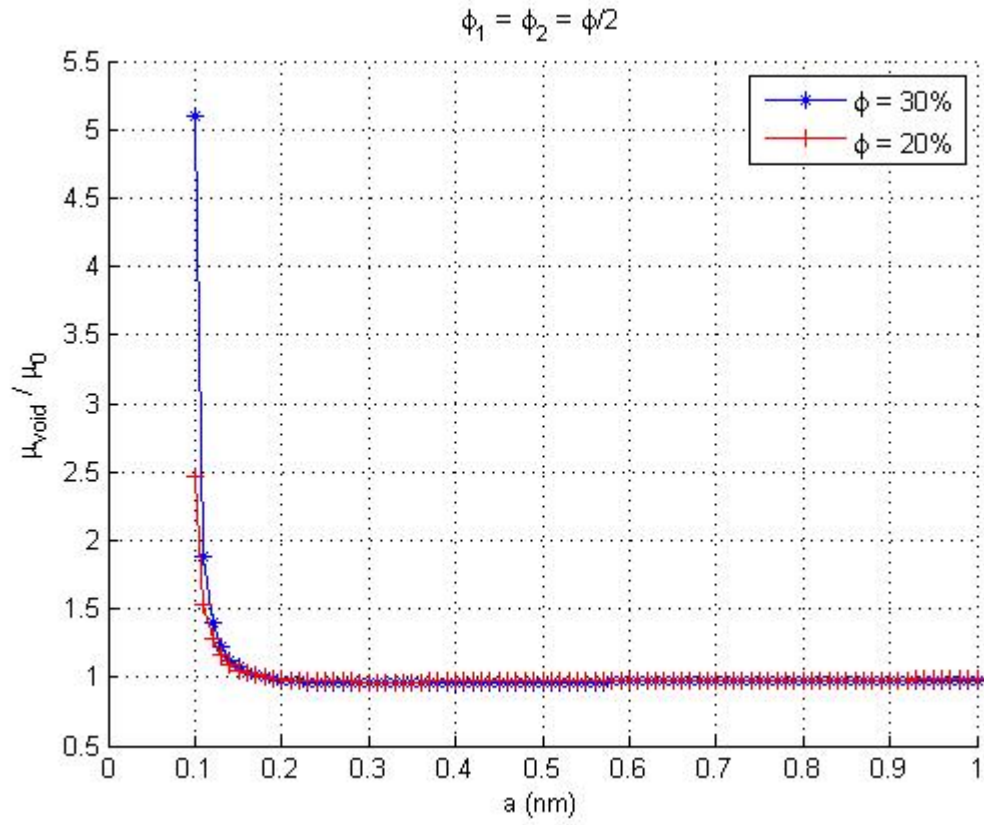
Figure 4.2 Normalized effective shear modulus against the radius of voids in the range of nanometer size with two different volume fractions and $\gamma_0 = 0.05 \ J / m^2$

4.6 Conclusions

The primary objective of the present chapter is to extend the work regarding the interface/surface energy effect on size-dependent effective moduli of a "two-phase" composite containing identical particles of the same property and size, based on the framework of Lin and Ju (2009) and the methodology of Huang and Sun (2007), to the one regarding the interface/surface energy effect on size-dependent effective moduli of a "three-phase" composite containing two particles of the distinct properties with the same size.

First of all, the interface/surface energy effect on the macroscopic mechanical behavior of a composite is investigated through starting with the finite deformation theory of a multi-phase hyperelastic medium. Then, the approximate formulation of a finitely deformed multiphase elastic medium by an infinitesimal deformation analysis is executed. According to the existence of the interface energy, even though under no external loading, there is still a "residual elastic field" induced by the interface stress. During the deformation process of a composite from the reference configuration to the current configuration, the changes of the size and shape of the interface leads to the change of this "residual elastic field". It is noticed that the governing equations describing the change of the "residual elastic field" due to the change of the configuration are formulated under the infinitesimal deformation approximation and hence lead to the use of the asymmetric interface stress in the prediction of the effective properties of heterogeneous materials with interface/surface energy effect. Therefore, the influence of the residual interface/surface energy can be taken into account. In particular, the theoretical framework is applied to obtain the analytical expressions of the effective bulk and shear moduli of a composite with spherical "equivalent inhomogeneities" (i.e. the inhomogeneities together

with the interface/surface energy). Hence, the interface/surface energy effect on the size-dependent effective moduli of a two-phase composite consisting of the matrix and randomly distributed spherical inhomogeneities is developed.

Secondly, the effective bulk and shear moduli of a three-phase composite containing randomly dispersed spherical particles of distinct elastic properties are separately formulated based on another framework with consideration to the concepts of probabilistic spatial distribution of spherical particles, pairwise particle interactions, and the ensemble-volume averaging (homogenization) procedure for three-phase elastic composites. Specifically, the approximate analytical solutions for the direct interactions between two different randomly located elastic spheres embedded in the matrix material are presented, followed by constructing the ensemble-volume averaged eigenstrains through the probabilistic pairwise particle interaction mechanism. Moreover, two non-equivalent formulations are considered in detail to derive effective elastic moduli of three-phase composites with no the interface/surface energy effect.

Later on, in combination with the above two formulations, effective elastic moduli of three-phase composites containing randomly dispersed distinct spherical particles with the interface/surface energy effect are analytically derived. In addition, numerical results and the corresponding discussions are presented to demonstrate the potential of this present model. Specifically, through the execution of some special cases, as well as the comparison with the results done in Chapter 3, it is further demonstrated that this developed analytical model for the interface/surface energy effect on effective moduli of three-phase composites containing randomly dispersed spherical particles of distinct elastic properties is applicable to reveal the influence of interface/surface energy in nano-scale composites. These comparisons and simulations encompass elastic matrices with randomly dispersed voids and/or particles. No

Monte Carlo simulations or finite element calculations are needed here.

Lastly, experimental validations are key parameters in the calibration of proposed models. Further experimental validations and comparisons will be performed once the associated experiment data become available. To the author's best knowledge, the experimental data associated with characterizations of effective elastic properties of three-phase composites containing particles and/or voids with the interface/surface energy effect are currently not available due to difficulties in performing such experimental works. For example, as the illustrative figures developed based on the framework in this chapter, it is found that the interface/surface effect decreases with the increase of the size of the voids and can be neglected when the radius of the void is larger than 10 nm. In other words, it is quite difficult to manufacture so small nanocomposites nowadays.

4.7 Appendix A: Formulations upon Finite Deformation Theory

The constitutive relations of the interface have been widely investigated by many researchers in the literature. But most of works on this subject are confined to the infinitesimal deformation approximations. Suppose that the interface/surface energy per unit area in the current configuration is denoted by γ. If the interface is assumed to be isotropic relative to the reference configuration κ_0, i.e. the underlying reference configuration is an undistorted state, then γ can be expressed as a function of the invariants of $\mathbf{U}_s$ and $\mathbf{V}_s$, or a function of J_1 and J_2, as follows,

$$J_1 = tr\ \mathbf{U}_s = tr\ \mathbf{V}_s$$

$$J_2 = \det\ \mathbf{U}_s = \det\ \mathbf{V}_s$$

(4.40)

where $\mathbf{U}_s$ and $\mathbf{V}_s$ are the right and left stretch tensors of the interface, respectively; J_1 and J_2 are the first and second invariants of $\mathbf{U}_s$ and $\mathbf{V}_s$. If the small deformation is concerned, the strain at the interface may be approximately expressed by

$$\mathbf{E}_s = \frac{1}{2}\left(\mathbf{u}\nabla_{0s} + \nabla_{0s}\mathbf{u}\right) = \mathbf{U}_s - \mathbf{i}_0 \qquad (4.41)$$

where ∇_{0s} is the surface gradient operator on operator in the reference configuration κ_0; $\mathbf{u}\nabla_{0s}$ is the displacement gradient of the interface; $\mathbf{i}_0$ is the second-order identity tensor in the tangent plane of the interface in the reference configuration. Substituting Eq. (3.41) into Eq. (3.40), J_1 and J_2 can be re-written as

$$J_1 = 2 + tr\ \mathbf{E}_s$$

$$J_2 = 1 + tr\ \mathbf{E}_s + \det\ \mathbf{E}_s$$

(4.42)

In the case of the isotropic interface and the small deformation, the interface Piola-Kirchhoff stresses of the first kind and second kind including "out-of-plane term" can be formulated as

116

$$\overset{(in)}{\mathbf{S}}_s = \overset{(in)}{\mathbf{F}}_s \cdot \overset{(1)}{\mathbf{T}}_s$$

$$= J_2 \left(\frac{\partial \gamma}{\partial J_1} + J_2 \frac{\partial \gamma}{\partial J_2} + \gamma \right) \mathbf{i}_0 + J_2 \frac{\partial \gamma}{\partial J_1} \mathbf{E}_s - J_2 \left(\frac{\partial \gamma}{\partial J_1} + J_2 \frac{\partial \gamma}{\partial J_2} + \gamma \right) (\nabla_{0s} \mathbf{u})$$

$$\overset{(out)}{\mathbf{S}}_s = \overset{(out)}{\mathbf{F}}_s \cdot \overset{(1)}{\mathbf{T}}_s \tag{4.43}$$

$$= J_2 \left(\frac{\partial \gamma}{\partial J_1} + J_2 \frac{\partial \gamma}{\partial J_2} + \gamma \right) \overset{(out)}{\mathbf{F}}_s$$

$$\mathbf{S}_s = \overset{(in)}{\mathbf{S}}_s + \overset{(out)}{\mathbf{S}}_s$$

$$\mathbf{T}_s = J_2 \left(\frac{\partial \gamma}{\partial J_1} + J_2 \frac{\partial \gamma}{\partial J_2} + \gamma \right) \mathbf{i}_0 - J_2 \left(\frac{\partial \gamma}{\partial J_1} + 2 J_2 \frac{\partial \gamma}{\partial J_2} + 2 \gamma \right) \mathbf{E}_s \tag{4.44}$$

where $\mathbf{F}_s$ is the "out-of-plane term" of surface gradient. And the Cauchy stress of the interface can be described by

$$\boldsymbol{\sigma}_s = \left(\frac{\partial \gamma}{\partial J_1} + J_2 \frac{\partial \gamma}{\partial J_2} + \gamma \right) \mathbf{i}_0 + \frac{\partial \gamma}{\partial J_1} \mathbf{E}_s + \left(\frac{\partial \gamma}{\partial J_1} + J_2 \frac{\partial \gamma}{\partial J_2} + \gamma \right) \left(\overset{(out)}{\mathbf{F}}_s + \overset{(out)^T}{\mathbf{F}}_s \right) \tag{4.45}$$

Therefore, it is found that $\mathbf{S}_s$, $\mathbf{T}_s$ and the Cauchy stress of the interface $\boldsymbol{\sigma}_s$ are not the same, even if the infinitesimal deformation approximation is performed. The situation is totally different from that in the three dimensional analysis in the traditional elasticity, in which there is no residual stress in the reference configuration. In other words, only through the beginning with the finite deformation theory, an appropriate infinitesimal interface stress is then chosen in the governing equations if the interface/interface energy effect is taken into account on the mechanical properties of a heterogeneous material.

4.8 Appendix B: Approximations upon Infinitesimal Deformation Analysis

In this section, the approximate equations of the changes of the interface stress and the Young-Laplace equation due to the change of configuration under the infinitesimal deformation is introduced. Then, the analytical equations for the effective moduli of a particle-reinforced composite is given through the application of the theory by Huang and Sun (2007), which depicts the effect of the liquid-like interface/surface energy on the effective moduli.

The governing equations, such as the equilibrium equations, based on one configuration are well-known in the infinitesimal analysis in the traditional elasticity. In order to study the interface energy effect, however, the residual elastic field induced by the interface energy should be taken into account. Although the interface induced the residual elastic field in the reference configuration or in the current configuration is not cared for, the change of the residual elastic field induced by the interface energy from the reference configuration to the current configuration is strongly concerned. Since after and before deformation, the Cauchy stresses (in the bulk material and at the interface) are not in the same configuration based on the Eulerian description, it is obvious that the difference of the Cauchy stresses cannot be used to represent this change. Therefore, the Lagrangian description is applicable, so that the generalized Young-Laplace equation based on the Lagrangian description given by Huang and Wang (2006) can then be expressed in terms of the interface Piola-Kirchhoff stress of the first kind in the following,

$$\mathbf{N} \cdot \left[\!\left[\mathbf{S}^0 \right]\!\right] \cdot \mathbf{N} = -\overset{(in)}{\mathbf{S}}_s : \mathbf{b}_0 - \left[\mathbf{N} \cdot \left(\overset{(out)}{\mathbf{S}}_s \right) \right] \cdot \nabla_{0s}$$

$$\mathbf{P}_0 \cdot \left[\!\left[\mathbf{S}^0 \right]\!\right] \cdot \mathbf{N} = -\overset{(in)}{\mathbf{S}}_s \cdot \nabla_{0s} + \left[\mathbf{N} \cdot \left(\overset{(out)}{\mathbf{S}}_s \right) \cdot \mathbf{b}_0 \right] \qquad (4.46)$$

$$\mathbf{P}_0 = \mathbf{I} - \mathbf{N} \otimes \mathbf{N}$$

where the symbol $\left[\!\left[\cdot \right]\!\right]$ denotes the discontinuity of a quantity across the interface; $\mathbf{S}^0$ is the first kind Piola-Kirchhoff stress in the bulk material; $\mathbf{I}$ is the unit tensor in three-dimensional space; $\mathbf{N}$ is the unit normal vector to the interface in the reference configuration κ_0; $\mathbf{b}_0$ is the curvature tensor of the interface in κ_0.

Obviously, the change of the residual elastic field induced by the interface energy can be re-written by adding the difference sign into the above equation, as follows,

$$\mathbf{N} \cdot \left[\!\left[\Delta\mathbf{S}^0 \right]\!\right] \cdot \mathbf{N} = -\Delta\overset{(in)}{\mathbf{S}}_s : \mathbf{b}_0 - \left[\mathbf{N} \cdot \left(\Delta\overset{(out)}{\mathbf{S}}_s \right) \right] \cdot \nabla_{0s}$$

$$\qquad (4.47)$$

$$\mathbf{P}_0 \cdot \left[\!\left[\Delta\mathbf{S}^0 \right]\!\right] \cdot \mathbf{N} = -\Delta\overset{(in)}{\mathbf{S}}_s \cdot \nabla_{0s} + \left[\mathbf{N} \cdot \left(\Delta\overset{(out)}{\mathbf{S}}_s \right) \cdot \mathbf{b}_0 \right]$$

where Δ denotes the difference of the quantities between the current and reference configurations. In order to account for the interface energy effect, the interface Piola-Kirchhoff stress of the first kind $\mathbf{S}_s$ should be employed in the analysis, as shown in the equations above. This is the key point addressed by Huang and Wang (2006), but the previous researchers seemed to ignore that in the study of the effective properties of a heterogeneous material with interface energy effect. Next, an infinitesimal deformation approximation is executed. In the case of the infinitesimal deformation, $\Delta\mathbf{S}^0$ in Eq. (4.47) could be approximated by the difference of the

bulk Cauchy stress between the current and reference configurations, while $\mathbf{S}_s$ in Eq. (4.43) is described in terms of the interface/surface free energy γ.

In addition, the equation of the interface/surface free energy is linearized in order to simplify the algebraic operations at the beginning of the research. Accordingly, γ can be written as

$$\gamma = \gamma_0 + \gamma_1 (J_1 - 2) + \gamma_2 (J_2 - 1) + \frac{1}{2}\gamma_{11}(J_1 - 2)^2 + \gamma_{12}(J_1 - 2)(J_2 - 1) + \frac{1}{2}\gamma_{22}(J_2 - 1)^2 + \cdots$$

(4.48)

$$\gamma_1 = \frac{\partial \gamma}{\partial J_1}\Big|_{J_1=2, J_2=1} \quad , \quad \gamma_2 = \frac{\partial \gamma}{\partial J_2}\Big|_{J_1=2, J_2=1}$$

Where γ_0, γ_1, γ_2 represent the intrinsic physical properties of the interface, and they are, and should be determined by the joining materials and the adhering condition. $\gamma_0 = \gamma(2,1)$ is equivalent to the interface/surface energy of a liquid-like material and hence reflects the nature of liquids, whereas γ_1 and γ_2 reflect the nature of solids; $J_1 - 2$ and $J_2 - 1$ are first-order small quantities. Suppose that only the first-order small quantities are considered in Eq. (4.43) and higher-order small quantities are neglected, from

$$J_2 \left(\frac{\partial \gamma}{\partial J_1} + J_2 \frac{\partial \gamma}{\partial J_2} + \gamma \right) = \gamma_0^* + \left(\gamma_0^* + \gamma_1^* \right) tr \, \mathbf{E}_s$$

(4.49)

and

$$J_2 \frac{\partial \gamma}{\partial J_1} = \gamma_1 + \left(\gamma_0 + \gamma_{11} + \gamma_{12} \right) tr \, \mathbf{E}_s$$

(4.50)

Then,

$$\mathbf{S}_s = \gamma_0^* \mathbf{i}_0 + \left(\gamma_0^* + \gamma_1^* \right) \left(tr\mathbf{E}_s \right) \mathbf{i}_0 - \gamma_0^* \nabla_{0s} \mathbf{u} + \gamma_1 \mathbf{E}_s + \gamma_0^* \, \mathbf{F}_s^{(out)}$$

(4.51)

$$\boldsymbol{\sigma}_s = \gamma_0^* \mathbf{i}_0 + \gamma_1^* \left(tr \, \mathbf{E}_s \right) \mathbf{i}_0 + \gamma_1 \mathbf{E}_s + \gamma_0^* \left(\overset{(out)}{\mathbf{F}_s} + \overset{(out)^T}{\mathbf{F}_s} \right) \tag{4.52}$$

where $\gamma_0^* = \gamma_0 + \gamma_1 + \gamma_2$, $\gamma_1^* = \gamma_1 + 2\gamma_2 + \gamma_{11} + 2\gamma_{12} + \gamma_{22}$, and γ_0^* and γ_1^* form the residual

interface/surface energy. For small deformation, $\mathbf{i}_0 + \left(\overset{(out)}{\mathbf{F}_s} + \overset{(out)^T}{\mathbf{F}_s} \right) = \mathbf{i}$ in the tangent plane T_y.

The similar expression with an assumption of the interface stress is dependent on the isotropic

linear function of the interface strain can be found by Gurtin and Murdoch (1975). Here, the

present formulation shows the interface stress in terms of the interface/surface energy. Later, as

the change of the interface stress due to the change of the configuration is discussed, this

theoretical framework is applied to predict the effective moduli of heterogeneous media with the

interface/surface energy effect. In the reference configuration κ_0, the "residual" interface

Piola-Kirchhoff stress of the first kind is expressed by

$$\mathbf{S}_s \, |_0 = \gamma_0^* \mathbf{i}_0 \tag{4.53}$$

Accordingly, in the case of the infinitesimal deformation, the difference of the interface

Piola-Kirchhoff stress of the first kind between the current and reference configurations, $\Delta \mathbf{S}_s$,

can be written as

$$\Delta \mathbf{S}_s = \left(\gamma_0^* + \gamma_1^* \right) \left(tr \mathbf{E}_s \right) \mathbf{i}_0 - \gamma_0^* \nabla_{0s} \mathbf{u} + \gamma_1 \mathbf{E}_s + \gamma_0^* \overset{(out)}{\mathbf{F}_s} \tag{4.54}$$

It is found that there are at least three independent material parameters γ_0^*, γ_1^* and γ_1 required

in the above equation. For some special cases, such as a spherical inhomogeneity embedded in

an infinite matrix material under the axisymmetric loading, $\nabla_{0s} \mathbf{u}$ may be regarded as a

symmetric second-order tensor in two-dimensional space. Eq. (4.54) is then written as

$$\Delta \mathbf{S}_s = \left(\gamma_0^* + \gamma_1^* \right) \left(tr\, \mathbf{E}_s \right) \mathbf{i}_0 - \left(\gamma_0^* - \gamma_1 \right) \mathbf{E}_s + \gamma_0^* \overset{(out)}{\mathbf{F}_s}$$

(4.55)

$$\text{Or,} \quad \Delta \mathbf{S}_s = \lambda_s \left(tr\, \mathbf{E}_s \right) \mathbf{i}_0 + 2\mu_s \mathbf{E}_s + \gamma_0^* \overset{(out)}{\mathbf{F}_s}$$

where λ_s and μ_s are called interface moduli, shown as follows,

$$\lambda_s = \gamma_0^* + \gamma_1^*$$

(4.56)

$$\mu_s = -\frac{1}{2}\left(\gamma_0^* - \gamma_1 \right) = -\frac{1}{2}\left(\gamma_0 + \gamma_2 \right)$$

It is noted that μ_s could be negative in some cases. In general, the interface/surface energy γ_0 at κ_0 is positive; otherwise a liquid or a solid would gain energy upon fragmentation, for example, as referred to the research by Haiss (2001). γ_2 is the change rate of the interface energy due to the change of the interface area, and the negative μ_s has been confirmed by Shenoy (2005) in his atomistic calculations. Substituting $\Delta \mathbf{S}_s$ in Eq. (4.54) or (4.55) into Eq. (5.47), the discontinuity conditions of the traction across the interface in the reference configuration κ_0 is generated. These discontinuity conditions, associated with other governing equations, can be used to predict the macroscopic mechanical response of composites with the interface energy effect.

4.9 Appendix C: Approximate local solutions of two interacting particles

Let us consider a three-phase composite consisting of an isotropic elastic matrix (phase 0) with the bulk modulus K_0 and shear modulus μ_0, randomly dispersed elastic spherical

particles (phase 1) with the bulk modulus K_1 and shear modulus μ_1, and randomly dispersed elastic spherical particles (phase 2) with the bulk modulus K_2 and shear modulus μ_2 (cf. Figure 4.3). In addition, the linearly elastic isotropic stiffness tensors for three distinct phases are expressed as

$$\left(C_\eta\right)_{ijkl} = \lambda_\eta \delta_{ij}\delta_{kl} + \mu_\eta \left(\delta_{ik}\delta_{jl} + \delta_{il}\delta_{jk}\right), \quad \eta = 0,1,2 \tag{4.57}$$

where λ_η and μ_η are the Lamé constants of the phase-η material.
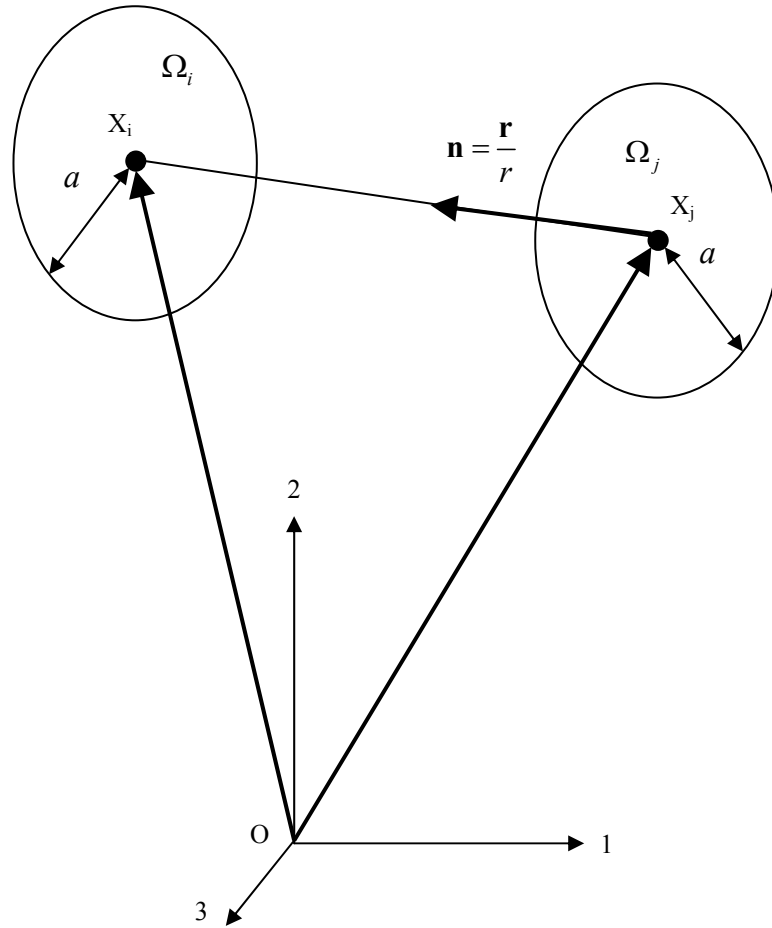
Figure 4.3 The schematic diagram for the two-particle interaction problem. r: spacing between the centers of two interacting fibers; $r = \left\|\mathbf{x}_i - \mathbf{x}_j\right\| = \left\|\mathbf{r}\right\| \quad (i,j = 1,2)$

Following the eigenstrain concept introduced by Eshelby (1957; 1961), the perturbed strain field $\varepsilon'(x)$ induced by particles can be related to the specified eigenstrains $\varepsilon^*(x)$ by replacing the particles with the matrix material. The key equation can be rephrased as follows:

$$\mathbf{C}_\eta : \left[\varepsilon^0 + \varepsilon'(x) \right] = \mathbf{C}_0 \left[\varepsilon^0 + \varepsilon'(x) - \varepsilon^*(x) \right], \quad \eta = 1,2 \tag{4.58}$$

where ε^0 is the uniform strain field induced by the far-field loads for a homogeneous matrix material only. Throughout the paper, the colon symbol ":" denotes the tensor contraction between a fourth-rank tensor and a second-rank tensor, while the dot symbol "·" represents the tensor multiplication between two four-rank tensors.

According to Eshelby (1957; 1961), the perturbed strain field induced by the distributed eigenstrain $\varepsilon^*(x)$ in a representative volume element (RVE) V reads

$$\varepsilon'(x) = \int_V \mathbf{G}(x - x') : \varepsilon^*(x') dx' \tag{4.59}$$

where $x, x' \in V$ and the components of the fourth-rank three-dimensional Green's function tensor $\mathbf{G}$ take the form

$$G_{ijkl} = \frac{1}{8\pi(1 - v_0)r^3} F_{ijkl} \left(-15, 3v_0, 3, 3 - 6v_0, -1 + 2v_0, 1 - 2v_0 \right) \tag{4.60}$$

where $i, j, k, l = 1, 2, 3$ (cf. Mura [36]), $r = x - x'$ and $r = \|x - x'\|$. The components of the tensor $\mathbf{F}$ – which depends on its arguments ($B_1, B_2, B_3, B_4, B_5, B_6$) – are defined by ($m = 1$ to 6):

$$\begin{aligned} F_{ijkl}(B_m) &\equiv B_1 n_i' n_j' n_k' n_l' + B_2 \left(\delta_{ik} n_j' n_l' + \delta_{il} n_j' n_k' + \delta_{jk} n_i' n_l' + \delta_{jl} n_i' n_k' \right) \\ &+ B_3 \delta_{ij} n_k' n_l' + B_4 \delta_{kl} n_i' n_j' + B_5 \delta_{ij} \delta_{kl} + B_6 \left(\delta_{ik} \delta_{jl} + \delta_{il} \delta_{jk} \right) \end{aligned} \tag{4.61}$$

with the normal vector $n' \equiv r/r$. All physical quantities refer to the Cartesian coordinates, and the summation convention applies here. Furthermore, δ_{ij} is the Kronecker delta, and v_0

defines the Poisson's ratio of the homogeneous matrix.

From Eqs. (4.58) and (4.59), we arrive at

$$-A_i : \boldsymbol{\varepsilon}^* (\mathbf{x}) = \boldsymbol{\varepsilon}^0 + \int_V \mathbf{G}(\mathbf{x} - \mathbf{x}') : \boldsymbol{\varepsilon}^* (\mathbf{x}') d\mathbf{x}' \tag{4.62}$$

for $\mathbf{x} \in V$ and

$$A_i \equiv (\mathbf{C}_i - \mathbf{C}_0)^{-1} \cdot \mathbf{C}_0 \tag{4.63}$$

Within the present two-sphere interaction context, the integral Eq. (4.62) can be recast as

$$-A_i : \boldsymbol{\varepsilon}^*_{(i)} (\mathbf{x}) = \boldsymbol{\varepsilon}^0 + \int_{\Omega_i} \mathbf{G}(\mathbf{x} - \mathbf{x}') : \boldsymbol{\varepsilon}^*_{(i)} (\mathbf{x}') d\mathbf{x}' + \int_{\Omega_j} \mathbf{G}(\mathbf{x} - \mathbf{x}') : \boldsymbol{\varepsilon}^*_{(j)} (\mathbf{x}') d\mathbf{x}', \quad i \neq j, \quad i, j = 1, 2 \tag{4.64}$$

where $\mathbf{x} \in \Omega_j$, and $\boldsymbol{\varepsilon}^*_{(i)} (\mathbf{x}')$ is the eigenstrain at $\mathbf{x}'$ in the i th sphere within the domain Ω_i.

As discussed earlier in Ju and Chen (1994a), the first-order solution for the eigenstrain, denoted by $\boldsymbol{\varepsilon}^{*0}_{(i)}$ for the i th phase, can be obtained by neglecting the last term in the right-hand side of Eq. (4.64), which represents the interaction effects due to the other sphere. The first-order formulation leads to

$$-A_i : \boldsymbol{\varepsilon}^{*0}_{(i)} (\mathbf{x}) = \boldsymbol{\varepsilon}^0 + \mathbf{S} : \boldsymbol{\varepsilon}^{*0}_{(i)} \tag{4.65}$$

where the Eshelby tensor $\mathbf{S}$ is defined as

$$\mathbf{S} \equiv \int_{\Omega_i} \mathbf{G}(\mathbf{x} - \mathbf{x}') d\mathbf{x}', \quad \mathbf{x}, \mathbf{x}' \in \Omega_i \tag{4.66}$$

The components of the fourth-rank interior-point Eshelby tensor $\mathbf{s}$ depend on the Poisson's ratio of the matrix (v_0) and the shape of the particle Ω_i. For a spherical particle, the tensor $\mathbf{s}$ reads

$$S_{ijkl} = \frac{1}{15(1-v_0)} \left\{ (5v_0 - 1) \delta_{ij} \delta_{kl} + (4 - 5v_0)(\delta_{ik} \delta_{jl} + \delta_{il} \delta_{jk}) \right\}, \quad i, j, k, l = 1, 2 \tag{4.67}$$

We refer to Mura (1987) for more details.

125

By subtracting the first-order solution Eq. (4.65) from Eq. (4.64), the effects of inter-particle interactions can be derived by solving the following integral equation:

$$-\mathbf{A}_i : \mathbf{d}^*_{(i)}(\mathbf{x}) = \int_{\Omega_j} \mathbf{G}(\mathbf{x} - \mathbf{x}') d\mathbf{x}' : \boldsymbol{\varepsilon}^{*0}_{(j)} + \int_{\Omega_i} \mathbf{G}(\mathbf{x} - \mathbf{x}') : \mathbf{d}^*_{(i)}(\mathbf{x}') d\mathbf{x}'$$

$$+ \int_{\Omega_j} \mathbf{G}(\mathbf{x} - \mathbf{x}') : \mathbf{d}^*_{(j)}(\mathbf{x}') d\mathbf{x}', \quad \text{for } \mathbf{x} \in \Omega_i, \quad i \neq j, \quad i, j = 1, 2 \tag{4.68}$$

where

$$\mathbf{d}^*_{(i)}(\mathbf{x}) = \boldsymbol{\varepsilon}^*_{(i)}(\mathbf{x}) - \boldsymbol{\varepsilon}^{*0}_{(i)} \tag{4.69}$$

To obtain the higher-order interaction correction for $\boldsymbol{\varepsilon}^*_{(i)}(\mathbf{x})$, one may expand the fourth-rank tensor $\mathbf{G}(\mathbf{x} - \mathbf{x}')$ in the domain Ω_i with respect to its center point $\mathbf{x}_j$; i.e.,

$$\mathbf{G}(\mathbf{x} - \mathbf{x}') = \mathbf{G}(\mathbf{x} - \mathbf{x}_j) - (\mathbf{x}' - \mathbf{x}_j) : \left[\nabla_\mathbf{x} \otimes \mathbf{G}(\mathbf{x} - \mathbf{x}_j) \right]$$

$$+ \frac{1}{2} \left[(\mathbf{x}' - \mathbf{x}_j) \otimes (\mathbf{x}' - \mathbf{x}_j) \right] : \left[\nabla_\mathbf{x} \otimes \nabla_\mathbf{x} \otimes \mathbf{G}(\mathbf{x} - \mathbf{x}_j) \right] + \cdots \tag{4.70}$$

where the relation

$$\nabla_{\mathbf{x}'} \otimes \mathbf{G}(\mathbf{x} - \mathbf{x}') = -\nabla_\mathbf{x} \otimes \mathbf{G}(\mathbf{x} - \mathbf{x}') \tag{4.71}$$

has been employed. From Eqs. (4.68) and (4.70), we arrive a

$$-\mathbf{A}_i : \mathbf{d}^*_{(i)}(\mathbf{x}) = \int_{\Omega_j} \mathbf{G}(\mathbf{x} - \mathbf{x}') d\mathbf{x}' : \boldsymbol{\varepsilon}^{*0}_{(j)} + \int_{\Omega_i} \mathbf{G}(\mathbf{x} - \mathbf{x}') : \mathbf{d}^*_{(i)}(\mathbf{x}') d\mathbf{x}'$$

$$+ \Omega_j \mathbf{G}(\mathbf{x} - \mathbf{x}_j) : \overline{\mathbf{d}}^*_{(j)}(\mathbf{x}_j) - \Omega_j a_j \left\{ \nabla_\mathbf{x} \otimes \mathbf{G}(\mathbf{x} - \mathbf{x}_j) \right\} : \overline{\mathbf{P}}^*_{(j)} \tag{4.72}$$

$$+ \frac{1}{2} \Omega_j a_j^2 \left\{ \nabla_\mathbf{x} \otimes \nabla_\mathbf{x} \otimes \mathbf{G}(\mathbf{x} - \mathbf{x}_j) \right\} : \overline{\mathbf{Q}}^*_{(j)} + \cdots$$

for $\mathbf{x} \in \Omega_i$ and $i \neq j$ (i, j = 1, 2). Here $\Omega = \Omega_i = \Omega_j = 4\pi a^3 / 3$ denotes the volume of a spherical particle, and $a = a_i = a_j$ defines its radius. Moreover, the averaged fields involved in Eq. (4.72) are defined as follows:

$$\overline{\mathbf{d}}^*_{(j)} \equiv \frac{1}{\Omega_j} \int_{\Omega_j} \mathbf{d}^*_{(j)}(\mathbf{x}) \, d\mathbf{x} \tag{4.73}$$

$$\overline{\mathbf{P}}^*_{(j)} \equiv \frac{1}{\Omega_j a_j} \int_{\Omega_j} (\mathbf{x} - \mathbf{x}_j) \otimes \mathbf{d}^*_{(j)}(\mathbf{x}) \, d\mathbf{x} \tag{4.74}$$

$$\overline{\mathbf{Q}}^*_{(j)} \equiv \frac{1}{\Omega_j a_j^2} \int_{\Omega_j} (\mathbf{x} - \mathbf{x}_j) \otimes (\mathbf{x} - \mathbf{x}_j) \otimes \mathbf{d}^*_{(j)}(\mathbf{x}) \, d\mathbf{x} \tag{4.75}$$

The third-rank tensor $\overline{\mathbf{P}}^*_{(j)}$ and the fourth-rank tensor $\overline{\mathbf{Q}}^*_{(j)}$ correspond to the dipole and quadrapole of $\mathbf{d}^*_{(j)}$ in the domain Ω_j, respectively. Due to the spherical symmetry of particles, the leading order of $\overline{\mathbf{P}}^*_{(j)}$ is of the order $O(\rho^4)$, rather than $O(\rho^3)$, by substituting Eq. (4.74) into Eq. (4.72). Here, $\rho \equiv a/r$, and r is the spacing between the centers of two spheres. By performing the volume average in Eq. (4.72) for the domain Ω_j and truncating those terms of higher order moments, the approximate equations $\overline{\mathbf{d}}^*_{(i)}$ for the local two-sphere interaction problem can be exhibited:

$$-\mathbf{A}_i : \overline{\mathbf{d}}^*_{(i)} = \mathbf{G}^2(\mathbf{x}_i - \mathbf{x}_j) : \boldsymbol{\varepsilon}^{*0}_{(j)} + \mathbf{S} : \overline{\mathbf{d}}^*_{(i)} + \mathbf{G}^1(\mathbf{x}_i - \mathbf{x}_j) : \overline{\mathbf{d}}^*_{(j)} + O(\rho^8) \tag{4.76}$$

where

$$\mathbf{G}^1 \equiv \int_{\Omega_1} \mathbf{G}(\mathbf{x} - \mathbf{x}_2) \, d\mathbf{x} = \int_{\Omega_2} \mathbf{G}(\mathbf{x}_1 - \mathbf{x}) \, d\mathbf{x} = \frac{1}{30(1-\nu_0)} \left(\rho^3 \mathbf{H}^1 + \rho^5 \mathbf{H}^2 \right) \tag{4.77}$$

$$\mathbf{G}^2 \equiv \frac{1}{\Omega} \int_{\Omega_1} \int_{\Omega_2} \mathbf{G}(\mathbf{x} - \mathbf{x}') \, d\mathbf{x}' d\mathbf{x} = \frac{1}{30(1-\nu_0)} \left(\rho^3 \mathbf{H}^1 + 2\rho^5 \mathbf{H}^2 \right) \tag{4.78}$$

and the components of $\mathbf{H}^1$ and $\mathbf{H}^2$ are rendered by

$$H^1_{ijkl}(\mathbf{x}_1 - \mathbf{x}_2) \equiv 5F_{ijkl}(-15, 3\nu_0, 3, 3 - 6\nu_0, -1 + 2\nu_0, 1 - 2\nu_0) \tag{4.79}$$

$$H^2_{ijkl}(\mathbf{x}_1 - \mathbf{x}_2) \equiv 3F_{ijkl}(35, -5, -5, -5, 1, 1) \tag{4.80}$$

127

It is noted that the leading-order error induced by dropping the higher order moments in Eq. (4.76) is of the order $O(\rho^8)$ since $\bar{\mathbf{P}}^*_{(i)}$ and $\Omega a \nabla_{\mathbf{x}} \otimes \mathbf{G}$ are of the order $O(\rho^4)$.

Moreover, Eq. (4.76) can be recast as

$$\left(\mathbf{A}_1 + \mathbf{S}\right):\overline{\mathbf{d}}^*_{(1)} + \mathbf{G}^1 : \overline{\mathbf{d}}^*_{(2)} = -\mathbf{G}^2 : \boldsymbol{\varepsilon}^{*0}_{(2)} \tag{4.81}$$

$$\mathbf{G}^1 : \overline{\mathbf{d}}^*_{(1)} + \left(\mathbf{A}_2 + \mathbf{S}\right):\overline{\mathbf{d}}^*_{(2)} = -\mathbf{G}^2 : \boldsymbol{\varepsilon}^{*0}_{(1)} \tag{4.82}$$

Therefore, the solutions of Eqs. (4.81) and (4.82) are

$$\overline{\mathbf{d}}^*_{(1)} = \left[\left(\mathbf{G}^1\right)^{-1}\cdot\left(\mathbf{A}_1 + \mathbf{S}\right) - \left(\mathbf{A}_2 + \mathbf{S}\right)^{-1}\cdot\mathbf{G}^1\right]^{-1}\left[\left(\mathbf{A}_2 + \mathbf{S}\right)^{-1}\cdot\mathbf{G}^2 : \boldsymbol{\varepsilon}^{*0}_{(1)} - \left(\mathbf{G}^1\right)^{-1}\cdot\mathbf{G}^2 : \boldsymbol{\varepsilon}^{*0}_{(2)}\right] \tag{4.83}$$

$$\overline{\mathbf{d}}^*_{(2)} = \left[\left(\mathbf{A}_1 + \mathbf{S}\right)^{-1}\cdot\mathbf{G}^1 - \left(\mathbf{G}^1\right)^{-1}\cdot\left(\mathbf{A}_2 + \mathbf{S}\right)\right]^{-1}\left[\left(\mathbf{G}^1\right)^{-1}\cdot\mathbf{G}^2 : \boldsymbol{\varepsilon}^{*0}_{(1)} - \left(\mathbf{A}_1 + \mathbf{S}\right)^{-1}\cdot\mathbf{G}^2 : \boldsymbol{\varepsilon}^{*0}_{(2)}\right] \tag{4.84}$$

where the leading orders of $\left(\mathbf{A}_2 + \mathbf{S}\right)^{-1}\cdot\mathbf{G}^1$ and $\left(\mathbf{G}^1\right)^{-1}\cdot\left(\mathbf{A}_1 + \mathbf{S}\right)$ are of the order $O(\rho^3)$ and $O(\rho^{-3})$ in Eq. (4.83), respectively. It is interesting to note that $\left(\mathbf{A}_2 + \mathbf{S}\right)^{-1}\cdot\mathbf{G}^1$ is truncated since its leading order is greater than the leading order of $\left(\mathbf{G}^1\right)^{-1}\cdot\left(\mathbf{A}_1 + \mathbf{S}\right)$. We also have $\rho < 1/2$.

Therefore, the solution of Eq. (4.83) is

$$\overline{\mathbf{d}}^*_{(1)} = \left(\mathbf{A}_1 + \mathbf{S}\right)^{-1}\cdot\left(\mathbf{G}^1\right)\cdot\left(\mathbf{A}_2 + \mathbf{S}\right)^{-1}\cdot\mathbf{G}^2 : \boldsymbol{\varepsilon}^{*0}_{(1)} - \left(\mathbf{A}_1 + \mathbf{S}\right)^{-1}\cdot\mathbf{G}^2 : \boldsymbol{\varepsilon}^{*0}_{(2)} \tag{4.85}$$

Similarly, Eq. (4.84) can be rephrased as

$$\overline{\mathbf{d}}^*_{(2)} = \left(\mathbf{A}_2 + \mathbf{S}\right)^{-1}\cdot\left(\mathbf{G}^1\right)\cdot\left(\mathbf{A}_1 + \mathbf{S}\right)^{-1}\cdot\mathbf{G}^2 : \boldsymbol{\varepsilon}^{*0}_{(2)} - \left(\mathbf{A}_2 + \mathbf{S}\right)^{-1}\cdot\mathbf{G}^2 : \boldsymbol{\varepsilon}^{*0}_{(1)} \tag{4.86}$$

4.10 Appendix D: Ensemble-volume averaged eigenstrains

To obtain the probabilistic ensemble-averaged solution of $\overline{\mathbf{d}}^*_{(i)}$ within the context of approximate pairwise local particle interaction, one has to integrate Eqs. (4.83) and (4.84) over all possible positions ($\mathbf{x}_j$) of the second particle for a given location of the first particle ($\mathbf{x}_i$). The ensemble-average process takes the form

$$\left\langle \overline{\mathbf{d}}^*_{(i)} \right\rangle (\mathbf{x}_i) = \int_{V-\Omega_i} \overline{\mathbf{d}}^*_{(i)} (\mathbf{x}_i - \mathbf{x}_j) P(\mathbf{x}_j \mid \mathbf{x}_i) \mathrm{d}\mathbf{x}_j, \quad i \neq j \tag{4.87}$$

in which $P(\mathbf{x}_j \mid \mathbf{x}_i)$ is the conditional probability density function for finding the second particle centered at $\mathbf{x}_j$ given the first particle centered at $\mathbf{x}_i$. Moreover, angled brackets define the ensemble-average operator. In this paper, a three-dimensional statistically isotropic and homogeneous two-point probability density function $P(\mathbf{x}_j \mid \mathbf{x}_i)$ is considered. The three-dimensional isotropic probabilistic integration domain V in Eq. (4.87) can therefore be evaluated as a sphere. Further, Ω_i in Eq. (4.87) defines the probabilistic "exclusion zone" for $\mathbf{x}_j$.

The two-point conditional probability function $P(\mathbf{x}_j \mid \mathbf{x}_i)$ is determined by the microstructure of a composite, which in turn depends on the particle volume fraction and underlying manufacturing processes. For illustration, the two-point conditional probability density function is taken as statistically isotropic and uniform, and obeys the following:

$$P(\mathbf{x}_j \mid \mathbf{x}_i) = \begin{cases} \dfrac{N}{V} & \text{if } r \geq 2a \\ 0 & \text{otherwise} \end{cases} \tag{4.88}$$

where $\dfrac{N}{V}$ is the three-dimensional number density of particles in a composite and r is the spacing between the centers of two spheres. By substituting Eq. (4.85) into (4.87), the explicit expression for $\left\langle \overline{\mathbf{d}}_{(1)}^{*} \right\rangle (\mathbf{x}_1)$ can be depicted as

$$
\begin{aligned}
\left\langle \overline{\mathbf{d}}_{(1)}^{*} \right\rangle (\mathbf{x}_1) = &\left[\int_{2a}^{\infty} \int_{\Theta} P(\mathbf{x}_2 \mid \mathbf{x}_1)(\mathbf{A}_1 + \mathbf{S})^{-1} \cdot (\mathbf{G}^1) \cdot (\mathbf{A}_2 + \mathbf{S})^{-1} \cdot \mathbf{G}^2 \, \mathrm{d}\Theta \, \mathrm{d}r \right] : \boldsymbol{\varepsilon}_{(1)}^{*0} \\
&- \left[\int_{2a}^{\infty} \int_{\Theta} P(\mathbf{x}_2 \mid \mathbf{x}_1)(\mathbf{A}_1 + \mathbf{S})^{-1} \cdot \mathbf{G}^2 \, \mathrm{d}\Theta \, \mathrm{d}r \right] : \boldsymbol{\varepsilon}_{(2)}^{*0}
\end{aligned}
\tag{4.89}
$$

where Θ signifies the spherical surface of radius r.

In what follows, we present two non-equivalent formulations to predict the effective elastic moduli of three-phase composites, involving "Formulation I" here and "Formulation II" in Section 4.3.2. Specifically, the following identities can be easily proved:

$$
\int_{\Theta} n_i n_j \mathrm{d}\Theta = \frac{4\pi r^2}{3} \delta_{ij}
\tag{4.90}
$$

$$
\int_{\Theta} n_i n_j n_k n_l \mathrm{d}\Theta = \frac{4\pi r^2}{15} \left(\delta_{ij}\delta_{kl} + \delta_{ik}\delta_{jl} + \delta_{il}\delta_{jk} \right)
\tag{4.91}
$$

where $\mathbf{n}$ is the normal vector at a point on Θ; i.e., $\mathbf{n} = \mathbf{r}/r$ with $\mathbf{r} = \mathbf{x}_2 - \mathbf{x}_1$. Using Eqs. (4.74)–(4.75) and Eqs. (4.90)–(4.91), it is straightforward to verify that the surface integral of $(\mathbf{A}_1 + \mathbf{S})^{-1} \cdot \mathbf{G}^2$ in the second line of Eq. (4.89) is identically zero. By carrying out the lengthy algebra and utilizing the identities (4.90)–(4.91), the ensemble integration for $\left\langle \overline{\mathbf{d}}_{(1)}^{*} \right\rangle (\mathbf{x}_1)$ reads

$$\left\langle \overline{\mathbf{d}}_{(1)}^{*} \right\rangle (\mathbf{x}_{1}) = \left\{ \phi_{2} \left(q_{1} + \frac{90}{64\beta_{1}\beta_{2}} \right) \delta_{ij}\delta_{kl} + \phi_{2} \left(q_{2} - \frac{135}{64\beta_{1}\beta_{2}} \right) \left(\delta_{ik}\delta_{jl} + \delta_{il}\delta_{jk} \right) \right.$$

$$\left. + \phi_{1} \left(q_{3} + \frac{90}{64\beta_{1}^{2}} \right) \delta_{ij}\delta_{kl} + \phi_{1} \left(q_{4} - \frac{135}{64\beta_{1}^{2}} \right) \left(\delta_{ik}\delta_{jl} + \delta_{il}\delta_{jk} \right) \right\} : \boldsymbol{\varepsilon}_{(1)}^{*0} \tag{4.92}$$

Here, $\phi_{i} = \dfrac{N_{i}}{V}\left(\dfrac{4}{3}\pi a^{3} \right)$, with $i = 1, 2,$ is the volume fraction of the i-phase particle. Other parameters in the above equation are summarized in Eqs (4.32) and (4.33).

Formulation II: The approximate ensemble-volume averaged eigenstrain tensor can be derived from Eqs. (4.73) and (4.88), and takes the form

$$\left\langle \overline{\boldsymbol{\varepsilon}}_{(1)}^{*} \right\rangle = \boldsymbol{\Gamma}^{1} : \boldsymbol{\varepsilon}_{(1)}^{*0} \tag{4.93}$$

Here, the components of the isotropic tensor $\boldsymbol{\Gamma}^{1}$ are

$$\Gamma_{ijkl}^{1} = r_{1}\delta_{ij}\delta_{kl} + r_{2}\left(\delta_{ik}\delta_{jl} + \delta_{il}\delta_{jk} \right) \tag{4.94}$$

in which

$$r_{1} = \phi_{2}t_{1} + \phi_{1}t_{3}$$
$$r_{2} = \frac{1}{2} + \phi_{2}t_{2} + \phi_{1}t_{4} \tag{4.95}$$

with

$$t_{1} = q_{1} + \frac{90}{64}\left(\frac{1}{\beta_{1}\beta_{2}} \right)$$
$$t_{2} = q_{2} - \frac{135}{64}\left(\frac{1}{\beta_{1}\beta_{2}} \right)$$
$$t_{3} = q_{3} + \frac{90}{64}\left(\frac{1}{\beta_{1}^{2}} \right) \tag{4.96}$$
$$t_{4} = q_{4} - \frac{135}{64}\left(\frac{1}{\beta_{1}^{2}} \right)$$

Similarly, the approximate ensemble-volume averaged eigenstrain tensor $\left\langle \overline{\varepsilon}_{(2)}^{*} \right\rangle$ reads

$$\left\langle \overline{\varepsilon}_{(2)}^{*} \right\rangle = \Gamma^{2} : \varepsilon_{(2)}^{*0} \tag{4.97}$$

The components of the isotropic tensor Γ^{2} are

$$\Gamma_{ijkl}^{2} = r_{3}\delta_{ij}\delta_{kl} + r_{4}\left(\delta_{ik}\delta_{jl} + \delta_{il}\delta_{jk}\right) \tag{4.98}$$

where

$$
\begin{aligned}
r_{3} &= \phi_{1}t_{5} + \phi_{2}t_{7} \\
r_{4} &= \frac{1}{2} + \phi_{1}t_{6} + \phi_{2}t_{8}
\end{aligned}
\tag{4.99}
$$

Other parameters in Eqs. (4.99) are exhibited as follows:

$$
\begin{aligned}
t_{5} &= q_{5} + \frac{90}{64}\left(\frac{1}{\beta_{1}\beta_{2}}\right) \\
t_{6} &= q_{6} - \frac{135}{64}\left(\frac{1}{\beta_{1}\beta_{2}}\right) \\
t_{7} &= q_{7} + \frac{90}{64}\left(\frac{1}{\beta_{2}^{2}}\right) \\
t_{8} &= q_{8} - \frac{135}{64}\left(\frac{1}{\beta_{2}^{2}}\right)
\end{aligned}
\tag{4.100}
$$

Formulation I: By neglecting the higher-order components $O\left(\rho^{5}\right)$ in Eqs. (4.77) and (4.78) and following the similar procedure as in "Formulation II", the approximate ensemble-volume averaged eigenstrain tensors become

$$
\begin{aligned}
\left\langle \overline{\varepsilon}_{(1)}^{*} \right\rangle &= \Gamma^{1} : \varepsilon_{(1)}^{*0} \\
\left\langle \overline{\varepsilon}_{(2)}^{*} \right\rangle &= \Gamma^{2} : \varepsilon_{(2)}^{*0}
\end{aligned}
\tag{4.101}
$$

where the components of the isotropic ensors Γ^{1} and Γ^{2} read

$$\Gamma^1_{ijkl} = r_1 \delta_{ij} \delta_{kl} + r_2 \left(\delta_{ik} \delta_{jl} + \delta_{il} \delta_{jk} \right)$$

$$\Gamma^2_{ijkl} = r_3 \delta_{ij} \delta_{kl} + r_4 \left(\delta_{ik} \delta_{jl} + \delta_{il} \delta_{jk} \right)$$

(4.102)

with

$$r_1 = \phi_2 q_1 + \phi_1 q_3$$

$$r_2 = \frac{1}{2} + \phi_2 q_2 + \phi_1 q_4$$

$$r_3 = \phi_1 q_5 + \phi_2 q_7$$

$$r_4 = \frac{1}{2} + \phi_1 q_6 + \phi_2 q_8$$

(4.103)

The parameters in Eq. (4.103) take the form:

$$q_1 = \frac{-5}{4} \left\{ \frac{\alpha_1 \left[2\beta_2 \left(11 - 11\nu_0 + 5\nu_0^2 \right) + 3\alpha_2 \left(10 - 10\nu_0 + 7\nu_0^2 \right) \right]}{\beta_1 \beta_2 \left(3\alpha_1 + 2\beta_1 \right) \left(3\alpha_2 + 2\beta_2 \right)} \right.$$

$$\left. + \frac{2\beta_1 \left[2\beta_2 \left(2 - 2\nu_0 + 5\nu_0^2 \right) + \alpha_2 \left(5 - 5\nu_0 + 17\nu_0^2 \right) \right]}{\beta_1 \beta_2 \left(3\alpha_1 + 2\beta_1 \right) \left(3\alpha_2 + 2\beta_2 \right)} \right\}$$

(4.104)

$$q_2 = \frac{5}{8} \left\{ \frac{2\beta_2 \left(11 - 11\nu_0 + 5\nu_0^2 \right) + 3\alpha_2 \left(10 - 10\nu_0 + 7\nu_0^2 \right)}{\beta_1 \beta_2 \left(3\alpha_2 + 2\beta_2 \right)} \right\}$$

(4.105)

$$q_3 = \frac{-5}{4} \left\{ \frac{2\beta_1 \left(2 - 2\nu_0 + 5\nu_0^2 \right) + \alpha_1 \left(10 - 10\nu_0 + 7\nu_0^2 \right)}{\beta_1^2 \left(3\alpha_1 + 2\beta_1 \right)} \right\}$$

(4.106)

$$q_4 = \frac{5}{8} \left\{ \frac{2\beta_1 \left(11 - 11\nu_0 + 5\nu_0^2 \right) + 3\alpha_1 \left(10 - 10\nu_0 + 7\nu_0^2 \right)}{\beta_1^2 \left(3\alpha_1 + 2\beta_1 \right)} \right\}$$

(4.107)

$$q_5 = \frac{-5}{4}\left\{ \frac{\alpha_2\left[2\beta_1\left(11-11v_0+5v_0^2\right)+3\alpha_1\left(10-10v_0+7v_0^2\right)\right]}{\beta_1\beta_2\left(3\alpha_1+2\beta_1\right)\left(3\alpha_2+2\beta_2\right)} \right.$$
$$\left. +\frac{2\beta_2\left[2\beta_1\left(2-2v_0+5v_0^2\right)+\alpha_1\left(5-5v_0+17v_0^2\right)\right]}{\beta_1\beta_2\left(3\alpha_1+2\beta_1\right)\left(3\alpha_2+2\beta_2\right)} \right\} \tag{4.108}$$

$$q_6 = \frac{5}{8}\left\{ \frac{2\beta_1\left(11-11v_0+5v_0^2\right)+3\alpha_1\left(10-10v_0+7v_0^2\right)}{\beta_1\beta_2\left(3\alpha_1+2\beta_1\right)} \right\} \tag{4.109}$$

$$q_7 = \frac{-5}{4}\left\{ \frac{2\beta_2\left(2-2v_0+5v_0^2\right)+\alpha_2\left(10-10v_0+7v_0^2\right)}{\beta_2^2\left(3\alpha_2+2\beta_2\right)} \right\} \tag{4.110}$$

$$q_8 = \frac{5}{8}\left\{ \frac{2\beta_2\left(11-11v_0+5v_0^2\right)+3\alpha_2\left(10-10v_0+7v_0^2\right)}{\beta_2^2\left(3\alpha_2+2\beta_2\right)} \right\} \tag{4.111}$$

with

$$\alpha_m = 2\left(5v_0-1\right)+10\left(1-v_0\right)\left(\frac{K_0}{K_m-K_0}-\frac{\mu_0}{\mu_m-\mu_0}\right),\quad m=1,2 \tag{4.112}$$

$$\beta_m = 2\left(4-5v_0\right)+15\left(1-v_0\right)\left(\frac{\mu_0}{\mu_m-\mu_0}\right),\quad m=1,2 \tag{4.113}$$

where K_0, K_m and μ_0, μ_m denote the bulk and shear moduli of the matrix and the m-phase particle.

4.11 References

[1] Adams, D. F., and Crane, D. A. (1984). "Finite-element micromechanical analysis of a unidirectional composite including longitudinal shear loading." *Computers & Structures*, 18(6), 1153-1165.

[2] Banthia, N., and Gupta, R. (2004). "Hybrid fiber reinforced concrete (HyFRC): fiber synergy in high strength matrices." *Materials and Structures*, 37(274), 707-716.

[3] Banthia, N., and Nandakumar, N. (2003). "Crack growth resistance of hybrid fiber reinforced cement composites." *Cement & Concrete Composites*, 25(1), 3-9.

[4] Banthia, N., and Soleimani, S. M. (2005). "Flexural response of hybrid fiber-reinforced cementitious composites." *Aci Materials Journal*, 102(6), 382-389.

[5] Benveniste, Y. (1987). "A new approach to the application of mori-tanaka theory in composite-materials." *Mechanics of Materials*, 6(2), 147-157.

[6] Blunt, J., and Ostertag, C. P. (2009). "Performance-based approach for the design of a deflection hardened hybrid fiber-reinforced concrete." *Journal of Engineering Mechanics-Asce*, 135(9), 978-986.

[7] Christensen, R. M., and Lo, K. H. (1979). "Solutions for effective shear properties in 3 phase sphere and cylinder models." *Journal of the Mechanics and Physics of Solids*, 27(4), 315-330.

[8] Doghri, I., and Friebel, C. (2005). "Effective elasto-plastic properties of inclusion-reinforced composites. Study of shape, orientation and cyclic response." *Mechanics of Materials*, 37(1), 45-68.

[9] Duan, H. L., Wang, J., Huang, Z. P., and Luo, Z. Y. (2005). "Stress concentration tensors of

inhomogeneities with interface effects." *Mechanics of Materials*, 37(7), 723-736.

[10] Eshelby, J. D. (1957). "The determination of the elastic field of an ellipsoidal inclusion, and related problems." *Proceedings of the Royal Society of London Series a-Mathematical and Physical Sciences*, 241(1226), 376-396.

[11] Hansen, J. P., and McDonald, I. R. (1986). "Theory of simple liquids. Second edition." *Theory of simple liquids. Second edition*.

[12] Hashin, Z. (1962). "The elastic moduli of heterogeneous materials." *Journal of the Applied Mechanics*, 29, 143-150.

[13] Hashin, Z. (1965). "On elastic behaviour of fibre reinforced materials of arbitrary transverse phase geometry." *Journal of the Mechanics and Physics of Solids*, 13(3), 119-134.

[14] Hashin, Z. (1972). "Theory of fiber reinforced materials." NASA CR-1974.

[15] Hashin, Z., Rosen, B.W. (1964). "The elastic moduli of fiber-reinforced materials. " *J. Appl. Mech.*, **31**, 223–232

[16] Hashin, Z., and Shtrikman, S. (1962b). "A variational approach to the theory of the elastic behaviour of polycrystals." *Journal of the Mechanics and Physics of Solids*, 10(4), 343-352.

[17] Hashin, Z., and Shtrikman, S. (1962a). "On some variational principles in anisotropic and nonhomogeneous elasticity." *Journal of the Mechanics and Physics of Solids*, 10(4), 335-342.

[18] Hill, R. (1964). "Theory of mechanical properties of fibre-strengthened materials .1. elastic behaviour." *Journal of the Mechanics and Physics of Solids*, 12(4), 199-212.

[19] Hill, R. (1964). "Theory of mechanical properties of fibre-strengthened materials .2. inelastic behaviour." *Journal of the Mechanics and Physics of Solids*, 12(4), 213-218.

[20] Hill, R. (1965a). "Theory of mechanical properties of fibre-strengthened materials .3.

self-consistent model." *Journal of the Mechanics and Physics of Solids*, 13(4), 189-198.

[21] Hill, R. (1965b). "A self-consistent mechanics of composite materials." *Journal of the Mechanics and Physics of Solids*, 13(4), 213-222.

[22] Honein, E. (1991). "Multiple inclusions in elastostatics." Ph.D. Dissertation at Stanford University.

[23] Huang, Z. P., and Sun, L. (2007). "Size-dependent effective properties of a heterogeneous material with interface energy effect: from finite deformation theory to infinitesimal strain analysis." *Acta Mechanica*, 190(1-4), 151-163.

[24] Huang, Z. P., and Wang, J. (2006). "A theory of hyperelasticity of multi-phase media with surface/interface energy effect." *Acta Mechanica*, 182(3-4), 195-210.

[25] Ju, J. W., and Chen, T. M. (1994b). "Effective elastic-moduli of 2-phase composites containing randomly dispersed spherical inhomogeneities." *Acta Mechanica*, 103(1-4), 123-144.

[26] Ju, J. W., and Chen, T. M. (1994c). "Micromechanics and effective elastoplastic behavior of 2-phase metal-matrix composites." *Journal of Engineering Materials and Technology-Transactions of the Asme*, 116(3), 310-318.

[27] Ju, J. W., and Chen, T. M. (1994a). "Micromechanics and effective moduli of elastic composites containing randomly dispersed ellipsoidal inhomogeneities." *Acta Mechanica*, 103(1-4), 103-121.

[28] Ju, J. W., and Ko, Y. F. (2008). "Micromechanical elastoplastic damage modeling of progressive interfacial arc debonding for fiber reinforced composites." *International Journal of Damage Mechanics*, 17(4), 307-356.

[29] Ju, J. W., and Ko, Y. F. (2008). "Micromechanical elastoplastic damage modeling of

progressive interfacial arc debonding for fiber reinforced composites." *International Journal of Damage Mechanics*, 17(4), 307-356.

[30] Ju, J. W., Ko, Y. F., and Ruan, H. N. (2006). "Effective elastoplastic damage mechanics for fiber-reinforced composites with evolutionary complete fiber debonding." *International Journal of Damage Mechanics*, 15(3), 237-265.

[31] Ju, J. W., Ko, Y. F., and Ruan, H. N. (2008). "Effective elastoplastic damage mechanics for fiber reinforced composites with evolutionary partial fiber debonding." *International Journal of Damage Mechanics*, 17(6), 493-537.

[32] Ju, J. W., Ko, Y. F., and Zhang, X. D. (2009). "Multi-level elastoplastic damage mechanics for elliptical fiber-reinforced composites with evolutionary fiber debonding." *International Journal of Damage Mechanics*, 18(5), 419-460.

[33] Ju, J. W., and Lee, H. K. (2000). "A micromechanical damage model for effective elastoplastic behavior of ductile matrix composites considering evolutionary complete particle debonding." *Computer Methods in Applied Mechanics and Engineering*, 183(3-4), 201-222.

[34] Ju, J. W., and Lee, H. K. (2001). "A micromechanical damage model for effective elastoplastic behavior of partially debonded ductile matrix composites." *International Journal of Solids and Structures*, 38(36-37), 6307-6332.

[35] Ju, J. W., and Sun, L. Z. (1999). "A novel formulation for the exterior-point Eshelby's tensor of an ellipsoidal inclusion." *Journal of Applied Mechanics-Transactions of the Asme*, 66(2), 570-574.

[36] Ju, J. W., and Sun, L. Z. (2001). "Effective elastoplastic behavior of metal matrix composites containing randomly located aligned spheroidal inhomogeneities. Part I:

micromechanics-based formulation." *International Journal of Solids and Structures*, 38(2), 183-201.

[37] Ju, J. W., and Tseng, K. H. (1996). "Effective elastoplastic behavior of two-phase ductile matrix composites: A micromechanical framework." *International Journal of Solids and Structures*, 33(29), 4267-4291.

[38] Ju, J. W., and Tseng, K. H. (1997). "Effective elastoplastic algorithms for ductile matrix composites." *Journal of Engineering Mechanics-Asce*, 123(3), 260-266.

[39] Ju, J. W., and Yanase, K. (2009). "Micromechanical Elastoplastic Damage Mechanics for Elliptical Fiber-Reinforced Composites with Progressive Partial Fiber Debonding." *International Journal of Damage Mechanics*, 18(7), 639-668.

[40] Ju, J. W., and Yanase, K. (2010). "Micromechanics and effective elastic moduli of particle-reinforced composites with near-field particle interactions." *Acta Mechanica*, 215(1-4), 135-153.

[41] Ju, J. W., and Yanase, K. (2011). "Micromechanical effective elastic moduli of continuous fiber-reinforced composites with near-field fiber interactions." *Acta Mechanica*, 216(1-4), 87-103.

[42] Ju, J. W., and Yanase, K. (2011). "Size-dependent probabilistic micromechanical damage mechanics for particle-reinforced metal matrix composites." *International Journal of Damage Mechanics*, 20(7), 1021-1048.

[43] Ju, J. W., Yanase, K., and Asme (2008). "Elastoplastic micromechanical damage mechanics for composites with progressive partial fiber debonding and thermal residual stress." *Proceedings of the Asme International Mechanical Engineering Congress and Exposition 2007, Vol 13: Processing and Engineering Applications of Novel Materials*, 277-281.

[44] Ju, J. W., and Zhang, X. D. (1998). "Micromechanics and effective transverse elastic moduli of composites with randomly located aligned circular fibers." *International Journal of Solids and Structures*, 35(9-10), 941-960.

[45] Ju, J. W., and Zhang, X. D. (2001). "Effective elastoplastic behavior of ductile matric composites containing randomly located aligned circular fibers." *International Journal of Solids and Structures*, 38(22-23), 4045-4069.

[46] Ko, Y.F. (2005). "Effective elastoplastic-damage model for fiber-reinforced metal matrix composites with evolutionary fibers debonding." Ph.D. Dissertation, University of California, Los Angeles.

[47] Ko, Y.-F., and Ju, J. W. (2012). "New higher-order bounds on effective transverse elastic moduli of three-phase fiber-reinforced composites with randomly located and interacting aligned circular fibers." *Acta Mechanica*, 223(11), 2437-2458.

[48] Ko, Y.-F., and Ju, J. W. (2013). "Effective transverse elastic moduli of three-phase hybrid fiber-reinforced composites with randomly located and interacting aligned circular fibers of distinct elastic properties and sizes." *Acta Mechanica*, 224(1), 157-182.

[49] Ko, Y. F., and Ju, J. W. (2013). "Effects of fiber cracking on elastoplastic-damage behavior of fiber-reinforced metal matrix composites." *International Journal of Damage Mechanics*, 22(1), 48-67.

[50] Kondo, K., Saito, N. (1986). "The influence of random fiber packing on the elastic properties of unidirectional composites." In: Composites '86: Recent Advances in Japan and the United States. Proceedings of Japan-U.S. CCM-III.

[51] Lee, H. K., and Ju, J. W. (2008). "3D micromechanics and effective moduli for brittle composites with randomly located interacting microcracks and inclusions." *International*

Journal of Damage Mechanics, 17(5), 377-417.

[52] Lin, P. J., and Ju, J. W. (2009). "Effective elastic moduli of three-phase composites with randomly located and interacting spherical particles of distinct properties." *Acta Mechanica*, 208(1-2), 11-26.

[53] Liu, H. T., and Sun, L. Z. (2004). "Effects of thermal residual stresses on effective elastoplastic behavior of metal matrix composites." *International Journal of Solids and Structures*, 41(8), 2189-2203.

[54] Liu, H. T., Sun, L. Z., and Ju, J. W. (2004). "An interfacial debonding model for particle-reinforced composites." *International Journal of Damage Mechanics*, 13(2), 163-185.

[55] Liu, H. T., Sun, L. Z., and Ju, J. W. (2006). "Elastoplastic modeling of progressive interfacial debonding for particle-reinforced metal-matrix composites." *Acta Mechanica*, 181(1-2), 1-17.

[56] Milton, G. W. (1982). "Bounds on the elastic and transport-properties of 2-component composites." *Journal of the Mechanics and Physics of Solids*, 30(3), 177-191.

[57] Milton, G. W., and Phanthien, N. (1982). "New bounds on effective elastic-moduli of 2-component materials." *Proceedings of the Royal Society of London Series a-Mathematical Physical and Engineering Sciences*, 380(1779), 305-331.

[58] Mori, T., and Tanaka, K. (1973). "Average stress in matrix and average elastic energy of materials with misfitting inclusions." *Acta Metallurgica*, 21(5), 571-574.

[59] Mura, T. (1987). "Micromechanics of defects in solids." 2nd edn. Kluwer, The Netherlands.

[60] Nemat-Nasser, S., Hori, M. (1993). "Micromechanics: overall properties of heterogeneous materials." Elsevier Science Publisher B. V., Netherlands.

[61] Nimmer, R. P., Bankert, R. J., Russell, E. S., Smith, G. A., and Wright, P. K. (1991). "Micromechanical modeling of fiber matrix interface effects in transversely loaded sic ti-6-4 metal matrix composites." *Journal of Composites Technology & Research*, 13(1), 3-13.

[62] Sharma, P., and Ganti, S. (2004). "Size-dependent Eshelby's tensor for embedded nano-inclusions incorporating surface/interface energies." *Journal of Applied Mechanics-Transactions of the Asme*, 71(5), 663-671.

[63] Silnutzer, N. (1972). "Effective constants of statistically homogeneous materials." Ph.D. Thesis, University of Pennsylvania.

[64] Soliman, E., Al-Haik, M., and Taha, M. R. (2012). "On and off-axis tension behavior of fiber reinforced polymer composites incorporating multi-walled carbon nanotubes." *Journal of Composite Materials*, 46(14), 1661-1675.

[65] Sun, L. Z., and Ju, J. W. (2001). "Effective elastoplastic behavior of metal matrix composites containing randomly located aligned spheroidal Inhomogeneities. Part II: applications." *International Journal of Solids and Structures*, 38(2), 203-225.

[66] Sun, L. Z., Ju, J. W., and Liu, H. T. (2003). "Elastoplastic modeling of metal matrix composites with evolutionary particle debonding." *Mechanics of Materials*, 35(3-6), 559-569.

[67] Sun, L. Z., Liu, H. T., and Ju, J. W. (2003). "Effect of particle cracking on elastoplastic behaviour of metal matrix composites." *International Journal for Numerical Methods in Engineering*, 56(14), 2183-2198.

[68] Torquato, S., and Lado, F. (1992). "Improved bounds on the effective elastic-moduli of random arrays of cylinders." *Journal of Applied Mechanics-Transactions of the Asme*, 59(1),

1-6.

[69] Walpole, L. J. (1966b). "On bounds for overall elastic moduli of inhomogeneous systems .2." *Journal of the Mechanics and Physics of Solids*, 14(5), 289-301.

[70] Walpole, L. J. (1966a). "On bounds for overall elastic moduli of inhomogeneous systems .i." *Journal of the Mechanics and Physics of Solids*, 14(3), 151-162.

[71] Walpole, L. J. (1969). "On overall elastic moduli of composite materials." *Journal of the Mechanics and Physics of Solids*, 17(4), 235-251.

[72] Wang, M., Zhang, Z., and Sun, Z. (2009). "The hybrid model and mechanical properties of hybrid composites reinforced with different diameter fibers." *Journal of Reinforced Plastics and Composites*, 28(3), 257-264.

[73] Weng, G. J. (1990). "The theoretical connection between mori tanaka theory and the hashin shtrikman walpole bounds." *International Journal of Engineering Science*, 28(11), 1111-1120.

[74] Zhao, Y. H., Tandon, G. P., and Weng, G. J. (1989). "Elastic-moduli for a class of porous materials." *Acta Mechanica*, 76(1-2), 105-130.

Chapter 5

INTERFACE ENERGY EFFECT ON SIZE-DEPENDENT EFFECTIVE TRANSVERSE ELASTIC MODULI OF THREE-PHASE HYBRID FIBER-REINFORCED COMPOSITES WITH RANDOMLY LOCATED AND INTERACTING ALIGNED CIRCULAR FIBERS OF DISTINCT ELASTIC PROPERTIES AND SIZES

ABSTRACT

In this chapter, the two-dimensional expressions of the interface/surface energy effect on size-dependent effective moduli of a composite material containing heterogeneous inclusions has been derived based on the similar procedure of formulations in Chapter 3, but the different part is to truncate "out-of-plane" terms in the first kind Piola-Kirchhoff surface stress and the Lagrangian description of the Young-Laplace equations. Associated with the applications of the probabilistic spatial distribution of circular fibers, the pairwise fiber interactions, and the ensemble-area homogenization method, the framework of effective transverse elastic moduli of a higher-order multi-scale structure for three-phase hybrid fiber-reinforced composites containing randomly located yet unidirectionally aligned circular fibers is then proposed. Specifically, the

two inhomogeneity phases feature distinct elastic properties and sizes. Two non-equivalent formulations are considered in detail to derive effective transverse elastic moduli of three-phase composites containing hybrid fibers with the interface/surface energy effect. Lastly, the analytical equations in some special cases for the influence of the liquid-like interface/surface energy on the effective transverse moduli of three-phase composites containing two distinct fibers are discussed. Moreover, numerical examples are implemented to illustrate the potential capability of the present method. It is further demonstrated that the results with the interface/surface energy effect in our model, different from the results given by preceding researchers, would be more applicable to the nanocomposites.

Key Words: Interface/surface energy effect; Three-phase hybrid fiber-reinforced composite; Finite deformation theory; Infinitesimal strain analysis; Micromechanical analytical framework; Probabilistic spatial distribution; Pairwise fiber interactions; Ensemble-area homogenization; Nanocomposite

5.1 Introduction

In general, conventional fiber-reinforced composite is regarded as a composite consisting of a single type of fiber embedded firmly in the matrix. It is demonstrated that the impact, compressive, and tensile capacity due to various damage or failure mechanisms during the loading history is limited. In contrast, if the incorporation of several different types and/or sizes of fibers in a matrix is achieved, so-called hybrid fiber-reinforced composite, it leads to

appealing and superior mechanical properties compared to conventional composites, and has been extensively considered and increasingly adopted in engineering design and manufacturing. Applications of the hybrid composites are in the areas of civil infrastructures, aerospace, automobile industries, medical devices, military equipments, etc. In addition, the strength of using hybrid composites is that one type of fiber can complement the other's weakness. In other word, they are complementary so that their strengths are standing out and their weaknesses can be prevented. Thus, optimum cost and performance can be achieved through proper material design. For example, Banthia and Nandakumar (2003) and Banthia and Gupta (2004) indicated that certain fiber combinations produce a best synergistic response. Banthia and Soleimani (2005) provided a state-of-the-art summary of various hybrid fiber combinations and correlative result effects on the flexural performance of the hybrid fiber-reinforced concrete (HyFRC). In addition, Blunt and Ostertag (2009) developed a numerical model that uses a nonlinear cracked hinge to characterize the flexural behavior of a beam element composed of hybrid fiber-reinforced concrete (HyFRC). Furthermore, Soliman et al. (2012) experimentally investigated the role of multi-walled carbon nanotubes (MWCNTs) on the tension (on-axis tension test) and in-plane shear (off-axis tension test) behaviors of carbon fiber-reinforced polymer composites. Wang et al. (2009) fabricated and investigated SiCF/CF and BF/CF fiber-reinforced epoxy resin hybrid composites by using carbon fiber (CF) as small-diameter fiber, and SiC fiber (SiCF) or boron fiber (BF) as larger-diameter fiber.

There are many published literatures and studies on the subject of predicting the effective elastic moduli of random heterogeneous multi-phase particle/fiber-reinforced composites. Most researchers, however, mainly focus on conventional composites with a single type of fiber/particle embedded in the matrix without considering the effects of different fiber/particle

diameters. Among them, several categories are of considerable interest to investigate.

The first category employs variational principles or linear comparison composites to obtain mathematical lower and upper bounds for effective elastic moduli of composites. For example, Hashin and Shtrikman (1962a; 1962b; 1963) proposed the upper and lower bounds for effective elastic moduli of multiphase materials based on the variational principles within the linear elasticity theory and, in generally, it is better than the Voigt and Reuss bounds. Furthermore, Hill (1964a; 1964b), Hashin and Rosen (1964), Hashin (1965), Walpole (1966a; 1966b; 1969), and Hashin (1972) are also selected references for this category. Nevertheless, Silnutnzer (1972), Milton (1982), Milton and Phan-Thien (1982), and Torquato and Lado (1992) investigated the "improved" higher-order mathematical bounds, which depend on the statistical microstructural information of random heterogeneous composite. For instance, Silnutzer (1972) derived improved bounds, which are referred to as the third-order (three-point) bounds, on effective in-plane bulk and shear moduli. Moreover, it is noted that the third-order bounds are narrower than the two-point bounds of Hashin's type.

The second category is known as the "effective medium approach" used for micromechanical estimation about effective moduli of composites, including the self-consistent method, the differential scheme, the generalized self-consistent method, and the Mori-Tanaka method (Mori and Tanaka, 1973). In the meanwhile, Hill (1965a; 1965b), Christensen and Lo (1979), Mori and Tanaka (1973), Benveniste (1987), and Weng (1990) are the popular references for the effective medium method. However, the effective medium methods as a group depend only on geometries of particles (inclusions) and volume fractions; in other words, they do not consider the spatial locations and/or probabilistic distributions of particles (inclusions). As the effective medium methods are inherently independent of the spatial or statistical particles

distribution, it is best appropriate for low particle concentrations or some limited special configurations.

The third category, in contrast with the second category, directly determined the micromechanics of effective properties of composites with randomly located and interacting inclusions by employing some approximations with certain special geometric configurations of inclusions dispersing in matrix materials. For example, Eshelby (1957) proposed an ellipsoidal inclusion embedded in an infinite matrix and developed the famous "Eshelby's equivalence principle". Mura (1987) mainly considered rigorous "local" micromechanics. Honein (1991) pointed out a general framework to solve the problem of two-circular inclusions in plane elastostatics, subjected to arbitrary loading by utilizing Kolosov–Muskhelishvili complex potentials. Nemat-Nasser and Hori (1993) also made a great contribution to this approach. However, only "local" field solutions were obtained through this approach. For this reason, a micromechanical higher-order ensemble-volume average method was constrcted by Ju and Chen (1994a; 1994b), based upon the framework by Eshelby (1957), to obtain the elastic effective moduli of multi-phase composites containing randomly dispersed ellipsoidal and spherical inhomogeneities, respectively. Upon this method, which considered the pairwise inclusion interactions, both "local" and "overall" field solutions can be obtained, and accordingly, the ensemble-volume averaged micromechanical field equations were formulated by the homogenization process. Soon after, along the line of Ju and Chen (1994a; 1994b), Ju and Zhang (1998), Ju and Yanase (2010; 2011), and Lin and Ju (2009) established the effective elastic moduli of composites with randomly located aligned circular fibers or randomly dispersed spherical particles featuring same/distinct elastic properties and the same sizes. Subsequently, Ko and Ju (2012; 2013) rendered the effective transverse elastic moduli of a three-phase composites

with randomly located aligned circular fibers of distinct elastic properties and sizes. In addition, emanating from the general framework of Ju and Chen (1994a; 1994b), Ju and co-workers further explored the micromechanical effective elastoplastic behaviors of two-phase metal matrix composites (Ju and Chen, 1994c; Ju and Tseng, 1996; Ju and Tseng, 1997; Ju and Zhang, 2001; Ju and Sun, 2001; Sun and Ju, 2001), the exact formulation for the exterior-point Eshelby's tensor of an ellipsoidal inclusion (Ju and Sun, 1999) and micromechanical damage models for effective elastoplastic behaviors of ductile matrix composites accommodating evolutionary particle debonding/cracking and interfacial fiber debonding with/without thermal residual stresses effects (Ju and Lee, 2000; Ju and Lee, 2001; Sun et al., 2003a; Sun et al., 2003b; Liu et al., 2004a; Liu et al., 2004b; Ko, 2005; Ju et al., 2006; Liu et al., 2006; Ju et al., 2008; Ju and Ko, 2008; Ju and Yanase, 2008; Lee and Ju, 2008; Ju et al., 2009; Ju and Yanase, 2009; Ju and Yanase, 2011; Ko and Ju, 2012).

Lastly, other categories utilized numerical solutions to analyze the effective properties of multi-phase composites. For example, Adams and Crane (1984), Nimmer et al. (1991), and Doghri and Friebel (2005) were based on the "finite element methods" to provide the effective properties of a composite by the developed "unit cell model" and some assumed periodic arrays of fibers. On contrast, "Rigid-Body-Spring-Model (RBSM) method" is another numerical approach to construct the effective properties of multi-phase composites, which can refer to Kawai (1978), Bolander and Saito (1998), Gedil et al. (2011; 2012), and Yamamoto et al. (2013). The introduction to RBSM and its application for finding the effective properties of multi-phase composites are presented in Chapter 7 of my research as well.

Nowadays, since the materials science and technique have been advanced to the characteristic size of a nano-scale solid in structures and composites, the interface/surface energy

effect on mechanical and physical properties of nanocomposites and nano-size structures becomes significant and cannot be ignored. Therefore, the interface/surface energy effect should be accounted into the deformation analysis of solids.

In Huang and Sun (2007), the change of the elastic fields induced by the interface energies and the interface stresses from the reference configuration to the current configuration was considered. It was emphasized that there are two kinds of fundamental equations required to be introduced in the solution of boundary-value problems for stress fields with the interface/surface energy effect. The first is the interface/surface constitutive relations, whereas the second is the discontinuity conditions of the stress across the interface, namely, the Young-Laplace equations. These two fundamental equations are used to predict the effective moduli of a composite material with the interface/surface energy effect. Although an infinitesimal strain analysis is employed to establish the governing equations induced by the interface/surface energy, the finite deformation analysis (also known as the large deformation analysis) of a multi-phase hyperelastic medium should be concerned at the beginning, according to reasons as follows:

(1) The mechanical response from the reference configuration to the current configuration should be considered in the study of the mechanical behavior of a composite material or a structure. In this regard, the change of the size and the shape of the interface in the process of the deformation reflect the change of the curvature tensor in the governing equations. In other words, the change of the deformation and the configuration leads to the change of the residual elastic field induced by the interface energy. In essence, hence, this is a finite deformation problem. Furthermore, the interface/surface energy effect is explicitly verified by the change of the residual elastic field due to the change of the configuration.

(2) To develop the governing equations with the interface/surface energy effect, a residual

elastic field induced by the interface energy and the interface stress in the material should be introduced, even though there is no external loading. That is to say, through accounting for the change of the residual elastic field upon the change of the configuration, the effect of the liquid-like interface/surface energy on the effective properties of a composite material can then be included. In this chapter, this type of the interface energy model is emphasized and discussed.

(3) The constitutive relations for the hyperelastic solids with the interface/surface energy effect at the finite deformation have been formulated by Huang and Wang (2006) and Huang and Sun (2007), as introduced in Section 5.7 Appendix A. Moreover, the approximation expressions of the changes of the interface stress and the Young-Laplace equations due to the change of the configuration through the infinitesimal deformation analysis can be found in Section 5.8 Appendix B. These constitutive relations are expressed in terms of the free energy of the interface per unit area at the current configuration, denoted by γ (see Section 5.8 Appendix B for more details).

In addition, composite materials have developed rapidly over the last several decades. They are usually designed to meet the diverse needs for enhancing material performance with advanced thermo-mechanical properties, reduced unit weights, versatile directionality, optimal anisotropy, etc., and for improving material mechanical strengths, elastic moduli, delamination resistance, fracture toughness and fatigue resistance. Reinforcements could be continuous in the form of fibers, or discontinuous in the form of particles or whiskers. Especially, for engineers and scientists, to predict and estimate overall mechanical properties and behaviors of random heterogeneous multi-phase composites are of quite interest in many science, technology, engineering and mathematical disciplines. In general, mechanical properties and behaviors of

composites are dependent on properties of constituent phases and microstructures of inhomogeneities, such as shapes, orientations, aspect ratios, volume fractions, random locations, etc.

The primary objective of the present chapter is to extend the work regarding the interface/surface energy effect on size-dependent effective moduli of a three-phase composite containing two "particles" of the distinct properties with the same size, based on the framework of Ko and Ju (2013) and the methodology of Huang and Sun (2007), to the one regarding the interface/surface energy effect on size-dependent effective transverse elastic moduli of three-phase hybrid fiber-reinforced composites containing two "fibers" of the distinct properties sizes. This model is achieved with consideration to mechanical properties of the constituent phases, volume fractions, spatial distributions of fibers, and direct inter-particle interactions. Specifically, the two inhomogeneity inclusions/phases feature distinct elastic properties and sizes. All fibers are considered non-intersecting, randomly located, and embedded firmly in the matrix with perfect interfaces. Two non-equivalent formulations are considered in detail to derive effective transverse elastic moduli of three-phase composites leading to new higher-order bounds. Hence, a higher-order micromechanical analytical framework is constructed based on the probabilistic spatial distribution of spherical particles, pairwise particle interactions, and the ensemble-volume averaging (homogenization) procedure for three-phase elastic composites.

In this chapter, before the analytical framework for the interface/surface energy effect on the size-dependent effective transverse elastic moduli of a three-phase hybrid fiber-reinforced composite with randomly located and interacting aligned circular fibers of distinct properties and sizes is investigated, the interface/surface energy effect on the size-dependent effective moduli of a two-phase composite consisting of the matrix and randomly distributed aligned circular fibers

is first considered in Section 5.2. Subsequently, in Section 5.3, the effective transverse elastic bulk and shear moduli of a three-phase composite containing randomly located cylindrical fibers featuring distinct elastic properties and sizes are separately formulated based on another framework with consideration to the concepts of probabilistic spatial distribution of spherical particles, pairwise particle interactions, and the ensemble-volume averaging (homogenization) procedure for three-phase elastic composites. Those concepts can be found in Section 5.9 Appendix C and Section 5.10 Appendix D. Specifically, in Section 5.9 Appendix C, the approximate analytical solutions for the direct interactions between two different randomly located elastic fibers embedded in the matrix material are presented, followed by the ensemble-volume averaged eigenstrains through the probabilistic pairwise particle interaction mechanism developed in Section 5.10 Appendix D. Also in Section 5.3, two non-equivalent formulations are considered in detail to derive effective elastic moduli of three-phase composites with no the interface/surface energy effect. Later on, in combination with the results from Section 5.2 and Section 5.3, effective transverse elastic moduli of three-phase hybrid fiber-reinforced composites containing randomly located and interacting aligned circular fibers of distinct elastic properties and sizes with the interface/surface energy effect are analytically derived in Section 5.4. Numerical results and the corresponding discussions are rendered in Section 5.5 to demonstrate the potential of this present model. Specifically, some special cases of the interface/surface energy effect on a three-phase composite containing randomly dispersed fibers of same/distinct properties embedded in an elastic matrix are executed in Section 5.5. Lastly, the conclusion is summarized in Section 5.6.

5.2 Effective Moduli of a Circular Fiber-Filled Composite

Based on the theoretical framework formulated in Section 5.7 Appendix A and Section 5.8 Appendix B, analytical equations used to predict the effective properties of a composite reinforced by spherical particles are developed in this section. In the past, Sharma and Ganti (2004) have formulated the effective bulk moduli of spherical particle-filled composites with the interface effect using the composite spheres assemblage (CSA) model (Hashin, 1962). Duan et al. (2005) derived the effective bulk and shear moduli of such composites using the composite spheres assemblage model, the Mori-Tanaka method (MTM) (Mori and Tanaka, 1973) and the generalized self-consistent method (GSCM) (Christensen and Lo, 1979). The difference between the present work in this chapter and those of Sharma and Ganti (2004) and Duan et al. (2005) is that: at the outset with the finite deformation theory proposed by Huang and Wang (2006), the infinitesimal deformation approximations of the interface/surface constitutive relation and the Young-Laplace equation based on the Lagrangian description in consideration to the change of the configuration are derived. Therefore, the requirement for using the asymmetric interface stress in the Young-Laplace equation is clearly verified and the effect of the residual interface/surface energy γ_0^* on the effective elastic moduli is shown. Assuming that an inhomogeneity incorporated with the interface is regarded as an "equivalent inhomogeneity", for a problem on the inhomogeneity with the interface/surface energy effect, the micromechanical scheme upon the present work for a two-phase or three-phase composite is applicable immediately. In this case, the volume averages of the stress and strain for the "equivalent inhomogeneity" have to be calculated on the matrix side due to the discontinuity of the stress across the interface. Consequently, the explicit derivation of the stress discontinuity conditions

across the interface is significant. The work in this chapter gives an understanding of the interface/surface energy effect by accounting for the change of the interface stress in Eq. (5.54) and Eq. (5.61) due to the change of the configuration, and the interface moduli are directly related to the parameters of the interface energy.

In this section, before the analytical framework for the interface/surface energy effect on the size-dependent effective transverse elastic moduli of a three-phase hybrid fiber-reinforced composite with randomly located and interacting aligned circular fibers of distinct properties and sizes is investigated, the interface/surface energy effect on the size-dependent effective moduli of a two-phase composite consisting of the matrix and randomly distributed aligned circular fibers is first considered.

Consider a two-phase composite composed of the matrix and randomly distributed circular fibers, in which the radius of an inhomogeneity is assumed to be a. The effective stiffness tensor of the composite, $\overline{\mathbf{L}}$, can be described as

$$\overline{\mathbf{L}} = \mathbf{L}_0 + \phi\left(\mathbf{L}_* - \mathbf{L}_0\right) : \mathbf{A}_r \tag{5.1}$$

where $\mathbf{L}_0$ and $\mathbf{L}_*$ are the stiffness tensors of the matrix and the "equivalent inhomogeneity" (namely, an inhomogeneity incorporated with the interface), respectively; ϕ is the volume-fraction sum of all inhomogeneities; $\mathbf{A}_r$ denotes the fourth-order global strain concentration tensor for the r th equivalent inhomogeneity. If the Ju and Chen's scheme (1994a; 1994b; 1994c) is applied, $\mathbf{A}_r$ is given by

$$\mathbf{A}_r \equiv \left(\mathbf{L}_* - \mathbf{L}_0\right)^{-1} \cdot \mathbf{L}_0 \tag{5.2}$$

Assuming all fibers are circular and both matrix and fibers are isotropic elastic, $\mathbf{A}_r$ in Eq. (5.2) can be advanced to express as

$$\mathbf{A}_r = \mathbf{A}^0 : \left[(1 - \phi) \mathbf{I}^{(1)} + \phi \mathbf{A}^0 \right]^{-1} \tag{5.3}$$

where $\mathbf{I}^{(1)}$ is the fourth-order unit tensor; $\mathbf{A}^0$ is the strain concentration tensor of the equivalent inhomogeneity in an infinite matrix corresponding to dilute distribution of inhomogeneities, or simply named the local strain concentration tensor if $\mathbf{A}_r$ is relatively considered as a global strain concentration tensor. It can be found that Eq. (5.3) coincides with the corresponding results obtained by using the Mori-Tanaka method (Benveniste, 1987; Weng, 1990) in the case of this section. Whereas, the corresponding expression of $\mathbf{A}_r$ given by the Eshelby method is written as

$$\mathbf{A}_r = \mathbf{A}^0 \tag{5.4}$$

Eq. (5.4) implies that the interactions among equivalent inhomogeneities may be neglected. In other words, each equivalent inhomogeneity can be treated as if it exists in a homogeneous matrix without the interference by other inhomogeneities.

In addition, if the inhomogeneities are randomly distributed and the composite material is statistically isotropic, then the elastic moduli in Eq. (5.1) can be expressed as

$$\overline{\mathbf{L}} = 3\overline{K} \mathbf{I}_m + 2\overline{\mu} \mathbf{I}_s$$

$$\mathbf{L}_0 = 3K_0 \mathbf{I}_m + 2\mu_0 \mathbf{I}_s \tag{5.5}$$

$$\mathbf{L}_* = 3K_* \mathbf{I}_m + 2\mu_* \mathbf{I}_s$$

where K_0, K_* and $\overline{K}$ are the bulk moduli of the matrix, the equivalent inhomogeneity and the composite, respectively; μ_0, μ_* and $\overline{\mu}$ are the shear moduli of the matrix, the equivalent inhomogeneity and the composite, respectively. It is also known that

$$\mathbf{I}_m = \frac{1}{3}\mathbf{I} \otimes \mathbf{I}, \quad \mathbf{I}_s = \mathbf{I}^{(1)} - \mathbf{I}_m \tag{5.6}$$

Substituting Eq. (5.6) into Eq. (5.5), Eq. (5.1) is further decoupled into

$$\bar{K} = K_0 + \phi(K_* - K_0)A_m$$

$$\bar{\mu} = \mu_0 + \phi(\mu_* - \mu_0)A_s \tag{5.7}$$

where A_m and A_s are the constants in the strain concentration tensors corresponding to the bulk and shear moduli, respectively, as follows,

$$A_m = \frac{K_0}{K_0 + (1-\phi)(K_* - K_0)\omega_m}$$

$$A_s = \frac{\mu_0}{\mu_0 + (1-\phi)(\mu_* - \mu_0)\omega_s} \tag{5.8}$$

and

$$\omega_m = \frac{3K_0}{3K_0 + 4\mu_0}$$

$$\omega_s = \frac{6(K_0 + 2\mu_0)}{5(3K_0 + 4\mu_0)} \tag{5.9}$$

ω_m and ω_s are components of the fourth-order Eshelby inclusion tensor. It is noted that the elastic moduli K_* and μ_* of the equivalent inhomogeneity can be obtained by using Eqs. (5.54) and (5.61) for this purpose. In the case of the spherical inhomogeneity of radius a, $\nabla_{0s}\mathbf{u}$ can be described in terms of the physical components $(u_r, u_\theta, u_\varphi)$ in a spherical polar coordinate system as the following equation,

$$\nabla_{0s}\mathbf{u} = \left(\frac{\partial u_\theta}{r\partial\theta} + \frac{u_r}{r}\right)\mathbf{e}_\theta \otimes \mathbf{e}_\theta + \left(\frac{\partial u_\varphi}{r\partial\theta} + \frac{u_r}{r}\right)\mathbf{e}_\theta \otimes \mathbf{e}_\varphi + \left(\frac{1}{r\sin\theta}\frac{\partial u_\theta}{\partial\varphi} - \cot\theta\frac{u_\varphi}{r}\right)\mathbf{e}_\varphi \otimes \mathbf{e}_\theta$$

$$+ \left(\frac{1}{r\sin\theta}\frac{\partial u_\varphi}{\partial\varphi} + \cot\theta\frac{u_\theta}{r} + \frac{u_r}{r}\right)\mathbf{e}_\varphi \otimes \mathbf{e}_\varphi$$

(5.10)

For the axisymmetric loading, $u_\varphi = 0$, and Eq. (5.10) is also applicable in plane coordinate.

Since u_r and u_θ are not dependent on φ, $\nabla_{0s}\mathbf{u}$ is a symmetric tensor, as shown below,

$$\nabla_{0s}\mathbf{u} = \left(\frac{\partial u_\theta}{r\partial\theta} + \frac{u_r}{r}\right)\mathbf{e}_\theta \otimes \mathbf{e}_\theta + \left(\cot\theta\frac{u_\theta}{r} + \frac{u_r}{r}\right)\mathbf{e}_\varphi \otimes \mathbf{e}_\varphi$$

(5.11)

In the above case, Eq. (5.61) may be replaced by Eq. (5.62). It is noticed that, in the reference configuration, the curvature tensor on the surface of the sphere with radius a is

$$\mathbf{b}_0 = -\frac{1}{a}\mathbf{i}_0$$

(5.12)

Eq. (5.54) can be expressed as

$$[\![\sigma_{rr}]\!]\,|_{r=a} = \frac{1}{a^2}\left(\gamma_0^* + 2\gamma_1^* + \gamma_1\right)\left(2u_r + u_\theta\cot\theta + \frac{\partial u_\theta}{\partial\theta}\right)\Big|_{r=a}$$

$$[\![\sigma_{r\theta}]\!]\,|_{r=a} = \frac{1}{a^2}\left[\left(\gamma_0^* + \gamma_1^*\right)u_\theta + \left(\gamma_1^* + \gamma_1\right)\left(u_\theta\cot^2\theta - \frac{\partial u_\theta}{\partial\theta}\cot\theta - \frac{\partial^2 u_\theta}{\partial\theta^2}\right)\Big|_{r=a}\right]$$

(5.13)

$$-\frac{1}{a^2}\left(\left(\gamma_0^* + 2\gamma_1^* + \gamma_1\right)\frac{\partial u_r}{\partial\theta}\right)\Big|_{r=a}$$

where the symbol $[\![\cdot]\!]$ denotes the discontinuity of a quantity across the interface. In order to compute the bulk modulus K_* of the equivalent inhomogeneity, suppose that a circular fiber is embedded in an infinite medium under the hydrostatic loading with the remote strain as

$$\mathbf{E}^\infty = \frac{1}{3}E_m\mathbf{I}$$

(5.14)

158

In this case, the displacement and stress fields in the inhomogeneity and matrix are given by

$$u_r^i = F_i r + \frac{G_i}{r^2}$$

$$\sigma_{rr}^i = 3K_i F_i - 4\mu_i \frac{G_i}{r^3}$$

(5.15)

The superscript $i = 1, 0$ denotes the quantities of the inhomogeneity and matrix, respectively. F_1, F_0, G_1 and G_0 are constants to be determined. In addition to the displacement continuity condition at the interface $r = a$, the elastic solution needs to satisfy the stress discontinuity condition in Eq. (5.13), namely,

$$\left(\sigma_{rr}^0 - \sigma_{rr}^1\right)|_{r=a} = \frac{2}{a^2}\left(\gamma_0^* + 2\gamma_1^* + \gamma_1\right)\left(u_r |_{r=a}\right)$$

(5.16)

According to the above conditions, the non-singular condition at the origin and the condition at infinity, the constants in Eq. (5.15) can be determined. Therefore, the (secant) bulk modulus K_* of the equivalent inhomogeneity can be obtained by

$$K_* = \frac{tr\langle \boldsymbol{\sigma}_* \rangle}{3tr\langle \boldsymbol{\varepsilon}_* \rangle}|_{r=a} = K_1 + \frac{2\left(\gamma_0^* + 2\gamma_1^* + \gamma_1\right)}{3a}$$

(5.17)

where $\langle \boldsymbol{\sigma}_* \rangle$ and $\langle \boldsymbol{\varepsilon}_* \rangle$ represent the volume averages of the stress and strain of the equivalent inhomogeneity that includes the inhomogeneity and the interface, respectively. $\gamma_0^* = \gamma_0 + \gamma_1 + \gamma_2$, $\gamma_1^* = \gamma_1 + 2\gamma_2 + \gamma_{11} + 2\gamma_{12} + \gamma_{22}$, and γ_0^* and γ_1^* form the residual interface/surface energy. Further, it is found that there are at least three independent material parameters γ_0^*, γ_1^* and γ_1 required in the above equation. About the detailed description of the interface/surface free energy γ, it can refer to Section 5.8 Appendix B.

Moreover, the shear modulus μ_* of the equivalent inhomogeneity can be found by

159

imposing a pure deviatoric remote strain at infinity as,

$$\mathbf{E}^{\infty} = E_e \left[\mathbf{e}_3 \otimes \mathbf{e}_3 - \frac{1}{2} \left(\mathbf{e}_1 \otimes \mathbf{e}_1 + \mathbf{e}_2 \otimes \mathbf{e}_2 \right) \right] \tag{5.18}$$

where $\mathbf{e}_1$, $\mathbf{e}_2$ and $\mathbf{e}_3$ are the base vectors in a rectangular Cartesian coordinate system. From the solution of Lur'e (1964), the displacement and stress fields in the inhomogeneity and matrix can be written by

$$u_r^1 = \left(12 v_1 A r^3 + 2 B r \right) P_2 \left(\cos \theta \right)$$

$$u_r^0 = \left(E_e r + \frac{2 \left(5 - 4 v_0 \right)}{r^2} C - \frac{3}{r^4} D \right) P_2 \left(\cos \theta \right)$$

$$u_\theta^1 = \left[\left(7 - 4 v_1 \right) A r^3 + B r \right] \frac{d P_2 \left(\cos \theta \right)}{d \theta}$$

$$u_\theta^0 = \left[\frac{1}{2} E_e r + \frac{\left(2 - 4 v_0 \right)}{r^2} C - \frac{1}{r^4} D \right] \frac{d P_2 \left(\cos \theta \right)}{d \theta}$$

$$\sigma_{rr}^1 = 2 \mu_1 \left(-6 v_1 A r^2 + 2 B \right) P_2 \left(\cos \theta \right)$$

$$\sigma_{rr}^0 = 2 \mu_0 \left[E_e - \frac{4 \left(5 - v_0 \right)}{r^3} C + \frac{12}{r^5} D \right] P_2 \left(\cos \theta \right)$$

$$\sigma_{r\theta}^1 = 2 \mu_1 \left[\left(7 + 2 v_1 \right) A r^2 + B \right] \frac{d P_2 \left(\cos \theta \right)}{d \theta} \tag{5.19}$$

$$\sigma_{r\theta}^0 = 2 \mu_0 \left[\frac{1}{2} E_e + \frac{2 \left(1 + v_0 \right)}{r^3} C - \frac{4}{r^5} D \right] \frac{d P_2 \left(\cos \theta \right)}{d \theta}$$

The superscripts 1 and 0 denote the quantities of the inhomogeneity and matrix, respectively. v_1 and v_0 are Poisson's ratios of the inhomogeneity and matrix, respectively. $P_2 \left(\cos \theta \right)$ is the

160

second-order Legendre polynomial. A, B, C and D are constants to be determined. Similarly, in addition to the displacement continuity condition at the interface $r=a$, the elastic solution needs to satisfy the stress discontinuity condition in Eq. (5.13). Then, the unknown constants can be determined in a way similar to that for the bulk modulus. The shear modulus μ_* of the equivalent inhomogeneity can be calculated by

$$\mu_* = \frac{\langle \sigma_* \rangle_e}{3\langle \varepsilon_* \rangle_e}\Big|_{r=a} = \frac{\mu_1 L + L_0 + L_1 + L_2}{L + L_3}$$

$$L = 10\left[4\mu_0\left(7-10\nu_1\right)+\mu_1\left(7+5\nu_1\right)\right]$$

$$L_0 = 5\left[4\mu_0\left(10\nu_1-7\right)+3\mu_1\left(7-15\nu_1\right)\right]\frac{\left(\gamma_0^*-2\gamma_1-\gamma_1^*\right)}{a}$$

$$L_1 = \left[12\mu_0\left(10\nu_1-7\right)+5\mu_1\left(91-139\nu_1\right)\right]\frac{\left(\gamma_1+\gamma_1^*\right)}{a}$$

$$L_2 = \frac{10\left(10\nu_1-7\right)\left[\left(\gamma_0^*-2\gamma_1-\gamma_1^*\right)^2+3\left(\gamma_1+\gamma_1^*\right)^2+4\left(\gamma_0^*-2\gamma_1-\gamma_1^*\right)\left(\gamma_1+\gamma_1^*\right)\right]}{a^2}$$

$$L_3 = \frac{-4\left(10\nu_1-7\right)\left(5\gamma_0^*+7\gamma_1+12\gamma_1^*\right)}{a}$$

(5.20)

where $\langle \sigma_* \rangle_e$ and $\langle \varepsilon_* \rangle_e$ are the effective average stress and the effective average strain of the equivalent inhomogeneity, respectively. It can be easily found that K_* and μ_* are not only functions of the elastic moduli of the inhomogeneity, such as K_1 and μ_1, but also functions of the size of particles, a.

In order to simplify the discussion, the expression of the interface/surface free energy can be linearized. Therefore, γ can be expanded as:

$$\gamma = \gamma_0 + \gamma_1 (J_1 - 2) + \gamma_2 (J_2 - 1) + \frac{1}{2}\gamma_{11}(J_1 - 2)^2 + \gamma_{12}(J_1 - 2)(J_2 - 1) + \frac{1}{2}\gamma_{22}(J_2 - 1)^2 + \cdots$$

$$\gamma_1 = \frac{\partial \gamma}{\partial J_1}\Big|_{J_1=2, J_2=1} \quad , \quad \gamma_2 = \frac{\partial \gamma}{\partial J_2}\Big|_{J_1=2, J_2=1} \tag{5.21}$$

where γ_0, γ_1, γ_2 represent the intrinsic physical properties of the interface, and they are, and should be determined by the joining materials and the adhering condition. $\gamma_0 = \gamma(2,1)$ is equivalent to the interface/surface energy of a liquid-like material and hence reflects the nature of liquids, whereas γ_1 and γ_2 reflect the nature of solids; $J_1 - 2$ and $J_2 - 1$ are first-order small quantities.

Moreover, the expression of the (secant) bulk modulus K_* of the equivalent inhomogeneity in Eq. (5.17) is derived for identical circular fibers of the same property. Therefore, it is rewritten in a general form for two different circular fibers of distinct properties and sizes as follows:

$$K_{*m} = \frac{tr\langle \boldsymbol{\sigma}_* \rangle_m}{3 tr\langle \boldsymbol{\varepsilon}_* \rangle_m}\Big|_{r=a} = K_m + \frac{2\left(\gamma_0^* + 2\gamma_1^* + \gamma_1\right)}{3a_m}; \quad m = 1,2 \tag{5.22}$$

where $\langle \boldsymbol{\sigma}_* \rangle_m$ and $\langle \boldsymbol{\varepsilon}_* \rangle_m$ represent the area averages of the stress and strain of two distinct equivalent inhomogeneities and each equivalent inhomogeneity includes the inhomogeneity and the interface, respectively. $\gamma_0^* = \gamma_0 + \gamma_1 + \gamma_2$, $\gamma_1^* = \gamma_1 + 2\gamma_2 + \gamma_{11} + 2\gamma_{12} + \gamma_{22}$, and γ_0^* and γ_1^* form the residual interface/surface energy. Further, it is found that there are at least three independent material parameters γ_0^*, γ_1^* and γ_1 required in the above equation. Here, the property of the interface/surface free energy γ is assumed to be the same and the interface/surface surrounds two distinct fibers.

Similarly, the shear modulus μ_{*m} in Eq. (5.20) of the equivalent inhomogeneity for two distinct fibers can be obtained as:

$$\mu_{*m} = \frac{\langle \sigma_* \rangle_{em}}{3 \langle \varepsilon_* \rangle_{em}} \Big|_{r=a} = \frac{\mu_m L_m + L_{0m} + L_{1m} + L_{2m}}{L_m + L_{3m}}; \quad m = 1, 2$$

$$L_m = 10 \left[4\mu_0 (7 - 10\nu_1) + \mu_1 (7 + 5\nu_1) \right]$$

$$L_{0m} = 5 \left[4\mu_0 (10\nu_1 - 7) + 3\mu_1 (7 - 15\nu_1) \right] \frac{\left(\gamma_0^* - 2\gamma_1 - \gamma_1^* \right)}{a_m}$$

$$L_{1m} = \left[12\mu_0 (10\nu_1 - 7) + 5\mu_1 (91 - 139\nu_1) \right] \frac{\left(\gamma_1 + \gamma_1^* \right)}{a_m}$$

$$L_{2m} = \frac{10(10\nu_1 - 7) \left[\left(\gamma_0^* - 2\gamma_1 - \gamma_1^* \right)^2 + 3\left(\gamma_1 + \gamma_1^* \right)^2 + 4\left(\gamma_0^* - 2\gamma_1 - \gamma_1^* \right)\left(\gamma_1 + \gamma_1^* \right) \right]}{a_m^2}$$

$$L_{3m} = \frac{-4(10\nu_1 - 7)\left(5\gamma_0^* + 7\gamma_1 + 12\gamma_1^* \right)}{a_m}$$

(5.23)

where $\langle \sigma_* \rangle_{em}$ and $\langle \varepsilon_* \rangle_{em}$ are the effective average stress and the effective average strain of the equivalent inhomogeneity, respectively. For each equivalent inhomogeneity ($m = 1, 2$), it can be easily found that K_{*m} and μ_{*m} are not only functions of the elastic moduli of the inhomogeneity, such as K_m and μ_m, but also the functions of the size (radius) of fibers, a_m.

5.3 Effective Transverse Elastic Moduli of Three-phase Composites Containing Unidirectionally Aligned Circular Fibers with Distinct Elastic Properties and Sizes

163

(with No Interface Energy Effect)

In this section, the effective transverse elastic moduli of composites containing many randomly dispersed unidirectionally aligned fibers of distinct elastic properties and sizes in three-phase composites (with no interface/surface energy effect), based on the theoretical framework formulated in Section 5.9 Appendix C and Section 5.10 Appendix D, are derived. Specifically, the probabilistic ensemble-area averaged pairwise local interaction solution for $\left\langle \overline{\boldsymbol{\varepsilon}}^{*}_{(i)} \right\rangle$ and other ensemble-area averaged field equations are utilized. In what follows, angle brackets for the ensemble-area operators will be dropped for the purpose of compactness.

According to Ju and Chen (1994a) and Zhao et al. (1989), the relations governing the ensemble-area averaged stress $\overline{\boldsymbol{\sigma}}$, the averaged strain $\overline{\boldsymbol{\varepsilon}}$, the uniform remote strain $\boldsymbol{\varepsilon}^0$, and the averaged eigenstrain $\overline{\boldsymbol{\varepsilon}}^{*}_{(i)}$ take the following form:

$$\overline{\boldsymbol{\sigma}} = \mathbb{C}_0 : \left(\overline{\boldsymbol{\varepsilon}} - \sum_{i=1}^{2} \phi^{(i)} \, \overline{\boldsymbol{\varepsilon}}^{*}_{(i)} \right) \tag{5.24}$$

$$\overline{\boldsymbol{\varepsilon}} = \boldsymbol{\varepsilon}^0 + \sum_{i=1}^{2} \phi^{(i)} \mathbb{S} : \overline{\boldsymbol{\varepsilon}}^{*}_{(i)} \tag{5.25}$$

$$\begin{aligned}
\overline{\boldsymbol{\sigma}} = \overline{\mathbb{C}} : \overline{\boldsymbol{\varepsilon}} &= \left[\mathbb{C}_0 \cdot \left(\mathbb{I} - \phi^{(1)} \boldsymbol{\Gamma}^{\mathrm{II}}_{(1)} \left(\underset{\sim}{\mathbb{U}}^{\mathrm{II}}_{(1)} \right)^{-1} - \phi^{(2)} \boldsymbol{\Gamma}^{\mathrm{II}}_{(2)} \left(\underset{\sim}{\mathbb{U}}^{\mathrm{II}}_{(2)} \right)^{-1} \right) \right] : \overline{\boldsymbol{\varepsilon}} \\
&= \left[\overline{\lambda} \delta_{ij} \delta_{kl} + \overline{\mu} \left(\delta_{ik} \delta_{jl} + \delta_{il} \delta_{jk} \right) \right] : \overline{\varepsilon}_{kl}; \quad i,j,k,l = 1,2
\end{aligned} \tag{5.26}$$

where the following relations are employed to derive the effective stiffness $\overline{\mathbb{C}}$:

$$\overline{\boldsymbol{\varepsilon}} = \underset{\sim}{\mathbb{U}}^{\mathrm{II}}_{(1)} : \overline{\boldsymbol{\varepsilon}}^{*0}_{(1)} = \left[-\mathbf{A}_1 - \mathbb{S} + \phi^{(1)} \mathbb{S} \cdot \boldsymbol{\Gamma}^{\mathrm{II}}_{(1)} + \phi^{(2)} \mathbb{S} \cdot \boldsymbol{\Gamma}^{\mathrm{II}}_{(2)} \left(\mathbf{A}_2 + \mathbb{S} \right)^{-1} \left(\mathbf{A}_1 + \mathbb{S} \right) \right] : \overline{\boldsymbol{\varepsilon}}^{*0}_{(1)} \tag{5.27}$$

$$\overline{\boldsymbol{\varepsilon}} = \underset{\sim}{\mathbb{U}}^{\mathrm{II}}_{(2)} : \overline{\boldsymbol{\varepsilon}}^{*0}_{(2)} = \left[-\mathbf{A}_2 - \mathbb{S} + \phi^{(1)} \mathbb{S} \cdot \boldsymbol{\Gamma}^{\mathrm{II}}_{(1)} \left(\mathbf{A}_2 + \mathbb{S} \right) \left(\mathbf{A}_1 + \mathbb{S} \right)^{-1} + \phi^{(2)} \mathbb{S} \cdot \boldsymbol{\Gamma}^{\mathrm{II}}_{(2)} \right] : \overline{\boldsymbol{\varepsilon}}^{*0}_{(2)} \tag{5.28}$$

Since all the fourth-rank tensors on the right-hand side of Eq. (5.26) are isotropic in two-dimension, the effective stiffness tensor $\overline{C}$ for these three-phase composites is also isotropic in 2D (or equivalently transversely isotropic in three-dimension). For the two-phase composites, simply let the two inhomogeneity phases be of the same elastic properties and sizes as within the proposed framework for three-phase composites. It is noted that based on the Eqs. (5.117)–(5.128) and Eqs. (5.143)–(5.156) in the Formulation I for the two-phase composites, it can be proved that $\gamma_1 = \gamma_{11}^{\text{I}} = \gamma_{12}^{\text{I}}$ and $\gamma_2 = \gamma_{21}^{\text{I}} = \gamma_{22}^{\text{I}}$.

In what follows, two different radial distribution functions will be considered, that is, (1) the uniform radial distribution function $g(\hat{r}) = 1$, as shown in Section 5.10.1; and (2) the general radial distribution function $g(\hat{r}) \neq 1$, as shown in Section 5.10.2. Under each radial distribution function, two non-equivalent formulations are considered in detail to predict the effective transverse elastic moduli of three-phase composites with no interface/surface energy effect, that is, "Formulation II" and "Formulation I". The following notations are adopted: the superscript "U", "G", "II", and "I" stand for the uniform radial distribution function, the general radial distribution function, Formulation II and Formulation I, respectively.

5.3.1 Uniform radial distribution function (URDF)

Formulation II: The effective plane-strain bulk modulus $\overline{K}_{\text{T}}^{\text{UII}}$ and the shear modulus $\overline{\mu}_{\text{T}}^{\text{UII}}$ of three-phase composites with no interface/surface energy effect can be explicitly evaluated as

$$\overline{K}_{\text{T}}^{\text{UII}} =$$
$$K_0 \left(1 + \frac{8(1-\nu_0)\left[(\alpha_2 + \beta_2)(\gamma_{11}^{\text{UII}} + \gamma_{21}^{\text{UII}})\phi^{(1)} + (\alpha_1 + \beta_1)(\gamma_{12}^{\text{UII}} + \gamma_{22}^{\text{UII}})\phi^{(2)}\right]}{(\alpha_1 + \beta_1)(\alpha_2 + \beta_2) - \left[4(\alpha_2 + \beta_2)(\gamma_{11}^{\text{UII}} + \gamma_{21}^{\text{UII}})\phi^{(1)} + 4(\alpha_1 + \beta_1)(\gamma_{12}^{\text{UII}} + \gamma_{22}^{\text{UII}})\phi^{(2)}\right]} \right) \quad (5.29)$$

$$\bar{\mu}_{\mathrm{T}}^{\mathrm{UII}} = \mu_0 \left(1 + \frac{8\left(1-\nu_0\right)\left(\phi^{(1)}\beta_2\gamma_{21}^{\mathrm{UII}} + \phi^{(2)}\beta_1\gamma_{22}^{\mathrm{UII}}\right)}{\beta_1\beta_2 - 2\left(3-4\nu_0\right)\left(\phi^{(1)}\beta_2\gamma_{21}^{\mathrm{UII}} + \phi^{(2)}\beta_1\gamma_{22}^{\mathrm{UII}}\right)} \right) \tag{5.30}$$

where $\phi^{(2)}$ and $\phi^{(1)}$ are the fiber volume fractions of phase 2 and phase 1, respectively. It is noted that the definition of the effective plane-strain bulk modulus is $\bar{K}_{\mathrm{T}} \equiv \bar{\lambda} + \bar{\mu}_{\mathrm{T}}$ where $\bar{\lambda}$ and $\bar{\mu}_{\mathrm{T}}$ are the effective Lamé constants.

5.3.2 General radial distribution function (GRDF)

Formulation II: The effective plane-strain bulk modulus $\bar{K}_{\mathrm{T}}^{\mathrm{GII}}$ and the shear modulus $\bar{\mu}_{\mathrm{T}}^{\mathrm{GII}}$ of three-phase composites with no interface/surface energy effect can be explicitly evaluated as

$$\bar{K}_{\mathrm{T}}^{\mathrm{GII}} =$$
$$K_0 \left(1 + \frac{8\left(1-\nu_0\right)\left[\left(\alpha_2+\beta_2\right)\left(\gamma_{11}^{\mathrm{GII}}+\gamma_{21}^{\mathrm{GII}}\right)\phi^{(1)} + \left(\alpha_1+\beta_1\right)\left(\gamma_{12}^{\mathrm{GII}}+\gamma_{22}^{\mathrm{GII}}\right)\phi^{(2)}\right]}{\left(\alpha_1+\beta_1\right)\left(\alpha_2+\beta_2\right) - \left[4\left(\alpha_2+\beta_2\right)\left(\gamma_{11}^{\mathrm{GII}}+\gamma_{21}^{\mathrm{GII}}\right)\phi^{(1)} + 4\left(\alpha_1+\beta_1\right)\left(\gamma_{12}^{\mathrm{GII}}+\gamma_{22}^{\mathrm{GII}}\right)\phi^{(2)}\right]} \right) \tag{5.31}$$

$$\bar{\mu}_{\mathrm{T}}^{\mathrm{GII}} = \mu_0 \left(1 + \frac{8\left(1-\nu_0\right)\left(\phi^{(1)}\beta_2\gamma_{21}^{\mathrm{GII}} + \phi^{(2)}\beta_1\gamma_{22}^{\mathrm{GII}}\right)}{\beta_1\beta_2 - 2\left(3-4\nu_0\right)\left(\phi^{(1)}\beta_2\gamma_{21}^{\mathrm{GII}} + \phi^{(2)}\beta_1\gamma_{22}^{\mathrm{GII}}\right)} \right) \tag{5.32}$$

To obtain Formulation I, simply replace the superscript "II" by "I" in Formulation II.

5.4 Effective Transverse Elastic Moduli of Three-phase Composites Containing Unidirectionally Aligned Circular Fibers with Distinct Elastic Properties and Sizes with Interface Energy Effect

In combination with the results from Section 5.2 and Section 5.3, effective transverse elastic moduli of three-phase hybrid fiber-reinforced composites containing randomly located and interacting aligned circular fibers of distinct elastic properties and sizes with the interface/surface energy effect are analytically derived in this section. In what follows, two different radial distribution functions will be considered, that is, (1) the uniform radial distribution function $g(\hat{r})=1$, as shown in Section 5.10.1; and (2) the general radial distribution function $g(\hat{r})\neq1$, as shown in Section 5.10.2. Under each radial distribution function, two non-equivalent formulations are considered in detail to predict the effective transverse elastic moduli of three-phase composites with no interface/surface energy effect, that is, "Formulation II" and "Formulation I". The following notations are adopted: the superscript "U," "G," "II," and "I" stand for the uniform radial distribution function, the general radial distribution function, Formulation II and Formulation I, respectively.

Moreover, required parameters regarding the interface/surface energy effect can be recast as follows:

$$\lambda = \frac{a_1}{a_2}$$

$$\eta = \frac{a_2}{a_1} = \frac{1}{\lambda}$$

(5.33)

$$\alpha_{*1} = 4(1-v_0)\left[\frac{k_0}{k_{*1}-k_0} - \frac{\mu_0}{\mu_{*1}-\mu_0}\right] + (4v_0-1)$$

$$\alpha_{*2} = 4(1-v_0)\left[\frac{k_0}{k_{*2}-k_0} - \frac{\mu_0}{\mu_{*2}-\mu_0}\right] + (4v_0-1)$$

$$\beta_{*1} = 4(1-v_0)\frac{\mu_0}{\mu_{*1}-\mu_0} + (3-4v_0)$$

$$\beta_{*2} = 4(1-v_0)\frac{\mu_0}{\mu_{*2}-\mu_0} + (3-4v_0)$$

(5.34)

167

where k_0, k_{*m} and μ_0, μ_{*m} ($m = 1, 2$) denote the bulk and shear moduli of the matrix and the m-phase equivalent inhomogeneity, respectively. k_{*m} and μ_{*m} are defined in Eq. (5.22) and Eq. (5.23).

5.4.1 Uniform radial distribution function (URDF)

Formulation II: The effective plane-strain bulk modulus $\bar{K}^{\mathrm{UII}}$ and the shear modulus $\bar{\mu}^{\mathrm{UII}}$ of three-phase composites with interface/surface energy effect can be explicitly evaluated as

$$\bar{K}^{\mathrm{UII}} =$$
$$K_0 \left\{ 1 + \frac{8(1-\nu_0)\left[(\alpha_{*2} + \beta_{*2})(\gamma_{*11}^{\mathrm{UII}} + \gamma_{*21}^{\mathrm{UII}})\phi^{(1)} + (\alpha_{*1} + \beta_{*1})(\gamma_{*12}^{\mathrm{UII}} + \gamma_{*22}^{\mathrm{UII}})\phi^{(2)}\right]}{(\alpha_{*1} + \beta_{*1})(\alpha_{*2} + \beta_{*2}) - \left[4(\alpha_{*2} + \beta_{*2})(\gamma_{*11}^{\mathrm{UII}} + \gamma_{*21}^{\mathrm{UII}})\phi^{(1)} + 4(\alpha_{*1} + \beta_{*1})(\gamma_{*12}^{\mathrm{UII}} + \gamma_{*22}^{\mathrm{UII}})\phi^{(2)}\right]} \right\} \quad (5.35)$$

$$K_0 = \frac{2(1+\nu_0)}{3(1-2\nu_0)}$$

$$\bar{\mu}^{\mathrm{UII}} = \mu_0 \left(1 + \frac{8(1-\nu_0)\left(\phi^{(1)}\beta_{*2}\gamma_{*21}^{\mathrm{UII}} + \phi^{(2)}\beta_{*1}\gamma_{*22}^{\mathrm{UII}}\right)}{\beta_{*1}\beta_{*2} - 2(3-4\nu_0)\left(\phi^{(1)}\beta_{*2}\gamma_{*21}^{\mathrm{UII}} + \phi^{(2)}\beta_{*1}\gamma_{*22}^{\mathrm{UII}}\right)} \right) \quad (5.36)$$

where $\phi^{(2)}$ and $\phi^{(1)}$ are the fiber volume fractions of phase 2 and phase 1, respectively. In addition, the parameters for Eqs. (5.35) and (5.36), such as $\gamma_{*11}^{\mathrm{UII}}$, $\gamma_{*21}^{\mathrm{UII}}$, $\gamma_{*12}^{\mathrm{UII}}$, $\gamma_{*22}^{\mathrm{UII}}$, etc., can be re-derived by substituting the above required parameters, Eqs (5.33)-(5.34), into the corresponding equations introduced in Section 5.10 Appendix D, they are then established.

5.4.2 General radial distribution function (GRDF)

Formulation II: The effective plane-strain bulk modulus $\bar{K}^{\mathrm{GII}}$ and the shear modulus $\bar{\mu}^{\mathrm{GII}}$ of

three-phase composites with interface/surface energy effect can be explicitly evaluated as

$$\bar{K}^{\mathrm{GII}} =$$
$$K_0 \Bigg\{ 1 +$$
$$\frac{8(1-v_0)\left[(\alpha_{*2}+\beta_{*2})(\gamma_{*11}^{\mathrm{GII}}+\gamma_{*21}^{\mathrm{GII}})\phi^{(1)} + (\alpha_{*1}+\beta_{*1})(\gamma_{*12}^{\mathrm{GII}}+\gamma_{*22}^{\mathrm{GII}})\phi^{(2)} \right]}{(\alpha_{*1}+\beta_{*1})(\alpha_{*2}+\beta_{*2}) - \left[4(\alpha_{*2}+\beta_{*2})(\gamma_{*11}^{\mathrm{GII}}+\gamma_{*21}^{\mathrm{GII}})\phi^{(1)} + 4(\alpha_{*1}+\beta_{*1})(\gamma_{*12}^{\mathrm{GII}}+\gamma_{*22}^{\mathrm{GII}})\phi^{(2)} \right]} \Bigg\} \quad (5.37)$$

$$K_0 = \frac{2(1+v_0)}{3(1-2v_0)}$$

$$\bar{\mu}^{\mathrm{GII}} = \mu_0 \left(1 + \frac{8(1-v_0)\left(\phi^{(1)}\beta_{*2}\gamma_{*21}^{\mathrm{GII}} + \phi^{(2)}\beta_{*1}\gamma_{*22}^{\mathrm{GII}} \right)}{\beta_{*1}\beta_{*2} - 2(3-4v_0)\left(\phi^{(1)}\beta_{*2}\gamma_{*21}^{\mathrm{GII}} + \phi^{(2)}\beta_{*1}\gamma_{*22}^{\mathrm{GII}} \right)} \right) \quad (5.38)$$

The parameters for Eqs. (5.37) and (5.38), such as $\gamma_{*11}^{\mathrm{GIII}}$, $\gamma_{*21}^{\mathrm{GII}}$, $\gamma_{*12}^{\mathrm{GII}}$, $\gamma_{*22}^{\mathrm{GII}}$, etc., can be re-derived by substituting the above required parameters, Eqs (5.33)-(5.34), into the corresponding equations introduced in Section 5.10 Appendix D. To obtain Formulation I, simply replace the superscript "II" by "I" in Formulation II.

5.5 Some numerical simulations

In the special event, suppose the URDF and Formulation II are adopted, that a matrix material contains identical fibers (i.e., $a_1 = a_2$, $\mu_1 = \mu_2$, $K_1 = K_2$), from Eq. (5.35) and Eq. (5.36), the effective moduli of the two equivalent inhomogeneities are the same, i.e., $K_{*1} = K_{*2}$, $\mu_{*1} = \mu_{*2}$. In the meanwhile, substituting the obtained K_{*m} in Eq. (5.17) and μ_{*m} in Eq. (5.20) into Eq. (5.34), the effective plane-strain bulk modulus $\bar{K}$ and the shear modulus $\bar{\mu}$ of

three-phase composites with interface/surface energy effect in Eqs. (5.35) and (5.36) reduce to

$$\bar{K} = \frac{1}{3}\left[\frac{12K_0\mu_0(1-\phi)+3K_1(3K_0+4\mu_0\phi)+2(3K_0+4\mu_0\phi)(\gamma_0^*+2\gamma_1^*+\gamma_1)/a}{3K_0\phi+4\mu_0+3K_1(1-\phi)+2(1-\phi)(\gamma_0^*+2\gamma_1^*+\gamma_1)/a}\right] \qquad (5.39)$$

$$\bar{\mu} = \mu_0 + \frac{15\mu_0\phi(1-v_0)\left[(\mu_1-\mu_0)L-\mu_0L_3+L_0+L_1+L_2\right]}{(1-\phi)\left[LL_4+10(L_5+L_6)+2(4-5v_0)L_2\right]+15\mu_0\phi(1-v_0)(L+L_3)}$$

$$L_4 = 2\mu_1(4-5v_0)+\mu_0(7-5v_0)$$

$$\qquad\qquad\qquad\qquad\qquad\qquad\qquad\qquad\qquad\qquad\qquad (5.40)$$

$$L_5 = \left[2\mu_0(7-10v_1)(5v_0-1)-3\mu_1(15v_1-7)(4-5v_0)\right](\gamma_0^*-2\gamma_1+\gamma_1^*)/a$$

$$L_6 = \left[2\mu_0(7-10v_1)(19-11v_0)+\mu_1(91-139v_1)(4-5v_0)\right](\gamma_1+\gamma_1^*)/a$$

Here, ϕ denotes the total particle volume fraction.

Two special cases resulting from Eqs. (5.39) and (5.40) are discussed in this section. The first special case is a porous material containing spherical nano-voids, and the corresponding effective bulk and shear moduli of the composite with the interface/surface energy effect can be obtained by substituting $K_1 = 0$ and $\mu_1 = 0$ into Eqs. (5.39) and (5.40), as follows,

$$\bar{K}_{void} = \frac{1}{3}\left[\frac{12K_0\mu_0(1-\phi)+2(3K_0+4\mu_0\phi)n_3}{3K_0\phi+4\mu_0+2(1-\phi)n_3}\right] \qquad (5.41)$$

170

$$\bar{\mu}_{void} = \frac{\mu_0}{2} \left[\frac{4(1-\phi)m_1\mu_0^2 + 4(2m_2 - \phi m_1)\mu_0 n_1 + 42m_4\mu_0 n_2 + (m_1\phi + 2m_3)n_2 n_3}{2(2\phi m_3 + m_1)\mu_0^2 + 4(\phi m_3 + m_2)\mu_0 n_1 + 21m_4\mu_0 n_2 + (1-\phi)m_3 n_2 n_3} \right]$$

$$m_1 = 7 - 5v_0$$

$$m_2 = 5 - 4v_0$$

$$m_3 = 4 - 5v_0$$

$$m_4 = 1 - v_0$$

$$n_1 = \frac{(\gamma_0^* + \gamma_1^*)}{a}$$

$$n_2 = \frac{(\gamma_1 - \gamma_0^*)}{a} \tag{5.42}$$

$$n_3 = \frac{(\gamma_0^* + 2\gamma_1^* + \gamma_1)}{a}$$

The second special case is a composite containing liquid-like circular inhomogeneities, namely, $\gamma_0^* = \gamma_0$, $\gamma_1^* = \gamma_1 = 0$, then the effective moduli of the composite with the interface/surface energy effect are

$$\bar{K}_{(\gamma_0)} = \frac{1}{3} \left[\frac{12K_0\mu_0(1-\phi) + 3K_1(3K_0 + 4\mu_0\phi) + 2(3K_0 + 4\mu_0\phi)\gamma_0/a}{3K_0\phi + 4\mu_0 + 3K_1(1-\phi) + 2(1-\phi)\gamma_0/a} \right] \tag{5.43}$$

$$\bar{\mu}_{(\gamma_0)} = \mu_0 + \frac{15\mu_0\phi(1-\nu_0)\left[(\mu_1-\mu_0)L - \mu_0 L_3^* + L_0 + L_1 + L_2^*\right]}{(1-\phi)\left[LL_4 + 10L_5 + 2(4-5\nu_0)L_2^*\right] + 15\mu_0\phi(1-\nu_0)(L+L_3^*)}$$

$$L_2^* = \frac{10(10\nu_1-7)\gamma_0^2}{a^2} \tag{5.44}$$

$$L_3^* = \frac{-20(10\nu_1-7)\gamma_0}{a}$$

From Eqs. (5.43) and (5.44), it is obviously seen that the interface/surface energy γ_0 affects the effective moduli of the composite.

Further, the effective bulk and shear moduli of the composite filled with spherical particles can be calculated by simply substituting $\gamma_0^* = 0$ into Eqs. (5.39) and (5.40), as shown in the following equations,

$$\bar{K} = \bar{K}_0 = \frac{1}{3}\left[\frac{12K_0\mu_0(1-f) + 3K_1(3K_0 + 4\mu_0 f)}{3K_0 f + 4\mu_0 + 3K_1(1-f)}\right] \tag{5.45}$$

$$\bar{\mu} = \bar{\mu}_0 = \mu_0 + \frac{\mu_0 f(1-\nu_0)(\mu_1-\mu_0)L}{\mu_0 fL} \tag{5.46}$$

$$L = 10\left[4\mu_0(7-10\nu_1) + \mu_1(7+5\nu_1)\right]$$

It is obvious that the effective moduli obtained by this way are not influenced by the residual interface energy, γ_0^*.

The following figures from the special cases of the porous material containing fiber-shape nano-voids, and the corresponding effective bulk and shear moduli of the composite with the interface/surface energy effect can be obtained by substituting $K_1 = K_2 = 0$ and $\mu_1 = \mu_2 = 0$ into Eqs. (5.39) and (5.40). Assume that the composite contains the liquid-like spherical

inhomogeneities, namely, $\gamma_0^* = \gamma_0$, $\gamma_1^* = \gamma_1 = 0$, $\nu_0 = 0$. Suppose that the bulk modulus of the matrix material is $K_0 = 2.5\,\text{GPa}$, and the shear modulus is $\mu_0 = 0.5\,\text{GPa}$. The surface is assumed to be liquid-like with a interface/surface energy $\gamma_0 = 0.05\,\text{J/m}^2$. The volume fractions of the sum of all voids are assumed to be $\phi = 20\%$ and $\phi = 30\%$, respectively. Accordingly, the variations of the normalized effective bulk and shear moduli for polypropylene containing fiber-shape voids are illustrated in **Figure 5.1** and **Figure 5.2**. In the figures, $\bar{K}_0$ and $\bar{\mu}_0$ are the effective bulk and shear moduli of the material without the interface/surface energy effect. From these two figures, it is found that the interface/surface effect decreases with the increase of the size of the voids and almost can be neglected when the radius of the void is larger than 30 nm. Although the result of effective shear modulus decreases with the decrement of the radius of the fiber-shape voids, this phenomenon is reasonable since the effective "plane-strain" shear modulus is applied to the three-phase hybrid fiber-reinforced composites in this chapter. It is obvious that the effect by the decrease of the surface area is much more than the effect by the interface/surface energy. It is further demonstrated that this developed analytical model for the interface/surface energy effect on effective moduli of three-phase composites containing randomly dispersed circular fibers of distinct elastic properties and sizes is applicable to reveal the influence of interface/surface energy in nano-scale composites.
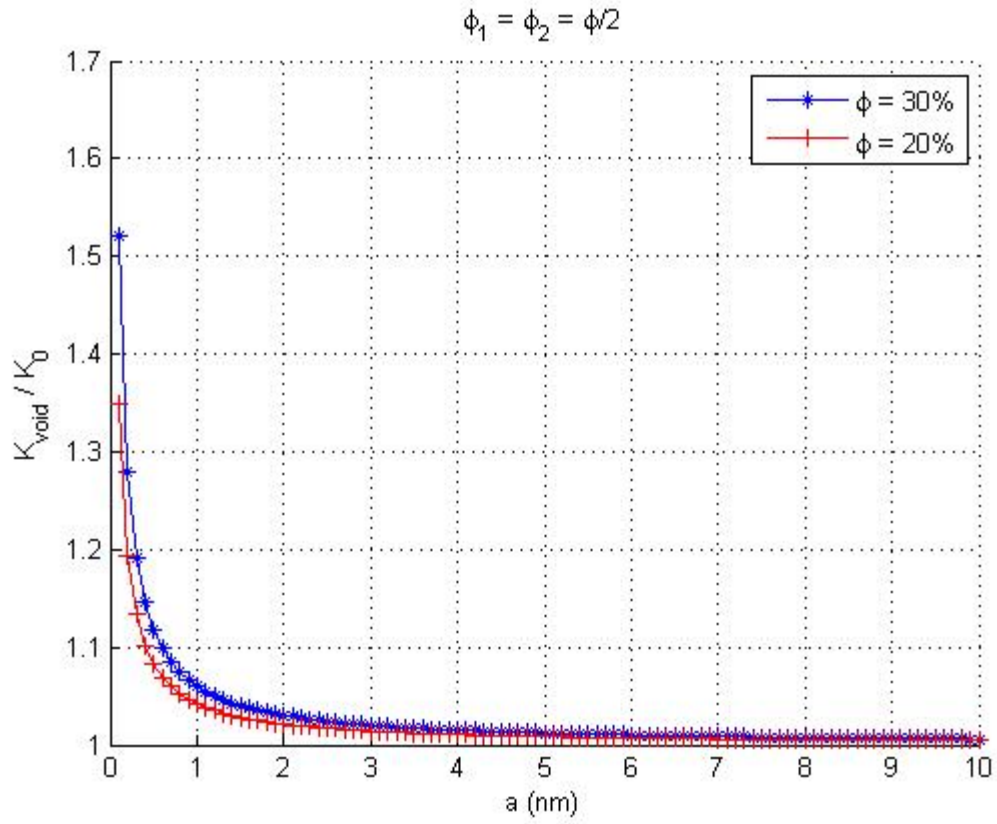
Figure 5.1 Normalized effective bulk modulus against the size of fiber-shape voids in the range of nanometer size with two different volume fractions and $\gamma_0 = 0.05 \ J / m^2$
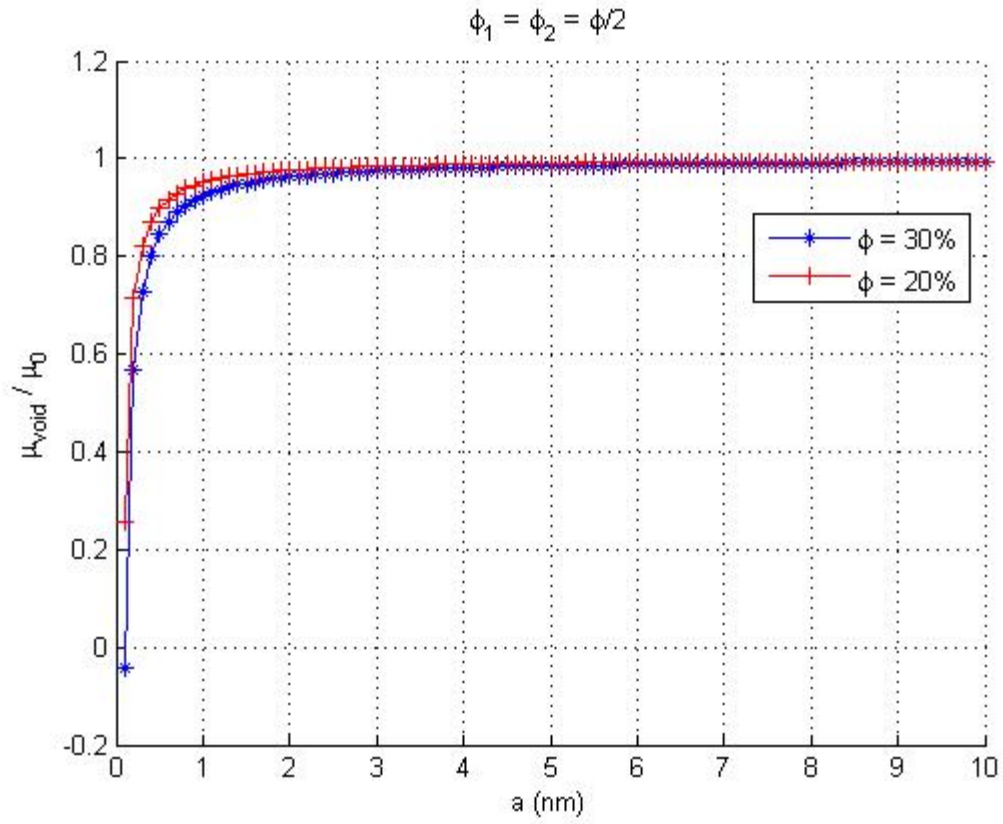
Figure 5.2 Normalized effective shear modulus against the size of fiber-shape voids in the range of nanometer size with two different volume fractions and $\gamma_0 = 0.05 \, J / m^2$

5.6 Conclusions

The primary objective of the present chapter is to extend the work regarding the interface/surface energy effect on size-dependent effective moduli of a three-phase composite containing two "particles" of the distinct properties with the same size, based on the framework of Ko and Ju (2013) and the methodology of Huang and Sun (2007), to the one regarding the interface/surface energy effect on size-dependent effective transverse elastic moduli of three-phase hybrid fiber-reinforced composites containing two "fibers" of the distinct properties and sizes.

First of all, the interface/surface energy effect on the macroscopic mechanical behavior of a composite is investigated through starting with the finite deformation theory of a multi-phase hyperelastic medium. Then, the approximate formulation of a finitely deformed multiphase elastic medium by an infinitesimal deformation analysis is executed. According to the existence of the interface energy, even though under no external loading, there is still a "residual elastic field" induced by the interface stress. During the deformation process of a composite from the reference configuration to the current configuration, the changes of the size and shape of the interface leads to the change of this "residual elastic field". It is noticed that the governing equations describing the change of the "residual elastic field" due to the change of the configuration are formulated under the infinitesimal deformation approximation and hence lead to the use of the asymmetric interface stress in the prediction of the effective properties of heterogeneous materials with interface/surface energy effect. Therefore, the influence of the residual interface/surface energy can be taken into account. In particular, the theoretical framework is applied to obtain the analytical expressions of the effective bulk and shear moduli

of a composite with spherical "equivalent inhomogeneities" (i.e. the inhomogeneities together with the interface/surface energy). Hence, the interface/surface energy effect on the size-dependent effective moduli of a two-phase composite consisting of the matrix and randomly distributed fiber-shape inhomogeneities is developed.

Secondly, the effective transverse elastic bulk and shear moduli of a three-phase composite containing randomly located cylindrical fibers featuring distinct elastic properties and sizes are separately formulated based on another framework with consideration to the concepts of probabilistic spatial distribution of spherical particles, pairwise particle interactions, and the ensemble-volume averaging (homogenization) procedure for three-phase elastic composites. Specifically, the approximate analytical solutions for the direct interactions between two different randomly located elastic fibers embedded in the matrix material are presented, followed by developing the ensemble-volume averaged eigenstrains through the probabilistic pairwise particle interaction mechanism. Moreover, two non-equivalent formulations are considered in detail to derive effective elastic moduli of three-phase composites with no the interface/surface energy effect.

Later on, in combination with the above two formulations, effective transverse elastic moduli of three-phase hybrid fiber-reinforced composites containing randomly located and interacting aligned circular fibers of distinct elastic properties and sizes with the interface/surface energy effect are analytically derived. In addition, numerical results and the corresponding discussions are rendered to demonstrate the potential of this present model. Specifically, some special cases of the interface/surface energy effect on a three-phase composite containing randomly dispersed fibers of same/distinct properties embedded in an elastic matrix are executed. It is further demonstrated that this developed analytical model for the interface/surface energy

177

effect on effective moduli of three-phase composites containing randomly dispersed circular fibers of distinct elastic properties and sizes is applicable to reveal the influence of interface/surface energy in nano-scale composites.

Lastly, experimental validations are key parameters in the calibration of proposed models. Further experimental validations and comparisons will be performed once the associated experiment data become available. To the author's best knowledge, the experimental data associated with characterizations of effective transverse elastic properties of three-phase hybrid fiber-reinforced composites with the interface/surface energy effect are currently not available due to difficulties in performing such experimental works. For example, as the illustrative figures developed based on the framework in this chapter, it is found that the interface/surface effect decreases with the increase of the size of the fiber-shape voids and can be neglected when the radius of the void is larger than 30 nm. In other words, it is quite difficult to manufacture so small nanocomposites nowadays.

It is known that continuous fiber-reinforced composites possess high strength and stiffness in the direction of fibers. The overall mechanical behavior of a fiber composite depends on the constituent properties of the matrix and reinforcements as well as the microstructure. Several possible damage modes exist for fiber composites, such as the interfacial fiber-matrix debonding, the matrix cracking, the fiber breakage, the fiber-pullout, and the shear sliding of fibers. Specifically, the dominant damage mechanism in continuous unidirectional two phase fiber-reinforced ductile composites featuring same elastic properties and sizes of fibers under transverse loading is the initiation and progressive interfacial partial fiber debonding (arc microcracks) or fiber cracking followed by plastic yielding (Ko, 2005; Ju et al., 2006; Ju et al., 2008; Ju and Ko, 2008; Ju et al., 2009; Ko and Ju, 2012).

Current studies will pave the way for future investigations in various damage mechanisms of continuous unidirectional three-phase hybrid fiber-reinforced composites with the interface/surface energy effect under transverse loadings. Thus, optimum cost and performance of hybrid fiber-reinforced composites with the interface/surface energy effect can be achieved through proper material design.

5.7 Appendix A: Formulations upon Finite Deformation Theory

The constitutive relations of the interface have been widely investigated by many researchers in the literature. But most of works on this subject are confined to the infinitesimal deformation approximations. Suppose that the interface/surface energy per unit area in the current configuration is denoted by γ. If the interface is assumed to be isotropic relative to the reference configuration κ_0, i.e. the underlying reference configuration is an undistorted state, then γ can be expressed as a function of the invariants of $\mathbf{U}_s$ and $\mathbf{V}_s$, or a function of J_1 and J_2, as follows,

$$J_1 = tr\, \mathbf{U}_s = tr\, \mathbf{V}_s$$

$$(5.47)$$

$$J_2 = \det \mathbf{U}_s = \det \mathbf{V}_s$$

where $\mathbf{U}_s$ and $\mathbf{V}_s$ are the right and left stretch tensors of the interface, respectively; J_1 and J_2 are the first and second invariants of $\mathbf{U}_s$ and $\mathbf{V}_s$. If the small deformation is concerned, the strain at the interface may be approximately expressed by

$$E_s = \frac{1}{2}\left(\mathbf{u}\nabla_{0s} + \nabla_{0s}\mathbf{u}\right) = \mathbf{U}_s - \mathbf{i}_0 \tag{5.48}$$

where ∇_{0s} is the surface gradient operator on operator in the reference configuration κ_0; $\mathbf{u}\nabla_{0s}$ is the displacement gradient of the interface; $\mathbf{i}_0$ is the second-order identity tensor in the tangent plane of the interface in the reference configuration. Substituting Eq. (5.48) into Eq. (5.47), J_1 and J_2 can be re-written as

$$J_1 = 2 + tr\ \mathbf{E}_s$$

$$J_2 = 1 + tr\ \mathbf{E}_s + \det\ \mathbf{E}_s \tag{5.49}$$

In the case of the isotropic interface and the small deformation, the interface Piola-Kirchhoff stresses of the first kind and second kind can be formulated as

$$\mathbf{S}_s = J_2\left(\frac{\partial\gamma}{\partial J_1} + J_2\frac{\partial\gamma}{\partial J_2} + \gamma\right)\mathbf{i}_0 + J_2\frac{\partial\gamma}{\partial J_1}\mathbf{E}_s - J_2\left(\frac{\partial\gamma}{\partial J_1} + J_2\frac{\partial\gamma}{\partial J_2} + \gamma\right)(\nabla_{0s}\mathbf{u}) \tag{5.50}$$

$$\mathbf{T}_s = J_2\left(\frac{\partial\gamma}{\partial J_1} + J_2\frac{\partial\gamma}{\partial J_2} + \gamma\right)\mathbf{i}_0 - J_2\left(\frac{\partial\gamma}{\partial J_1} + 2J_2\frac{\partial\gamma}{\partial J_2} + 2\gamma\right)\mathbf{E}_s \tag{5.51}$$

and the Cauchy stress of the interface can be described by

$$\boldsymbol{\sigma}_s = \left(\frac{\partial\gamma}{\partial J_1} + J_2\frac{\partial\gamma}{\partial J_2} + \gamma\right)\mathbf{i}_0 + \frac{\partial\gamma}{\partial J_1}\mathbf{E}_s \tag{5.52}$$

Therefore, it is found that $\mathbf{S}_s$, $\mathbf{T}_s$ and the Cauchy stress of the interface $\boldsymbol{\sigma}_s$ are not the same, even if the infinitesimal deformation approximation is performed. The situation is totally different from that in the three dimensional analysis in the traditional elasticity, in which there is no residual stress in the reference configuration. In other words, only through the beginning with the finite deformation theory, an appropriate infinitesimal interface stress is then chosen in the governing equations if the interface/interface energy effect is taken into account on the

mechanical properties of a heterogeneous material.

5.8 Appendix B: Approximations upon Infinitesimal Deformation Analysis

In this section, the approximate equations of the changes of the interface stress and the Young-Laplace equation due to the change of configuration under the infinitesimal deformation is introduced. Then, the analytical equations for the effective moduli of a particle-reinforced composite is given through the application of the theory by Huang and Sun (2007), which depicts the effect of the liquid-like interface/surface energy on the effective moduli.

The governing equations, such as the equilibrium equations, based on one configuration are well-known in the infinitesimal analysis in the traditional elasticity. In order to study the interface energy effect, however, the residual elastic field induced by the interface energy should be taken into account. Although the interface induced the residual elastic field in the reference configuration or in the current configuration is not cared for, the change of the residual elastic field induced by the interface energy from the reference configuration to the current configuration is strongly concerned. Since after and before deformation, the Cauchy stresses (in the bulk material and at the interface) are not in the same configuration based on the Eulerian description, it is obvious that the difference of the Cauchy stresses cannot be used to represent this change. Therefore, the Lagrangian description is applicable, so that the generalized Young-Laplace equation based on the Lagrangian description given by Huang and Wang (2006) can then be expressed in terms of the interface Piola-Kirchhoff stress of the first kind in the following,

$$\mathbf{N} \cdot \left[\!\left[\mathbf{S}^0 \right]\!\right] \cdot \mathbf{N} = -\mathbf{S}_s : \mathbf{b}_0$$

$$\mathbf{P}_0 \cdot \left[\!\left[\mathbf{S}^0 \right]\!\right] \cdot \mathbf{N} = -\mathbf{S}_s \cdot \nabla_{0s} \qquad (5.53)$$

$$\mathbf{P}_0 = \mathbf{I} - \mathbf{N} \otimes \mathbf{N}$$

where the symbol $\left[\!\left[\cdot \right]\!\right]$ denotes the discontinuity of a quantity across the interface; $\mathbf{S}^0$ is the first kind Piola-Kirchhoff stress in the bulk material; $\mathbf{I}$ is the unit tensor in three-dimensional space; $\mathbf{N}$ is the unit normal vector to the interface in the reference configuration κ_0; $\mathbf{b}_0$ is the curvature tensor of the interface in κ_0.

Obviously, the change of the residual elastic field induced by the interface energy can be re-written by adding the difference sign into the above equation, as follows,

$$\mathbf{N} \cdot \left[\!\left[\Delta\mathbf{S}^0 \right]\!\right] \cdot \mathbf{N} = -\Delta\mathbf{S}_s : \mathbf{b}_0$$

$$\qquad (5.54)$$

$$\mathbf{P}_0 \cdot \left[\!\left[\Delta\mathbf{S}^0 \right]\!\right] \cdot \mathbf{N} = -\Delta\mathbf{S}_s \cdot \nabla_{0s}$$

where Δ denotes the difference of the quantities between the current and reference configurations. In order to account for the interface energy effect, the interface Piola-Kirchhoff stress of the first kind $\mathbf{S}_s$ should be employed in the analysis, as shown in the equations above. This is the key point addressed by Huang and Wang (2006), but the previous researchers seemed to ignore that in the study of the effective properties of a heterogeneous material with the interface energy effect. Next, an infinitesimal deformation approximation is executed. In the case of the infinitesimal deformation, $\Delta\mathbf{S}^0$ in Eq. (5.54) could be approximated by the difference of the bulk Cauchy stress between the current and reference configurations, while $\mathbf{S}_s$ in Eq. (5.50) is described in terms of the interface/surface free energy γ.

In addition, the equation of the interface/surface free energy is linearized in order to simplify the algebraic operations at the beginning of the research. Accordingly, γ can be written as

$$\gamma = \gamma_0 + \gamma_1 (J_1 - 2) + \gamma_2 (J_2 - 1) + \frac{1}{2}\gamma_{11}(J_1 - 2)^2 + \gamma_{12}(J_1 - 2)(J_2 - 1) + \frac{1}{2}\gamma_{22}(J_2 - 1)^2 + \dots.$$

$$(5.55)$$

$$\gamma_1 = \frac{\partial \gamma}{\partial J_1}\Big|_{J_1=2, J_2=1} \quad , \quad \gamma_2 = \frac{\partial \gamma}{\partial J_2}\Big|_{J_1=2, J_2=1}$$

where γ_0, γ_1, γ_2 represent the intrinsic physical properties of the interface, and they are, and should be determined by the joining materials and the adhering condition. $\gamma_0 = \gamma(2,1)$ is equivalent to the interface/surface energy of a liquid-like material and hence reflects the nature of liquids, whereas γ_1 and γ_2 reflect the nature of solids; $J_1 - 2$ and $J_2 - 1$ are first-order small quantities. Suppose that only the first-order small quantities are considered in Eq. (5.50) and higher-order small quantities are neglected, from

$$J_2 \left(\frac{\partial \gamma}{\partial J_1} + J_2 \frac{\partial \gamma}{\partial J_2} + \gamma \right) = \gamma_0^* + \left(\gamma_0^* + \gamma_1^* \right) tr \, \mathbf{E}_s$$

$$(5.56)$$

and

$$J_2 \frac{\partial \gamma}{\partial J_1} = \gamma_1 + \left(\gamma_0 + \gamma_{11} + \gamma_{12} \right) tr \, \mathbf{E}_s$$

$$(5.57)$$

Then,

$$\mathbf{S}_s = \gamma_0^* \mathbf{i}_0 + \left(\gamma_0^* + \gamma_1^* \right)\left(tr \, \mathbf{E}_s \right) \mathbf{i}_0 - \gamma_0^* \nabla_{0s} \mathbf{u} + \gamma_1 \mathbf{E}_s$$

$$(5.58)$$

$$\boldsymbol{\sigma}_s = \gamma_0^* \mathbf{i}_0 + \gamma_1^* \left(tr \, \mathbf{E}_s \right) \mathbf{i}_0 + \gamma_1 \mathbf{E}_s$$

$$(5.59)$$

where $\gamma_0^* = \gamma_0 + \gamma_1 + \gamma_2$, $\gamma_1^* = \gamma_1 + 2\gamma_2 + \gamma_{11} + 2\gamma_{12} + \gamma_{22}$, and γ_0^* and γ_1^* form the residual

interface/surface energy. The similar expression with an assumption of the interface stress is dependent on the isotropic linear function of the interface strain can be found by Gurtin and Murdoch (1975). Here, the present formulation shows the interface stress in terms of the interface/surface energy. Later, as the change of the interface stress due to the change of the configuration is discussed, this theoretical framework is applied to predict the effective moduli of heterogeneous media with the interface/surface energy effect. In the reference configuration κ_0, the "residual" interface Piola-Kirchhoff stress of the first kind is expressed by

$$\mathbf{S}_s\,|_0 = \gamma_0^* \mathbf{i}_0 \tag{5.60}$$

Accordingly, in the case of the infinitesimal deformation, the difference of the interface Piola-Kirchhoff stress of the first kind between the current and reference configurations, $\Delta \mathbf{S}_s$, can be written as

$$\Delta \mathbf{S}_s = \left(\gamma_0^* + \gamma_1^*\right)\left(tr\,\mathbf{E}_s\right)\mathbf{i}_0 - \gamma_0^* \nabla_{0s}\mathbf{u} + \gamma_1 \mathbf{E}_s \tag{5.61}$$

It is found that there are at least three independent material parameters γ_0^*, γ_1^* and γ_1 required in the above equation. For some special cases, such as a spherical inhomogeneity embedded in an infinite matrix material under the axisymmetric loading, $\nabla_{0s}\mathbf{u}$ may be regarded as a symmetric second-order tensor in two-dimensional space. Eq. (5.61) is then written as

$$\Delta \mathbf{S}_s = \left(\gamma_0^* + \gamma_1^*\right)\left(tr\,\mathbf{E}_s\right)\mathbf{i}_0 - \left(\gamma_0^* + \gamma_1\right)\mathbf{E}_s$$

$$\tag{5.62}$$

$$\text{Or,}\quad \Delta \mathbf{S}_s = \lambda_s\left(tr\,\mathbf{E}_s\right)\mathbf{i}_0 + 2\mu_s \mathbf{E}_s$$

where λ_s and μ_s are called the interface moduli, shown as follows,

184

$$\lambda_s = \gamma_0^* + \gamma_1^*$$

$$\mu_s = -\frac{1}{2}\left(\gamma_0^* - \gamma_1\right) = -\frac{1}{2}\left(\gamma_0 + \gamma_2\right)$$

(5.63)

It is noted that μ_s could be negative in some cases. In general, the interface/surface energy γ_0 at κ_0 is positive; otherwise a liquid or a solid would gain energy upon fragmentation, for example, as referred to the research by Haiss (2001). γ_2 is the change rate of the interface energy due to the change of the interface area, and the negative μ_s has been confirmed by Shenoy (2005) in his atomistic calculations. Substituting $\Delta \mathbf{S}_s$ in Eq. (5.61) or (5.62) into Eq. (5.50), the discontinuity conditions of the traction across the interface in the reference configuration κ_0 is generated. These discontinuity conditions, associated with other governing equations, can be used to predict the macroscopic mechanical response of composites with the interface energy effect.

5.9 Appendix C: Approximate local solutions of two interacting fibers

Let us consider a three-phase composite consisting of an isotropic elastic matrix (phase 0) with the plane-strain bulk modulus K_0 and the plane-strain shear modulus μ_0, randomly located unidirectionally aligned elastic circular fibers (phase 1) with radius a_1, the plane-strain bulk modulus K_1, and the plane-strain shear modulus μ_1, as well as randomly located unidirectionally aligned elastic circular fibers (phase 2) with radius a_2, the plane-strain bulk modulus K_2, and the plane-strain shear modulus μ_2 (cf. Figures 5.3 and 5.4). Since

plane-strain is assumed, the fiber interaction exists only in the same cutting plane as shown in Figure 5.2. In addition, the plane-strain linearly elastic isotropic stiffness tensors for *three* distinct phases are expressed as

$$\left(C_\eta\right)_{ijkl} = \lambda_\eta \delta_{ij}\delta_{kl} + \mu_\eta \left(\delta_{ik}\delta_{jl} + \delta_{il}\delta_{jk}\right), \quad \eta = 0,1,2 \tag{5.64}$$

where λ_η and μ_η are the Lamé constants of the phase-η material.
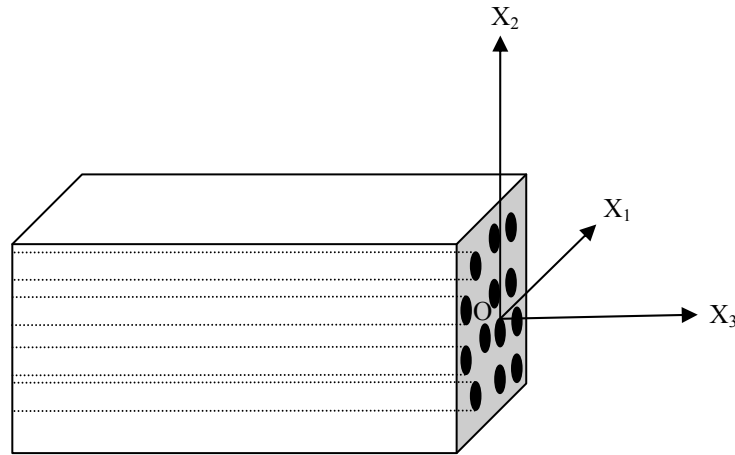
Figure 5.3 A schematic plot for a composite reinforced by unidirectionally aligned yet randomly located cylindrical fibers

186
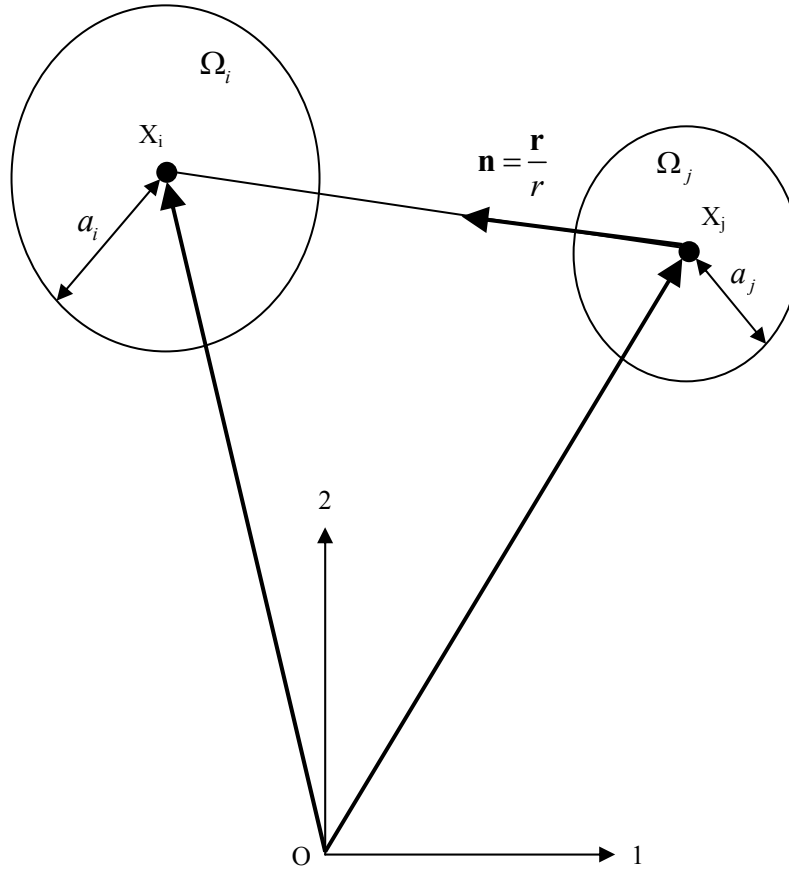
Figure 5.4 The schematic diagram for the two-fiber interaction problem. r: spacing between the centers of two interacting fibers; $r = \left\| \mathbf{x}_i - \mathbf{x}_j \right\| = \left\| \mathbf{r} \right\|$ $(i, j = 1, 2)$

Following the eigenstrain concept introduced by Eshelby (1957), the perturbed strain field $\boldsymbol{\varepsilon}'(\mathbf{x})$ induced by fibers can be related to the specified eigenstrains $\boldsymbol{\varepsilon}^*(\mathbf{x})$ by replacing the fibers with the matrix material. The key equation can be rephrased as follows:

$$\mathbf{C}_\eta : \left[\boldsymbol{\varepsilon}^0 + \boldsymbol{\varepsilon}'(\mathbf{x}) \right] = \mathbf{C}_0 \left[\boldsymbol{\varepsilon}^0 + \boldsymbol{\varepsilon}'(\mathbf{x}) - \boldsymbol{\varepsilon}^*(\mathbf{x}) \right], \quad \eta = 1, 2 \tag{5.65}$$

187

where $\boldsymbol{\varepsilon}^0$ is the uniform strain field induced by the far-field loads for a homogeneous matrix material only. Throughout the paper, the colon symbol ":" denotes the tensor contraction between a fourth-rank tensor and a second-rank tensor, while the dot symbol "·" represents the tensor multiplication between two four-rank tensors.

According to Eshelby (1957), the perturbed strain field induced by the distributed eigenstrain $\boldsymbol{\varepsilon}^*(\mathbf{x})$ in a representative area element (RAE) A reads

$$\boldsymbol{\varepsilon}'(\mathbf{x}) = \int_A \mathbf{G}(\mathbf{x} - \mathbf{x}') : \boldsymbol{\varepsilon}^*(\mathbf{x}') d\mathbf{x}' \tag{5.66}$$

where $\mathbf{x}, \mathbf{x}' \in A$ and the components of the fourth-rank two-dimensional Green's function tensor $\mathbf{G}$ are given by ($i, j, k, l = 1, 2$; cf. Mura (1987)):

$$G_{ijkl} = \frac{1}{4\pi(1-\nu_0)r'^2} F_{ijkl}(-8, 2\nu_0, 2, 2-4\nu_0, -1+2\nu_0, 1-2\nu_0) \tag{5.67}$$

where $\mathbf{r} \equiv \mathbf{x} - \mathbf{x}'$ and $r' = \|\mathbf{r}'\|$. The components of the fourth-rank tensor $\mathbf{F}$ – which depends on its arguments ($B_1, B_2, B_3, B_4, B_5, B_6$) – are defined by ($m = 1$–$6$):

$$
\begin{aligned}
F_{ijkl}(B_m) &\equiv B_1 n_i' n_j' n_k' n_l' + B_2 \left(\delta_{ik} n_j' n_l' + \delta_{il} n_j' n_k' + \delta_{jk} n_i' n_l' + \delta_{jl} n_i' n_k' \right) \\
&+ B_3 \delta_{ij} n_k' n_l' + B_4 \delta_{kl} n_i' n_j' + B_5 \delta_{ij} \delta_{kl} + B_6 \left(\delta_{ik} \delta_{jl} + \delta_{il} \delta_{jk} \right)
\end{aligned} \tag{5.68}
$$

with the normal vector $n' \equiv \mathbf{r} / r$. All physical quantities refer to the Cartesian coordinates, and the summation convention applies. Moreover, δ_{ij} denotes the Kronecker delta and ν_0 is the Poisson's ratio of the matrix material. From Eqs. (5.65) and (5.66), we arrive at

$$-\mathbf{A}_i : \boldsymbol{\varepsilon}^*(\mathbf{x}) = \boldsymbol{\varepsilon}^0 + \int_A \mathbf{G}(\mathbf{x} - \mathbf{x}') : \boldsymbol{\varepsilon}^*(\mathbf{x}') d\mathbf{x}', \quad \mathbf{x} \in A \tag{5.69}$$

$$\mathbf{A}_i = [\mathbf{C}_i - \mathbf{C}_0]^{-1} \bullet \mathbf{C}_0 \tag{5.70}$$

Within the present two-circular fibers interaction context, the integral Eq. (5.69) can be

recast as

$$-A_i : \boldsymbol{\varepsilon}^*_{(i)}(\mathbf{x}) = \boldsymbol{\varepsilon}^0 + \int_{\Omega_i} \mathbf{G}(\mathbf{x}-\mathbf{x'}) : \boldsymbol{\varepsilon}^*_{(i)}(\mathbf{x'}) d\mathbf{x'} + \int_{\Omega_j} \mathbf{G}(\mathbf{x}-\mathbf{x'}) : \boldsymbol{\varepsilon}^*_{(j)}(\mathbf{x'}) d\mathbf{x'},$$

$$i \neq j, \quad i,j = 1,2$$

(5.71)

where $\mathbf{x} \in \Omega_i$, and $\boldsymbol{\varepsilon}^*_{(i)}(\mathbf{x'})$ is the eigenstrain at $\mathbf{x'}$ in the i th circular fiber within the domain Ω_i.

As discussed earlier in Ju and Chen (1994a), the first-order solution for the eigenstrain, denoted by $\boldsymbol{\varepsilon}^{*0}_{(i)}$ for the i th phase, can be obtained by neglecting the last term in the right-hand side of Eq. (5.71), which represents the interaction effects due to the other circular fiber. The first-order formulation leads to

$$-A_i : \boldsymbol{\varepsilon}^{*0}_{(i)}(\mathbf{x}) = \boldsymbol{\varepsilon}^0 + \mathbf{S} : \boldsymbol{\varepsilon}^{*0}_{(i)}$$

(5.72)

where the Eshelby tensor $\mathbf{S}$ is defined as

$$\mathbf{S} = \int_{\Omega_i} \mathbf{G}(\mathbf{x}-\mathbf{x'}) d\mathbf{x'}, \quad \mathbf{x}, \mathbf{x'} \in \Omega_i$$

(5.73)

The components of the fourth-rank interior-point Eshelby tensor $\mathbf{S}$ for a cylindrical fiber are given by Mura (1987), Ju and Sun (2001), Sun and Ju (2001), and Ju and Zhang (1998). It depends on the Poisson's ratio of the matrix (ν_0) and the shape of the fiber cross-sectional domain Ω_i. In particular, for a two-dimensional circular domain, the components of $\mathbf{S}$ are (see Mura (1987) for more details):

$$S_{ijkl} = \frac{1}{8(1-\nu_0)}\left\{(4\nu_0-1)\delta_{ij}\delta_{kl} + (3-4\nu_0)(\delta_{ik}\delta_{jl} + \delta_{il}\delta_{jk})\right\}, \quad i,j,k,l = 1,2$$

(5.74)

By subtracting the first-order solution Eq. (5.72) from Eq. (5.71), the effects of inter-fiber interactions can be derived by solving the following integral equation:

189

$$-\mathbf{A}_i : \mathbf{d}_{(i)}^*(\mathbf{x}) = \int_{\Omega_j} \mathbf{G}(\mathbf{x}-\mathbf{x}')d\mathbf{x}' : \boldsymbol{\varepsilon}_{(j)}^{*0} + \int_{\Omega_i} \mathbf{G}(\mathbf{x}-\mathbf{x}') : \mathbf{d}_{(i)}^*(\mathbf{x}')d\mathbf{x}'$$

$$+ \int_{\Omega_j} \mathbf{G}(\mathbf{x}-\mathbf{x}') : \mathbf{d}_{(j)}^*(\mathbf{x}')d\mathbf{x}', \quad \text{for } \mathbf{x} \in \Omega_i, \quad i \neq j \text{ and } i,j = 1,2 \tag{5.75}$$

where

$$\mathbf{d}_{(i)}^*(\mathbf{x}) = \boldsymbol{\varepsilon}_{(i)}^*(\mathbf{x}) - \boldsymbol{\varepsilon}_{(i)}^{*0} \tag{5.76}$$

To obtain the higher-order interaction correction for $\boldsymbol{\varepsilon}_{(i)}^*(\mathbf{x})$, one may expand the fourth-rank tensor $\mathbf{G}(\mathbf{x}-\mathbf{x}')$ in the domain Ω_i with respect to its center point $\mathbf{x}_j$; i.e.,

$$\mathbf{G}(\mathbf{x}-\mathbf{x}') = \mathbf{G}(\mathbf{x}-\mathbf{x}_j) - (\mathbf{x}'-\mathbf{x}_j) : \left[\nabla_{\mathbf{x}} \otimes \mathbf{G}(\mathbf{x}-\mathbf{x}_j) \right]$$

$$+ \frac{1}{2} \left[(\mathbf{x}'-\mathbf{x}_j) \otimes (\mathbf{x}'-\mathbf{x}_j) \right] : \left[\nabla_{\mathbf{x}} \otimes \nabla_{\mathbf{x}} \otimes \mathbf{G}(\mathbf{x}-\mathbf{x}_j) \right] + \cdots \tag{5.77}$$

where the relation

$$\nabla_{\mathbf{x}'} \otimes \mathbf{G}(\mathbf{x}-\mathbf{x}') = -\nabla_{\mathbf{x}} \otimes \mathbf{G}(\mathbf{x}-\mathbf{x}') \tag{5.78}$$

has been employed. From Eqs. (5.75) and (5.77), we arrive a

$$-\mathbf{A}_i : \mathbf{d}_{(i)}^*(\mathbf{x}) = \int_{\Omega_j} \mathbf{G}(\mathbf{x}-\mathbf{x}')d\mathbf{x}' : \boldsymbol{\varepsilon}_{(j)}^{*0} + \int_{\Omega_i} \mathbf{G}(\mathbf{x}-\mathbf{x}') : \mathbf{d}_{(i)}^*(\mathbf{x}')d\mathbf{x}'$$

$$+ \Omega_j \mathbf{G}(\mathbf{x}-\mathbf{x}_j) : \overline{\mathbf{d}}_{(j)}^*(\mathbf{x}_j) - \Omega_j a_j \left\{ \nabla_{\mathbf{x}} \otimes \mathbf{G}(\mathbf{x}-\mathbf{x}_j) \right\} : \overline{\mathbf{P}}_{(j)}^* \tag{5.79}$$

$$+ \frac{1}{2} \Omega_j a_j^2 \left\{ \nabla_{\mathbf{x}} \otimes \nabla_{\mathbf{x}} \otimes \mathbf{G}(\mathbf{x}-\mathbf{x}_j) \right\} : \overline{\mathbf{Q}}_{(j)}^* + \cdots$$

for $\mathbf{x} \in \Omega_i$ and $i \neq j$ $(i, j = 1, 2)$. Here $\Omega_i = \pi a_i^2$ and $\Omega_j = \pi a_j^2$ denote the cross-sectional area of a fiber in phase i and j, respectively; a_i and a_j define the fiber radius in phase i and j, respectively. Furthermore, the average fields involved in Eq. (5.79) are defined as follows:

$$\overline{\mathbf{d}}_{(j)}^* = \frac{1}{\Omega_j} \int_{\Omega_j} \mathbf{d}_{(j)}^*(\mathbf{x}')d\mathbf{x}' \; ; \qquad \overline{\mathbf{P}}_{(j)}^* = \frac{1}{\Omega_j a_j} \int_{\Omega_j} (\mathbf{x}'-\mathbf{x}_j) \otimes \mathbf{d}_{(j)}^*(\mathbf{x}')d\mathbf{x}' \tag{5.80}$$

$$\overline{\mathbf{Q}}^*_{(j)} = \frac{1}{\Omega_j a_j^2} \int_{\Omega_j} \left(\mathbf{x}'-\mathbf{x}_j\right) \otimes \left(\mathbf{x}'-\mathbf{x}_j\right) \otimes \mathbf{d}^*_{(j)}(\mathbf{x}') d\mathbf{x}' \qquad (5.81)$$

The third-rank tensor $\overline{\mathbf{P}}^*_{(j)}$ and the fourth-rank tensor $\overline{\mathbf{Q}}^*_{(j)}$ correspond to the dipole and quadrupole of $\mathbf{d}^*_{(j)}$ in the domain Ω_j, respectively. Due to the circular symmetry of fibers, the leading order of $\overline{\mathbf{P}}^*_{(j)}$ can be shown to be of the order $O(\rho^3)$, rather than $O(\rho^2)$, by substituting Eqs. (5.79) into (5.80). Here, $\rho_j = a_j / r$ and r are the spacing between the centers of two interacting fibers. By performing the area average of Eq. (5.79) for the domain Ω_j and neglecting those terms of higher-order moments in Eq. (5.79), the approximate equations for $\overline{\mathbf{d}}^*_{(i)}$ for the local two-fiber interaction problem can be obtained. Let $i = 1$, $j = 2$, Eqs. (5.82)–(5.85) are derived. In addition, let $i = 2, j = 1$, Eqs. (5.86)–(5.89) are obtained.

$$-\mathbf{A}_1 : \Omega_1 \overline{\mathbf{d}}^*_{(1)} = \Omega_{12} \overline{\mathbf{G}}^{21} : \boldsymbol{\varepsilon}^{*0}_{(2)} + \Omega_1 \mathbf{S} : \overline{\mathbf{d}}^*_{(1)} + \Omega_2 \overline{\mathbf{G}}^{11} : \overline{\mathbf{d}}^*_{(2)} + O(\rho^6) \qquad (5.82)$$

where

$$\overline{\mathbf{d}}^*_{(1)} = \frac{1}{\Omega_1} \int_{\Omega_1} \mathbf{d}^*_{(1)}(\mathbf{x}') d\mathbf{x}' \quad ; \qquad \mathbf{S} = \int_{\Omega_1} \mathbf{G}(\mathbf{x}-\mathbf{x}') d\mathbf{x}', \quad \mathbf{x} \in \Omega_1, \mathbf{x}' \in \Omega_1 \qquad (5.83)$$

$$\overline{\mathbf{G}}^{21} = \frac{1}{\Omega_{12}} \int_{\Omega_1} \int_{\Omega_2} \mathbf{G}(\mathbf{x}-\mathbf{x}') d\mathbf{x}' d\mathbf{x} = \frac{1}{8(1-\nu_0)} \left[\rho_1 \rho_2 \mathbf{H}^1 + \left(\frac{\rho_1^3 \rho_2 + \rho_1 \rho_2^3}{2} \right) \mathbf{H}^2 \right] \qquad (5.84)$$

$$\overline{\mathbf{G}}^{11} = \int_{\Omega_1} \mathbf{G}(\mathbf{x}-\mathbf{x}_2) d\mathbf{x} = \frac{1}{8(1-\nu_0)} \left(\rho_1^2 \mathbf{H}^1 + \frac{\rho_1^4}{2} \mathbf{H}^2 \right), \quad \text{with } \mathbf{x} \in \Omega_1, \mathbf{x}_2 \in \Omega_2 \qquad (5.85)$$

In addition, we have

$$-\mathbf{A}_2 : \Omega_2 \overline{\mathbf{d}}^*_{(2)} = \Omega_{21} \overline{\mathbf{G}}^{12} : \boldsymbol{\varepsilon}^{*0}_{(1)} + \Omega_2 \mathbf{S} : \overline{\mathbf{d}}^*_{(2)} + \Omega_1 \overline{\mathbf{G}}^{22} : \overline{\mathbf{d}}^*_{(1)} + O(\rho^6) \qquad (5.86)$$

in which

$$\overline{\mathbf{d}}_{(2)}^* = \frac{1}{\Omega_2} \int_{\Omega_2} \mathbf{d}_{(2)}^*(\mathbf{x}') d\mathbf{x}' \; ; \qquad \mathbf{S} = \int_{\Omega_2} \mathbf{G}(\mathbf{x} - \mathbf{x}') d\mathbf{x}', \quad \mathbf{x} \in \Omega_2, \mathbf{x}' \in \Omega_2 \tag{5.87}$$

$$\overline{\mathbf{G}}^{12} = \frac{1}{\Omega_{21}} \int_{\Omega_2} \int_{\Omega_1} \mathbf{G}(\mathbf{x} - \mathbf{x}') d\mathbf{x}' d\mathbf{x} = \frac{1}{8(1-v_0)} \left[\rho_1 \rho_2 \mathbf{H}^1 + \left(\frac{\rho_1^3 \rho_2 + \rho_1 \rho_2^3}{2} \right) \mathbf{H}^2 \right] \tag{5.88}$$

$$\overline{\mathbf{G}}^{22} = \int_{\Omega_2} \mathbf{G}(\mathbf{x} - \mathbf{x}_1) d\mathbf{x} = \frac{1}{8(1-v_0)} \left(\rho_2^2 \mathbf{H}^1 + \frac{\rho_2^4}{2} \mathbf{H}^2 \right), \quad \text{with } \mathbf{x} \in \Omega_2, \mathbf{x}_1 \in \Omega_1 \tag{5.89}$$

and the components of $\mathbf{H}^1$ and $\mathbf{H}^2$ are rendered by

$$H_{ijkl}^1 (\mathbf{x}_1 - \mathbf{x}_2) \equiv 2F_{ijkl}(-8, 2v_0, 2, 2 - 4v_0, -1 + 2v_0, 1 - 2v_0)$$
$$H_{ijkl}^2 (\mathbf{x}_1 - \mathbf{x}_2) \equiv 2F_{ijkl}(24, -4, -4, -4, 1, 1) \tag{5.90}$$

Moreover, we define $\rho_1 = a_1 / r$, $\rho_2 = a_2 / r$, $\Omega_{12} = \pi a_1 a_2$, and $\Omega_{21} = \Omega_{12} = \pi a_1 a_2$.

It is interesting to note that $\overline{\mathbf{G}}^{11}$ in Eqs. (5.85) and $\overline{\mathbf{G}}^{22}$ in (5.89) are different from the Eshelby tensor $\mathbf{S}$ in Eqs. (5.83) and in (5.87). One may refer to $\overline{\mathbf{G}}^{11}$ and $\overline{\mathbf{G}}^{22}$ as the "exterior-point Eshelby tensors" since the integrals in Eqs. (5.85) and (5.89) involve an exterior-point outside the integration domain. It should be noted that the leading order induced by truncating the higher-order moments in Eqs. (5.82) and (5.86) is of the order $O(\rho^6)$, since both $\overline{\mathbf{P}}_{(j)}^*$ and $\Omega_j a_j \{ \nabla_{\mathbf{x}} \otimes \mathbf{G}(\mathbf{x} - \mathbf{x}_j) \}$ are of the order $O(\rho^3)$. Moreover, Eqs. (5.82) and (5.86) can be recast as

$$\Omega_1 (\mathbf{A}_1 + \mathbf{S}) : \overline{\mathbf{d}}_{(1)}^* + \Omega_2 \overline{\mathbf{G}}^{11} : \overline{\mathbf{d}}_{(2)}^* = -\Omega_{12} \overline{\mathbf{G}}^{21} : \varepsilon_{(2)}^{*0}$$
$$\Omega_1 \overline{\mathbf{G}}^{22} : \overline{\mathbf{d}}_{(1)}^* + \Omega_2 (\mathbf{A}_2 + \mathbf{S}) : \overline{\mathbf{d}}_{(2)}^* = -\Omega_{12} \overline{\mathbf{G}}^{12} : \varepsilon_{(1)}^{*0} \tag{5.91}$$

Therefore, the solutions of Eq. (5.91) are

$$\overline{\mathbf{d}}_{(1)}^* = \frac{\Omega_{12}}{\Omega_1} \left[\left(\overline{\mathbf{G}}^{11} \right)^{-1} \cdot (\mathbf{A}_1 + \mathbf{S}) - \left(\overline{\mathbf{G}}^{22} \right)^{-1} \cdot (\mathbf{A}_2 + \mathbf{S})^{-1} \right]^{-1}$$
$$\cdot \left[(\mathbf{A}_2 + \mathbf{S})^{-1} \cdot \overline{\mathbf{G}}^{12} : \varepsilon_{(1)}^{*0} - \left(\overline{\mathbf{G}}^{11} \right)^{-1} \cdot \overline{\mathbf{G}}^{21} : \varepsilon_{(2)}^{*0} \right] \tag{5.92}$$

192

$$\overline{\mathbf{d}}_{(2)}^{*} = \frac{\Omega_{12}}{\Omega_2}\left[\overline{\mathbf{G}}^{11}\cdot\left(\mathbf{A}_1+\mathbf{S}\right)^{-1}-\left(\overline{\mathbf{G}}^{22}\right)^{-1}\cdot\left(\mathbf{A}_2+\mathbf{S}\right)\right]^{-1}$$
$$\cdot\left[\left(\overline{\mathbf{G}}^{22}\right)^{-1}\cdot\overline{\mathbf{G}}^{12}:\boldsymbol{\varepsilon}_{(1)}^{*0}-\overline{\mathbf{G}}^{21}\cdot\left(\mathbf{A}_1+\mathbf{S}\right)^{-1}:\boldsymbol{\varepsilon}_{(2)}^{*0}\right]$$

(5.93)

where the leading orders of $\overline{\mathbf{G}}^{22}\left(\mathbf{A}_2+\mathbf{S}\right)^{-1}$ and $\left(\overline{\mathbf{G}}^{11}\right)^{-1}\left(\mathbf{A}_1+\mathbf{S}\right)$ are of the order of $O\left(\rho^2\right)$

and $O\left(\rho^{-2}\right)$ in Eq. (5.92), respectively. We note that $\overline{\mathbf{G}}^{22}\left(\mathbf{A}_2+\mathbf{S}\right)^{-1}$ is truncated since its

leading order is greater than the leading order of $\left(\overline{\mathbf{G}}^{11}\right)^{-1}\left(\mathbf{A}_1+\mathbf{S}\right)$. We also have $\rho_1<1/2$,

$\rho_2<1/2$, and $\rho_1+\rho_2<1$:

$$\overline{\mathbf{d}}_{(1)}^{*} = \frac{\Omega_{12}}{\Omega_1}\left[\left(\mathbf{A}_1+\mathbf{S}\right)^{-1}\cdot\overline{\mathbf{G}}^{11}\cdot\left(\mathbf{A}_2+\mathbf{S}\right)^{-1}\cdot\overline{\mathbf{G}}^{12}:\boldsymbol{\varepsilon}_{(1)}^{*0}-\left(\mathbf{A}_1+\mathbf{S}\right)^{-1}\cdot\overline{\mathbf{G}}^{21}:\boldsymbol{\varepsilon}_{(2)}^{*0}\right]$$

(5.94)

Similarly, Eq. (5.93) can be rephrased as

$$\overline{\mathbf{d}}_{(2)}^{*} = \frac{\Omega_{12}}{\Omega_2}\left[\left(\mathbf{A}_2+\mathbf{S}\right)^{-1}\cdot\overline{\mathbf{G}}^{22}\cdot\left(\mathbf{A}_1+\mathbf{S}\right)^{-1}\cdot\overline{\mathbf{G}}^{21}:\boldsymbol{\varepsilon}_{(2)}^{*0}-\left(\mathbf{A}_2+\mathbf{S}\right)^{-1}\cdot\overline{\mathbf{G}}^{12}:\boldsymbol{\varepsilon}_{(1)}^{*0}\right]$$

(5.95)

5.10 Appendix D: Ensemble-area averaged eigenstrains

To obtain the probabilistic ensemble-averaged solution of $\overline{\mathbf{d}}_{(1)}^{*}$ within the context of

approximate pairwise local fiber interaction, one has to integrate Eq. (5.94) over all possible

positions ($\mathbf{x}_2$) of the phase 2 fiber and positions ($\mathbf{x}_1$) of the phase 1 fiber for a given location of

the phase 1 fiber ($\mathbf{x}_1$). Similarly, to find $\overline{\mathbf{d}}_{(2)}^{*}$, one has to integrate Eq. (5.95) over all possible

positions ($\mathbf{x}_1$) of the phase 1 fiber and positions ($\mathbf{x}_2$) of the phase 2 fiber for a given location of

the phase 2 fiber ($\mathbf{x}_2$). The ensemble-average process takes the form:

$$\left\langle \overline{\mathbf{d}}_{(i)}^{*} \right\rangle (\mathbf{x}_i) = \int_{A-\Omega_i} \overline{\mathbf{d}}_{(i)}^{*} (\mathbf{x}_i - \mathbf{x}_j) P(\mathbf{x}_j \mid \mathbf{x}_i) d\mathbf{x}_j, \quad i \neq j \tag{5.96}$$

$$i = 1, \ j = 2: \quad \left\langle \overline{\mathbf{d}}_{(1)}^{*} \right\rangle (\mathbf{x}_1) = \int_{A-\Omega_1} \overline{\mathbf{d}}_{(1)}^{*} (\mathbf{x}_1 - \mathbf{x}_2) P(\mathbf{x}_2 \mid \mathbf{x}_1) d\mathbf{x}_2 \tag{5.97}$$

$$i = 2, \ j = 1: \quad \left\langle \overline{\mathbf{d}}_{(2)}^{*} \right\rangle (\mathbf{x}_2) = \int_{A-\Omega_2} \overline{\mathbf{d}}_{(2)}^{*} (\mathbf{x}_2 - \mathbf{x}_1) P(\mathbf{x}_1 \mid \mathbf{x}_2) d\mathbf{x}_1 \tag{5.98}$$

The two-point conditional probability function $P(\mathbf{x}_j \mid \mathbf{x}_i)$ is determined by the microstructure of a composite, which in turn depends on the fiber volume fractions and underlying manufacturing processes. For illustration, the two-point conditional probability density function takes the following form:

$$P(\mathbf{x}_j \mid \mathbf{x}_i) = \begin{cases} \dfrac{(N_i + N_j)}{A} g(\hat{r}), & \text{if } \hat{r} \geq 1, \text{ where } \hat{r} \equiv r/(a_1 + a_2), \ r > (a_1 + a_2) \\ 0, & \text{otherwise} \end{cases} \tag{5.99}$$

where $i, j = 1, 2$, $i \neq j$; N_i and N_i / A are the numbers of fibers and the 2D number density of fibers in phase i in a composite, respectively; N_j and N_j / A are the numbers of fibers and the 2D number density of fibers in phase j (distinct material property and size of phase i) in a composite, respectively; r is the spacing between centers of two fibers. Further, $g(\hat{r})$ denotes the 2D transversely isotropic "radial distribution function" (Hansen and McDonald (1986); Torquato and Lado (1992)).

By substituting Eqs. (5.94) into (5.97), the explicit expression for $\left\langle \overline{\mathbf{d}}_{(1)}^{*} \right\rangle (\mathbf{x}_1)$ can be depicted as

$$\left\langle \overline{\mathbf{d}}_{(1)}^{*} \right\rangle \left(\mathbf{x}_{1} \right) = \int_{A-\Omega_{1}} \overline{\mathbf{d}}_{(1)}^{*} \left(\mathbf{x}_{1} - \mathbf{x}_{2} \right) P \left(\mathbf{x}_{2} \mid \mathbf{x}_{1} \right) d\mathbf{x}_{2}$$

$$= \int_{A-\Omega_{1}} \frac{\Omega_{12}}{\Omega_{1}} \left[\left(\mathbf{A}_{1} + \mathbf{S} \right)^{-1} \overline{\mathbf{G}}^{11} \left(\mathbf{A}_{2} + \mathbf{S} \right)^{-1} \overline{\mathbf{G}}^{12} : \boldsymbol{\varepsilon}_{(1)}^{*0} - \left(\mathbf{A}_{1} + \mathbf{S} \right)^{-1} \overline{\mathbf{G}}^{21} : \boldsymbol{\varepsilon}_{(2)}^{*0} \right] P \left(\mathbf{x}_{2} \mid \mathbf{x}_{1} \right) d\mathbf{x}_{2}$$

$$= \frac{\Omega_{12}}{\Omega_{1}} \int_{a_{1}+a_{2}}^{\infty} \int_{0}^{2\pi} \left[\left(\mathbf{A}_{1} + \mathbf{S} \right)^{-1} \overline{\mathbf{G}}^{11} \left(\mathbf{A}_{2} + \mathbf{S} \right)^{-1} \overline{\mathbf{G}}^{12} : \boldsymbol{\varepsilon}_{(1)}^{*0} \right] P \left(\mathbf{x}_{2} \mid \mathbf{x}_{1} \right) d\mathbf{x}_{2} \qquad (5.100)$$

$$+ \frac{\Omega_{12}}{\Omega_{1}} \int_{2a_{1}}^{\infty} \int_{0}^{2\pi} \left[\left(\mathbf{A}_{1} + \mathbf{S} \right)^{-1} \overline{\mathbf{G}}^{11} \left(\mathbf{A}_{2} + \mathbf{S} \right)^{-1} \overline{\mathbf{G}}^{12} : \boldsymbol{\varepsilon}_{(1)}^{*0} \right] P \left(\mathbf{x}_{1} \mid \mathbf{x}_{1} \right) d\mathbf{x}_{1}$$

Here, we can prove that

$$\int_{A-\Omega_{1}} \frac{\Omega_{12}}{\Omega_{1}} \left[\left(\mathbf{A}_{1} + \mathbf{S} \right)^{-1} \overline{\mathbf{G}}^{21} : \boldsymbol{\varepsilon}_{(2)}^{*0} \right] P \left(\mathbf{x}_{2} \mid \mathbf{x}_{1} \right) d\mathbf{x}_{2} = 0 \qquad (5.101)$$

where $\int_{0}^{2\pi} \mathbf{H}^{1} \left(\mathbf{n} \right) d\theta = 0$; $\int_{0}^{2\pi} \mathbf{H}^{2} \left(\mathbf{n} \right) d\theta = 0$ as shown in Ju and Zhang (1998); A is the infinitely large 2D transversely isotropic probabilistic (not physical) integration domain; Ω_{1} is the probabilistic "exclusion zone" for $\mathbf{x}_2$. In addition, the following identities can be easily derived:

$$\int_{0}^{2\pi} n_{i} n_{j} d\theta = \pi \delta_{ij}; \quad \int_{0}^{2\pi} n_{i} n_{j} n_{k} n_{l} d\theta = \frac{\pi}{4} \left(\delta_{ij} \delta_{kl} + \delta_{ik} \delta_{jl} + \delta_{il} \delta_{jk} \right) \qquad (5.102)$$

Similarly, by substituting Eqs. (5.95) into (5.98), the explicit expression for $\left\langle \overline{\mathbf{d}}_{(2)}^{*} \right\rangle \left(\mathbf{x}_{2} \right)$ can be expressed as

$$\left\langle \overline{\mathbf{d}}_{(2)}^{*} \right\rangle \left(\mathbf{x}_{2} \right) = \int_{A-\Omega_{2}} \overline{\mathbf{d}}_{(2)}^{*} \left(\mathbf{x}_{2} - \mathbf{x}_{1} \right) P \left(\mathbf{x}_{1} \mid \mathbf{x}_{2} \right) d\mathbf{x}_{1}$$

$$= \int_{A-\Omega_{2}} \frac{\Omega_{12}}{\Omega_{2}} \left[\left(\mathbf{A}_{2} + \mathbf{S} \right)^{-1} \overline{\mathbf{G}}^{22} \left(\mathbf{A}_{1} + \mathbf{S} \right)^{-1} \overline{\mathbf{G}}^{21} : \boldsymbol{\varepsilon}_{(2)}^{*0} - \left(\mathbf{A}_{2} + \mathbf{S} \right)^{-1} \overline{\mathbf{G}}^{12} : \boldsymbol{\varepsilon}_{(1)}^{*0} \right] P \left(\mathbf{x}_{1} \mid \mathbf{x}_{2} \right) d\mathbf{x}_{1}$$

$$= \frac{\Omega_{12}}{\Omega_{2}} \int_{a_{1}+a_{2}}^{\infty} \int_{0}^{2\pi} \left[\left(\mathbf{A}_{2} + \mathbf{S} \right)^{-1} \overline{\mathbf{G}}^{22} \left(\mathbf{A}_{1} + \mathbf{S} \right)^{-1} \overline{\mathbf{G}}^{21} : \boldsymbol{\varepsilon}_{(2)}^{*0} \right] P \left(\mathbf{x}_{1} \mid \mathbf{x}_{2} \right) d\mathbf{x}_{1} \qquad (5.103)$$

$$+ \frac{\Omega_{12}}{\Omega_{2}} \int_{2a_{2}}^{\infty} \int_{0}^{2\pi} \left[\left(\mathbf{A}_{2} + \mathbf{S} \right)^{-1} \overline{\mathbf{G}}^{22} \left(\mathbf{A}_{1} + \mathbf{S} \right)^{-1} \overline{\mathbf{G}}^{21} : \boldsymbol{\varepsilon}_{(2)}^{*0} \right] P \left(\mathbf{x}_{2} \mid \mathbf{x}_{2} \right) d\mathbf{x}_{2}$$

195

Here, we can also prove that

$$\int\limits_{A-\Omega_2} \frac{\Omega_{12}}{\Omega_2} \left[\left(\mathbf{A}_2 + \mathbf{S} \right)^{-1} \overline{\mathbf{G}}^{12} : \boldsymbol{\varepsilon}_{(1)}^{*0} \right] P\left(\mathbf{x}_1 \mid \mathbf{x}_2 \right) d\mathbf{x}_1 = 0 \tag{5.104}$$

In what follows, two different radial distribution functions will be considered, that is, (1) the uniform radial distribution function $g(\hat{r}) = 1$ and (2) the general radial distribution function $g(\hat{r}) \neq 1$ in Eq. (5.99). Under each radial distribution function, we present two non-equivalent formulations to predict the effective transverse elastic moduli of three-phase composites, that is, "Formulation II" and "Formulation I." The following notations are adopted: the superscript "U," "G," "II," and "I" stand for the uniform radial distribution function, the general radial distribution function, Formulation II and Formulation I, respectively.

5.10.1 Uniform radial distribution function (URDF): $g(\hat{r}) = 1$

This event corresponds to the simplest approximation for $g(\hat{r})$ since it tends to underestimate the probability of the surrounding fibers at high fiber volume fraction during the ensemble-area averaging process. Therefore, this case may be regarded as the "lower bound" for microstructure and is more suitable for low fiber concentrations.

Formulation II: By carrying out lengthy algebra and utilizing the identities of Eqs. (5.80), (5.99), and (5.102), the approximate ensemble-area averaged eigenstrain tensor $\left\langle \overline{\boldsymbol{\varepsilon}}_{(1)}^{*} \right\rangle$ can be derived as

$$\left\langle \overline{\boldsymbol{\varepsilon}}_{(1)}^{*} \right\rangle^{UII} = \underset{\sim}{\boldsymbol{\Gamma}}_{(1)}^{UII} : \boldsymbol{\varepsilon}_{(1)}^{*0} \tag{5.105}$$

196

Here, the components of the isotropic tensor $\underset{\sim}{\Gamma}_{(1)}^{\mathrm{UII}}$ are as follows:

$$\underset{\sim}{\Gamma}_{(1)}^{\mathrm{UII}} = \gamma_{11}^{\mathrm{UII}}\delta_{ij}\delta_{kl} + \gamma_{21}^{\mathrm{UII}}\left(\delta_{ik}\delta_{jl} + \delta_{il}\delta_{jk}\right) \tag{5.106}$$

$$\gamma_{11}^{\mathrm{UII}} = \frac{\phi^{(2)}}{4}\mathbf{U}_{21}^{\mathrm{UII}} + \frac{\phi^{(1)}}{4}\mathbf{U}_{11}^{\mathrm{UII}}; \quad \gamma_{21}^{\mathrm{UII}} = \frac{1}{2} + \frac{\phi^{(2)}}{4}\mathbf{V}_{21}^{\mathrm{UII}} + \frac{\phi^{(1)}}{4}\mathbf{V}_{11}^{\mathrm{UII}} \tag{5.107}$$

$$\mathbf{U}_{21}^{\mathrm{UII}} = f_{11}^{\mathrm{U}} + \frac{6}{\beta_1\beta_2}\left[\frac{\lambda^2 + 2\lambda^4}{(1+\lambda)^4} - \frac{\lambda^4 + \lambda^6}{(1+\lambda)^6}\right]; \quad \mathbf{U}_{11}^{\mathrm{UII}} = t_{11}^{\mathrm{U}} + \frac{15}{16\beta_1^2} \tag{5.108}$$

$$\mathbf{V}_{21}^{\mathrm{UII}} = f_{21}^{\mathrm{U}} - \frac{6}{\beta_1\beta_2}\left[\frac{\lambda^2 + 2\lambda^4}{(1+\lambda)^4} - \frac{\lambda^4 + \lambda^6}{(1+\lambda)^6}\right]; \quad \mathbf{V}_{11}^{\mathrm{UII}} = t_{21}^{\mathrm{U}} - \frac{15}{16\beta_1^2} \tag{5.109}$$

$$\lambda = \frac{a_1}{a_2}$$

$$\beta_1 = 4(1-\nu_0)\frac{\mu_0}{\mu_1 - \mu_0} + (3 - 4\nu_0) \tag{5.110}$$

$$\beta_2 = 4(1-\nu_0)\frac{\mu_0}{\mu_2 - \mu_0} + (3 - 4\nu_0)$$

where $\phi^{(2)}$ and $\phi^{(1)}$ are the fiber volume fractions of phase 2 and phase 1, respectively.

Similarly, the approximate ensemble-area averaged eigenstrain tensor $\left\langle \overline{\boldsymbol{\varepsilon}}_{(2)}^* \right\rangle$ is

$$\left\langle \overline{\boldsymbol{\varepsilon}}_{(2)}^* \right\rangle^{\mathrm{UII}} = \underset{\sim}{\Gamma}_{(2)}^{\mathrm{UII}} : \boldsymbol{\varepsilon}_{(2)}^{*0} \tag{5.111}$$

Here, the components of the isotropic tensor $\underset{\sim}{\Gamma}_{(2)}^{\mathrm{UII}}$ read:

$$\underset{\sim}{\Gamma}_{(2)}^{\mathrm{UII}} = \gamma_{12}^{\mathrm{UII}}\delta_{ij}\delta_{kl} + \gamma_{22}^{\mathrm{UII}}\left(\delta_{ik}\delta_{jl} + \delta_{il}\delta_{jk}\right) \tag{5.112}$$

$$\gamma_{12}^{\mathrm{UII}} = \frac{\phi^{(1)}}{4}\mathbf{U}_{12}^{\mathrm{UII}} + \frac{\phi^{(2)}}{4}\mathbf{U}_{22}^{\mathrm{UII}}; \quad \gamma_{22}^{\mathrm{UII}} = \frac{1}{2} + \frac{\phi^{(1)}}{4}\mathbf{V}_{12}^{\mathrm{UII}} + \frac{\phi^{(2)}}{4}\mathbf{V}_{22}^{\mathrm{UII}} \tag{5.113}$$

$$\mathbf{U}_{12}^{\mathrm{UII}} = f_{12}^{\mathrm{U}} + \frac{6}{\beta_1\beta_2}\left[\frac{\eta^2 + 2\eta^4}{(1+\eta)^4} - \frac{\eta^4 + \eta^6}{(1+\eta)^6}\right]; \quad \mathbf{U}_{22}^{\mathrm{UII}} = t_{12}^{\mathrm{U}} + \frac{15}{16\beta_2^2} \tag{5.114}$$

$$\mathbf{V}_{12}^{\text{UII}} = f_{22}^{\text{U}} - \frac{6}{\beta_1 \beta_2} \left[\frac{\eta^2 + 2\eta^4}{(1+\eta)^4} - \frac{\eta^4 + \eta^6}{(1+\eta)^6} \right]; \quad \mathbf{V}_{22}^{\text{UII}} = t_{22}^{\text{U}} - \frac{15}{16\beta_2^2} \tag{5.115}$$

$$\eta = \frac{a_2}{a_1} = \frac{1}{\lambda}$$

$$\beta_1 = 4(1-\nu_0)\frac{\mu_0}{\mu_1 - \mu_0} + (3-4\nu_0) \tag{5.116}$$

$$\beta_2 = 4(1-\nu_0)\frac{\mu_0}{\mu_2 - \mu_0} + (3-4\nu_0)$$

Formulation I: By neglecting the higher-order components $O\left(\rho_1^4 / 2\right)$ associated with $\mathbf{H}^2$ in Eq. (5.85), $O\left(\rho_2^4 / 2\right)$ associated with $\mathbf{H}^2$ in Eq. (5.89), and $O\left(\frac{\rho_1^3 \rho_2 + \rho_1 \rho_2^3}{2}\right)$ associated with $\mathbf{H}^2$ in Eq. (5.88) and following similar procedures as in "Formulation II," the approximate ensemble-area averaged eigenstrain tensor $\left\langle \overline{\boldsymbol{\varepsilon}}_{(1)}^* \right\rangle$ becomes

$$\left\langle \overline{\boldsymbol{\varepsilon}}_{(1)}^* \right\rangle^{\text{UI}} = \underset{\sim}{\boldsymbol{\Gamma}}_{(1)}^{\text{UI}} : \boldsymbol{\varepsilon}_{(1)}^{*0} \tag{5.117}$$

Here, the components of the isotropic tensor $\underset{\sim}{\boldsymbol{\Gamma}}_{(1)}^{\text{UI}}$ are as follows:

$$\underset{\sim}{\boldsymbol{\Gamma}}_{(1)}^{\text{UI}} = \gamma_{11}^{\text{UI}} \delta_{ij} \delta_{kl} + \gamma_{21}^{\text{UI}} \left(\delta_{ik}\delta_{jl} + \delta_{il}\delta_{jk} \right) \tag{5.118}$$

$$\gamma_{11}^{\text{UI}} = \frac{\phi^{(2)}}{4} \mathbf{U}_{21}^{\text{UI}} + \frac{\phi^{(1)}}{4} \mathbf{U}_{11}^{\text{UI}}; \quad \gamma_{21}^{\text{UI}} = \frac{1}{2} + \frac{\phi^{(2)}}{4} \mathbf{V}_{21}^{\text{UI}} + \frac{\phi^{(1)}}{4} \mathbf{V}_{11}^{\text{UI}} \tag{5.119}$$

$$\mathbf{U}_{21}^{\text{UI}} = f_{11}^{\text{U}}; \quad \mathbf{U}_{11}^{\text{UI}} = t_{11}^{\text{U}}; \quad \mathbf{V}_{21}^{\text{UI}} = f_{21}^{\text{U}}; \quad \mathbf{V}_{11}^{\text{UI}} = t_{21}^{\text{U}} \tag{5.120}$$

$$f_{11}^{U} = \frac{-4\lambda^2}{(1+\lambda)^2} \frac{\left\{ \alpha_1 \left[2\alpha_2 + (3-2\nu_0)\beta_2 \right] + \beta_1 \left[4\nu_0\alpha_2 + (2\nu_0+1)\beta_2 \right] \right\}}{\beta_1 \beta_2 (\alpha_1 + \beta_1)(\alpha_2 + \beta_2)}$$

$$t_{11}^{U} = \frac{1}{\beta_1^2} \left[-2 + \frac{(1-2\nu_0)\beta_1}{\alpha_1 + \beta_1} \right]$$

$$f_{21}^{U} = \frac{-4\lambda^2}{(1+\lambda)^2} \frac{(2\alpha_2 + 3\beta_2 - 2\nu_0\beta_2)}{\beta_1 \beta_2 (\alpha_2 + \beta_2)} \tag{5.121}$$

$$t_{21}^{U} = \frac{1}{\beta_1^2} \left[2 + \frac{(1-2\nu_0)\beta_1}{\alpha_1 + \beta_1} \right]$$

$$\alpha_1 = 4(1-\nu_0)\left[\frac{k_0}{k_1 - k_0} - \frac{\mu_0}{\mu_1 - \mu_0} \right] + (4\nu_0 - 1)$$

$$\alpha_2 = 4(1-\nu_0)\left[\frac{k_0}{k_2 - k_0} - \frac{\mu_0}{\mu_2 - \mu_0} \right] + (4\nu_0 - 1) \tag{5.122}$$

Similarly, the approximate ensemble-area averaged eigenstrain tensor $\left\langle \bar{\boldsymbol{\varepsilon}}_{(2)}^{*} \right\rangle$ is

$$\left\langle \bar{\boldsymbol{\varepsilon}}_{(2)}^{*} \right\rangle^{\text{UI}} = \underset{\sim}{\boldsymbol{\Gamma}}_{(2)}^{\text{UI}} : \boldsymbol{\varepsilon}_{(2)}^{*0} \tag{5.123}$$

Here, the components of the isotropic tensor $\underset{\sim}{\boldsymbol{\Gamma}}_{(2)}^{\text{UI}}$ are as follows:

$$\underset{\sim}{\boldsymbol{\Gamma}}_{(2)}^{\text{UI}} = \gamma_{12}^{\text{UI}} \delta_{ij}\delta_{kl} + \gamma_{22}^{\text{UI}} \left(\delta_{ik}\delta_{jl} + \delta_{il}\delta_{jk} \right) \tag{5.124}$$

$$\gamma_{12}^{\text{UI}} = \frac{\phi^{(1)}}{4}\mathbf{U}_{12}^{\text{UI}} + \frac{\phi^{(2)}}{4}\mathbf{U}_{22}^{\text{UI}}; \quad \gamma_{22}^{\text{UI}} = \frac{1}{2} + \frac{\phi^{(1)}}{4}\mathbf{V}_{12}^{\text{UI}} + \frac{\phi^{(2)}}{4}\mathbf{V}_{22}^{\text{UI}} \tag{5.125}$$

$$\mathbf{U}_{12}^{\text{UI}} = f_{12}^{U}; \quad \mathbf{U}_{22}^{\text{UI}} = t_{12}^{U}; \quad \mathbf{V}_{12}^{\text{UI}} = f_{22}^{U}; \quad \mathbf{V}_{22}^{\text{UI}} = t_{22}^{U} \tag{5.126}$$

$$f_{12}^{U} = \frac{-4\eta^2}{(1+\eta)^2} \frac{\left\{\alpha_2\left[2\alpha_1 + (3-2\nu_0)\beta_1\right] + \beta_2\left[4\nu_0\alpha_1 + (2\nu_0+1)\beta_1\right]\right\}}{\beta_1\beta_2(\alpha_1+\beta_1)(\alpha_2+\beta_2)}$$

$$t_{12}^{U} = \frac{1}{\beta_2^2}\left[-2 + \frac{(1-2\nu_0)\beta_2}{\alpha_2+\beta_2}\right]$$

$$f_{22}^{U} = \frac{-4\eta^2}{(1+\eta)^2} \frac{(2\alpha_1 + 3\beta_1 - 2\nu_0\beta_1)}{\beta_1\beta_2(\alpha_1+\beta_1)}$$

(5.127)

$$t_{22}^{U} = \frac{1}{\beta_2^2}\left[2 + \frac{(1-2\nu_0)\beta_2}{\alpha_2+\beta_2}\right]$$

$$\alpha_1 = 4(1-\nu_0)\left[\frac{k_0}{k_1-k_0} - \frac{\mu_0}{\mu_1-\mu_0}\right] + (4\nu_0 - 1)$$

(5.128)

$$\alpha_2 = 4(1-\nu_0)\left[\frac{k_0}{k_2-k_0} - \frac{\mu_0}{\mu_2-\mu_0}\right] + (4\nu_0 - 1)$$

5.10.2 General radial distribution function (GRDF): $g(\hat{r}) \neq 1$

This event corresponds to the complex approximation for $g(\hat{r})$ since it tends to overestimate the probability of the surrounding fibers at low fiber volume fraction during the ensemble-area averaging process. Therefore, this case may be regarded as the "upper bound" for microstructure and is more suitable for high fiber concentrations. For example, at higher volume fractions, it is sometimes assumed that the two-point conditionally probability function obeys the so-called thermodynamic equilibrium radial distribution function (ERDF), also known as accurately in the Percus-Yevick approximation (Hansen and McDonald (1986); Torquato and Lado (1992)), as follows:

$$g(\hat{r}) = H(\hat{r}-1)\left[1 + A(\hat{r})\phi\right]; \quad \hat{r} \equiv r/(a_1+a_2)$$

$$A(\hat{r}) = \frac{4}{\pi}\left[\pi - 2\sin^{-1}\left(\frac{\hat{r}}{2}\right) - \hat{r}\left(1 - \frac{\hat{r}^2}{4}\right)^{1/2}\right]H(2-\hat{r})$$

(5.129)

$$H(x) = \begin{cases} 0, & \text{if } x \leq 0 \\ 1, & \text{if } x > 0 \end{cases} \tag{5.130}$$

Formulation II: We write

$$\left\langle \overline{\boldsymbol{\varepsilon}}_{(1)}^{*} \right\rangle^{\text{GII}} = \underset{\sim}{\boldsymbol{\Gamma}}_{(1)}^{\text{GII}} : \boldsymbol{\varepsilon}_{(1)}^{*0} \tag{5.131}$$

$$\underset{\sim}{\boldsymbol{\Gamma}}_{(1)}^{\text{GII}} = \gamma_{11}^{\text{GII}} \delta_{ij}\delta_{kl} + \gamma_{21}^{\text{GII}}\left(\delta_{ik}\delta_{jl} + \delta_{il}\delta_{jk}\right) \tag{5.132}$$

$$\gamma_{11}^{\text{GII}} = \frac{\phi^{(2)}}{4}\mathbf{U}_{21}^{\text{GII}} + \frac{\phi^{(1)}}{4}\mathbf{U}_{11}^{\text{GII}}; \quad \gamma_{21}^{\text{GII}} = \frac{1}{2} + \frac{\phi^{(2)}}{4}\mathbf{V}_{21}^{\text{GII}} + \frac{\phi^{(1)}}{4}\mathbf{V}_{11}^{\text{GII}} \tag{5.133}$$

$$\mathbf{U}_{21}^{\text{GII}} = f_{11}^{\text{G}} + \left(\frac{1}{\beta_1\beta_2}\right)\left[24\left(2\lambda^4 + \lambda^2\right)\mathbf{Y}_{32}\left(g\right) - 36\left(\lambda^6 + \lambda^4\right)\mathbf{Y}_{52}\left(g\right)\right]$$

$$\mathbf{U}_{11}^{\text{GII}} = t_{11}^{\text{G}} + \left(\frac{1}{\beta_1^2}\right)\left[72\mathbf{Y}_{31}\left(g\right) - 72\mathbf{Y}_{51}\left(g\right)\right] \tag{5.134}$$

$$\mathbf{V}_{21}^{\text{GII}} = f_{21}^{\text{G}} + \left(\frac{1}{\beta_1\beta_2}\right)\left[-24\left(2\lambda^4 + \lambda^2\right)\mathbf{Y}_{32}\left(g\right) + 36\left(\lambda^6 + \lambda^4\right)\mathbf{Y}_{52}\left(g\right)\right]$$

$$\mathbf{V}_{11}^{\text{GII}} = t_{21}^{\text{G}} + \left(\frac{1}{\beta_1^2}\right)\left[-72\mathbf{Y}_{31}\left(g\right) + 72\mathbf{Y}_{51}\left(g\right)\right] \tag{5.135}$$

$$\mathbf{Y}_{32}\left(g\right) = \int_0^{\frac{1}{1+\lambda}} \rho_2^3 g\left(\rho_2\right)\mathrm{d}\rho_2; \quad \mathbf{Y}_{52}\left(g\right) = \int_0^{\frac{1}{1+\lambda}} \rho_2^5 g\left(\rho_2\right)\mathrm{d}\rho_2$$

$$\mathbf{Y}_{31}\left(g\right) = \int_0^{\frac{1}{2}} \rho_1^3 g\left(\rho_1\right)\mathrm{d}\rho_1; \quad \mathbf{Y}_{51}\left(g\right) = \int_0^{\frac{1}{2}} \rho_1^5 g\left(\rho_1\right)\mathrm{d}\rho_1 \tag{5.136}$$

Similarly, we have

$$\left\langle \overline{\boldsymbol{\varepsilon}}_{(2)}^{*} \right\rangle^{\text{GII}} = \underset{\sim}{\boldsymbol{\Gamma}}_{(2)}^{\text{GII}} : \boldsymbol{\varepsilon}_{(2)}^{*0} \tag{5.137}$$

$$\underset{\sim}{\boldsymbol{\Gamma}}_{(2)}^{\text{GII}} = \gamma_{12}^{\text{GII}} \delta_{ij}\delta_{kl} + \gamma_{22}^{\text{GII}}\left(\delta_{ik}\delta_{jl} + \delta_{il}\delta_{jk}\right) \tag{5.138}$$

$$\gamma_{12}^{\mathrm{GII}} = \frac{\phi^{(1)}}{4} \mathbf{U}_{12}^{\mathrm{GII}} + \frac{\phi^{(2)}}{4} \mathbf{U}_{22}^{\mathrm{GII}}; \quad \gamma_{22}^{\mathrm{GII}} = \frac{1}{2} + \frac{\phi^{(1)}}{4} \mathbf{V}_{12}^{\mathrm{GII}} + \frac{\phi^{(2)}}{4} \mathbf{V}_{22}^{\mathrm{GII}} \tag{5.139}$$

$$\mathbf{U}_{12}^{\mathrm{GII}} = f_{12}^{\mathrm{G}} + \left(\frac{1}{\beta_1 \beta_2}\right) \left[24\left(2\eta^4 + \eta^2\right) \mathrm{P}_{31}(g) - 36\left(\eta^6 + \eta^4\right) \mathrm{P}_{51}(g) \right]$$

$$\mathbf{U}_{22}^{\mathrm{GII}} = t_{12}^{\mathrm{G}} + \left(\frac{1}{\beta_2^2}\right) \left[72 \mathrm{P}_{32}(g) - 72 \mathrm{P}_{52}(g) \right] \tag{5.140}$$

$$\mathbf{V}_{12}^{\mathrm{GII}} = f_{22}^{\mathrm{G}} + \left(\frac{1}{\beta_1 \beta_2}\right) \left[-24\left(2\eta^4 + \eta^2\right) \mathrm{P}_{31}(g) + 36\left(\eta^6 + \eta^4\right) \mathrm{P}_{51}(g) \right]$$

$$\mathbf{V}_{22}^{\mathrm{GII}} = t_{22}^{\mathrm{G}} + \left(\frac{1}{\beta_2^2}\right) \left[-72 \mathrm{P}_{32}(g) + 72 \mathrm{P}_{52}(g) \right] \tag{5.141}$$

$$\mathrm{P}_{31}(g) = \int\limits_0^{\frac{1}{1+\eta}} \rho_1^3 g(\rho_1) \mathrm{d}\rho_1; \quad \mathrm{P}_{51}(g) = \int\limits_0^{\frac{1}{1+\eta}} \rho_1^5 g(\rho_1) \mathrm{d}\rho_1$$

$$\mathrm{P}_{32}(g) = \int\limits_0^{\frac{1}{2}} \rho_2^3 g(\rho_2) \mathrm{d}\rho_2; \quad \mathrm{P}_{52}(g) = \int\limits_0^{\frac{1}{2}} \rho_2^5 g(\rho_2) \mathrm{d}\rho_2 \tag{5.142}$$

Formulation I: We write

$$\left\langle \overline{\boldsymbol{\varepsilon}}_{(1)}^* \right\rangle^{\mathrm{GI}} = \underset{\sim}{\boldsymbol{\Gamma}}_{(1)}^{\mathrm{GI}} : \boldsymbol{\varepsilon}_{(1)}^{*0} \tag{5.143}$$

$$\underset{\sim}{\boldsymbol{\Gamma}}_{(1)}^{\mathrm{GI}} = \gamma_{11}^{\mathrm{GI}} \delta_{ij} \delta_{kl} + \gamma_{21}^{\mathrm{GI}} \left(\delta_{ik} \delta_{jl} + \delta_{il} \delta_{jk} \right) \tag{5.144}$$

$$\gamma_{11}^{\mathrm{GI}} = \frac{\phi^{(2)}}{4} \mathbf{U}_{21}^{\mathrm{GI}} + \frac{\phi^{(1)}}{4} \mathbf{U}_{11}^{\mathrm{GI}}; \quad \gamma_{21}^{\mathrm{GI}} = \frac{1}{2} + \frac{\phi^{(2)}}{4} \mathbf{V}_{21}^{\mathrm{GI}} + \frac{\phi^{(1)}}{4} \mathbf{V}_{11}^{\mathrm{GI}} \tag{5.145}$$

$$\mathbf{U}_{21}^{\mathrm{GI}} = f_{11}^{\mathrm{G}}; \quad \mathbf{U}_{11}^{\mathrm{GI}} = t_{11}^{\mathrm{G}}; \quad \mathbf{V}_{21}^{\mathrm{GI}} = f_{21}^{\mathrm{G}}; \quad \mathbf{V}_{11}^{\mathrm{GI}} = t_{21}^{\mathrm{G}} \tag{5.146}$$

$$f_{11}^{G} = \frac{\omega_{11}}{\beta_1 \beta_2} Y_{12}(g) 4\lambda^2$$

$$t_{11}^{G} = \frac{4S_{11}}{\beta_1^2} Y_{11}(g)$$

$$f_{21}^{G} = \frac{\omega_{12}}{\beta_1 \beta_2} Y_{12}(g) 4\lambda^2 \qquad (5.147)$$

$$t_{21}^{G} = \frac{4S_{12}}{\beta_1^2} Y_{11}(g)$$

$$\omega_{11} = \frac{-2\left\{\alpha_1\left[2\alpha_2 + (3-2\nu_0)\beta_2\right] + \beta_1\left[4\nu_0\alpha_2 + (2\nu_0+1)\beta_2\right]\right\}}{(\alpha_1+\beta_1)(\alpha_2+\beta_2)}$$

$$\omega_{12} = \frac{2\left[2\alpha_2 + (3-2\nu_0)\beta_2\right]}{\alpha_2+\beta_2}$$

$$S_{11} = 2\left[-2 + \frac{(1-2\nu_0)\beta_1}{\alpha_1+\beta_1}\right] \qquad (5.148)$$

$$S_{12} = 2\left[2 + \frac{(1-2\nu_0)\beta_1}{\alpha_1+\beta_1}\right]$$

$$Y_{11}(g) = \int_0^{\frac{1}{2}} \rho_1 g(\rho_1) d\rho_1$$

$$Y_{12}(g) = \int_0^{\frac{1}{1+\lambda}} \rho_2 g(\rho_2) d\rho_2 \qquad (5.149)$$

Similarly, we write

$$\left\langle \overline{\boldsymbol{\varepsilon}}_{(2)}^{*} \right\rangle^{GI} = \mathbf{\underset{\sim}{\Gamma}}_{(2)}^{GI} : \boldsymbol{\varepsilon}_{(2)}^{*0} \qquad (5.150)$$

$$\mathbf{\underset{\sim}{\Gamma}}_{(2)}^{GI} = \gamma_{12}^{GI} \delta_{ij} \delta_{kl} + \gamma_{22}^{GI}\left(\delta_{ik}\delta_{jl} + \delta_{il}\delta_{jk}\right) \qquad (5.151)$$

$$\gamma_{12}^{GI} = \frac{\phi^{(1)}}{4} U_{12}^{GI} + \frac{\phi^{(2)}}{4} U_{22}^{GI}; \quad \gamma_{22}^{GI} = \frac{1}{2} + \frac{\phi^{(1)}}{4} V_{12}^{GI} + \frac{\phi^{(2)}}{4} V_{22}^{GI} \qquad (5.152)$$

$$U_{12}^{GI} = f_{12}^{G}; \quad U_{22}^{GI} = t_{12}^{G}; \quad V_{12}^{GI} = f_{22}^{G}; \quad V_{22}^{GI} = t_{22}^{G} \qquad (5.153)$$

$$f_{12}^{G} = \frac{e_{11}}{\beta_1 \beta_2} P_{11}(g) 4\eta^2$$

$$t_{12}^{G} = \frac{4g_{11}}{\beta_2^2} P_{12}(g)$$

$$f_{22}^{G} = \frac{e_{12}}{\beta_1 \beta_2} P_{11}(g) 4\eta^2$$ (5.154)

$$t_{22}^{G} = \frac{4g_{12}}{\beta_2^2} P_{12}(g)$$

$$e_{11} = \frac{-2\left\{\alpha_2\left[2\alpha_1 + (3-2\nu_0)\beta_1\right] + \beta_2\left[4\nu_0\alpha_1 + (2\nu_0+1)\beta_1\right]\right\}}{(\alpha_1 + \beta_1)(\alpha_2 + \beta_2)}$$

$$e_{12} = \frac{2\left[2\alpha_1 + (3-2\nu_0)\beta_1\right]}{\alpha_1 + \beta_1}$$

$$g_{11} = 2\left[-2 + \frac{(1-2\nu_0)\beta_2}{\alpha_2 + \beta_2}\right]$$ (5.155)

$$g_{12} = 2\left[2 + \frac{(1-2\nu_0)\beta_2}{\alpha_2 + \beta_2}\right]$$

$$P_{11}(g) = \int_0^{\frac{1}{1+\eta}} \rho_1 g(\rho_1) \mathrm{d}\rho_1$$

$$P_{12}(g) = \int_0^{\frac{1}{2}} \rho_2 g(\rho_2) \mathrm{d}\rho_2$$ (5.156)

5.11 References

[1] Adams, D. F., and Crane, D. A. (1984). "Finite-element micromechanical analysis of a unidirectional composite including longitudinal shear loading." *Computers & Structures*, 18(6), 1153-1165.

[2] Banthia, N., and Gupta, R. (2004). "Hybrid fiber reinforced concrete (HyFRC): fiber synergy in high strength matrices." *Materials and Structures*, 37(274), 707-716.

[3] Banthia, N., and Nandakumar, N. (2003). "Crack growth resistance of hybrid fiber reinforced cement composites." *Cement & Concrete Composites*, 25(1), 3-9.

[4] Banthia, N., and Soleimani, S. M. (2005). "Flexural response of hybrid fiber-reinforced cementitious composites." *Aci Materials Journal*, 102(6), 382-389.

[5] Benveniste, Y. (1987). "A new approach to the application of mori-tanaka theory in composite-materials." *Mechanics of Materials*, 6(2), 147-157.

[6] Blunt, J., and Ostertag, C. P. (2009). "Performance-based approach for the design of a deflection hardened hybrid fiber-reinforced concrete." *Journal of Engineering Mechanics-Asce*, 135(9), 978-986.

[7] Christensen, R. M., and Lo, K. H. (1979). "Solutions for effective shear properties in 3 phase sphere and cylinder models." *Journal of the Mechanics and Physics of Solids*, 27(4), 315-330.

[8] Doghri, I., and Friebel, C. (2005). "Effective elasto-plastic properties of inclusion-reinforced composites. Study of shape, orientation and cyclic response." *Mechanics of Materials*, 37(1), 45-68.

[9] Duan, H. L., Wang, J., Huang, Z. P., and Luo, Z. Y. (2005). "Stress concentration tensors of

inhomogeneities with interface effects." *Mechanics of Materials*, 37(7), 723-736.

[10] Eshelby, J. D. (1957). "The determination of the elastic field of an ellipsoidal inclusion, and related problems." *Proceedings of the Royal Society of London Series a-Mathematical and Physical Sciences*, 241(1226), 376-396.

[11] Hansen, J. P., and McDonald, I. R. (1986). "Theory of simple liquids. Second edition." *Theory of simple liquids. Second edition*.

[12] Hashin, Z. (1962). "The elastic moduli of heterogeneous materials." *Journal of the Applied Mechanics*, 29, 143-150.

[13] Hashin, Z. (1965). "On elastic behaviour of fibre reinforced materials of arbitrary transverse phase geometry." *Journal of the Mechanics and Physics of Solids*, 13(3), 119-134.

[14] Hashin, Z. (1972). "Theory of fiber reinforced materials." NASA CR-1974.

[15] Hashin, Z., Rosen, B.W. (1964). "The elastic moduli of fiber-reinforced materials. " *J. Appl. Mech.*, **31**, 223–232

[16] Hashin, Z., and Shtrikman, S. (1962b). "A variational approach to the theory of the elastic behaviour of polycrystals." *Journal of the Mechanics and Physics of Solids*, 10(4), 343-352.

[17] Hashin, Z., and Shtrikman, S. (1962a). "On some variational principles in anisotropic and nonhomogeneous elasticity." *Journal of the Mechanics and Physics of Solids*, 10(4), 335-342.

[18] Hill, R. (1964). "Theory of mechanical properties of fibre-strengthened materials .1. elastic behaviour." *Journal of the Mechanics and Physics of Solids*, 12(4), 199-212.

[19] Hill, R. (1964). "Theory of mechanical properties of fibre-strengthened materials .2. inelastic behaviour." *Journal of the Mechanics and Physics of Solids*, 12(4), 213-218.

[20] Hill, R. (1965a). "Theory of mechanical properties of fibre-strengthened materials .3.

self-consistent model." *Journal of the Mechanics and Physics of Solids*, 13(4), 189-198.

[21] Hill, R. (1965b). "A self-consistent mechanics of composite materials." *Journal of the Mechanics and Physics of Solids*, 13(4), 213-222.

[22] Honein, E. (1991). "Multiple inclusions in elastostatics." Ph.D. Dissertation at Stanford University.

[23] Huang, Z. P., and Sun, L. (2007). "Size-dependent effective properties of a heterogeneous material with interface energy effect: from finite deformation theory to infinitesimal strain analysis." *Acta Mechanica*, 190(1-4), 151-163.

[24] Huang, Z. P., and Wang, J. (2006). "A theory of hyperelasticity of multi-phase media with surface/interface energy effect." *Acta Mechanica*, 182(3-4), 195-210.

[25] Ju, J. W., and Chen, T. M. (1994b). "Effective elastic-moduli of 2-phase composites containing randomly dispersed spherical inhomogeneities." *Acta Mechanica*, 103(1-4), 123-144.

[26] Ju, J. W., and Chen, T. M. (1994c). "Micromechanics and effective elastoplastic behavior of 2-phase metal-matrix composites." *Journal of Engineering Materials and Technology-Transactions of the Asme*, 116(3), 310-318.

[27] Ju, J. W., and Chen, T. M. (1994a). "Micromechanics and effective moduli of elastic composites containing randomly dispersed ellipsoidal inhomogeneities." *Acta Mechanica*, 103(1-4), 103-121.

[28] Ju, J. W., and Ko, Y. F. (2008). "Micromechanical elastoplastic damage modeling of progressive interfacial arc debonding for fiber reinforced composites." *International Journal of Damage Mechanics*, 17(4), 307-356.

[29] Ju, J. W., and Ko, Y. F. (2008). "Micromechanical elastoplastic damage modeling of

progressive interfacial arc debonding for fiber reinforced composites." *International Journal of Damage Mechanics*, 17(4), 307-356.

[30] Ju, J. W., Ko, Y. F., and Ruan, H. N. (2006). "Effective elastoplastic damage mechanics for fiber-reinforced composites with evolutionary complete fiber debonding." *International Journal of Damage Mechanics*, 15(3), 237-265.

[31] Ju, J. W., Ko, Y. F., and Ruan, H. N. (2008). "Effective elastoplastic damage mechanics for fiber reinforced composites with evolutionary partial fiber debonding." *International Journal of Damage Mechanics*, 17(6), 493-537.

[32] Ju, J. W., Ko, Y. F., and Zhang, X. D. (2009). "Multi-level elastoplastic damage mechanics for elliptical fiber-reinforced composites with evolutionary fiber debonding." *International Journal of Damage Mechanics*, 18(5), 419-460.

[33] Ju, J. W., and Lee, H. K. (2000). "A micromechanical damage model for effective elastoplastic behavior of ductile matrix composites considering evolutionary complete particle debonding." *Computer Methods in Applied Mechanics and Engineering*, 183(3-4), 201-222.

[34] Ju, J. W., and Lee, H. K. (2001). "A micromechanical damage model for effective elastoplastic behavior of partially debonded ductile matrix composites." *International Journal of Solids and Structures*, 38(36-37), 6307-6332.

[35] Ju, J. W., and Sun, L. Z. (1999). "A novel formulation for the exterior-point Eshelby's tensor of an ellipsoidal inclusion." *Journal of Applied Mechanics-Transactions of the Asme*, 66(2), 570-574.

[36] Ju, J. W., and Sun, L. Z. (2001). "Effective elastoplastic behavior of metal matrix composites containing randomly located aligned spheroidal inhomogeneities. Part I:

micromechanics-based formulation." *International Journal of Solids and Structures*, 38(2), 183-201.

[37] Ju, J. W., and Tseng, K. H. (1996). "Effective elastoplastic behavior of two-phase ductile matrix composites: A micromechanical framework." *International Journal of Solids and Structures*, 33(29), 4267-4291.

[38] Ju, J. W., and Tseng, K. H. (1997). "Effective elastoplastic algorithms for ductile matrix composites." *Journal of Engineering Mechanics-Asce*, 123(3), 260-266.

[39] Ju, J. W., and Yanase, K. (2009). "Micromechanical Elastoplastic Damage Mechanics for Elliptical Fiber-Reinforced Composites with Progressive Partial Fiber Debonding." *International Journal of Damage Mechanics*, 18(7), 639-668.

[40] Ju, J. W., and Yanase, K. (2010). "Micromechanics and effective elastic moduli of particle-reinforced composites with near-field particle interactions." *Acta Mechanica*, 215(1-4), 135-153.

[41] Ju, J. W., and Yanase, K. (2011). "Micromechanical effective elastic moduli of continuous fiber-reinforced composites with near-field fiber interactions." *Acta Mechanica*, 216(1-4), 87-103.

[42] Ju, J. W., and Yanase, K. (2011). "Size-dependent probabilistic micromechanical damage mechanics for particle-reinforced metal matrix composites." *International Journal of Damage Mechanics*, 20(7), 1021-1048.

[43] Ju, J. W., Yanase, K., and Asme (2008). "Elastoplastic micromechanical damage mechanics for composites with progressive partial fiber debonding and thermal residual stress." *Proceedings of the Asme International Mechanical Engineering Congress and Exposition 2007, Vol 13: Processing and Engineering Applications of Novel Materials*, 277-281.

[44] Ju, J. W., and Zhang, X. D. (1998). "Micromechanics and effective transverse elastic moduli of composites with randomly located aligned circular fibers." *International Journal of Solids and Structures*, 35(9-10), 941-960.

[45] Ju, J. W., and Zhang, X. D. (2001). "Effective elastoplastic behavior of ductile matric composites containing randomly located aligned circular fibers." *International Journal of Solids and Structures*, 38(22-23), 4045-4069.

[46] Ko, Y.F. (2005). "Effective elastoplastic-damage model for fiber-reinforced metal matrix composites with evolutionary fibers debonding." Ph.D. Dissertation, University of California, Los Angeles.

[47] Ko, Y.-F., and Ju, J. W. (2012). "New higher-order bounds on effective transverse elastic moduli of three-phase fiber-reinforced composites with randomly located and interacting aligned circular fibers." *Acta Mechanica*, 223(11), 2437-2458.

[48] Ko, Y.-F., and Ju, J. W. (2013). "Effective transverse elastic moduli of three-phase hybrid fiber-reinforced composites with randomly located and interacting aligned circular fibers of distinct elastic properties and sizes." *Acta Mechanica*, 224(1), 157-182.

[49] Ko, Y. F., and Ju, J. W. (2013). "Effects of fiber cracking on elastoplastic-damage behavior of fiber-reinforced metal matrix composites." *International Journal of Damage Mechanics*, 22(1), 48-67.

[50] Kondo, K., Saito, N. (1986). "The influence of random fiber packing on the elastic properties of unidirectional composites." In: Composites '86: Recent Advances in Japan and the United States. Proceedings of Japan-U.S. CCM-III

[51] Lee, H. K., and Ju, J. W. (2008). "3D micromechanics and effective moduli for brittle composites with randomly located interacting microcracks and inclusions." *International*

Journal of Damage Mechanics, 17(5), 377-417.

[52] Lin, P. J., and Ju, J. W. (2009). "Effective elastic moduli of three-phase composites with randomly located and interacting spherical particles of distinct properties." *Acta Mechanica*, 208(1-2), 11-26.

[53] Liu, H. T., and Sun, L. Z. (2004). "Effects of thermal residual stresses on effective elastoplastic behavior of metal matrix composites." *International Journal of Solids and Structures*, 41(8), 2189-2203.

[54] Liu, H. T., Sun, L. Z., and Ju, J. W. (2004). "An interfacial debonding model for particle-reinforced composites." *International Journal of Damage Mechanics*, 13(2), 163-185.

[55] Liu, H. T., Sun, L. Z., and Ju, J. W. (2006). "Elastoplastic modeling of progressive interfacial debonding for particle-reinforced metal-matrix composites." *Acta Mechanica*, 181(1-2), 1-17.

[56] Milton, G. W. (1982). "Bounds on the elastic and transport-properties of 2-component composites." *Journal of the Mechanics and Physics of Solids*, 30(3), 177-191.

[57] Milton, G. W., and Phanthien, N. (1982). "New bounds on effective elastic-moduli of 2-component materials." *Proceedings of the Royal Society of London Series a-Mathematical Physical and Engineering Sciences*, 380(1779), 305-331.

[58] Mori, T., and Tanaka, K. (1973). "Average stress in matrix and average elastic energy of materials with misfitting inclusions." *Acta Metallurgica*, 21(5), 571-574.

[59] Mura, T. (1987). "Micromechanics of defects in solids." 2nd edn. Kluwer, The Netherlands.

[60] Nemat-Nasser, S., Hori, M. (1993). "Micromechanics: overall properties of heterogeneous materials." Elsevier Science Publisher B. V., Netherlands.

[61] Nimmer, R. P., Bankert, R. J., Russell, E. S., Smith, G. A., and Wright, P. K. (1991). "Micromechanical modeling of fiber matrix interface effects in transversely loaded sic ti-6-4 metal matrix composites." *Journal of Composites Technology & Research*, 13(1), 3-13.

[62] Sharma, P., and Ganti, S. (2004). "Size-dependent Eshelby's tensor for embedded nano-inclusions incorporating surface/interface energies." *Journal of Applied Mechanics-Transactions of the Asme*, 71(5), 663-671.

[63] Silnutzer, N. (1972). "Effective constants of statistically homogeneous materials." Ph.D. Thesis, University of Pennsylvania.

[64] Soliman, E., Al-Haik, M., and Taha, M. R. (2012). "On and off-axis tension behavior of fiber reinforced polymer composites incorporating multi-walled carbon nanotubes." *Journal of Composite Materials*, 46(14), 1661-1675.

[65] Sun, L. Z., and Ju, J. W. (2001). "Effective elastoplastic behavior of metal matrix composites containing randomly located aligned spheroidal Inhomogeneities. Part II: applications." *International Journal of Solids and Structures*, 38(2), 203-225.

[66] Sun, L. Z., Ju, J. W., and Liu, H. T. (2003). "Elastoplastic modeling of metal matrix composites with evolutionary particle debonding." *Mechanics of Materials*, 35(3-6), 559-569.

[67] Sun, L. Z., Liu, H. T., and Ju, J. W. (2003). "Effect of particle cracking on elastoplastic behaviour of metal matrix composites." *International Journal for Numerical Methods in Engineering*, 56(14), 2183-2198.

[68] Torquato, S., and Lado, F. (1992). "Improved bounds on the effective elastic-moduli of random arrays of cylinders." *Journal of Applied Mechanics-Transactions of the Asme*, 59(1),

1-6.

[69] Walpole, L. J. (1966b). "On bounds for overall elastic moduli of inhomogeneous systems .2." *Journal of the Mechanics and Physics of Solids*, 14(5), 289-301.

[70] Walpole, L. J. (1966a). "On bounds for overall elastic moduli of inhomogeneous systems .i." *Journal of the Mechanics and Physics of Solids*, 14(3), 151-162.

[71] Walpole, L. J. (1969). "On overall elastic moduli of composite materials." *Journal of the Mechanics and Physics of Solids*, 17(4), 235-251.

[72] Wang, M., Zhang, Z., and Sun, Z. (2009). "The hybrid model and mechanical properties of hybrid composites reinforced with different diameter fibers." *Journal of Reinforced Plastics and Composites*, 28(3), 257-264.

[73] Weng, G. J. (1990). "The theoretical connection between mori tanaka theory and the hashin shtrikman walpole bounds." *International Journal of Engineering Science*, 28(11), 1111-1120.

[74] Zhao, Y. H., Tandon, G. P., and Weng, G. J. (1989). "Elastic-moduli for a class of porous materials." *Acta Mechanica*, 76(1-2), 105-130.

Chapter 6

PARTICLE-SIZE AND INTERFACE ENERGY EFFECTS ON ENERGY DISSIPATION DUE TO INTERFACIAL DEBONDING IN NANOCOMPOSITES

ABSTRACT

In this chapter, both of the particle-size and interface/surface energy effects on the energy dissipation due to the interfacial debonding between the particles and the matrix in nanocomposites are investigated. The size distribution of particles is supposed to comply to the logarithmic normal distribution, while the probability of the interfacial debonding between the particles and the matrix is considered to satisfy the Weibull's distribution function. Then, the formulation of the energy dissipation due to the interfacial debonding is developed. Accordingly, several results regarding the particle-size and interface/surface energy effects on the energy dissipation due to the damage evolution are illustrated after a series of numerical calculations. Among these numerical results, the damage energy dissipation crest with respect to the average size of particles is found to demonstrate that the energy dissipation due to the damage evolution extremely depends on the size of particles and interface/surface energy in nanocomposites.

Key Words: Particle-size effect; Interface/surface energy effect; Energy dissipation; Interfacial

debonding; Damage evolution; Nanocomposite

6.1 Introduction

It is well known that the toughness of materials mainly depends on the energy dissipation, and this topic is especially significant for the research on the mechanical behavior and physical property of composite materials. Hence, many researchers devote their attention to work on the mechanism of the energy dissipation in toughening polymeric matrix materials filled with nano-size particles (Kurauchi and Ohta, 1984; Bai et al., 2001). Nowadays, these kinds of nanocomposites have been extensively used as advanced engineering materials. When it comes to nano-size particles, for example, calcium carbonate (Avella et al., 2001; Thio et al., 2002), silica (Musto et al., 2004; Rong et al., 2004), and clay (Varlot et al., 2001) are very popular nano-size particles in composites.

The energy dissipation due to the damage evolution in particle-filled polymers is mainly induced by the interfacial debonding between the particles and the matrix. Although the energy dissipation due to the damage evolution, namely damage energy dissipation, is usually much less than the viscous dissipation and/or plastic dissipation, it may cause the eventual failure of the composites. Accordingly, the strength of composites is definitely influenced by the damage evolution. Even though nano-size particles are relatively very small in composites, the interfacial debonding between the particles and the matrix could still happen under the action of some special conditions, such as the application of the high triaxial-stress loading.

In this chapter, the damage energy dissipation between the nano-size particles and the

polymeric matrix in nanocomposites will be investigated based on the following assumptions and steps. Firstly, the size distribution of particles is supposed to obey the logarithmic normal function, and the probability of the interfacial debonding is considered to agree with the Weibull's distribution function. Secondly, the total area of the interfaces is established in terms of the total number of the debonded particles per unit volume. Thirdly, by the combination of the concepts in the first two steps, the analytical equation of the energy dissipation due to the interfacial debonding can be formulated. Lastly, after the analytical equation is developed, a series of the numerical calculations, as well as several numerical results, would be executed. In the meanwhile, the effects of the loading magnitude, the interface/surface energy, the volume fraction of particles, the average radius of particles, and the particle-size dispersion on the damage energy dissipation may be discussed numerically as well. Therefore, the size effect of particles on the energy dissipation due to the damage evolution can be studied based on the numerical results. Further, the energy dissipation due to the damage evolution is found to be obviously affected by the size effect of particles.

In addition, because the composites containing nano-scale particles are concerned, the damage energy dissipation is considered to be strongly affected by the interface/surface energy between particles and the matrix as well. The numerical results with the distinct interface/surface energies are discussed in the following. The introduction to the interface/surface energy can be found in Chapter 1.

6.2 Formulation of Damage Energy Dissipation in nanocomposites

Suppose that the polymeric matrix can be treated as viscoelastic materials in nanocomposites, and the full damage evolution takes place due to the interfacial debonding between the particles and the matrix in nanocomposites under the application of external loads. Furthermore, the shape of particles is assumed to be spherical, and the full interfacial debonding between particles and the matrix comes up under the action of the high triaxial-stress loading. Suppose that there is a single particle embedded in the viscoelastic matrix material, the critical value of the average normal stress at the interface between a particle and the viscoelastic matrix can be approximately expressed by

$$\sigma_{cr} \approx \sqrt{\frac{\gamma}{a} \cdot \frac{4E(0)}{(1+v)}} \tag{6.1}$$

where γ is the interface/surface energy (both two bonded surfaces between the particle and the matrix); a is the radius of a particle; $E(0)$ is the initial modulus of the viscoelastic matrix; v is the Poisson's ratio of the matrix, which is assumed to be a constant. The detailed formulation of the critical value of the average normal stress at the interface between a particle and the viscoelastic matrix is derived in Section 6.5 Appendix A. From Eq. (6.1), it is found that the critical normal stress at the interface is related to the size of a particle, while the size of each particle is varied.

In addition, suppose that the size distribution of particles obeys the logarithmic normal distribution, and the corresponding analytical equation can be obtained from the research by J.K. Chen et al. (2003; 2006), which is shown in the following

$$n_p(a) = \frac{N_p}{\sqrt{2\pi}a \ln \omega} \cdot \exp\left[-\frac{\ln^2(a/a_0)}{2\ln^2 \omega}\right]$$

$$\tag{6.2}$$

$$a_{min} \le a \le a_{max}$$

217

where a_o is the average radius of particles; $a_{\min}$ and $a_{\max}$ are the minimum radius and maximum radius of particles, respectively; ω is the particle-size dispersion; N_p is the total number of particles per unit volume.

Let the initial volume fraction of particles is f_{p0}, accordingly, N_p may be written as

$$N_p = \frac{f_{p0}}{(4/3)\pi a_0^3}$$

(6.3)

Moreover, the Weibull's distribution function is used to represent the probability of interfacial debonding, P, and it can be characterized by

$$P = 1 - \exp\left[-\left(\frac{\sigma - \sigma_{cr}}{\sigma_u}\right)^m\right]$$

$$\sigma \geq \sigma_{cr}$$

(6.4)

where σ_u and m are material parameters; σ is the average normal stress at the interface. Suppose that the stress tensor of a particle is denoted by $\boldsymbol{\sigma_p}$, then, the average normal stress at the interface can be formed by

$$\sigma = \frac{1}{A}\int_A \boldsymbol{n} \cdot \boldsymbol{\sigma_p} \cdot \boldsymbol{n}\, dA$$

(6.5)

where A is the total surface area of a particle; $\boldsymbol{n}$ is the unit normal vector of the surface. If the remote stress or remote strain is given, the stress tensor of a particle, $\boldsymbol{\sigma_p}$, may be derived by using the Eshelby's equivalent inclusion method (Eshelby, 1957; Chen et al., 2003) and Ju and Chen's scheme (Ju and Chen, 1994a; 1994b) or Mori-Tanaka's scheme (Mori and Tanaka, 1973). The detailed derivation is described in Section 6.6 Appendix B.

Suppose that $\sigma > \sigma_{cr}$ is considered, the number of the debonded particles per unit volume

with the radius between a and $a+da$ can be expressed by

$$n_N\left(a,\sigma\right)=n_p\left(a\right)Pda \tag{6.6}$$

Then, the total surface area of the debonded particles in a unit volume of the composite is obtained as the following equation,

$$S=\int_{a_{\min}}^{a_{\max}}4\pi a^2 n_N da \tag{6.7}$$

Further, suppose that the interfacial debonding between the particles and the matrix comes up, the elastic strain energy stored in the matrix and the particles will release to form new surfaces. If the interface/surface energy of all interfaces between the particles and the matrix is assumed to be the same, that is, γ is a constant, the energy dissipation due to damage evolution may be developed by

$$U_d=\gamma\cdot S=\gamma\int_{a_{\min}}^{a_{\max}}4\pi a^2 n_N da \tag{6.8}$$

where γ is the interface/surface energy (both two bonded surfaces between the particle and the matrix). If the average normal stress of particles, σ, is determined, therefore, the energy dissipation due to damage evolution, U_d, can be obtained by Eq. (6.8).

6.3 Numerical Results for Size Effect of Particles on Damage Energy Dissipation

The research objective regarding the investigation of the size effect between the nano-size and micro-size particles on the energy dissipation due to the interfacial debonding between the particles and the matrix is pretty complex. In general, when the volume fraction, f_{p0}, is given,

the total surface area of the nano-size particles is much larger than that of the micro-size particles. Specifically, more energy dissipation due to the interfacial debonding between the particles of nanometer size and the polymeric matrix occurs than that between the particles of micrometer size and the polymeric matrix if supposed that full interfacial deboinding takes place between all particles and the matrix. In other words, the smaller the size of particles that the polymeric matrix is filled with, the more difficult the possibility of interfacial debonding becomes. Accordingly, it is also possible that the energy dissipation due to the damage evolution between the particles of nanometer size and the matrix is less than that between the particles of micrometer size and the matrix because of the decreased probability of the interfacial debonding. Therefore, the size effect of the energy dissipation due to the damage evolution is very challenging and worthy to study attentively.

In nanocomposites, the size effect of the nano-size particles on the macroscopic properties of the composites is notable. Since the size distribution of particles is a continuous function, the size effect of particles on the damage evolution is studied statistically. Specifically, the variation of U_d against the average radius, a_0, the interface/surface energy, γ, and particle-size dispersion, ω, is investigated in this section.

Suppose that the material parameters of the following numerical results are chosen as

$$v = 0.4$$

$$f_{p0} = 0.1$$

$$E(0) = 1.6 \ GPa$$

$$\gamma = 0.01 \ J/m^2$$

$$\sigma_u = 0.2E(0)$$

$$\omega = 1.5$$

$$m = 2$$

$$a_{\min} = 0.1 nm$$

$$a_{\max} = 100 \ \mu m$$

Then, the numerical results of the energy dissipation due to the damage evolution, namely, the damage energy dissipation against the average radius of particles are illustrated in **Figures 6.1-6.13**. Furthermore, the digitized points in **Figures 6.1-6.6** are given by J.K. Chen's research (Chen et al., 2007), which are used for the comparison of the numerical results between Ju and Chen's scheme (Ju and Chen, 1994a; 1994b) and Mori-Tanaka's scheme (Mori and Tanaka, 1973).

The plots of U_d against a_0 with different values of f_{p0} are shown in **Figures 6.1-6.4**. From **Figure 6.1**, it can be seen that if the average radius of particles, a_0, is in the range of nanometer size, the damage energy dissipation increases monotonically with the increase of a_0. On the contrary, the illustrative result in **Figure 6.2** shows that the damage energy dissipation decreases monotonically with the increase of a_0 if a_0 is in the range of micrometer size.

Similarly, **Figures 6.3 and 6.4** display the curve of the damage energy dissipation against the average radius of particles in the case of the larger interface/surface energy, $\gamma = 0.05 \, J / m^2$. Under this situation, the damage energy dissipation in the composites filled with particles of nanometer size, called nanocomposites, could be less than that in composites filled with particles of micrometer size, called microcomposites.

It is obvious that the size effect of the particles of nanometer size on the damage energy dissipation is quite different from that of the particles of micrometer size. This kind of phenomenon is deserving of notice and discussion. For the illustrations of the damage energy dissipation against the average radius of particles of micrometer size, as shown in **Figures 6.2 and 6.4**, the results are acceptable. It is easy to recognize a concept that the interfacial debonding between the matrix and the particles of the smaller size may produce more damage energy dissipation since the particles of the smaller size have larger total surface area of all interfaces under a consistent volume fraction of f_{p0}. Hence, the results in **Figures 6.2 and 6.4** demonstrate this concept when the composite is filled with particles of micrometer size. However, for the illustrations of the damage energy dissipation against the average radius of particles of nanometer size, as shown in **Figures 6.1 and 6.3**, the results reveal a totally different phenomenon from that of particles of micrometer size. A widely accepted opinion is that the particles in the range of nanometer size become more difficult to debond with the decrease of a_0. In other words, the smaller size the particle is in nanocomposites, the less possibility that interfacial debonding occurs. Consequently, the energy dissipation due to the interfacial debonding decreases with the decrease of a_0.

In addition, by the comparison between the nanocomposites and the microcomposites, it is found that the damage energy dissipation decreases with the increase of the interface/surface

energy, as compared **Figure 6.1** with **Figure 6.3**, or **Figure 6.2** and **Figure 6.4**.
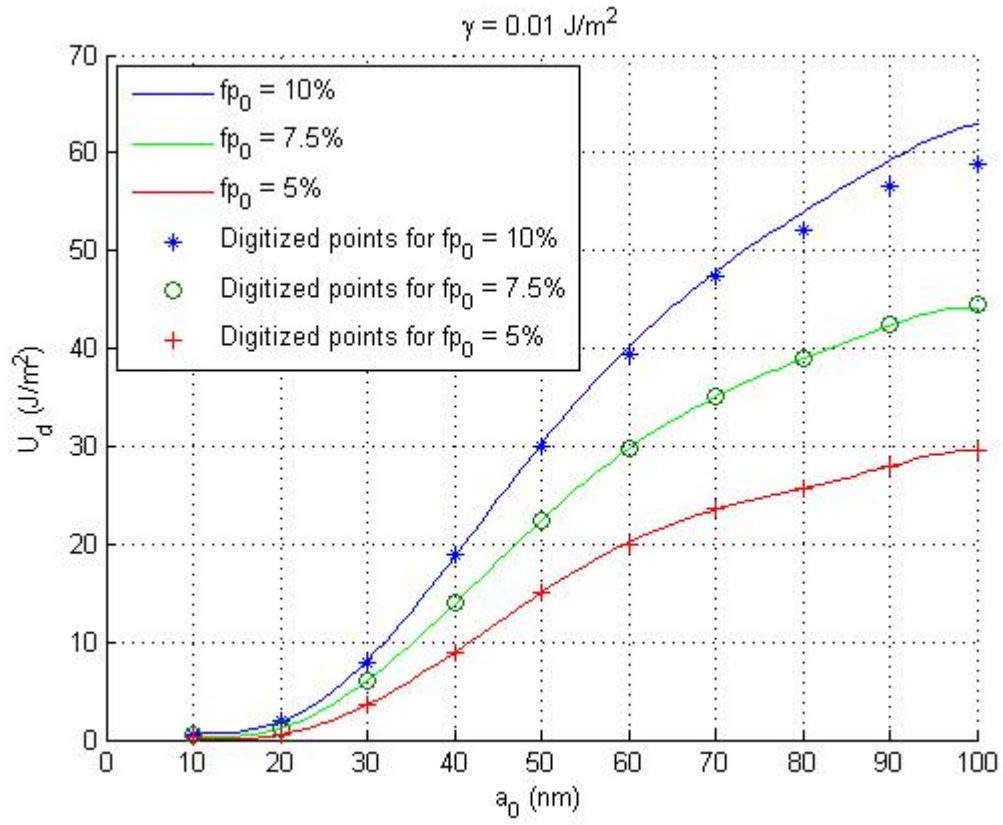
Figure 6.1 Damage energy dissipation against the average radius of particles in the range of nanometer size with the different volume fraction of particles and $\gamma = 0.01 J / m^2$
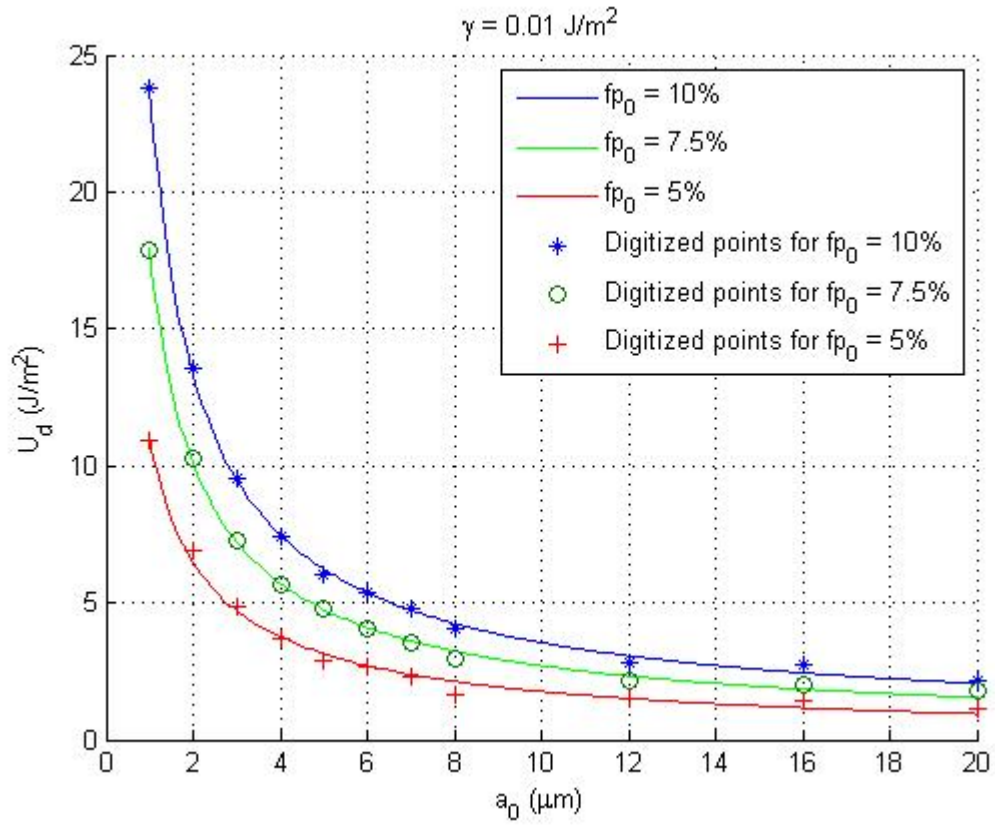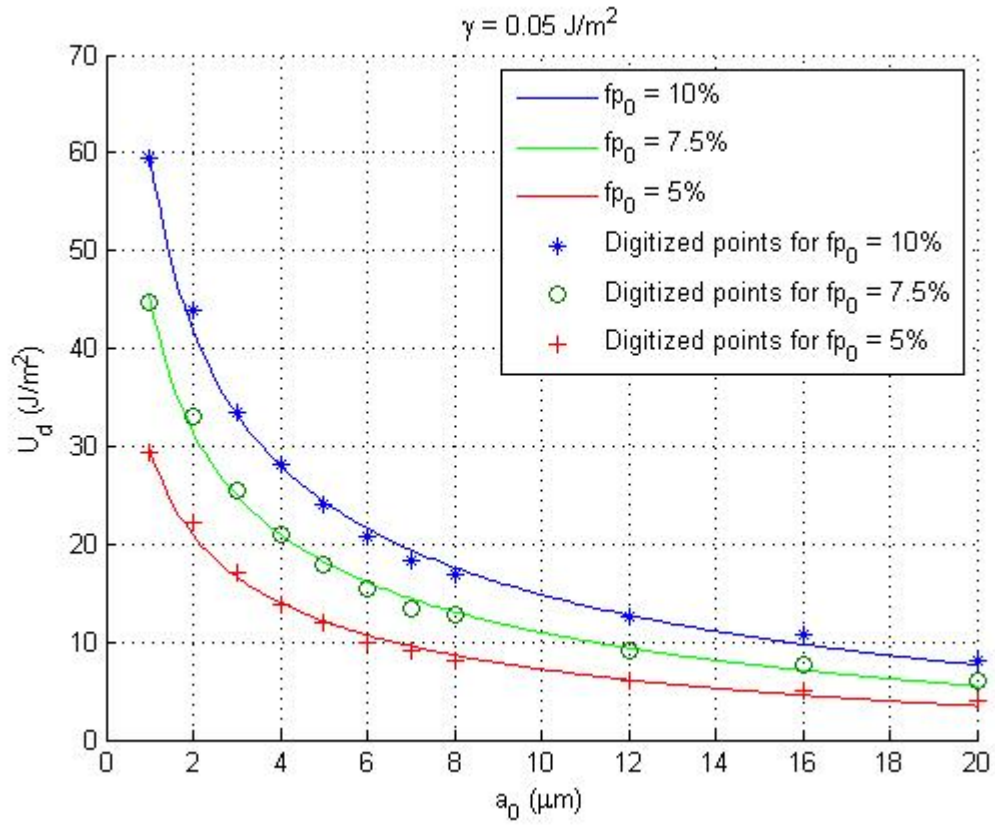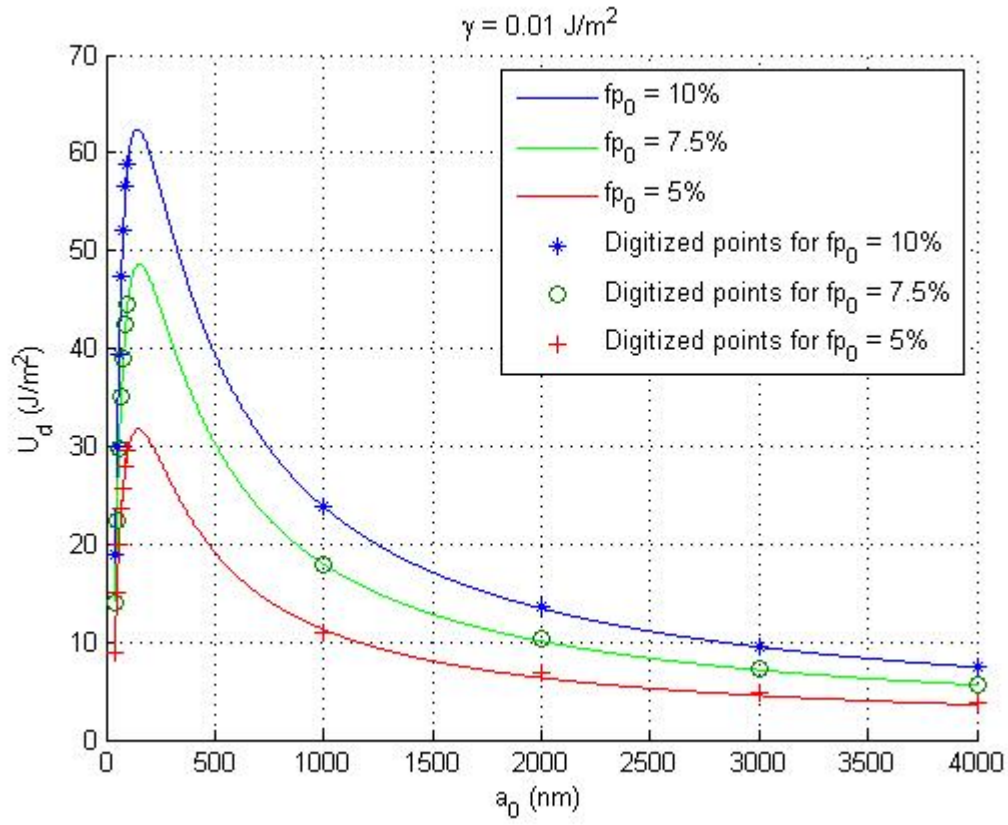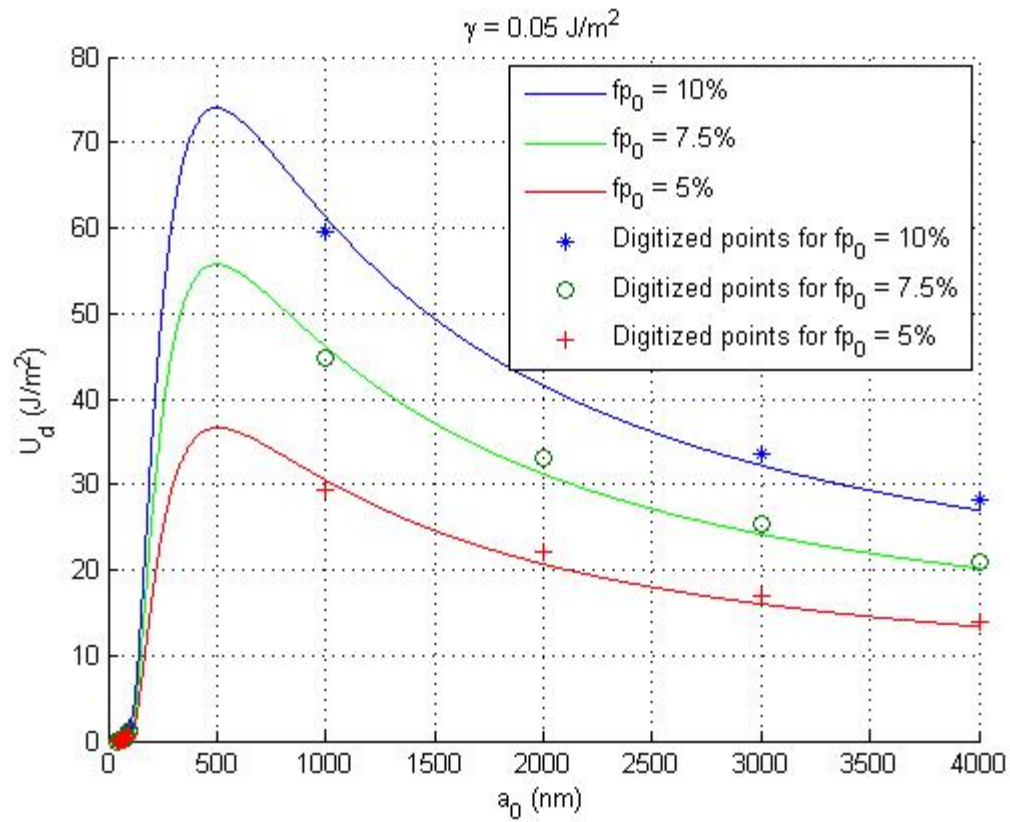
Figure 6.2 Damage energy dissipation against the average radius of particles in the range of micrometer size with the different volume fraction of particles and $\gamma = 0.01 J / m^2$
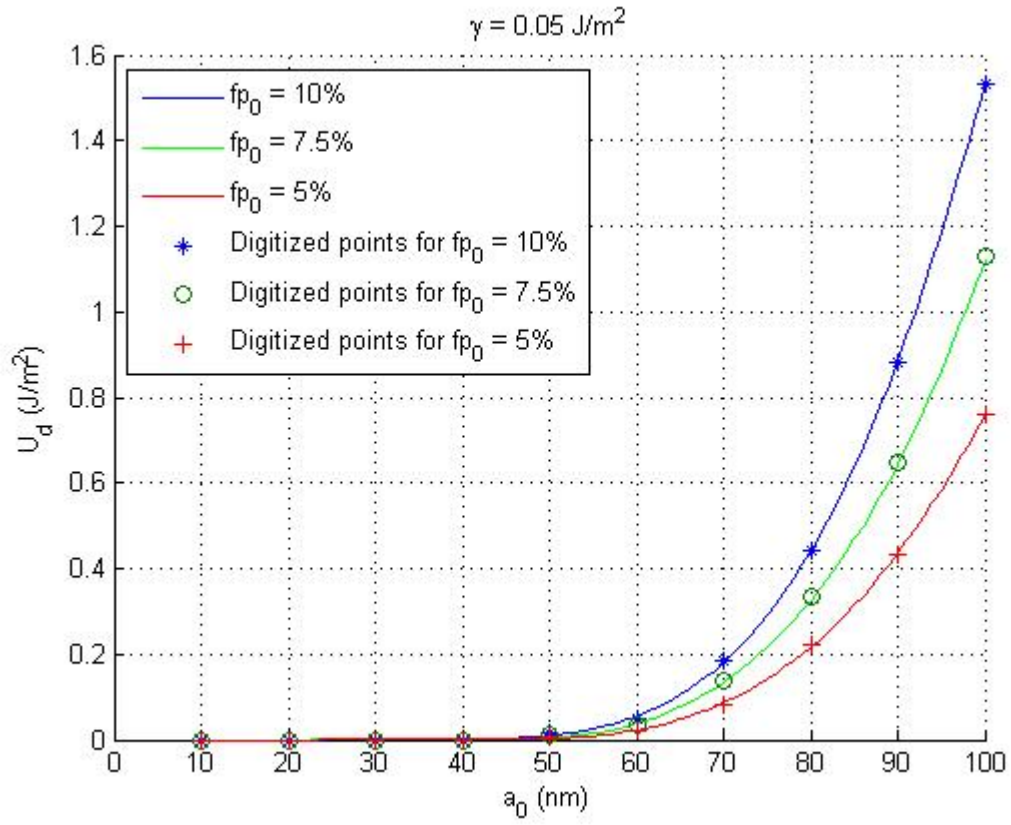
Figure 6.3 Damage energy dissipation against the average radius of particles in the range of nanometer size with the different volume fraction of particles and $\gamma = 0.05\,J\,/\,m^2$

Figure 6.4 Damage energy dissipation against the average radius of particles in the range of micrometer size with the different volume fraction of particles and $\gamma = 0.05\,J\,/\,m^2$

The size effect of particles with distinct interface/surface energies against the average radius of particles from nanometer size to micrometer size on the damage energy dissipation is shown in **Figures 6.5 and 6.6**. It can be found that there is a damage energy dissipation crest which locates close to a critical size, a_{0cr} (e.g. $a_{0cr} \approx 140 \, nm$ for $\sigma = 30 \, MPa$ and $\gamma = 0.01 \, J/m^2$ (Chen et al., 2007)). When $a_0 \leq a_{0cr}$, the damage energy dissipation increases with the increase of a_0, and this portion of the curve could be defined as the characteristic of the nanocomposite. Otherwise, the damage energy dissipation decreases with the increase of a_0, and this portion of the curve could be defined as the characteristic of the microcomposite.

In addition, under the same average normal stress at the interface and interface/surface energy, it can be observed that the critical size with the different volume fraction of particles is almost the same. That is, the position of the damage energy dissipation crest would not be affected by the change of the volume fraction of particles.

Figure 6.5 Damage energy dissipation against the average radius of particles of from nanometer

size to micrometer size with the different volume fraction of particles and $\gamma = 0.01 J / m^2$

Figure 6.6 Damage energy dissipation against the average radius of particles of from nanometer

size to micrometer size with the different volume fraction of particles and $\gamma = 0.05\,J\,/\,m^2$

From **Figure 6.7**, it is seen that the crest of the damage energy dissipation moves with the different average normal stress at the interface, σ. The numerical results regarding the movement of the crest and the variation of the value of the crests with the different σ can also be observed in Figure 6.7. It can be noticed that the position of the crest of the damage energy dissipation changes towards small size direction of a_0 with the increase of σ. For example, when σ increases from 30 MPa to 90 MPa, the position of the crest moves from 140 nm to 16 nm. The variation of the position of the damage energy dissipation crest, a_{0cr}, with the different σ is illustrated in **Figure 6.8**.
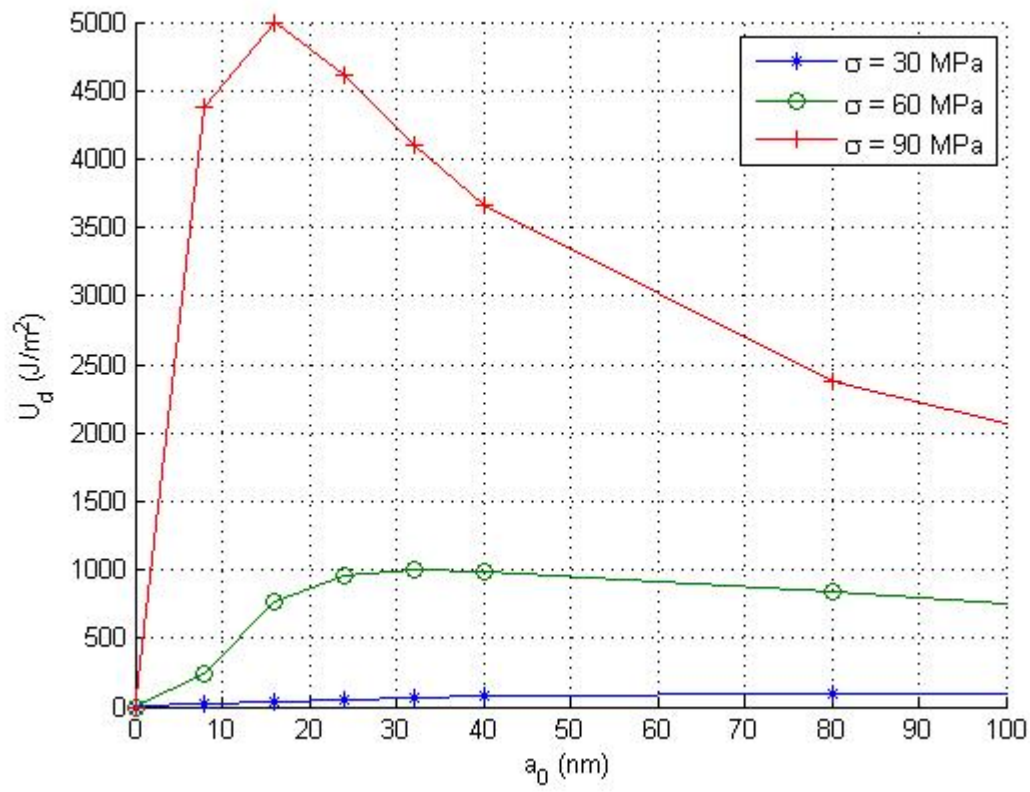
Figure 6.7 Damage energy dissipation crests against the average radius with the different average normal stresses at the interface
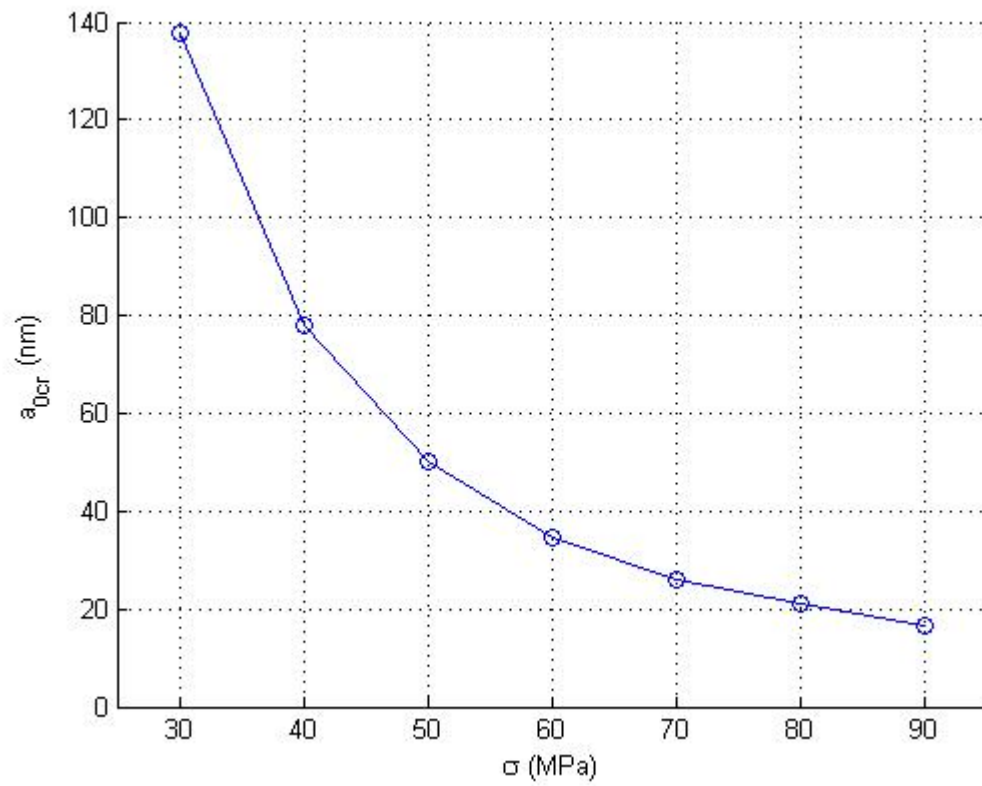
Figure 6.8 Critical sizes of the damage energy dissipation crest against the different average normal stress at the interface

In **Figures 6.9, 6.10 and 6.11**, the effects of the particle-size dispersion, ω, the interface/surface energy, γ, and the average normal stress at the interface, σ, on the damage energy dissipation are illustrated, respectively. From **Figure 6.9**, it is found that the damage energy dissipation increases with the increase of ω. From **Figure 6.10**, the damage energy dissipation decreases because the interfacial debonding occurs more difficultly with the increase of γ. It can be seen that if γ is larger than a threshold limit value, the damage energy dissipation does not occur. That is, none of the interfacial debonding between the particles and the matrix takes place. This situation is verified by the experimental results given by Zhang's research group (Yang et al., 2006). They studied the tensile properties of polyamide 66 (PA66, DuPont Zytel 101) filled with TiO_2 particles. The first type of the composite is PA/300 (PA66 filled with TiO_2 particles with the diameter of 300 nm), and the second type of the composite is PA/21 (PA66 filled with TiO_2 particles with the diameter of 21 nm). Eventually, the tensile test shows that the modulus and the strength of two types of the composites are almost the same. This result implies that the interface/surface energy is large enough so that there is no damage evolution in the composites, even under the large difference in the size of two nano-particles. From **Figure 6.11** (in which $\sigma_{cr0} = \sigma_{cr}\mid_{a=a_0}$), it is found that the damage energy dissipation increases with the increase of σ, and this phenomenon reflects consistently with the result shown in **Figure 6.12**.
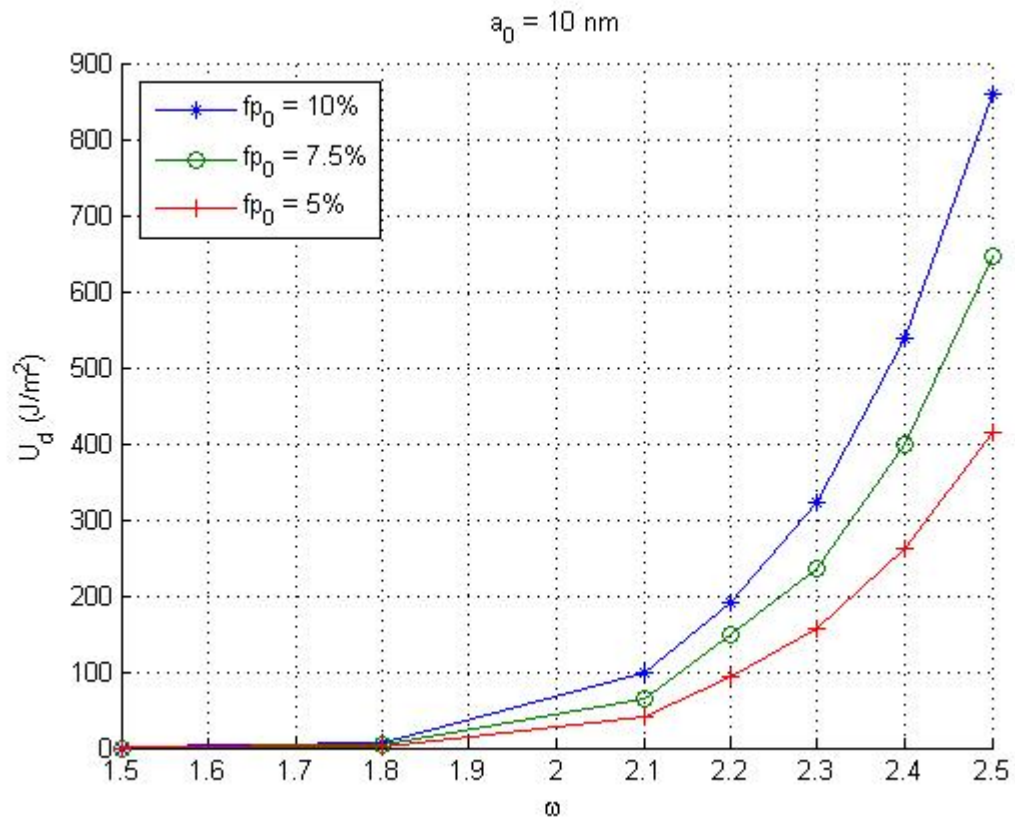
Figure 6.9 Damage energy dissipation against the particle-size dispersion with the different volume fraction of particles
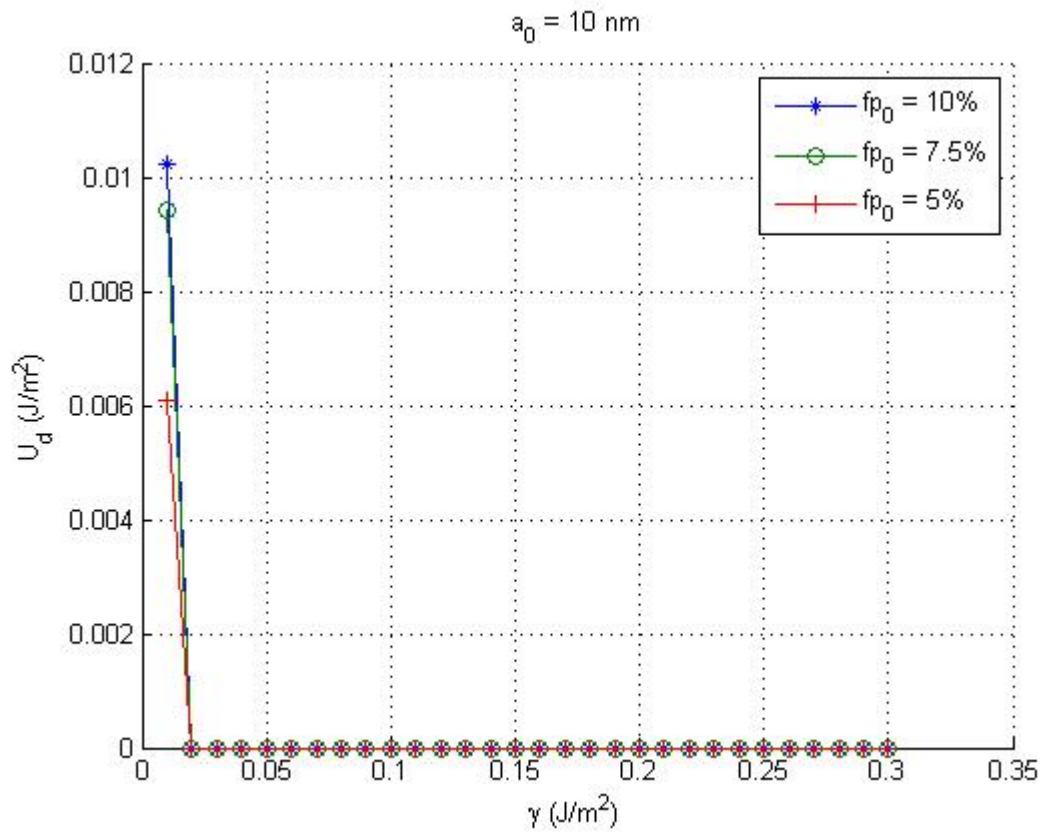
Figure 6.10 Damage energy dissipation against the interface/surface energy with the diffe

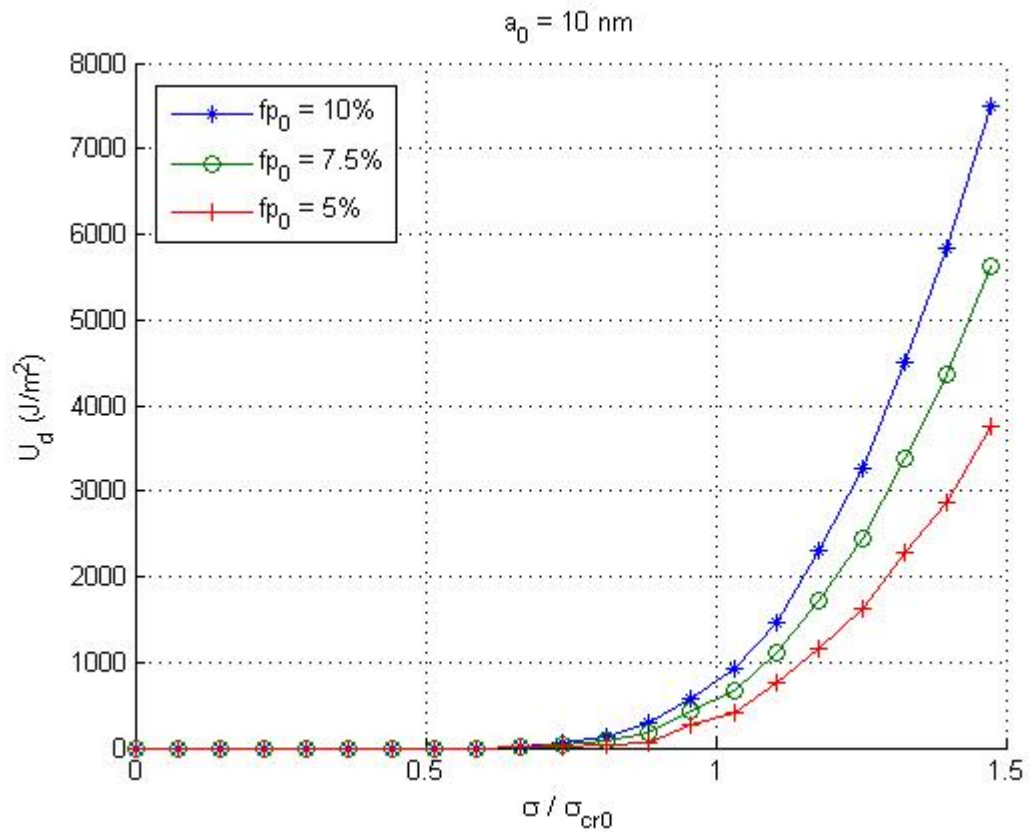rent volume fraction of particles

Figure 6.11 Damage energy dissipation against the average normal stress at the interface with the different volume fraction of particles
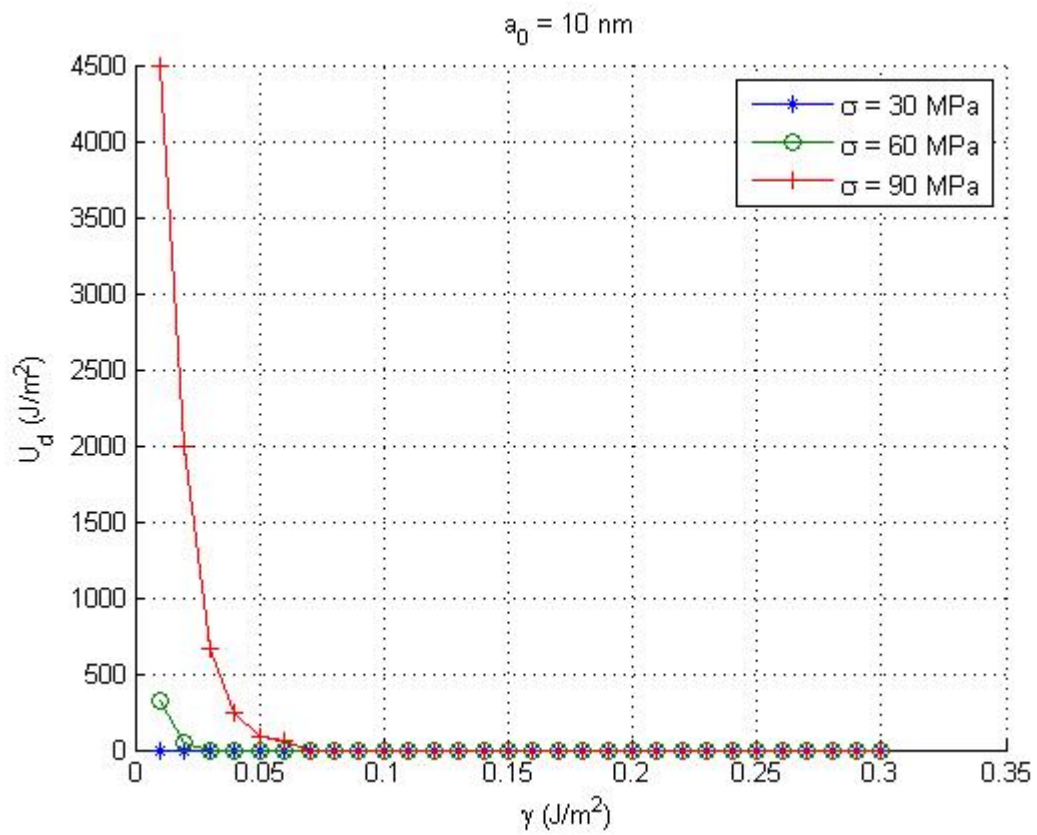
Figure 6.12 Damage energy dissipation against the interface/surface energy with the differe

nt average normal stress at the interface

Figure 6.13 shows the relation between the volume fraction of particles, f_{p0}, and the average radius, a_0, with the same damage energy dissipation. Suppose that the damage energy dissipation remains constant, the larger the value of f_{p0} is, the bigger the a_0 becomes. Moreover, if the average radius, a_0, is fixed, the larger the value of f_{p0} is, the more the damage energy dissipation in nanocomposites becomes. This conclusion is the same as the result shown in **Figures 6.1 and 6.3**.
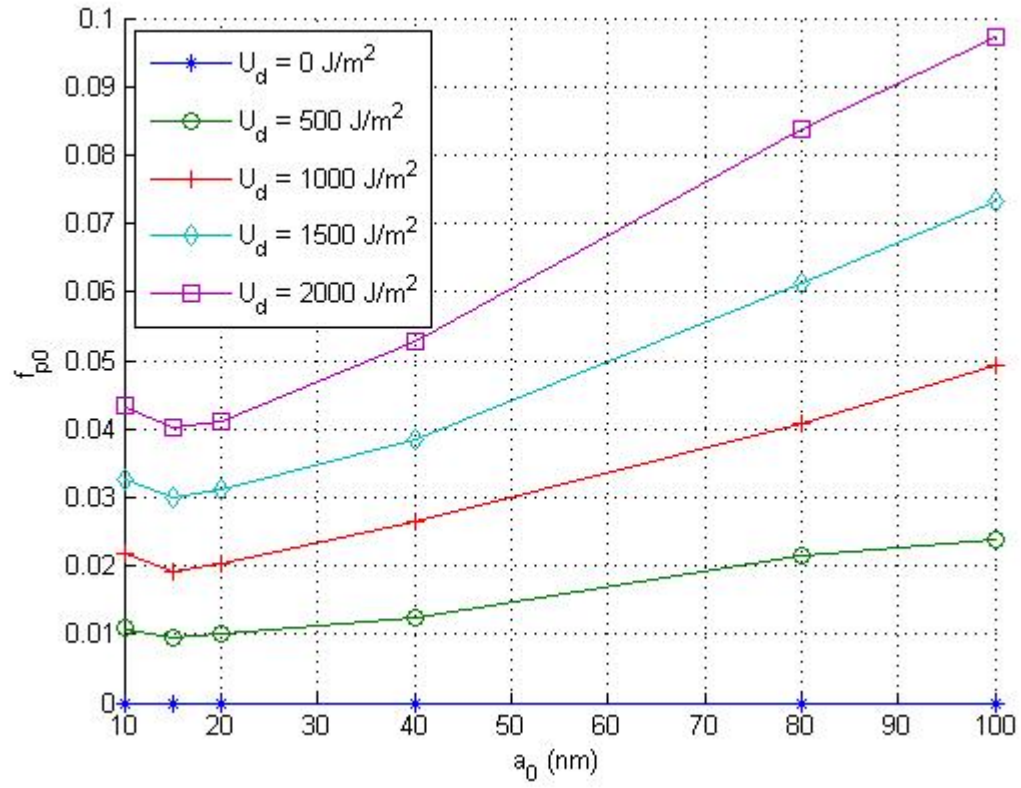
Figure 6.13 Volume fraction of particles against the average radius of particles with the different damage energy dissipation

6.4 Conclusions

(1) There exists a characteristic crest for each curve of the damage energy dissipation with respect to the average radius of particles, a_0. Moreover, the position of the crest moves towards small size direction of a_0 with the average normal stress of σ increases. When the average radius of particles is less than the critical average size, a_{0cr}, the composite possesses the characteristic of the nanocomposite. That is, the damage energy dissipation increases with the increase of the average radius. This is the special phenomenon of the size effect on the damage energy dissipation in nanocomposites, which is completely different from that in microcomposites.

(2) The effects of the larger particle-size dispersion, the larger average normal stress at the interface, and the smaller interface/surface energy between the particles and the matrix materials may result in more energy dissipation due to the interfacial debonding between particles and the matrix.

(3) For a given damage energy dissipation, the larger average size of particles in the range of nanometer size is, the more volume fraction of particles requires. Moreover, if the average radius, a_0, is fixed, the larger the value of f_{p0} is, the more the damage energy dissipation in nanocomposites becomes.

6.5 Appendix A: Critical Normal Stress at the Interface between the Particle and the Viscoelastic Matrix

The effect of the remote deviatoric stress on the interfacial debonding between a particle and the matrix may be disregarded under the high triaxial remote stress (Chen et al., 2003). Therefore, only the spherical symmetric case is accounted for the calculation of the approximate critical normal stress, σ_{cr}, and the corresponding illustration is shown in **Figure 6.14**. Suppose that the radii of an elastic particle and the viscoelastic matrix are denoted by a and b ($b \gg a$), respectively. Moreover, an uniform tensile normal stress, Σ, is applied to the surface of the matrix. The constitutive relation of the viscoelastic matrix may be expressed by

$$\sigma_0(t) = \int_{-\infty}^{t} L(t-\tau) : \dot{\varepsilon}_0(\tau) d\tau \tag{6.9}$$

where $L(t)$ is the fourth order relaxation modulus.
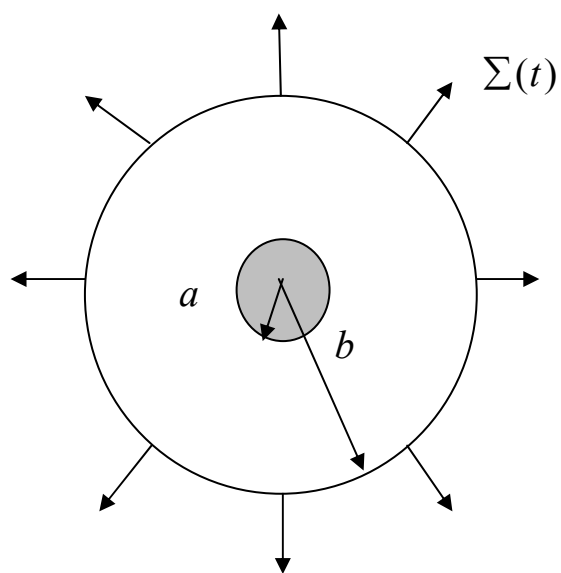
Figure 6.14 A spherical particle is embedded in the viscoelastic matrix

Suppose that the interfacial debonding occurs at an instantaneous moment, t_{cr}. At this moment, there are jumping values of the stress, strain, and displacement in the matrix and the particle. If the jumping value of A is defined by

$$[A] = A(t_{cr}^+) - A(t_{cr}^-)$$ (6.10)

From Eq. (6.9), the jumping values of the stress and strain of the matrix can be described by

$$[\sigma_0] = \sigma_0(t_{cr}^+) - \sigma_0(t_{cr}^-) = \int_{t_{cr}^-}^{t_{cr}^+} L(t_{cr} - \tau) : d\varepsilon_0$$

That is to say,

$$[\sigma_0] = L(0) : [\varepsilon_0]$$ (6.11)

Eq. (6.11) implies that the relation between the jumping values of the stress and strain in the viscoelastic matrix at the instantaneous moment, t_{cr}, is linear elastic.

Consider the energy conservation at t_{cr}, and neglect the kinetic energy in the system, it is found that

$$[W] = [U_m] + [U_p] + \gamma 4\pi a^2$$ (6.12)

where $[W]$ is the jumping value of the work done by external forces; $[U_m]$ and $[U_p]$ are the released strain energy from the matrix and the particle, respectively; γ is the interface/surface energy between the particle and matrix (both two bonded surfaces).

Since the condition shown in Fig. 4.14 is a spherical symmetric case, only one displacement component takes place in the matrix and the particle. Therefore, the jumping value of the displacement at the surface of the particle is obtained by

$$\left[u_{(p)}(a)\right] = -\frac{\sigma_{cr}}{k_{(p)}} \tag{6.13}$$

where σ_{cr} is the critical normal stress at the surface of the particle when $t -> t_{cr}$; $k_{(p)}$ is the bulk modulus of the particle.

Meanwhile, it is known that

$$[W] = \Sigma(t_{cr})\left[u_{(m)}(b)\right]4\pi b^2 \tag{6.14}$$

$$[U_p] = \frac{1}{2}\sigma_{cr}\left[u_{(p)}(a)\right]4\pi a^2 \tag{6.15}$$

$$[U_m] = -\frac{1}{2}\sigma_{cr}\left[u_{(m)}(a)\right]4\pi a^2 + \Sigma(t_{cr})\left[u_{(m)}(b)\right]4\pi b^2 \tag{6.16}$$

where $\left[u_{(m)}\right]$ is the jumping value of the displacement in the matrix. Further, for the spherical symmetric problem, it is easy to obtain that

$$\left[u_{(m)}(a)\right] = \frac{\sigma_{cr}}{4\left(\dfrac{1}{a^3} - \dfrac{1}{b^3}\right)}\left(\frac{4a}{k_{(p)}b^3} + \frac{1}{\mu(0)a^2}\right) \tag{6.17}$$

where $\mu(0)$ is the initial shearing modulus of the matrix. Substituting Eqs. (6.13)-(6.17) into Eq. (6.12) and letting $b \gg a$, it is found that

$$\sigma_{cr} \approx \sqrt{\frac{\gamma}{a}\frac{1}{\left(\dfrac{1}{2k_{(p)}} + \dfrac{1}{8\mu(0)}\right)}} \tag{6.18}$$

If the value of the bulk modulus of the particle is much higher than that of the shearing modulus of the matrix, namely, the strength of the particle is much higher than that of the matrix, the Eq. (6.18) can be approximately expressed as

$$\sigma_{cr} \approx \sqrt{\frac{\gamma}{a} 8\mu(0)} = \sqrt{\frac{\gamma}{a} \cdot \frac{4E(0)}{(1+v)}}$$

<div align="right">(6.19)</div>

$$\mu(0) = \frac{E(0)}{2(1+v)}$$

6.6 Appendix B: Formulation of the Stress Tensor of a Particle under the Remote Strain

Executing the Laplace transform of Eq. (6.9) leads to the following equation,

$$\bar{\sigma}_0 = s\bar{L} : \bar{\varepsilon}_0$$

<div align="right">(6.20)</div>

Eq. (6.20) above implies that the Laplace transform of the constitutive relation of the viscoelastic matrix may be considered as a "linear elastic" material with the fourth order modulus "$s\bar{L}$". Therefore, the Eshelby's equivalent inclusion method can be used to carry out the stress tensor of a particle, as follows,

$$\bar{\sigma}_p = L_p : (\bar{\varepsilon}_p) = s\bar{L} : (\bar{\varepsilon}_p - \bar{\varepsilon}_p^*)$$

<div align="right">(6.21)</div>

where L_p is the modulus of the particle, $\bar{\varepsilon}_p^*$ is the Laplace transform of the eigen-strain of the particle.

Since the Poisson's ratio of the matrix material, v, is assumed to be a constant, based on the Eshelby's formula, it is found that

$$\bar{\varepsilon}_p - \bar{\varepsilon}^\infty = S : \bar{\varepsilon}_p^*$$

<div align="right">(6.22)</div>

where $\bar{\varepsilon}^\infty$ is the Laplace transform of the remote strain, and S is the Eshelby's tensor.

Because the modulus of the particle is much higher than that of the matrix, the particle

<div align="center">245</div>

could be regarded to be rigid. Consequently, the strain of the particle can be ignored, that is,

$$\bar{\varepsilon}_p \approx 0 \tag{6.23}$$

Substituting Eqs. (6.22) and (6.23) into Eq. (6.21) results in

$$\bar{\sigma}_p = s\bar{L} : S^{-1} : \bar{\varepsilon}^{\infty} \tag{6.24}$$

Executing the inverse of Lapalce transform of Eq. (6.A16) obtains

$$\sigma_p = \int_{-\infty}^{t} L(t-\tau) : S^{-1} : \dot{\varepsilon}^{\infty}(\tau) d\tau \tag{6.25}$$

If Ju and Chen's scheme (Ju and Chen, 1994a; 1994b) or Mori-Tanaka's scheme (Mori and Tanaka, 1973) is considered, Eq. (6.25) can be performed in the case of a great number of particles embedded in the matrix by replacing the remote strain with the average strain of matrix, $\langle \varepsilon_0 \rangle$.

6.7 References

[1] Avella, M., Errico, M. E., and Martuscelli, E. (2001). "Novel PMMA/CaCO3 nanocomposites abrasion resistant prepared by an in situ polymerization process." *Nano Letters*, 1(4), 213-217.

[2] Bai, S. L., Chen, J. K., Huang, Z. P., and Liu, Z. D. (2001). "Interface effect on the mechanical behaviour of rigid particle filled polymer." Polymer International, 50(2), 222-228.

[3] Chen, J.K., Huang, Z.P., and Zhu, J. (2007). "Size effect of particles on the damage dissipation in nanocomposites." Composites Science and Technology, 67(14), 2990-2996.

[4] Chen, J. K., Huang, Z. P., and Bai, S. L. (2006). "Statistical evolution of microvoids in particle-filled polymers under plate impact." Fracture of Materials: Moving Forwards, H. Y. H. X. H. M. Liu, ed., 111-116.

[5] Chen, J. K., Huang, Z. P., and Mai, Y. W. (2003). "Constitutive relation of particulate-reinforced viscoelastic composite materials with debonded microvoids." Acta Materialia, 51(12), 3375-3384.

[6] Eshelby, J. D. (1957). "The determination of the elastic field of an ellipsoidal inclusion, and related problems." Proceedings of the Royal Society of London Series a-Mathematical and Physical Sciences, 241(1226), 376-396.

[7] Ju, J. W., and Chen, T. M. (1994a). "Micromechanics and effective moduli of elastic composites containing randomly dispersed ellipsoidal inhomogeneities." *Acta Mechanica*, 103(1-4), 103-121.

[8] Ju, J. W., and Chen, T. M. (1994b). "Effective elastic-moduli of 2-phase composites containing randomly dispersed spherical inhomogeneities." *Acta Mechanica*, 103(1-4), 123-144.

[9] Ju, J. W., and Chen, T. M. (1994c). "Micromechanics and effective elastoplastic behavior of 2-phase metal-matrix composites." *Journal of Engineering Materials and Technology-Transactions of the Asme*, 116(3), 310-318.

[10] Kurauchi, T., and Ohta, T. (1984). "Energy-absorption in blends of polycarbonate with ABS and SAN." Journal of Materials Science, 19(5), 1699-1709.

[11] Mori, T., and Tanaka, K. (1973). "Average stress in matrix and average elastic energy of materials with misfitting inclusions." Acta Metallurgica, 21(5), 571-574.

[12] Musto, P., Ragosta, G., Scarinzi, G., and Mascia, L. (2004). "Polyimide-silica

nanocomposites: spectroscopic, morphological and mechanical investigations." Polymer, 45(5), 1697-1706.

[13] Rong, M. Z., Zhang, M. Q., Pan, S. L., and Friedrich, K. (2004). "Interfacial effects in polypropylene-silica nanocomposites." Journal of Applied Polymer Science, 92(3), 1771-1781.

[14] Thio, Y. S., Argon, A. S., Cohen, R. E., and Weinberg, M. (2002). "Toughening of isotactic polypropylene with CaCO3 particles." Polymer, 43(13), 3661-3674.

[15] Varlot, K., Reynaud, E., Kloppfer, M. H., Vigier, G., and Varlet, J. (2001). "Clay-reinforced polyamide: Preferential orientation of the montmorillonite sheets and the polyamide crystalline lamellae." Journal of Polymer Science Part B-Polymer Physics, 39(12), 1360-1370.

[16] Yang, J. L., Zhang, Z., Schlarb, A. K., and Friedrich, K. (2006). "On the characterization of tensile creep resistance of polyamide 66 nanocomposites. Part I. Experimental results and general discussions." Polymer, 47(8), 2791-2801.

Chapter 7

INTRODUCTION TO RIGID-BODY-SPRING MODEL (RBSM) METHOD AND PAVE THE WAY FOR FUTURE INVESTIGATIONS IN INTERFACE ENERGY EFFECT

ABSTRACT

Rigid-Body-Spring Model (RBSM) method is recommended and introduced in this chapter. The reasons are as follows. Firstly, when the phases become more multiple, the formulations for analytical solutions are more complicated, difficult, tedious and time-consuming to derive. Secondly, in reality, the practical construction materials usually contain multi-phases, like concrete, wood, brick, masonry, etc. Accordingly, finding an easy and convenient method to estimate the interface/surface energy effect on those materials with multiple phases, so as to replace time-consuming and complicated micromechanical operations for the multiple-phase composites, is worth investigating and developing. Thirdly, 3D RBSM method is easy to incorporate with our present model by adding the illustrative results based on the interface/surface energy effect into RBSM's constitutive model. Furthermore, the correlative constitutive model parameters/factors between theory and practice can be modified at all times through continuous experiments and accumulative experiences. In addition, RBSM is capable of simulating the crack propagation and patterns, illustrating stress distribution, providing effective

properties of the composite materials, etc. It is beneficial for researchers to observe the external internal variations in the materials by using visible illustrations. In this study, a case based on the numerically simulation for the degradation of the shear strength after flexural yielding of RC structures subjected to cyclic loading using three-dimensional Rigid-Body-Spring Model (3D RBSM) is introduced. Subsequently, the illustrative results of stress distributions and crack patterns are obtained. Specifically, through the cyclic loading, the phenomenon of the flexural behavior gradually replaced by the shear behavior is found based on the compressive stress distribution; in the meantime, the applicability of 3D RBSM is confirmed. Furthermore, a comparison of two RC structures under between cyclic loading and monotonic loading is executed to demonstrate different degradation mechanisms of the shear strength after flexural yielding. Finally, once this our present model with the interface/surface energy effect can be involved in the developed 3D RBSM method, the effective properties of multi-phase composites with the interface/surface energy effect is expected to be easily found through the RBSM method without complicated, difficult, tedious, and time-consuming formulations. However, nano-composite experiments are very expensive and difficult to execute at present technology. We hope in the early future, the science and technology will advance to implement nano-composite experiments easily, conveniently and cheap.

Key Words: Rigid-Body-Spring Model; Cyclic Loading; Stress Distribution; Crack Pattern, Flexural Behavior; Shear Behavior; Failure Mode; Interface/surface energy

7.1 Introduction

Some applicable methods and/or programs are able to cooperate with our present model with the interface/surface energy effect, such as Finite Element Method (FEM), Rigid-Body-Spring Model (RBSM) method, ABAQUS, COMSOL, etc. Among them, RBSM method is recommended and introduced in this chapter. The reasons are:

(1) When the phases become more multiple, the formulations for analytical solutions are more complicated, difficult, tedious and time-consuming to derive.

(2) In reality, the practical construction materials usually contain multi-phases, like concrete, wood, brick, masonry, etc. Accordingly, finding an easy and convenient method to estimate the interface/surface energy effect on those materials with multiple phases, so as to replace time-consuming and complicated micromechanical operations for the multiple-phase composites, is worth investigating and developing.

(3) 3D RBSM method is easy to incorporate with our present model by adding the illustrative results based on the interface/surface energy effect into RBSM's constitutive model. Furthermore, the correlative constitutive model parameters/factors between theory and practice can be modified at all times through continuous experiments and accumulative experiences. In addition, RBSM is capable of simulating the crack propagation and patterns, illustrating stress distribution, providing effective properties of the composite materials, etc. It is beneficial for researchers to observe the external internal variations in the materials by using visible illustrations.

In the following sections, a case is used to introduce the methodology of 3D RBSM.

As Furuhashi's research (2013), the shear failure after flexural yielding occurs under cyclic

loading is investigated. The typical explanation is that the shear failure mode occurs under cyclic loading due to the degradation of the shear strength subjected to cyclic loading after flexural yielding based on the increase of the displacement, although the shear strength originally is higher than the flexural strength in the initial stage, as shown in **Figure 7.1**. According to the explanation, curves for the shear strength degradation were proposed by statistical procedures of many testing results (Priestley et al., 1996; Ohe and Yoshikawa, 2002). However, the mechanism of the shear failure under cyclic loading has not been clarified, and the degradation of the shear strength has not been evaluated determinately.
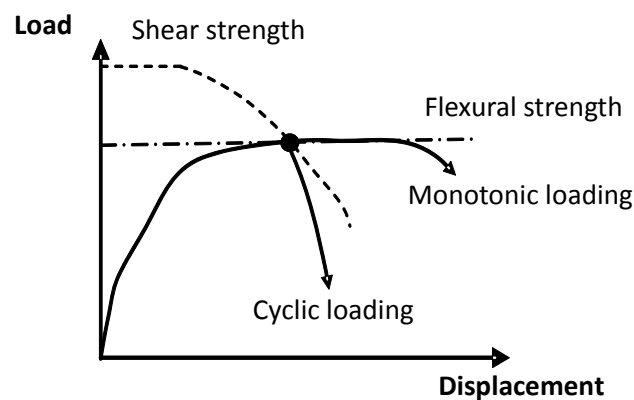
Figure 7.1 Shear failure after flexural yielding

In this study, the shear failure after flexural yielding of RC beams subjected to cyclic loading was simulated using 3D Rigid-Body-Spring Model (3D RBSM) with the constitutive model; meanwhile, the applicability of this method was confirmed. Moreover, by investigating illustrative results of compressive stress distributions and crack patterns, the degradation

mechanism of the shear strength according to the increase of the displacement, as well as the failure mode, was evaluated numerically.

7.2 Numerical model

7.2.1   Three-Dimensional Rigid-Body-Spring Model (3D RBSM)

In RBSM, concrete is modeled as an assemblage of rigid particles interconnected by springs along their boundary surfaces, shown in **Figure 7.2(a)**, which is easy to simulate concrete cracking process and its effects. The crack pattern is strongly affected by the mesh design as the cracks initiate and propagate through the interface boundaries of particles. Therefore, a random geometry of rigid particles is generated by a Voronoi diagram, as seen in **Figure 7.2(b)**, which reduces mesh bias on the initiation and propagation of potential cracks.

The response of the spring model provides an insight into the interaction among the particles, which is different from models based on continuum mechanics. In this model, each rigid particle has three translational and three rotational degrees of freedom defined at the nuclei (or nodal points) that define the particles according to the Voronoi diagram, as shown in **Figure 7.2(a)**. The boundary surface of two particles is divided into several triangles with a center of gravity and vertices of the surface. One normal and two shear springs are set at the center of each triangle. By distributing the springs in this way, over the Voronoi facet common to two neighboring nodal points, this model accounts for the effects of bending and torsional moment without the need to set any rotational springs (Gedik et al., 2011).

(a) Rigid-Body-Spring model   (b) Voronoi diagram
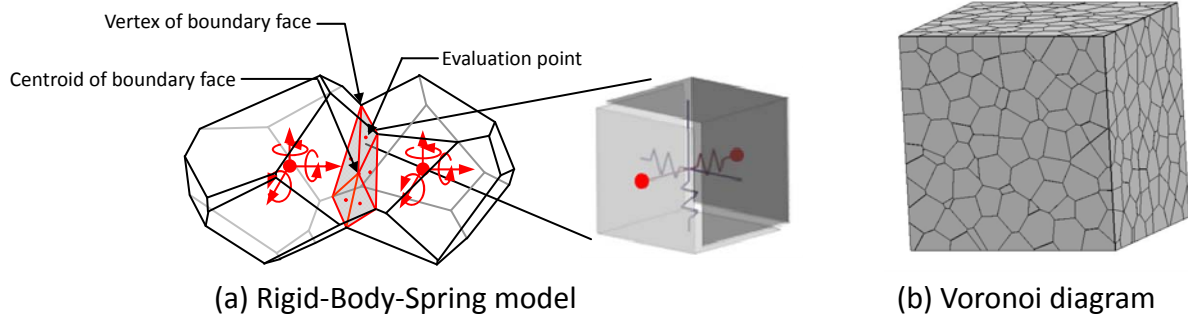
Figure 7.2 Rigid-Body-Spring model and Voronoi diagram

7.2.2   Concrete Material Model

The constitutive models for tension, compression and shear that are used in 3D RBSM are shown in **Figure 7.3** (Yamamoto et al., 2013). The tensile model for normal springs is shown in **Figure 7.3(a)**. Up to tensile strength, the tensile behavior of concrete is modeled as linear elastic and, after cracking, a bilinear softening branch according to 1/4 model is assumed. In the model, σ_t, g_f and h represent tensile strength, tensile fracture energy, and distance between nuclei, respectively. **Figure 7.3(b)** shows the stress-strain relationship for compression of normal springs that was modeled as a S-shape curve combining two quadratic functions. The parameters of σ_c, ε_{c2}, α_{c1} and α_{c2} shown in Fig. 3b are material parameters which controlled the nonlinearlity of the compression behavior of the normal spring under hydrostatic pressure.

The shear stress-strain relationship represents the combination of two shear springs. The envelope of the stress-strain relationship for shear is given in **Figure 7.3(c)**. The stress elastically increases up to the shear strength with the slope of shear modulus G and softening behavior is also assumed. β is the shear-softening coefficient. It is assumed that the shear softening

coefficient β depends upon the stress of the normal spring as represented in **Figure 7.3(d)**, where, β_0, β_{max} and χ are the parameters of dependency on the normal spring for the shear-softening coefficient. The Mohr-Coulomb criterion is assumed as the failure criteria for the shear spring, as shown in **Figure 7.3(e)**, where c and ɸ are cohesion and the angle of internal friction, respectively. Moreover, it is assumed that the shear stress decreases with an increase in crack width at the cracked surface, which is similar to Saito's model (Saito and Hikosaka, 1999). The calibrated parameters are shown in **Table 7.1**.

Table 7.1 Model parameters

Normal spring							Shear spring							
Elastic modulus	Tensile response		Compressive response				Elastic modulus	Fracture criterion			Softening behavior			
E N/mm^2	σ_t N/mm^2	g_f N/mm^2	σ_c N/mm^2	ε_{c2}	α_{c1}	α_{c2}	$\eta = G/E$	c N/mm^2	φ degree	σ_b N/mm^2	β_0	β_{max}	χ	κ
$1.4E^*$	$0.8f_t^*$	$0.5G_f^*$	$1.5f_c'^*$	-0.015	0.15	0.25	0.35	$0.14f_c'^*$	37	$0.65f_c'^*$	-0.05	-0.02	-0.01	-0.3

* The macroscopic material parameters obtained from the concrete specimens tests

E^* : Young's modulus, f_t^* : Tensile strength, G_f^* : Fracture energy, $f_c'^*$: Compressive strength

(a) Tension model of normal spring

(b) Compression model of normal spring

(c) Shear spring model

(d) Softening coefficient of shear spring

(e) Mohr-Coulumb type criterion
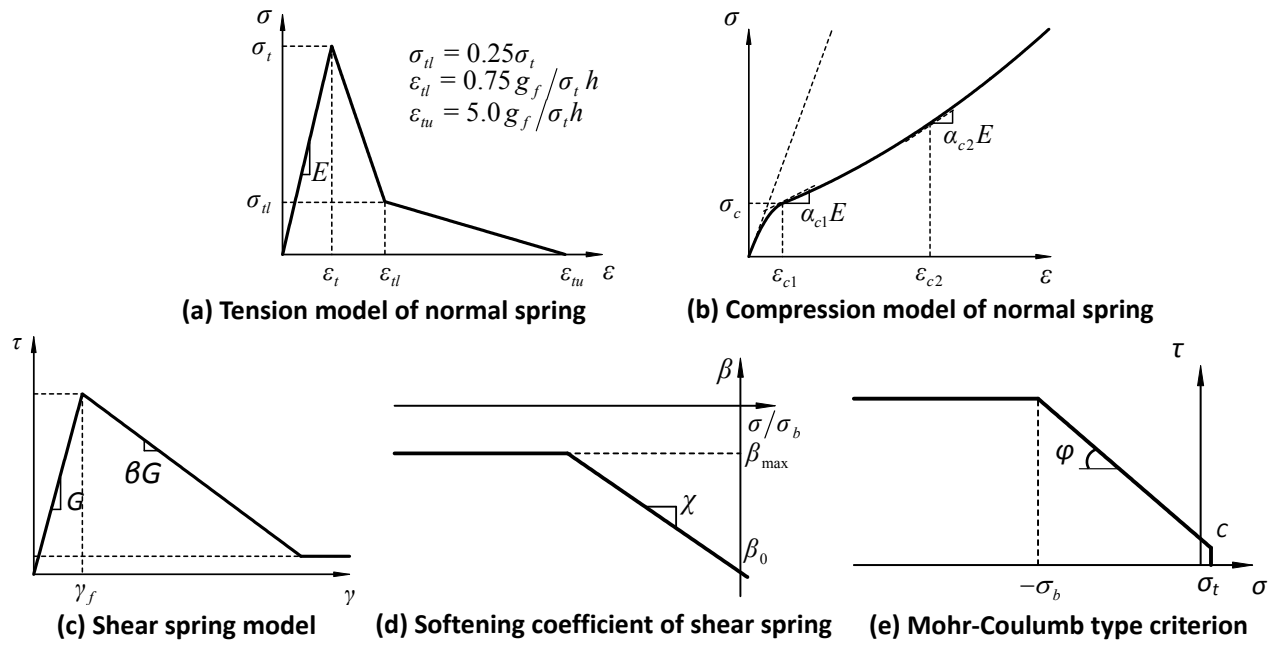
Figure 7.3 Constitutive model for concrete

(a) Normal spring

(b) Shear spring (σ = constant)
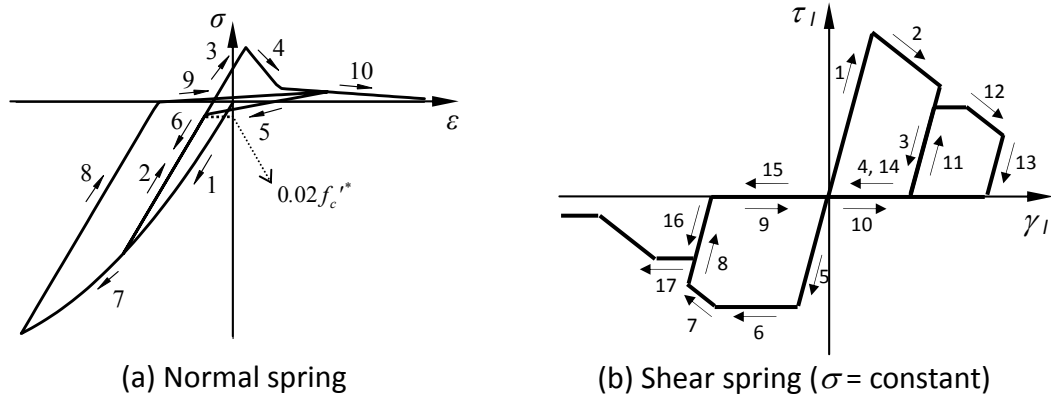
Figure 7.4 Hysteresis of stress-strain relation

256

Figure 7.4(a) shows the typical hysteresis loop of the normal spring (Yamamoto et al., 2013). The unloading paths in the tension zone pass toward the point of stress σ = -0.02f$_c$' on the compression loading path. The reloading paths in the tension zone pass toward the start point of the unloading. The stiffness of the unloading in the compression zone is initial elastic modulus E. **Figure 7.4(b)** shows the typical hysteresis loop of the shear spring. The stiffness of the unloading and reloading is initial elastic modulus G. In addition, after the stress reaches to zero on the unloading path, the stress keeps zero until the strain reaches to the residual strain of the opposite sign.

7.2.3 Reinforcement Model

Reinforcement is modeled as a series of regular beam elements (**Figure 7.5**) that can be freely located within the structure, regardless of the concrete mesh design. Three translational and three rotational degrees of freedom are defined at each beam node. The reinforcement is attached to the concrete particles by means of zero-size link elements that provide a load-transfer mechanism between the beam node and the concrete particles. For the reinforcing bar, the bilinear kinematic hardening model is applied. The hardening coefficient is 1/100. Crack development is strongly affected by the bond interaction between concrete and reinforcement. The bond stress-slip relationship is provided in the spring parallel to the reinforcement of linked element as shown in **Figure 7.6**.
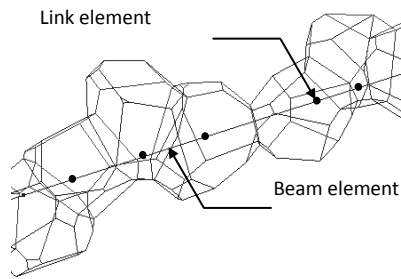
Figure 7.5 Reinforcement models
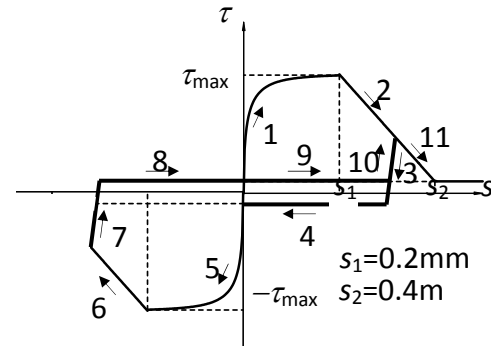
Figure 7.6 Bond - slip relationship

7.3 Analytical Model

7.3.1   Generation of Analytical Model

The cantilever type of a RC beam, as shown in **Figure 7.7**, was simulated. The specimen has the uniform cross-section of 150×200 mm2 and shear span of 640 mm. Two longitudinal reinforcements of D13 were arranged at upper and lower sides with the cover thickness of 40 mm, and web reinforcements were not arranged. This specimen was tested by Machida et al. (1985) and the shear failure after flexural yielding under cyclic loading was observed when the displacement is 20 mm ($4\delta_y$).

Figure 7.8 shows analytical model which was modeled by Voronoi diagram. The average element size is about 20mm. The analytical model was modeled as a uniform cross-sectional member, and the plate element was modeled in the footing part to restrain the deformation. All reinforcements were modeled as beam elements. It is assumed that the compressive strength of the concrete is 40.5 N/mm^2, and the yielding stress of longitudinal reinforcements is 380 N/mm^2.
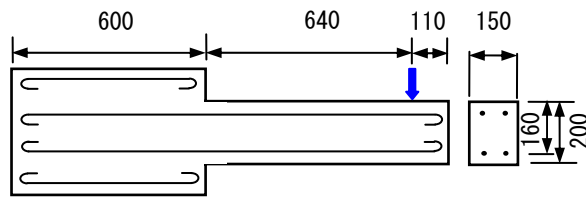
Figure 7.7 Dimension of specimen
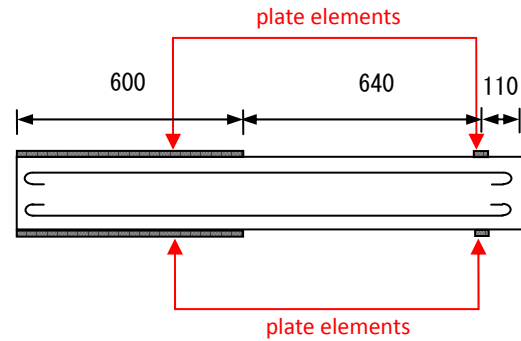
Figure 7.8 Analytical model

In the analysis, the displacement of the loading plate element was controlled and alternative cyclic loading with an incremental deformation of δ_y (5mm) was applied. Monotonic loading analysis was also conducted in order to compare with the results under cyclic loading.

7.3.2 Applicability of 3D RBSM to Shear Failure after Flexural Yielding

Figure 7.9 shows the load-displacement relationship obtained by the analysis. The black line shows the result of cyclic loading analysis, the red line shows the result of monotonic loading analysis and the blue line shows the experimental results (Machida, 1985). The

envelopes for load-displacement curves of cyclic and monotonic loading are almost same until 2δy (10 mm). However, the load carrying capacity under cyclic loading decreases after 3δy. At 4δy, the shear failure occurs in the test, the load carrying capacity decreases rapidly, and the shape of the hysteresis loop changes to S-shape remarkably. This type of the behavior is usually observed in the test of the shear failure of RC columns. The difference between the results of cyclic and monotonic loading analysis increases with the increase of the displacement.

Figure 7.10 and **Figure 7.11** show the deformations at 20 mm (4δy) obtained from the monotonic and cyclic loading analysis, respectively. It is understood that the flexural behavior is dominant in the monotonic loading case. On the other hand, in the cyclic loading case, the diagonal crack is dominant and the flexure crack does not develop. Moreover, it is observed that the deformation extends to lateral direction and X-shape cracks occur. This result is clearly different from the monotonic one and shows typical shear failure behavior. The applicability of 3D RBSM to the shear failure after flexural yielding under cyclic loading is confirmed.
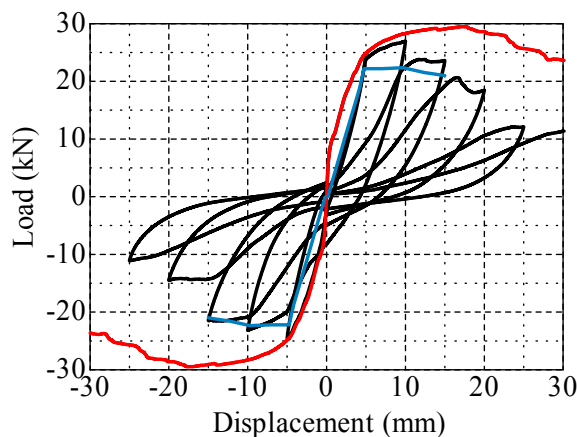
Figure 7.9 Load-displacement
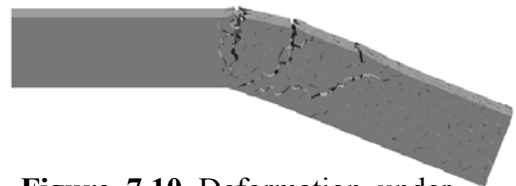
Figure 7.10 Deformation under monotonic loading at 20mm (4δ$_y$)
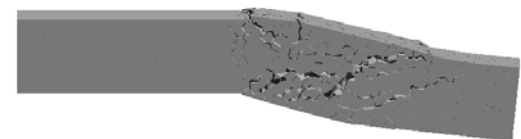
Figure 7.11 Deformation under cyclic loading at 20mm (4δ$_y$)

7.3.3   Evaluation of Shear Strength Degradation

As described in Introduction, the reason why the shear failure after flexural yielding occurs is that the shear strength degrades under cyclic loading, although the shear strength (Vc in **Figure 7.12**) is higher than the flexural strength (Pu in **Figure 7.12**) in the initial stage. Therefore, the degradation mechanism of the shear strength should be clarified quantitatively in order to evaluate the shear failure after flexural yielding. However, it is difficult to understand the degradation behavior in the test, since the degraded shear strength in the test is given by only a point on load-displacement relationship (Point A in **Figure 7.12**). In order to obtain the shear strength degradation behavior, an analytical method was proposed. **Figure 7.12** shows a concept of the proposed method (Furuhashi et al., 2013), and the detail of this method is explained in the following.
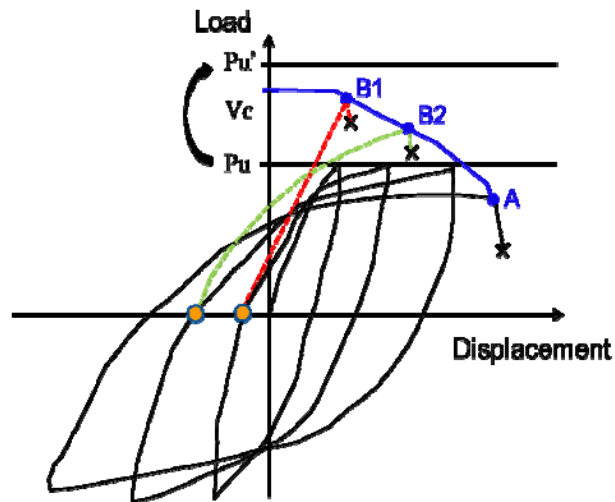
Figure 7.12 Concept of method

It is supposed that shear failure after yielding occur due to the degradation of the shear strength as the blue line in **Figure 7.12**. The values of the shear strength on blue line, such as B1 and B2, after the increase of the displacement under cyclic loading can not be obtained, because the load does not increase over Pu which corresponds to the flexural strength. However, if the flexural strength at each cycle is changed over the blue line in the analysis, the shear strength can be obtained. In order to achieve the requirement, it was proposed that the yielding stress of longitudinal reinforcements is replaced by the higher values at orange points in each cycle in **Figure 7.12**, which results in an increase of the flexural strength to Pu'. Then, the shear strength of the blue line less than increased flexural strength Pu' is calculated. The proposed method is based on fact that the yielding stress of longitudinal reinforcements increase only on the flexural strength and does not influence on the shear strength. This method utilizes the merit of numerical analysis which can consider the virtual situation.

The proposed method explained is applied to RC members. The yield stress of the longitudinal reinforcement is increased from 380 to 900 N/mm2 at each cycle, when the load is zero after unloading in negative loadings.

Figure 7.13 shows load-displacement relationship obtained from the proposed method. The shear strength obviously degrades with the increase of displacement. The shear strength after $1\delta y$ loading degrades little from the initial strength and the strength is higher from the flexural strength. Therefore, the shear failure does not occur at the stage in the test. On the other hand, the shear strength after $3\delta y$ degrades remarkably. Because the degraded shear strength is lower than the flexural strength in **Figure 7.9**, the shear failure occurs independently on increasing the yield stress of the longitudinal reinforcement.

The shear strength degradation under monotonic loading is evaluated using the same

method. The yield stress of the longitudinal reinforcement is increased after unloading until zero load at each displacement under monotonic loading. **Figure 7.14** shows load-displacement relationship to obtain the shear strength after flexural yielding. The shear strength hardly degrades until 3δy loading. The shear strength gradually decreases after 3δy loading, and the each post-peak behavior coincides. This result shows obviously different from the result under cyclic loading.
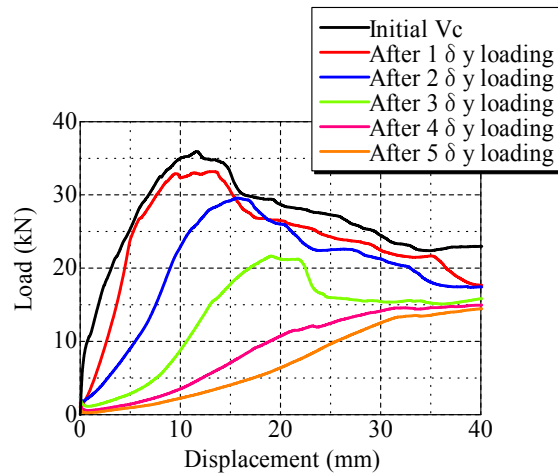

Figure 7.13 Load-displacement relationship for RC member under cyclic loading
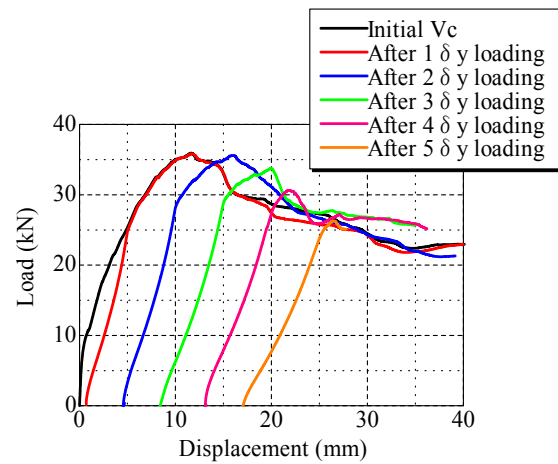
Figure 7.14 Load-displacement relationship for RC member under monotonic loading

7.4 Results Discussion

7.4.1 Stress Distribution and Crack Propagation of RC Structures under Cyclic Load

In order to better observe the variation of the stress behavior and clearly recognize the degradation of the shear strength in the proposed RC cantilever beam subjected to cyclic loading, several illustrations of stress distributions in sequence for the middle longitudinal cross-section of the beam were developed using 3D RBSM programming. In the meanwhile, a series of illustrations of crack patterns corresponding to the stress distributions was also produced so as to reveal distinct crack types during different cycles of the loading. The load-displacement relationship for the applied cyclic loading is shown in **Figure 7.15**. The feature of load-displacement relationship is that the hysteresis loops change from the spindle-shape to the
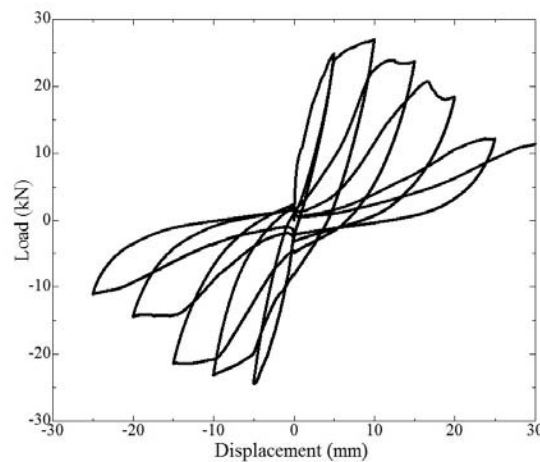
Figure 7.15 Load-displacement relationship of the applied cyclic loading

S-shape with the increasing displacement.

7.4.1.1 Stress Distribution

Two distinct cycles, in which the shapes of hysteresis loops are changed and maximum loads decrease, were implemented to display the distinct behavior of stress-distributions. The executive manner of the two cycles is illustrated in **Figure 7.16**.
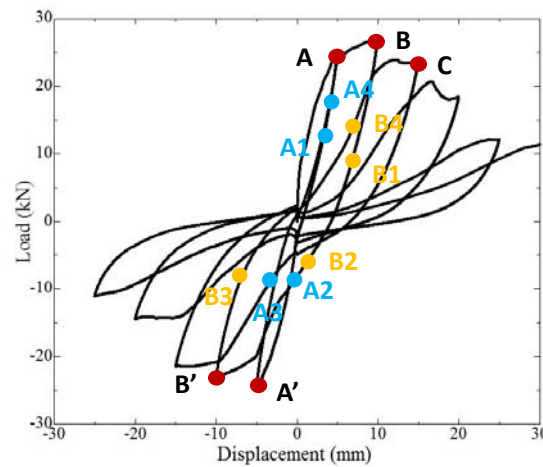

Figure 7.16 Illustration of two distinct cycles

The first cycle starts from point A to point B through point A', while the second cycle is from point B to point C via point B'. At each cycle, four points were picked for the purpose of investigating and comparing distinct stress distributions. For example, for the first cycle, A1, A2, A3 and A4 are selected; on the other hand, B1, B2, B3 and B4 are chosen for the second cycle. The results of the stress distributions under the first and second cycle, executed by means of 3D

RBSM programming, are shown in **Figure 7.17(a)** and **Figure 7.18(a)**, respectively. In the meantime, **Figure 7.17(b)** and **Figure 7.18(b)** represent the corresponding crack pattern to the stress distribution at each point generated for the assistance in understanding of correlative deformation of the beam at each point. In addition, **Figure 7.17(b)** and **Figure 7.18(b)** are further used to interpret the crack propagation in the following section.

In **Figure 7.17(a)** and **Figure 7.18(a)**, the largest to smallest quantity of the compression is exhibited as colors of red, orange, and yellow in order, and the green color represents the zero compressive stress.

From **Figure 7.17(a)**, it is discovered that in this cycle, the stress behavior is almost dominated by the compression behavior at upper and lower part of cross section. The distribution is usually observed in flexural behavior. Even after a full first cycle, the stress distribution at point A does not much differ from the stress distribution at point B. The only notice of interest is expansion to middle part of cross section. This implies that the stress behavior is going to change.

From **Figure 7.18(a)**, it is found that the stress behavior gradually converts from the flexural behavior to the shear behavior during the second cycle. Specifically, after half of the second cycle, the stress distribution of the compression behavior becomes diagonal. This means that the shear behavior forms progressively, as shown from the stress distribution at point B' toward point C. Eventually, at point C, it is obvious that the shear behavior is dominant at this moment.

In conclusion, the shear behavior would take over the compression behavior gradually with the increasing number of the cycles of the loading. As a result, a RC structure under more cyclic loading tends to perform a severer shear failure with the more remarkable shear behavior.
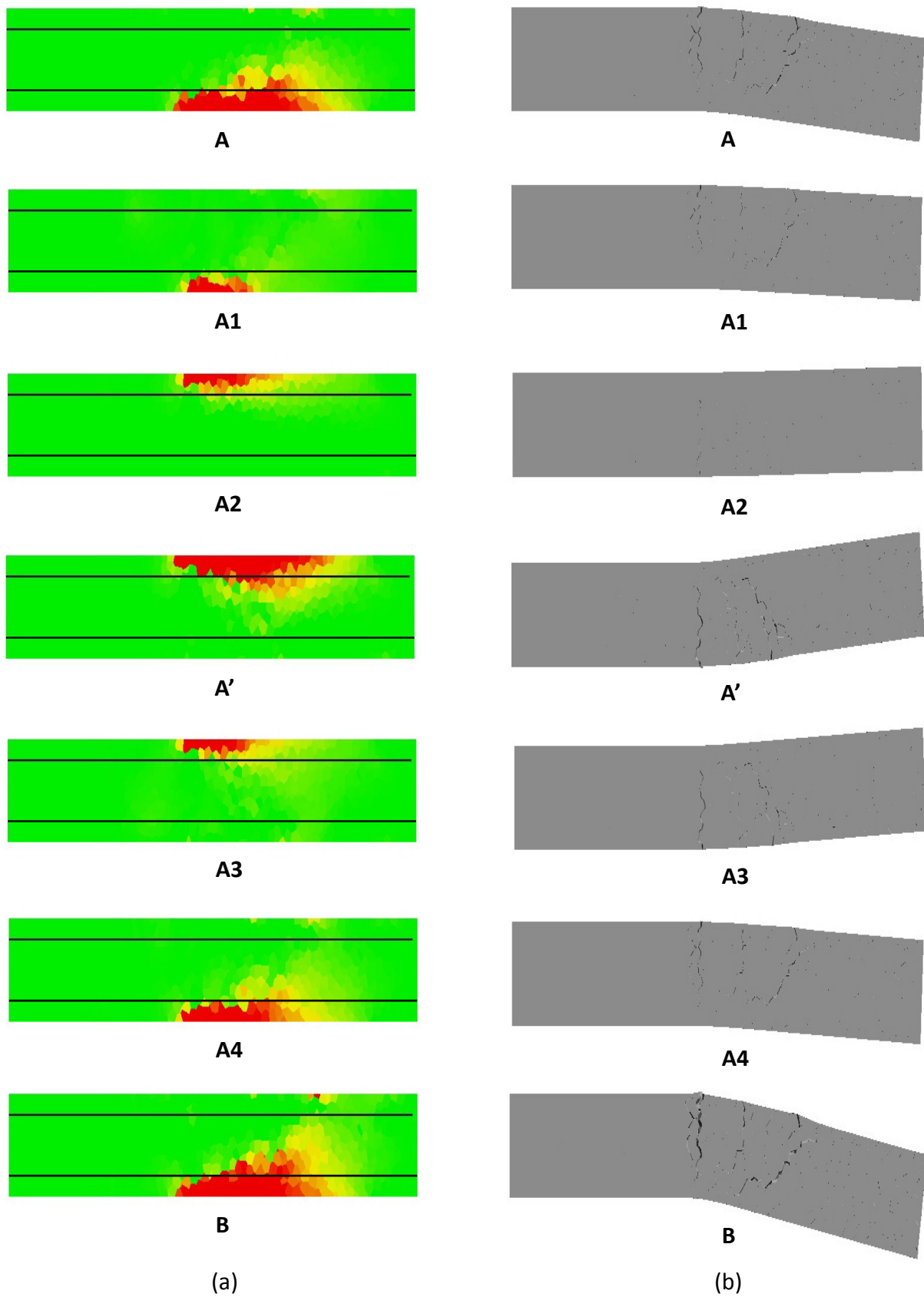
Figure 7.17 (a) Stress distributions at different points of the first cycle of the loading; (b) Crack patterns at different points of the first cycle of the loading
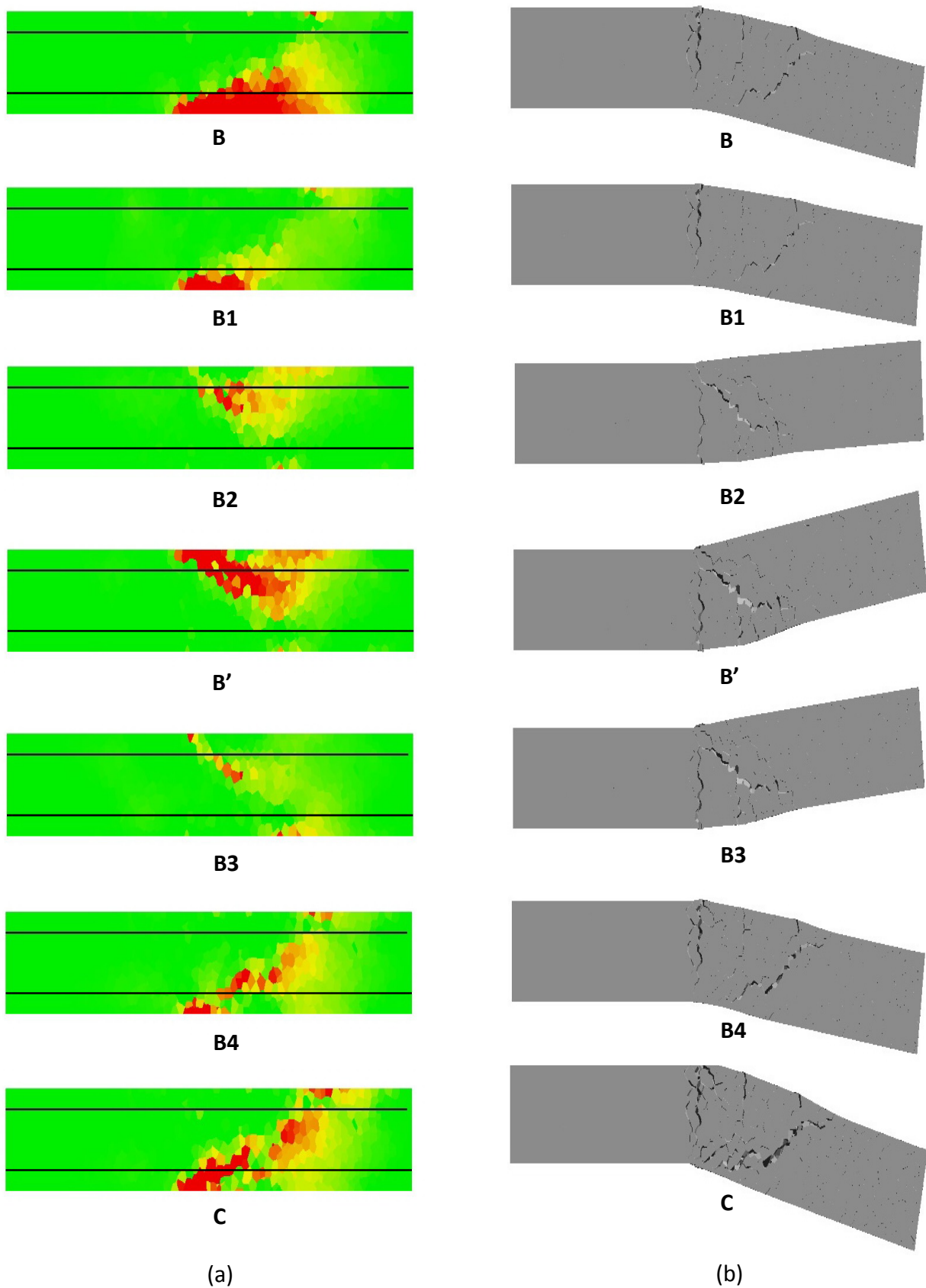
Figure 7.18 (a) Stress distributions at different points of the second cycle of the loading;

(b) Crack patterns at different points of the second cycle of the loading

Furthermore, the simulated results obtained from 3D RBSM programming agree with the explanation of that the shear failure occurs due to the severe degradation of the shear strength under cyclic loading after flexural yielding as described in Introduction.

7.4.1.2 Crack Propagation

In **Figure 7.17 (b)** and **Figure 7.18 (b)**, the magnification factor of 10 is used consistently throughout all the illustrations of crack patterns in order for the clear and accurate identifying the difference among the cracks and deformations at different points.

From **Figure 7.17 (b)**, it can be seen that within the first cycle of the loading, only the flexural cracks occur at each point, except that there begins a slight shear crack appearing at the last point (i.e. Point B). This phenomenon agrees with the description in Section 7.4.1.1 of the stress distribution. That is, the flexural behavior is dominant during this cycle in either the positive or negative deformation. In addition, from the observation of Point B in **Figure 7.17 (a)**, a distinct stress distribution begins to occur at the top of the beam at Point B; accordingly, this result agrees with the initial appearance of the stress crack at Point B, as shown at Point B in **Figure 7.17 (b)**.

Figure 7.18 (b) demonstrates that the behavior of stress distributions changes from the flexural behavior to the shear behavior, as illustrated in **Figure 7.18 (a)**. In other words, more and more shear cracks are appeared within the second cycle of the loading, whereas the flexural cracks don't have outstanding variations of the width and amount at this stage. Eventually, at the last point (i.e. Point C), it is found that a remarkable shear crack is going to penetrate the lateral cross-section. The distinct shear cracks appear at B2 between the flexural cracks, though load value is small. The behavior from positive to negative deformation in cyclic loading may

269

influence to initiation of the shear crack. Thus, the illustrations of the crack pattern during the second cycle of the loading confirms that the eventually damage of this proposed RC cantilever beam subjected to cyclic loading results from the shear failure mode.

7.4.2   Comparison of Stress Distribution and Failure Mode at Peak Load between Cyclic Loading and Monotonic Loading

In order to study how significant the cyclic loading influences the RC structure on stress distributions and crack patterns, as well as failure modes, in this section, a contrast is induced for the comparison. That is, this contrast is an identical RC structure with the same properties and arrangements of both concrete and steel materials compared to the analytical model, except the applied loading conditions. To be specific, the monotonic loading is applied to the contrast. In this section, only three cycles/loops of loading conditions are developed and compared as it is quite time-consuming to simulate the entire load-displacement curves up to peak loads for the last two models under cyclic loading. However, from the results of RC structures subjected to the first three cycles/loops of either the cyclic loading or the monotonic loading, the data obtained from the 3D RBSM programming are much enough to investigate obviously the big difference between two RC structures under different loading conditions.

Two identical RC structures with the same material properties and arrangements, but different loading conditions applied, are simulated in this section. **Figure 7.19 (a)** and **Figure 7.19 (b)** show the stress distributions at individual peak load for the first three cycles of the cyclic loading and the first three loops of the monotonic loading, respectively. In the figure, the colorful patches have the same definition with the Section 7.4.1.1.

From the stress distributions illustrated in **Figure 7.19**, it is found that the range of the stress distribution at each peak load decreases extraordinarily from the first cycle to the third cycle under cyclic loading, as shown in **Figure 7.19 (a)**. On the contrary, the range of the stress distribution at each peak load slightly decreases from the first loop to the third loop of the monotonic loading, as shown in **Figure 7.19 (b)**. The difference is observed at the compression stress zone due to the bending moment. Under cyclic loading, the compression stress due to the bending moment is lost and flexural behavior does not contribute to the load carrying capacity. This phenomenon implies that the cyclic loading greatly affects the strength of RC structures. This strength should belong to the shear strength of RC structures as mentioned in Introduction so that the shear strength of RC structures degrades much while subjected to cyclic loading.

7.4.2.1 Stress Distribution

Two identical RC structures with the same material properties and arrangements, but different loading conditions applied, are simulated in this section. The upper portions of **Figure 7.19 (a)** and **Figure 7.19 (b)** show the stress distributions at individual peak load for the first three cycles of the cyclic loading and the first three loops of the monotonic loading, respectively. In the figure, the colorful patches have the same definition with the Section 7.4.1.1.

From the stress distributions illustrated in **Figure 7.19**, it is found that the range of the stress distribution at each peak load decreases extraordinarily from the first cycle to the third cycle under the cyclic loading, as shown in the upper portion of **Figure 7.19 (a)**. On the contrary, the range of the stress distribution at each peak load slightly decreases from the first loop to the third loop of the loading. This phenomenon implies that the cyclic loading greatly affects the strength of RC structures. This strength should belong to shear strength of RC structures as mentioned in

Section 7.1 so that the shear strength of RC structures degrades much while subjected to the cyclic loading.

7.4.2.2 Crack propagation

In the lower portions of **Figure 7.19 (a)** and **Figure 7.19 (b)**, the crack patterns are simulated as well in order to identify the failure modes for two identical RC structures under distinct loading conditions. In the figure, the magnification factor of 10 is used consistently throughout all the illustrations of crack patterns in order for the clear and accurate identifying the difference among the cracks and deformations at different points.

From **Figure 7.19 (a)**, it is discovered that within the cyclic loading, the shear cracks on RC structures become larger after a cycle, whereas the flexural cracks don't grow a lot. That is, the shear cracks on RC structures under the cyclic loading apparently develop in width, length and number after every cycle, but there is not much change for the flexural cracks in width, length and number. This phenomenon agrees with the concept that the shear behaviour eventually dominates the failure mode when RC structures are subjected to the cyclic loading.

On the contrary, the behaviour on RC structures subjected to the monotonic loading composes both compression behaviour and shear behaviour. As simulated in **Figure 7.19 (b)**, not only the shear cracks on RC structures become larger after each loop, but also the flexural cracks grow. That is, the shear cracks and the flexural cracks on RC structures develop in width, length and number after every loop under the monotonic loading. This demonstrates that the failure mode on RC structures under the monotonic loading could be dominated by the shear failure or the flexural failure depending on the factors of materials, properties, etc. of the RC structures.
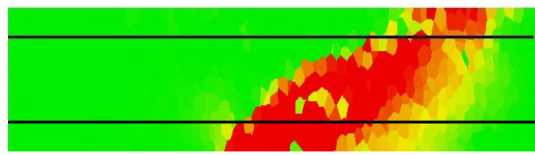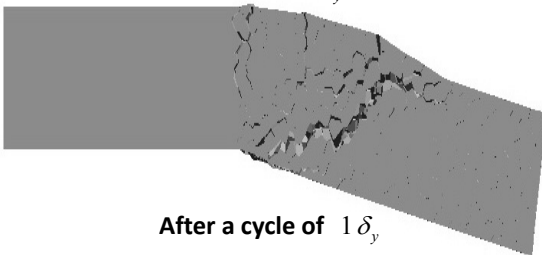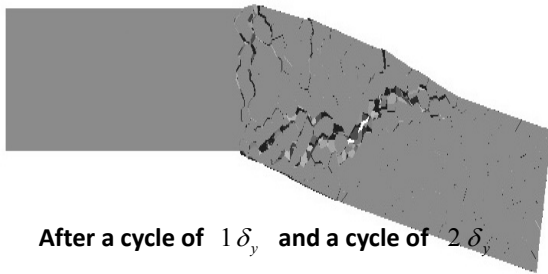
After a cycle of $1\delta_y$
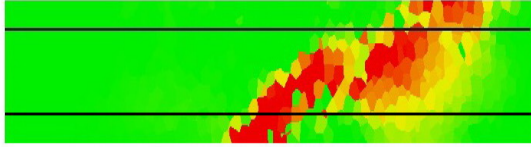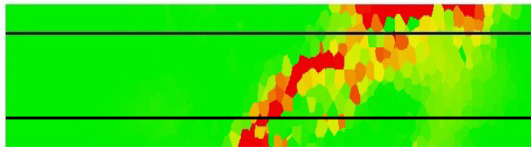
After a loop of 1 yielding displacement $(1\delta_y)$
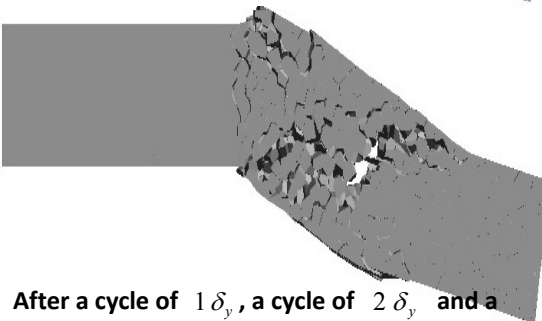
After a cycle of $1\delta_y$ and a cycle of $2\delta_y$

After a loop of 2 yielding displacements

After a cycle of $1\delta_y$, a cycle of $2\delta_y$ and a cycle of $3\delta_y$
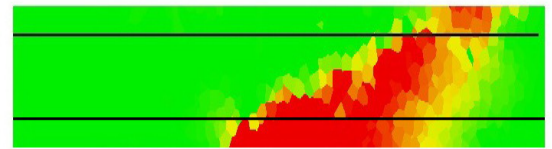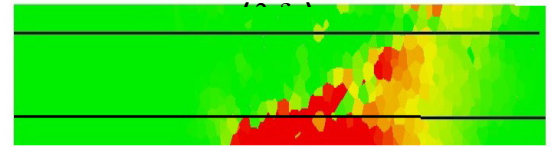
After a loop of 3 yielding displacements $(3\delta_y)$

After a cycle of $1\delta_y$

After a loop of 1 yielding displacement $(1\delta_y)$

After a cycle of $1\delta_y$ and a cycle of $2\delta_y$
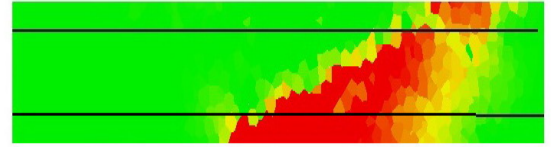
After a loop of 2 yielding displacements

After a cycle of $1\delta_y$, a cycle of $2\delta_y$ and a cycle of $3\delta_y$
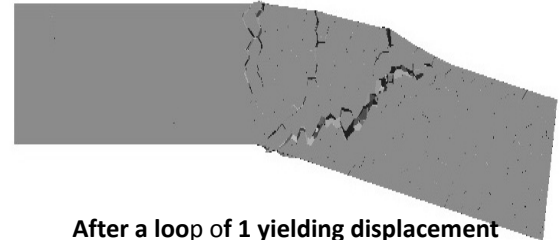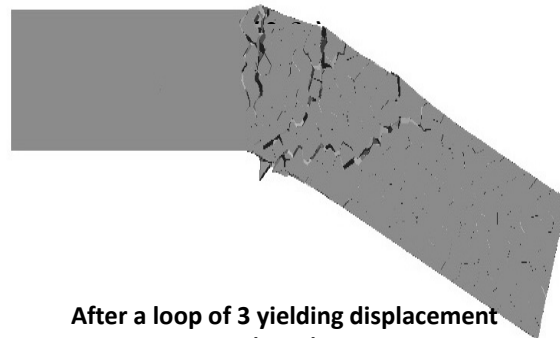
After a loop of 3 yielding displacement $(3\delta_y)$

(a)

(b)
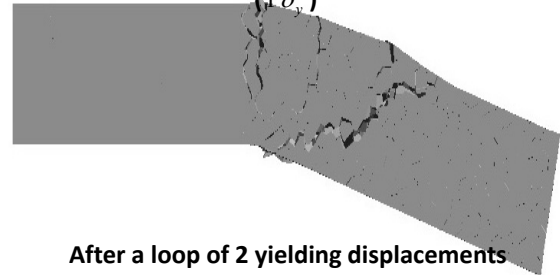
Figure 7.19 Stress distributions and crack patterns at the peak load of each cycle/loop

condition for two identical RC cantilever beams under

(a) the cyclic loading; (b) the monotonic loading, respectively

7.4.3   Stress Distribution and Crack Propagation of RC Structures under Cyclic Load

In this section, the RC structure with stirrups, shown in **Figure 7.20**, subjected to the cyclic loading is used to compare with the RC structure without stirrups. Similarly with the previous section, the stress distributions and crack patterns are investigated. Furthermore, the failure modes are studied as well.
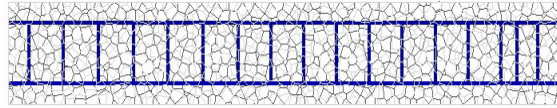
Figure 7.20 Analytical model of RC structure with stirrups

7.4.3.1 Stress Distribution

Suppose the same cyclic loading shown in **Figure 7.15** is acted on the RC structure with stirrups. The stress distributions of the Point A to Point C through A' and B' are shown in **Figure 7.21 (a)**, respectively. Compare this figure with **Figure 7.17 (a)** and **Figure 7.18 (a)**, it is obvious that the stress distributions are clearly dominated by the compression behaviour. That is, few variation of the stress distribution is seen in different stages, which is quite different from the stress distributions shown in **Figure 7.17 (a)** and **Figure 7.18 (a)**. Therefore, this phenomenon confirms that stirrups can improve the shear-resisting capacity of RC structures under the cyclic loading.

7.4.3.2 Crack propagation

In **Figure 7.21 (b)**, the magnification factor of 10 is used throughout all the illustrations of crack patterns, consistent with the previous sections.

From **Figure 7.21 (b)**, it is seen that the crack patterns on RC structures with stirrups subjected to the cyclic loading are primarily flexural cracks. Moreover, after more cycles of the loading, only the flexural cracks on RC structures become larger in width, length and number. This demonstrates that the failure mode on RC structures with stirrups under the cyclic loading should be flexural failure, which is different from the case of the RC structure under the cyclic loading but without stirrups shown in **Figure 7.17 (b)** and **Figure 7.18 (b)**.
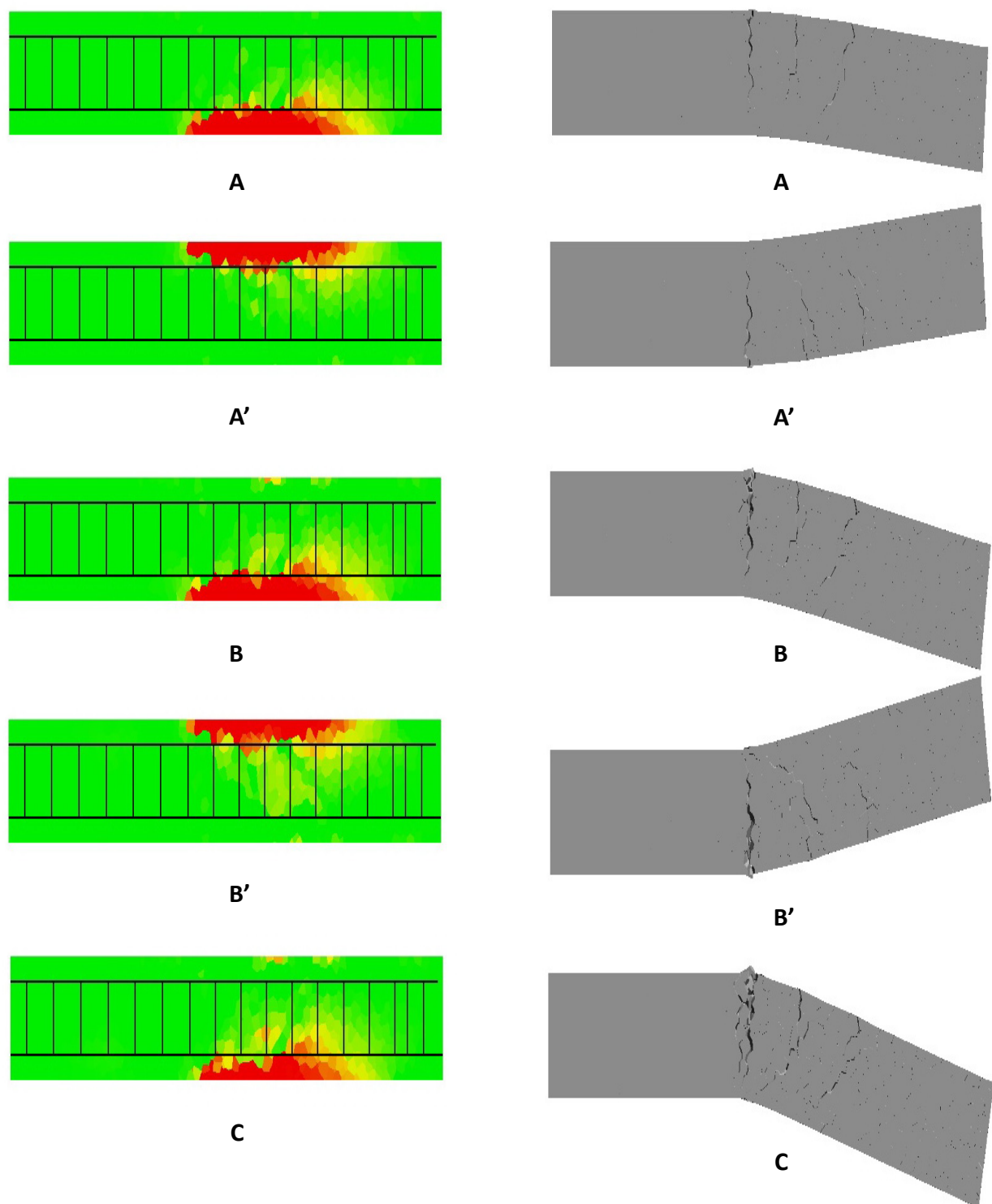
Figure 7.21 (a) Stress distributions at different points for RC structure with stirrups under cyclic loading; (b) Crack patterns at different points for RC structure with stirrups under cyclic loading

7.5 Results Discussion

(1) Technically speaking, RBSM method consists of the physical and mechanical behaviors of several constitutive models, such as concrete, steel rebar, etc. In the meanwhile, through various experimental designs, the corresponding parameters for the physical and mechanical behaviors used in the constitutive models are thus found. Therefore, after the constitutive model for nano-scale materials with the interface/surface energy effect based on the nano-mechanical framework in Chapters 3, 4, and 5 is formulated, 3D RBSM method is easy to incorporate with our present model by adding the analytical solutions and illustrative results into RBSM's constitutive model. For example, most of the parameters in constitutive models have the proportional or linear relations between the theoretical model and practical experiment. Therefore, at the beginning of deciding the parameter/factor in the constitutive model regarding the nano-composite materials with the interface/surface energy effect, the proportional relation between the theoretical model and practical experiment can be assumed, as follows,

$$\bar{K}' = \alpha \bar{K} \tag{7.1}$$

$$\bar{\mu}' = \beta \, \bar{\mu} \tag{7.2}$$

Where $\bar{K}$ and $\bar{\mu}$ are the effective moduli of the composite with the interface/surface energy effect, which can refer to Chapters 3, 4, and 5 for different types of inclusions and phases. α and β are the constitutive model parameters (corrected factors) between the theoretical model and practical experiment. They can be constants, polynomials, or functions. $\bar{K}'$ and $\bar{\mu}'$ are the effective moduli of the composite with the interface/surface energy effect after correction. Moreover, operated with the correlative experiments regarding

nanocomposite materials, the constitutive model parameters for the nano-scale materials with the interface/surface energy effect can be obtained. Furthermore, the correlative constitutive model parameters between theory and practice can be modified at all times through continuous experiments and accumulative experiences. Once this expected constitutive model is completed and involved in the developed 3D RBSM method, the effective properties of multi-phase composites with the interface/surface energy effect can be easily found through the RBSM method without complicated, difficult, tedious, and time-consuming formulations. However, nano-composite experiments are very expensive and difficult to execute at present technology. We hope in the early future, the science and technology will advance to implement nano-composite experiments easily, conveniently and cheap.

(2) 3D RBSM can simulate the shear failure after flexural yielding under cyclic loading. Accurate cracks and illustrative stress distribution can be developed and investigated using 3D RBSM programming.

(3) Curves for the degradation of the shear strength obtained by 3D RBSM analytical model show similar behavior with the proposed formula which obtained by statistical procedures, so that the possibility to evaluate the degraded shear strength using numerical analysis is confirmed.

(4) It is found that the shear behavior would take over the flexural behavior gradually with the increasing number of the cycles of the loading. As a result, a RC structure under more cyclic loading tends to perform a severer shear failure with the more remarkable shear behavior.

(5) It is discovered that within the cyclic loading, the shear cracks on RC structures become larger after a cycle, whereas the flexural cracks don't grow a lot. That is, the shear cracks on

RC structures under cyclic loading apparently develop in width, length and number after every cycle, but there is not much change for the flexural cracks in width, length and number. This phenomenon agrees with the concept that the shear behavior eventually dominates the failure mode when RC structures are subjected to cyclic loading.

7.6 Conclusions

Some applicable methods and/or programs are able to cooperate with our present model with the interface/surface energy effect, such as Finite Element Method (FEM), Rigid-Body-Spring Model (RBSM) method, ABAQUS, COMSOL, etc. Among them, RBSM method is recommended and introduced in this chapter. The reasons are as follows. Firstly, when the phases become more multiple, the formulations for analytical solutions are more complicated, difficult, tedious and time-consuming to derive. Secondly, in reality, the practical construction materials usually contain multi-phases, like concrete, wood, brick, masonry, etc. Accordingly, finding an easy and convenient method to estimate the interface/surface energy effect on those materials with multiple phases, so as to replace time-consuming and complicated micromechanical operations for the multiple-phase composites, is worth investigating and developing. Lastly, 3D RBSM method is easy to incorporate with our present model by adding the illustrative results based on the interface/surface energy effect into RBSM's constitutive model. Furthermore, the correlative constitutive model parameters between theory and practice can be modified at all times through continuous experiments and accumulative experiences. In addition, RBSM is capable of simulating the crack propagation and patterns, illustrating stress

distribution, providing effective properties of the composite materials, etc. It is beneficial for researchers to observe the external internal variations in the materials by using visible illustrations.

Technically speaking, RBSM method consists of the physical and mechanical behaviors of several constitutive models, such as concrete, steel rebar, etc. In the meanwhile, through various experimental designs, the corresponding parameters for the physical and mechanical behaviors used in the constitutive models are thus found. Therefore, after the constitutive model for nano-scale materials with the interface/surface energy effect based on the nano-mechanical framework in Chapters 3, 4, and 5 is formulated, 3D RBSM method is easy to incorporate with our present model by adding the analytical solutions and illustrative results into RBSM's constitutive model. Furthermore, operated with the correlative experiments regarding nanocomposite materials, the constitutive model parameters for the nano-scale materials with the interface/surface energy effect can be obtained. Moreover, the correlative constitutive model parameters between theory and practice can be modified at all times through continuous experiments and accumulative experiences. Once this expected constitutive model is completed and involved in the developed 3D RBSM method, the effective properties of multi-phase composites with the interface/surface energy effect can be easily found through the RBSM method without complicated, difficult, tedious, and time-consuming formulations. However, nano-composite experiments are very expensive and difficult to execute at present technology. We hope in the early future, the science and technology will advance to implement nano-composite experiments easily, conveniently and cheap.

7.7 Acknowledgements

7.8 References

[1]   Furuhashi, H., Nakamura, H., Yamamoto, Y. (2013). "Numerical Study on Shear Strength Degradation after Flexural Yielding of RC Member Subjected to Cyclic Loading." EASEC-13.

[2]   Gedik, Y. H., Nakamura, H., Yamamoto, Y., Kunieda, M. (2011). "Evaluation of Three-Dimensional Effects in Short Deep Beams using a Rigid-Body-Spring-Model." *Cement and Concrete Composites*, 33(9), pp. 978-991.

[3]   Machida, A., Mutsuyoshi, H., Toyoda, K. (1985). "Evaluation of the Ductility of Reinforced Concrete Members." Annual Journal of Japan Concrete Institute, Vol. 7, No. 1, pp. 629-632.

[4]   Ohe, R., Yoshikawa, H. (2002). "Study on shear strength degradation of single reinforced concrete columns under repeated large deformation." Doboku Gakkai Ronbunshuu E. V-56, No. 711, pp. 59–71.

[5]   Priestley, M. J. N., Seible, F., Carvi, G. M. (1996). "Seimic Design of Retrofit of Bridges." A Wiley-Interscience Publication.

[6]   Saito, S., Hikosaka, H. (1999). "Numerical Analysis of Reinforced Concrete Structures Using Spring Network Model." *Journal of Materials*, Concrete Structures and Pavements, Vol. 44, No. 627, pp. 289-303.

[7]   Yamamoto, Y., Nakamura, H., Kuroda, I., Furuya, N. (2013). "Simulation of Crack

Propagation in RC Shear Wall Using a 3D Rigid-Body-Spring Model with Random Geometry." FraMCoS-8.

Chapter 8

SUMMARY AND FUTURE WORK

8.1 Summary

Nowadays, since the materials science and technique have been further advanced to the characteristic size of solids and liquids in the nano-size structures and nanocomposites, the interface/surface energy effect on the mechanical and physical properties and damage energy dissipation of a nano-scale material or composite becomes significant and cannot be ignored. Therefore, the interface/surface energy and particle-size effects on the effective properties and the damage dissipation in nanocomposites are investigated. In this research, two viewpoints of observing the interface/surface energy effect are provided in Chapter 3 and Chapter 4. The first is studying the interface/surface energy effect on the effective properties of the composite material upon the mechanism of micromechanics, while the second is investigating the interface/surface energy effect on the energy dissipation due to the interfacial debonding between the particles and the matrix in the framework of the probability, such as the logarithmic normal distribution and Weibull's distribution function.

In Chapters 3, the interface/surface energy effect, regarded as the change of the residual elastic field induced by the interface stress from the reference configuration to the current configuration, is investigated. Beginning with the finite deformation analysis of a multi-phase hyperelastic medium, the interface energy effect on the macroscopic mechanical behavior of a

composite is studied. In particular, the approximate formulation of a finitely deformed multiphase elastic medium by an infinitesimal deformation analysis is emphasized. Moreover, due to the existence of the interface energy, even under no external loading, there is still a "residual elastic field" induced by the interface stress. In the process of the deformation of a composite from the reference configuration to the current configuration, the changes of the size and shape of the interface result in the change of this "residual elastic field". In addition, the governing equations describing the change of the "residual elastic field" due to the change of configuration are derived under the infinitesimal deformation approximation. Then, while the asymmetric interface stress is used in the Young-Laplace equation, the analytical equations of the size-dependent effective moduli of a particle-filled composite material with interface energy effect are developed. Therefore, the influence of the residual surface/interface tension can be taken into account. Later, the analytical expressions and corresponding illustrative results regarding the effective moduli of the composite containing spherical "equivalent inhomogeneities" (i.e. inhomogeneities together with the interface/surface energy) are discussed. It is found that the results with the interface/surface energy effect can also be applied to the nanocomposites, which is different from the results given by preceding researchers. In other words, the analytical results in this research can be applicable in nanocomposites, even if the formulations are mainly derived upon the mechanism of micromechanics. In addition, through the illustrative figures developed based on the analytical expressions, it can be found that the interface/surface effect decreases with the increase of the size of the voids and almost can be neglected when the radius of the void is larger than 10 nm. Moreover, it can be seen that the larger the interface/surface energy becomes, the more the effect of the interface/surface energy is on the effective moduli of the composite. Lastly, excluding the results produced by the Eshelby

method, the results developed by Ju and Chen's model and Mori-Tanaka's model are extremely approaching.

In Chapter 4, the primary objective is to extend the work regarding the interface/surface energy effect on size-dependent effective moduli of a "two-phase" composite containing identical particles of the same property and size, based on the framework of Lin and Ju (2009) and the methodology of Huang and Sun (2007), to the one regarding the interface/surface energy effect on size-dependent effective moduli of a "three-phase" composite containing two particles of the distinct properties with the same size. Before the analytical framework for the interface/surface energy effect on the size-dependent effective moduli of a three-phase composite with randomly located and interacting spherical particles of distinct properties is investigated, the interface/surface energy effect on the size-dependent effective moduli of a two-phase composite consisting of the matrix and randomly distributed spherical inhomogeneities is first considered by executing similar procedure in Chapter 3. Subsequently, the effective bulk and shear moduli of a three-phase composite containing randomly dispersed spherical particles of distinct elastic properties are separately formulated based on another framework with consideration to the concepts of probabilistic spatial distribution of spherical particles, pairwise particle interactions, and the ensemble-volume averaging (homogenization) procedure for three-phase elastic composites. Specifically, the approximate analytical solutions for the direct interactions between two different randomly located elastic spheres embedded in the matrix material are presented, followed by constructing the ensemble-volume averaged eigenstrains through the probabilistic pairwise particle interaction mechanism. Moreover, two non-equivalent formulations are considered in detail to derive effective elastic moduli of three-phase composites with no the interface/surface energy effect. Later on, in combination with the above two formulations,

effective elastic moduli of three-phase composites containing randomly dispersed distinct spherical particles with the interface/surface energy effect are analytically derived. In addition, numerical results and the corresponding discussions are presented to demonstrate the potential of this present model. Specifically, through the execution of some special cases, as well as the comparison with the results done in Chapter 3, it is further demonstrated that this developed analytical model for the interface/surface energy effect on effective moduli of three-phase composites containing randomly dispersed spherical particles of distinct elastic properties is applicable to reveal the influence of interface/surface energy in nano-scale composites. These comparisons and simulations encompass elastic matrices with randomly dispersed voids and/or particles. No Monte Carlo simulations or finite element calculations are needed here.

In Chapter 5, the primary objective of the present chapter is to extend the work regarding the interface/surface energy effect on size-dependent effective moduli of a three-phase composite containing two "particles" of the distinct properties with the same size, based on the framework of Ko and Ju (2013) and the methodology of Huang and Sun (2007), to the one regarding the interface/surface energy effect on size-dependent effective transverse elastic moduli of three-phase hybrid fiber-reinforced composites containing two "fibers" of the distinct properties sizes. Before the analytical framework for the interface/surface energy effect on the size-dependent effective transverse elastic moduli of a three-phase hybrid fiber-reinforced composite with randomly located and interacting aligned circular fibers of distinct properties and sizes is investigated, the interface/surface energy effect on the size-dependent effective moduli of a two-phase composite consisting of the matrix and randomly distributed aligned circular fibers is first considered. Subsequently, the effective transverse elastic bulk and shear moduli of a three-phase composite containing randomly located cylindrical fibers featuring distinct elastic

properties and sizes are separately formulated based on another framework with consideration to the concepts of probabilistic spatial distribution of spherical particles, pairwise particle interactions, and the ensemble-volume averaging (homogenization) procedure for three-phase elastic composites. Specifically, the approximate analytical solutions for the direct interactions between two different randomly located elastic fibers embedded in the matrix material are presented, followed by developing the ensemble-volume averaged eigenstrains through the probabilistic pairwise particle interaction mechanism. Moreover, two non-equivalent formulations are considered in detail to derive effective elastic moduli of three-phase composites with no the interface/surface energy effect. Later on, in combination with the above two formulations, effective transverse elastic moduli of three-phase hybrid fiber-reinforced composites containing randomly located and interacting aligned circular fibers of distinct elastic properties and sizes with the interface/surface energy effect are analytically derived. In addition, numerical results and the corresponding discussions are rendered to demonstrate the potential of this present model. Specifically, some special cases of the interface/surface energy effect on a three-phase composite containing randomly dispersed fibers of same/distinct properties embedded in an elastic matrix are executed. It is further demonstrated that this developed analytical model for the interface/surface energy effect on effective moduli of three-phase composites containing randomly dispersed circular fibers of distinct elastic properties and sizes is applicable to reveal the influence of interface/surface energy in nano-scale composites.

In Chapter 6, both of the particle-size and interface/surface energy effects on the energy dissipation due to the interfacial debonding between the particles and the matrix in nanocomposites are investigated. The size distribution of particles is supposed to comply to the logarithmic normal distribution, while the probability of the interfacial debonding between the

287

particles and the matrix is considered to satisfy the Weibull's distribution function. Then, the formulation of the energy dissipation due to the interfacial debonding is developed. Accordingly, several results regarding the particle-size and interface/surface energy effects on the energy dissipation due to the damage evolution are illustrated after a series of numerical calculations. Among these numerical results, the damage energy dissipation crest with respect to the average size of particles is found to demonstrate that the energy dissipation due to the damage evolution extremely depends on the size of particles and interface/surface energy in nanocomposites. From the analysis of the numerical results, it is found that there exists a characteristic crest for each curve of the damage energy dissipation with respect to the average radius of particles, a_0. Moreover, the position of the crest moves towards small size direction of a_0 with the average normal stress of σ increases. When the average radius of particles is less than the critical average size, a_{0cr}, the composite possesses the characteristic of the nanocomposite. That is, the damage energy dissipation increases with the increment of the average radius. This is the special phenomenon of the size effect on the damage energy dissipation in nanocomposites, which is completely different from that in microcomposites. In addition, the effects of the larger particle-size dispersion, the larger average normal stress at the interface, and the smaller interface/surface energy between the particles and the matrix materials may result in more energy dissipation due to the interfacial debonding between particles and the matrix. Finally, for a given damage energy dissipation, the larger the average size of particles in the range of nanometer size is, the more volume fraction the a particle requires. Moreover, if the average radius, a_0, is fixed, the larger the value of f_{p0} is, the more the damage energy dissipation in nanocomposites becomes.

Another method, called Rigid-Body-Spring Model (RBSM) method, is introduced in

Chapter 7. The reasons are as follows. Firstly, when the phases become more multiple, the formulations for analytical solutions are more complicated, difficult, tedious and time-consuming to derive. Secondly, in reality, the practical construction materials usually contain multi-phases, like concrete, wood, brick, masonry, etc. Accordingly, finding an easy and convenient method to estimate the interface/surface energy effect on those materials with multiple phases, so as to replace time-consuming and complicated micromechanical operations for the multiple-phase composites, is worth investigating and developing. Lastly, 3D RBSM method is easy to incorporate with our present model by adding the illustrative results based on the interface/surface energy effect into RBSM's constitutive model. Furthermore, the correlative constitutive model parameters between theory and practice can be modified at all times through continuous experiments and accumulative experiences. In addition, RBSM is capable of simulating the crack propagation and patterns, illustrating stress distribution, providing effective properties of the composite materials, etc. It is beneficial for researchers to observe the external internal variations in the materials by using visible illustrations. Technically speaking, RBSM method consists of the physical and mechanical behaviors of several constitutive models, such as concrete, steel rebar, etc. In the meanwhile, through various experimental designs, the corresponding parameters for the physical and mechanical behaviors used in the constitutive models are thus found. Therefore, after the constitutive model for nano-scale materials with the interface/surface energy effect based on the nano-mechanical framework in Chapters 3, 4, and 5 is formulated, 3D RBSM method is easy to incorporate with our present model by adding the analytical solutions and illustrative results into RBSM's constitutive model. Furthermore, operated with the correlative experiments regarding nanocomposite materials, the constitutive model parameters for the nano-scale materials with the interface/surface energy effect can be

obtained. Moreover, the correlative constitutive model parameters between theory and practice can be modified at all times through continuous experiments and accumulative experiences. Once this expected constitutive model is completed and involved in the developed 3D RBSM method, the effective properties of multi-phase composites with the interface/surface energy effect can be easily found through the RBSM method without complicated, difficult, tedious, and time-consuming formulations. However, nano-composite experiments are very expensive and difficult to execute at present technology. We hope in the early future, the science and technology will advance to implement nano-composite experiments easily, conveniently and cheap.

8.2 Future Work

The main objective of this research is to develop the characteristic analytical expressions of the effective properties and the damage energy dissipation of the composite, especially the nanocomposite, with the interface/surface energy and particle-size effects. In general, since parts of the special cases/illustrations and/or formulations in the research is established with some assumptions, such as the axisymmetric stresses or loads, symmetric geometry of structures, fewer phases of composites, small deformation, linear elastic moduli of materials, linearized parameters, etc., our further work is to modify and impose more complicated conditions and/or multi-physical parameters into the present analytical expressions. In other words, there still exists some insufficient aspects in the present model, and these are particularly discussed in the following points:

(1) In this research, two viewpoints of observing the interface/surface energy effect are

provided. For example, the influence of the interface/surface energy on the effective moduli of a composite upon the mechanism of micromechanics is investigated, while that on the damage energy dissipation based on the framework of the probability for the size distribution and interfacial debonding between particles and the matrix is studied. However, the interaction and connection between these two models is not developed yet. Thus, there still exists a big step for the complicated and challenging mathematical derivations and formulations.

(2) It is known that continuous fiber-reinforced composites possess high strength and stiffness in the direction of fibers. The overall mechanical behavior of a fiber composite depends on the constituent properties of the matrix and reinforcements as well as the microstructure. Several possible damage modes exist for fiber composites, such as the interfacial fiber-matrix debonding, the matrix cracking, the fiber breakage, the fiber-pullout, and the shear sliding of fibers. Specifically, the dominant damage mechanism in continuous unidirectional two phase fiber-reinforced ductile composites featuring same elastic properties and sizes of fibers under transverse loading is the initiation and progressive interfacial partial fiber debonding (arc microcracks) or fiber cracking followed by plastic yielding (Ko, 2005; Ju et al., 2006; Ju et al., 2008; Ju and Ko, 2008; Ju et al., 2009; Ko and Ju, 2012). Current studies will pave the way for future investigations in various damage mechanisms of continuous unidirectional three-phase hybrid fiber-reinforced composites with the interface/surface energy effect under transverse loadings. Thus, optimum cost and performance of hybrid fiber-reinforced composites with the interface/surface energy effect can be achieved through proper material design.

(3) Since some simpler special cases are used to create the illustrative results either in Chapters

3, 4, 5 and in Chapter 6, other physical and mechanical parameters may be considered in the following model, such as specific materials, dimensions, shapes and sizes of the composite constituents, thermal effect, dynamic-elastic, and even the interactions among the above parameters. However, the formulating and computational processes are usually time-consuming, especially if more types of multi-phase materials and multi-physical parameters are imposed in a model at the same time. Therefore, it is necessary and convenient to cooperate with some useful applicable programs, like ABAQUS, COMSOL, etc., in the analysis of multi-phase composites and multi-physical parameters. In the meantime, another method, called Rigid-Body-Spring Model (RBSM) method, is introduced in Chapter 7. 3D RBSM performs excellent in simulating the crack propagation and patterns, illustrating stress distribution, providing effective properties of the composite material, etc. Therefore, if constitutive illustrative or analytical models for nano-scale inclusions with the interface/surface energy effect can be formulated based on the framework constructed in Chapters 3, 4, and 5, combined with the execution of the correlative experiments regarding the specific nanocomposite materials, the model parameters for the nano-scale inclusions are thus obtained. Once this expected model is completed, the effective properties, including elastic and plastic parts, of multi-phase composites will be easy found by using RBSM method.

(4) In general, the displacement gradient of the interface is not necessary to be symmetric in Chapters 3, 4, and 5. For instance, for a cylindrical inclusion embedded in an infinite matrix, the displacement gradient of the interface could be expressed in terms of the physical components (u_r, u_θ, u_z) in a cylindrical polar coordinate system (r, θ, z), as follows

$$\nabla_{0s}\mathbf{u} = \left(\frac{1}{r}\frac{\partial u_\theta}{\partial \theta} + \frac{u_r}{r}\right)\mathbf{e}_\theta \otimes \mathbf{e}_\theta + \frac{\partial u_z}{r\partial \theta}\mathbf{e}_\theta \otimes \mathbf{e}_z + \frac{\partial u_\theta}{\partial z}\mathbf{e}_z \otimes \mathbf{e}_\theta + \frac{\partial u_z}{\partial z}\mathbf{e}_z \otimes \mathbf{e}_z \qquad (8.1)$$

Obviously, under an anti-plane shear deformation, Eq. (8.1) is not a symmetric tensor. In this case, an asymmetric Piola-Kirchhoff stress, Eq. (3.50), has to be used in Eq. (3.43).

(5) In Chapter 3, the Ju and Chen's scheme, Mori-Tanaka approximation method and Eshelby method are used to predict the effective moduli of a composite. For spherical inclusions, pointed out by Weng (1990), the effective moduli derived from the Mori-Tanaka method are identical to the Hashin-Shtrikman bounds (Hashin and Shtrikman, 1963). Actually, once K_* and μ_* are obtained, the effective moduli can also be calculated by using other micromechanical schemes such as the generalized self-consistent method (Christensen, 1979), the double-inclusion method (Nemat-Nasser and Hori, 1999), and the IDD estimate (Zheng et al., 2001). It could be interesting to establish the corresponding expressions of the effective moduli of the composite in the future to provide different viewpoints to study the difference of various models. Moreover, it is very possible to improve the present model from the comparison among a variety of models.

(6) In Chapters 3, 4, and 5, although circular or spherical inhomogeneities are only considered in the above discussion, the method can also be applied to the materials with inhomogeneities of different shapes and geometries. As K_* and μ_* are related to the size of the inhomogeneity, inhomogeneities with different shapes should be regarded as different "equivalent inhomogeneities".

(7) The interface is assumed to be elastically isotropic. However, in many materials such as single crystals, the interface may be anisotropic. In this case, the interface constitutive relations for anisotropic materials given by Huang and Wang (2006) may be used, and the

293

effective moduli and damage energy dissipation of the composite can still be predicted by using the similar procedure in Chapters 3, 4, 5 and 6. The greater difficulty lies in that there exists more material parameters and the algebraic operations for the analytical expressions, so the process of the formulations and derivations must be more complicated.

(8) Experimental validations are key parameters in the calibration of proposed models. Further experimental validations and comparisons will be performed once the associated experimental data become available. To the author's best knowledge, the experimental data associated with Chapters 3, 4, and 5 are currently not available due to difficulties in performing such experimental works. For example, as the illustrative figures developed based on the framework in Chapters 3, 4, and 5, it is found that the interface/surface effect decreases with the increase of the size of the fiber-shape voids and can be neglected when the radius of the void is larger than 5 nm. In other words, it is quite difficult to manufacture so small nanocomposites nowadays. Similarly, there exists an absence of the corresponding experimental data for the purpose of comparison with the present analytical models in Chapter 6. Once the corresponding experimental data become available, it would be very helpful to examine and test the accuracy and validity of the illustrative results and concepts developed by our present models and to further modify and improve the present models.

8.3 References

[1] Christensen, R. M., and Lo, K. H. (1979). "Solutions for effective shear properties in 3 phase sphere and cylinder models." *Journal of the Mechanics and Physics of Solids*, 27(4),

315-330.

[2] Hashin, Z., Shtrikman, S. A. (1963). "A variational approach to the theory of the elastic behavior of multiphase materials." *Journal of the Mech. Phys. Solids*, 11, 127-140.

[3] Ju, J. W., and Chen, T. M. (1994a). "Micromechanics and effective moduli of elastic composites containing randomly dispersed ellipsoidal inhomogeneities." *Acta Mechanica*, 103(1-4), 103-121.

[4] Ju, J. W., and Chen, T. M. (1994b). "Effective elastic-moduli of 2-phase composites containing randomly dispersed spherical inhomogeneities." *Acta Mechanica*, 103(1-4), 123-144.

[5] Ju, J. W., and Chen, T. M. (1994c). "Micromechanics and effective elastoplastic behavior of 2-phase metal-matrix composites." *Journal of Engineering Materials and Technology-Transactions of the Asme*, 116(3), 310-318.

[6] Lin, P. J., Ju, J. W. (2009). "Effective elastic moduli of three-phase composites with randomly located and interacting spherical particles of distinct properties." *Acta Mechanica*, 208, 11-26.

[7] Mori, T., and Tanaka, K. (1973). "Average stress in matrix and average elastic energy of materials with misfitting inclusions." *Acta Metallurgica*, 21(5), 571-574.

[8] Nemat-Nasser, S., Hori, M. (1999). "Micromechanics: overall properties of heterogeneous elastic solids." North-Holland, Amsterdam, 2nd edition.

[9] Weng, G. J. (1990). "The theoretical connection between Mori-Tanaka theory and the Hashin-Shtrikman-Walpole bounds." *International Journal of Engineering Science*, 28(11), 1111-1120.

[10] Zheng, Q. S., and Du, D. X. (2001). "An explicit and universally applicable estimate for the

effective properties of multiphase composites which accounts for inclusion distribution."

Journal of the Mechanics and Physics of Solids, 49(11), 2765-2788.